THE UNIVERSITY
of ADELAIDE

Quantifying Australian atmospheric properties for a Gamma-ray Observatory to operate at energies greater than 10 TeV

Tristan William Sudholz
For the degree of Masters of Science (Astrophysics)

Principal Supervisor: Prof. B.R. Dawson
Co-Supervisors: Dr. G.P. Rowell & EProf. R.W. Clay

April, 2014

Declaration

I, Tristan William Sudholz, certify that this work contains no material which has been accepted for the award of any other degree or diploma in any university or other tertiary institution and, to the best of my knowledge and belief, contains no material previously published or written by another person, except where due reference has been made in the text. In addition, I certify that no part of this work will, in the future, be used in a submission for any other degree or diploma in any university or other tertiary institution without the prior approval of the University of Adelaide and where applicable, any partner institution responsible for the joint-award of this degree.

I give consent to this copy of my thesis, when deposited in the University Library, being made available for loan and photocopying, subject to the provisions of the Copyright Act 1968.

I also give permission for the digital version of my thesis to be made available on the web, via the Universitys digital research repository, the Library catalogue and also through web search engines, unless permission has been granted by the University to restrict access for a period of time.

Tristan William Sudholz

Abstract

Newly proposed $\geqslant$ 10 TeV (1 TeV = 10^{12} eV) imaging atmospheric Cherenkov technique (IACT) γ-ray experiments will need optimal sites for their construction and operation at energies above 10 TeV. Quantifying the optical properties of Australian atmospheres will be part of a site survey to determine the viability of possible IACT Australian sites. Atmospheric optical properties need to be quantified as a TeV IACT γ-ray array detects Cherenkov radiation that has propagated through the atmosphere within the visible spectrum. For the optimum collection of Cherenkov radiation, sites with the highest optical atmospheric transmission are ideal. Another optical property of concern is the night sky background (NSB) level. NSB photons are a form of background noise that can cause accidental triggering, therefore sites with the lowest levels of NSB are desired. Further information on IACT and the NSB is presented in Chapter 2.

The optical properties of the Australian atmosphere which I quantified for the site surveys were the optical transmission and the NSB. The optical transmission was measured through the star extinction coefficient. The star extinction coefficient and the NSB were found through the method of photometry using a Pentax K10D digital single lens reflex (DSLR) camera. Because a Pentax K10D DSLR camera has not previously been used for this purpose, I initially conducted viability tests on its ability to measure the NSB and star extinction coefficients. I will present these results in Chapter 5. Data collected from multiple trips to Fowlers Gap in New South Wales, Australia, were used for this purpose. I will present the results of star extinction coefficient and NSB level measurements in Chapter 6.

To further help understand the effects of atmospheric conditions, I have investigated the effects of differing levels of aerosols and the effects of cirrus clouds on the performance of a simulated $\geqslant$ 10 TeV IACT γ-ray array. I give more information about simulated IACT γ-ray array's in Chapter 3 and present the results in Chapter 4. The effects of cirrus clouds were investigated as these clouds occur at a similar height to the maximum emission of Cherenkov photons for γ-ray shower energies around 10 TeV.

Acknowledgements

I would like to acknowledge the support and encouragement I received while completing this research. I would like to thank my supervisors, Bruce Dawson, Gavin Rowell, and Roger Clay, for all of their guidance, advice and support. I would like to thank my fianc for her unending patience, understanding and belief that I could complete this thesis. I would like to thanks my parents for their encouragement and support, both financial and emotional. I would like to thank Kathy's parents for their encouragement and support. Finally, I would like to thank the rest of the High Energy Group's members who I have had lively discussions with and shared a drink with at the Adelaide Uni Staff Club.

Contents

Chapter 1

Introduction

The main purpose of Very High Energy (VHE) γ-ray astronomy is to study the non-thermal universe. In particular, its purpose is to study the origins and the acceleration mechanisms of cosmic-rays, which were first identified in 1912 by Victor Hess [1]. Cosmic-rays are protons or more complex nuclei that have arrived from outside of the Earth. γ-rays are secondary particles which may be produced from neutral pion decay resulting from proton-proton interactions, from Inverse Compton scattering of electrons, or from the Synchrotron Self-Compton process. γ-rays are useful messenger particles as they are charge neutral, which allows them to travel in straight lines through cosmic magnetic fields, unlike charged particles[1]. VHE γ-ray astronomy covers the energy range from 10^{11} eV to 10^{14} eV.

The first ground-based Cherenkov detectors were inspired by the flux prediction of TeV (1 TeV = 10^{12} eV) γ-rays from the Crab Nebula by Cocconi [2]. The first ground-based TeV γ-ray detectors did not observe any γ-ray showers when basing their experiments on this result. It was later found that the predicted flux was 1000 times larger than the actual detected flux. The Smithsonian Astrophysical Observatory 10 metre optical reflector [3] was the first experiment to have some partial success in detecting the TeV γ-ray spectrum of the Crab Nebula. The observation was not considered to be statistically significant but was a stepping stone to the first significant detection. The Whipple Observatory (until 1981 known as the Smithsonian Astrophysical Observatory) was the first Imaging Atmospheric Cherenkov Technique (IACT) telescope to achieve a significant detection of the Crab Nebula. The 9σ detection was achieved by effectively separating the small number of γ-ray events from the large number of background cosmic-ray events. This signal from the Crab Nebula was the first strong evidence that TeV γ-ray sources exist [4]. The observation was done with the use of an optical telescope that contained a 37-pixel camera (using photomultiplier tubes as the pixels) that recorded an image of each extensive air shower (EAS) that was viewed. The separation of γ-ray and cosmic-ray events was achieved by using an analysis technique developed by Hillas [5]. Hillas' analysis technique separated γ-ray events from cosmic-ray events by exploiting differences in certain shower image parameters. These parameters became known as the Hillas parameters. I

---

[1] This does not apply as much to the highest energy cosmic-rays ($> 10^{19}$ eV). Cosmic-rays above this energy have less deviated paths due to their large gyro-radii. Detected particles above this energy are believed to have effectively travelled with very little deviation.

cover IACT telescopes in further detail in Chapter 2.

The first experiment to combine stereoscopic detection with IACT was the HEGRA (High Energy Gamma RAy) experiment [6]. Stereoscopic IACT involves using multiple telescopes to image the light emitted from an EAS. Stereoscopic detection yielded improved angular resolution, better energy reconstruction and strong background suppression to increase sensitivity. Some of the current experiments that have observed VHE γ-rays with stereoscopic IACT are H.E.S.S. [7] and CANGAROO III [8] in the southern hemisphere and MAGIC [9] and VERITAS [10] in the northern hemisphere. I cover stereoscopic detection and IACT arrays in Chapter 3.

To date, these experiments have detected ~ 130 confirmed TeV γ-ray sources [11], covering a wide range of objects. Both galactic and extra-galactic objects have been associated with TeV γ-rays. Examples of galactic objects associated with TeV γ-rays include:

- **Supernova Remnants (SNR):** A source mechanism for TeV γ-rays from SNR is the interaction of particles from a supernova with molecular clouds. Supernova remnants result from the ejection of particles in a shock wave after the collapse of a star. The resultant emission of TeV γ-rays can come from either hadronic or leptonic acceleration processes. The energy from supernovae may be responsible for the bulk of cosmic ray production in the galaxy. An example of TeV γ-rays observed from a SNR is RX J1713.7-3946 [12].

- **Pulsar Wind Nebulae (PWN):** The source of TeV γ-rays for a PWN is from the accelerated particles within a shock region. A pulsar is a rapidly rotating neutron star, containing strong magnetic fields. The region is produced when pulsar generated particles interact with the ambient medium. An example of TeV γ-rays observed from a PWN is the Crab Nebula [4].

- **Massive Stellar Clusters:** The source of TeV γ-rays within a massive stellar cluster may be accelerated particles contained in collision regions. The collision regions are believed to be created by interacting fast and strong winds from massive stars bound in multiple star systems. An example of TeV γ-rays observed from a massive stellar cluster is HESS J1023-575 [13] .

- **γ-ray Binaries:** The source of TeV γ-rays in a γ-ray binary is particles interacting around a compact object. A γ-ray binary can be formed when a compact object, like a neutron star or black hole, acretes materials from a companion star. A γ-ray binary may exhibit processes found in active galactic nuclei but on a smaller scale. An example of TeV γ-rays observed from a γ-ray binary is PSR B1259-63 [14].

An example of a type of an extra-galactic object associated with TeV γ-rays is:

- **BL Lacertae (BL Lac) object:** The source of TeV γ-rays in BL Lac objects is the beam of particles emitted from jets interacting with the ambient medium. A BL Lac object is a type of active galactic nucleus (AGN). BL

Lac objects are characterised by rapid and large-amplitude flux variability. Emission from Markarian 501 is an example of TeV γ-rays observed from a BL Lac object [15].

There is also a set of detected TeV γ-ray sources that currently have no known galactic or extra-galactic object associated with them.

1.1 Motivation

To obtain more information about a source, it is useful to identify the γ-ray differential energy spectrum. Measuring the differential energy spectrum can give information on the acceleration processes. Figure 1.1 and Figure 1.2 give examples of two types of observed spectra. Figure 1.1 is of SNR RXJ1713.7-3946 [16] observed by H.E.S.S. It is a prime example of a source that contains a cut-off (or a down turn) in the energy spectrum, while Figure 1.2 is of two H.E.S.S. sources [17] with differential energy spectra that have no observable high energy cut-off. The absence of a cut-off could be explained by the acceleration process at the source producing γ-rays that are more energetic than the current observation limit of VHE γ-ray experiments. One of the main motivators for γ-ray astronomy above 10 TeV is to observe cut-offs in differential energy spectra (if any) that could occur above the current observable energy range.

Experiments like H.E.S.S. have limited capacity to observe shower energies above 10 TeV due to the limited size of their "effective collecting area" (A_{eff}) (see Chapter 2 for further details). To demonstrate the need for new experiments to observe γ-rays above 10 TeV, I will show how the A_{eff} for H.E.S.S. (a current experiment in operation) impacts on the required observing time for TeV γ-ray sources. I calculate an estimated observing time for H.E.S.S. in an energy region above and below 10 TeV and will show that the observing time for an energy region above 10 TeV is unreasonably large. Using the H.E.S.S. source J1857+026 differential energy spectrum, fitted with a power law [17]:

$$\frac{dN}{dE} = 6.1 \times 10^{-8} E^{-2.39} \ \ (\mathrm{TeV})^{-1}\ \mathrm{m}^{-2}\ \mathrm{s}^{-1} \tag{1.1}$$

I can obtain the γ-ray flux (Γ) in the energy range of 1-10 TeV with the following equation:

$$\begin{aligned} \Gamma &= \int_1^{10} \frac{\mathrm{dN}}{\mathrm{dE}}\,\mathrm{dE} \qquad (1.2) \\ \Gamma &= 6.8 \times 10^{-8} \int_1^{10\mathrm{TeV}} \mathrm{E}^{-2.39}\,\mathrm{dE} \\ &= 4.2 \times 10^{-8}\ \ \mathrm{m}^{-2}\ \ \mathrm{s}^{-1} \end{aligned}$$

For the energy region of 1-10 TeV, H.E.S.S. has an A_{eff} of around 2 × 10^5 m^2 for a zenith angle of 20°. The A_{eff} of H.E.S.S. is shown in Figure 1.3. I can obtain

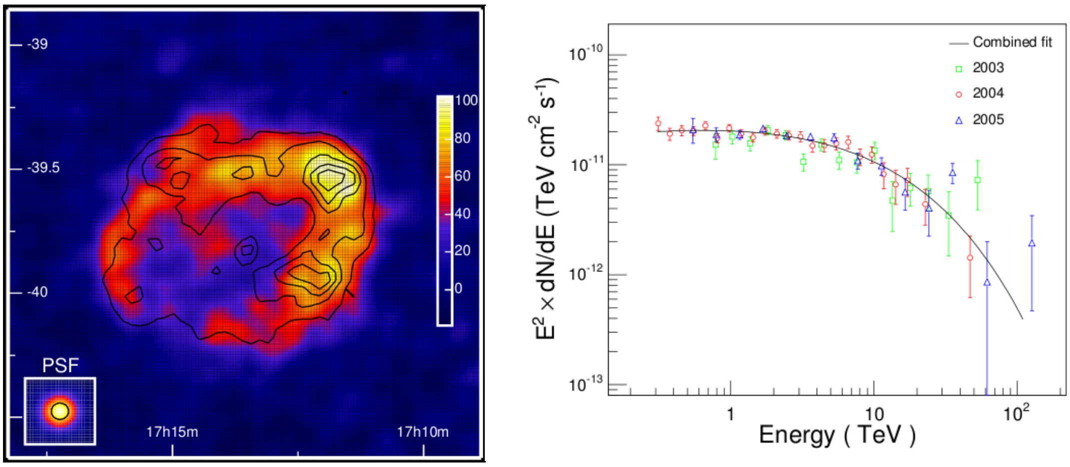

(a) (b)

Figure 1.1: (a) Image of HESS source SNR RXJ1713.7-3946, an example of TeV γ-rays observed from a supernova remnant (SNR) and (b) the differential energy spectrum of SNR RXJ1713.7-3946. This spectrum is an example of a source with a very well defined cut-off energy. Images taken from [16].

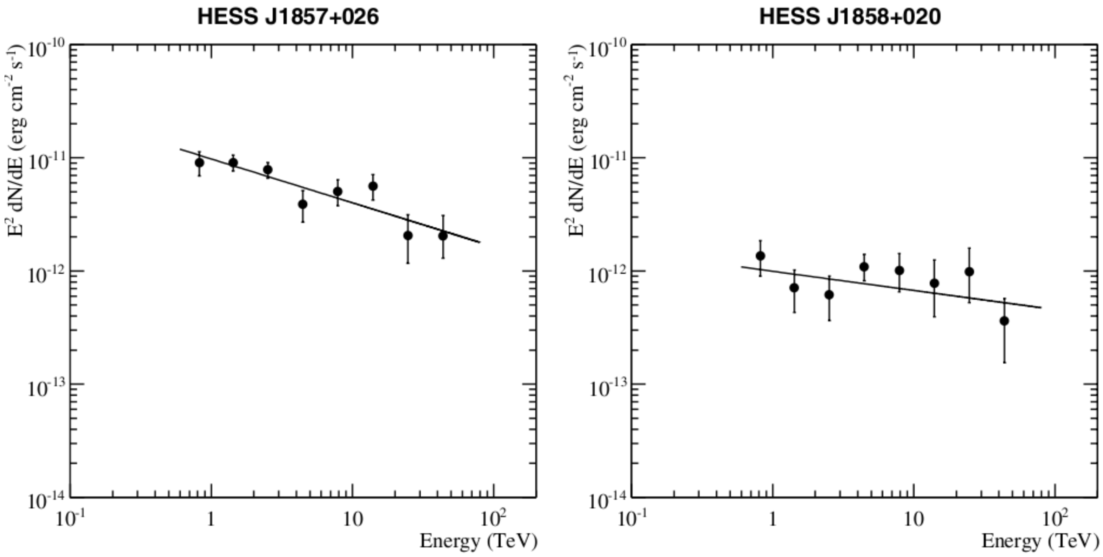

Figure 1.2: Two examples of differential energy spectra that contain no observed cut-off in their spectra between $\sim$ 1 TeV and 50 TeV. HESS J1857+026 has a power-law spectral fit of 6.1×10^8 E$^{-2.39}$ m^{-2} s^{-1} (TeV)$^{-1}$, while HESS J1857+020 has a power-law spectral fit of 0.6×10^8 E$^{-2.17}$ m^{-2} s^{-1} (TeV)$^{-1}$. Both of these sources have no identified counterparts. Plots taken from [17].

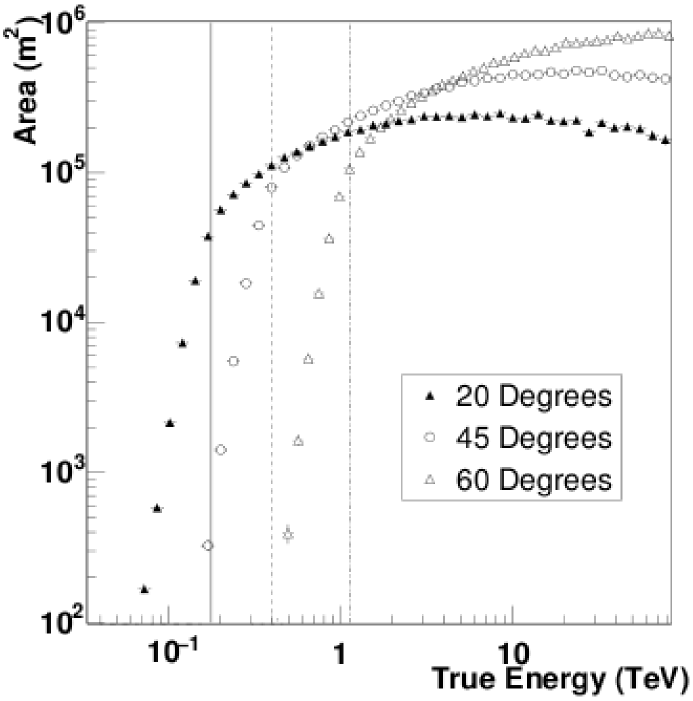

Figure 1.3: The "effective collecting area" (A_{eff}) of the H.E.S.S. experiment as a function of energy for three different zenith angles. Plot taken from [18].

an estimate of the γ-ray detection rate (r_γ) from:

$$\begin{aligned} r_\gamma &= A_{eff} \times \Gamma \qquad (1.3) \\ &= (2.0 \times 10^5 \ \mathrm{m}^2) \times (4.2 \times 10^{-8} \ \mathrm{m}^{-2} \ \mathrm{s}^{-1}) \\ &= 8.0 \times 10^{-3} \ \mathrm{s}^{-1} \end{aligned}$$

or a γ-ray detection about 1 every 120 seconds. If I were to impose a minimum detection of 10 γ-rays to achieve a satisfactorily small statistical uncertainty on the detection rate, I would require an observing time of about 20 minutes. However, if the calculation is repeated for an energy region of between 91 and 100 TeV, I find that the required observing time is about 170 hours for a minimum detection of 10 γ-rays. This calculated observing time far exceeds what could be considered reasonable to discover a new source. In comparison, 100 hours is required for detailed studies, like spectral analysis, for observations around 1 TeV. To observe above 10 TeV, a new instrument with a much larger A_{eff} needs to be employed if using similar techniques to H.E.S.S and previous experiments. To have similar γ-ray count rates above 10 TeV to those which H.E.S.S. observes above 1 TeV, the instrument would need an A_{eff} of around 10 km^2 (10^7 m^2). This instrument would then allow observations in this relatively unknown high energy area of VHE γ-ray astronomy. New proposals like CTA [19] and *TenTen* [20] have design ideas for building instruments that fit this criterion.

1.2 Present Work

These proposed experiments with A_{eff} of around 10 km^2 (like CTA and *Ten-Ten*) will need to be constructed at optimal sites for operation at energies above 10 TeV. The viability of Australian sites for construction of these experiments will be determined through site surveys. Part of these site surveys will include quantifying the optical properties of Australian atmospheres. Atmospheric optical properties need to be quantified as the TeV γ-ray array detects Cherenkov radiation that is propagated through the atmosphere. For the optimum collection of atmospheric Cherenkov radiation, sites with the highest optical atmospheric transmission are ideal. Another optical property to be measured is the night sky background (NSB) level. NSB photons are a form of background noise and can cause accidental triggering of the telescope, therefore sites with the lowest levels of NSB are desired. In Chapter 4, I investigate the effects of differing levels of atmospheric transmission on the performance of a simulated IACT γ-ray array to operate at energies greater than 10 TeV. The level of atmospheric transmission in my modelling was changed through the introduction of aerosols. The effects of cirrus clouds on the simulated IACT array performance were quantified.

As part of the Australian site surveys, I developed a method using a Pentax K10D digital single lens reflex (DSLR) camera to quantify the optical transmission (measured through the star extinction coefficient) and the NSB, and applied this method during a site survey of Fowlers Gap in New South Wales. Because a Pentax K10D DSLR camera has not previously been used for this purpose, I initially conducted viability tests on its ability to measure the NSB and star extinction coefficients. I will present these results in Chapter 5. Data collected from multiple trips to Fowlers Gap was used for this purpose. I will present the results of star extinction coefficients and NSB levels measurements from the trips to Fowlers Gap in Chapter 6.

Chapter 2

The Imaging Atmospheric Cherenkov Technique (IACT)

The imaging atmospheric Cherenkov technique (IACT) is a ground-based technique that uses optical telescopes to image Cherenkov radiation produced from extensive air showers (EAS). Using this technique, TeV γ-rays can be observed. In this chapter I discuss IACT telescopes, the night sky background (NSB), EAS, Cherenkov radiation and the Earth's atmosphere. I explain electromagnetic and hadronic EAS and their ability to produce Cherenkov radiation. The Earth's atmosphere is discussed as it is an interactive medium for particle interactions to produce EAS, while Rayleigh and aerosol scattering within the atmosphere effect the Cherenkov radiation propagating to ground level. Detection of NSB by optical telescopes is discussed as it is a form of background noise that can cause false triggering within an IACT telescope.

2.1 IACT Telescopes

A single Cherenkov telescope is the basic unit of an IACT array. Single telescopes consist of optical mirrors and they employ photomultiplier tubes (PMTs) as pixels in their camera. An example of a Cherenkov telescope and the camera from the H.E.S.S. experiment [7] are shown in Figure 2.1. An image of the EAS is produced if a telescope is within the Cherenkov light pool. A diagrammatic example of how a telescope can observe an EAS shower, when within the Cherenkov light pool, is shown in Figure 2.2. The "effective collecting area" (A_{eff}) of a Cherenkov telescope is defined by the size of the Cherenkov light pool that triggers the telescope, not by the physical size of the telescope. Hence, a detection can be achieved even if the EAS is not directed straight towards the telescope. The A_{eff} varies from shower to shower, depending on a number of variables including:

- Shower energy
- Arrival angle from the zenith
- Telescope Field of View (FoV) and mirror size
- Distance between the telescope and the shower's core on the ground
- Telescope trigger settings

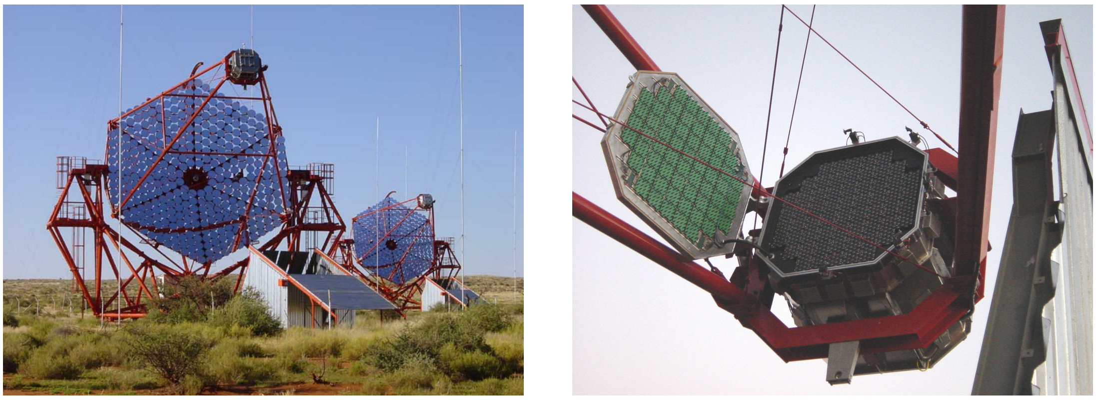

Figure 2.1: Shown here is an example of an imaging atmospheric Cherenkov technique (IACT) telescope (left) and a camera containing photomultiplier tubes (right). Pictures are from the H.E.S.S. experiment [7].

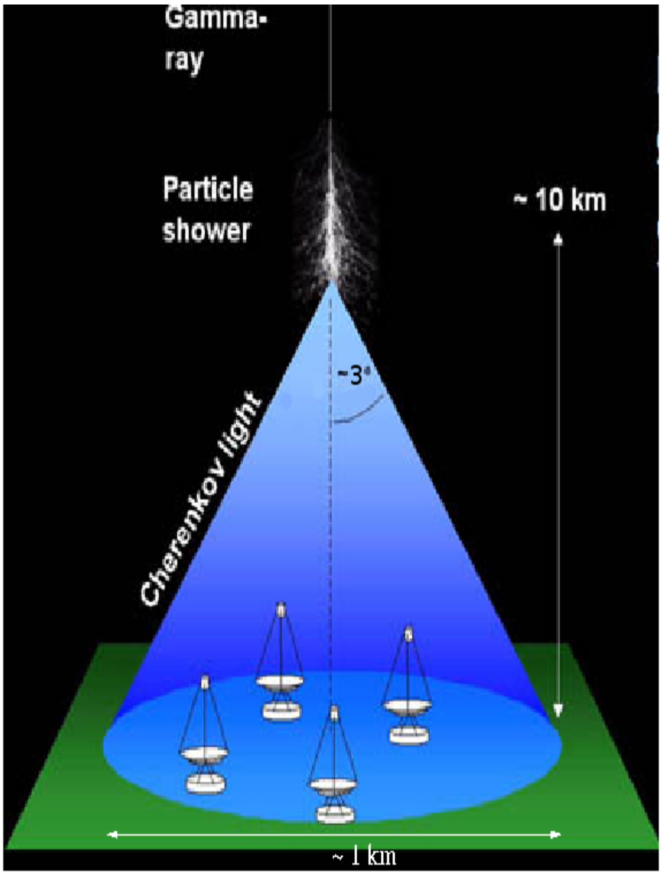

Figure 2.2: Here is an example of a Cherenkov light pool with a diameter of 1 km. The light pool is formed from the Cherenkov light emitted by secondary charged particles interacting with atmospheric molecules between ~ 26 - 10 km a.s.l. Also shown here are 4 telescopes viewing the Cherenkov radiation by being within the light pool.

When detecting Cherenkov light from EAS, the telescope will also detect photons from the night sky background (NSB) (see Subsection 2.1.1 for further details). NSB photons are described as any photons other than Cherenkov photons. To minimise triggers from NSB photons, a trigger condition can be set to require a group of nearby pixels to be above a certain signal threshold. Studies [21, 22] have shown that the triggers from NSB can be reduced by increasing the number of pixels within the group containing signals above a threshold. Once the threshold is reached, the telescope is said to be triggered and the whole camera is read-out.

To further increase the efficiency of γ-ray detection, multiple telescopes are used to image the same EAS. Figure 2.2 shows how this can be achieved by having multiple telescopes within the Cherenkov light pool. A multiple telescope system is called an IACT array (see Chapter 3 for further details).

2.1.1 Night Sky Background

The NSB is measured by detecting photons from a "dark" area of the sky, where no discernible objects like stars or galaxies are detected. Sources of these NSB photons are airglow, zodiacal light, scattered starlight and man-made light.

- **Airglow**: This phenomenon occurs where light is emitted from atoms or molecules in the upper atmosphere that have been excited by solar particles or UV radiation during the day. The brightness of the airglow can vary depending on the section of sky observed, the time of night and solar activity. In Figure 2.3, the change in solar activity is defined as $S_{\odot}$ and varies between ~ 0.8 and 2 [23]. Therefore the measured airglow can vary significantly. Airglow is the brightest component, which can account for approximately 60 percent of the total NSB.

- **Zodiacal Light:** This is the result of sunlight being scattered by dust within the ecliptic plane. On average across the whole sky, Zodiacal light contributes about 30 percent of the total brightness of the NSB. The contribution can increase to as much as 50 percent of the NSB when measurements are taken closer to the ecliptic plane. For more information about zodiacal light and the history of the research see [24]

- **Scattered Starlight:** This contribution to the NSB is from scattering starlight by interstellar dust. Scattered starlight is most strongly observed near the galactic plane. Most of the scattered starlight is from stars between the visible magnitudes of 6 and 16.

- **Man-made Light:** The main source of man-made light tends to be street-lamps. The light emitted from sodium, mercury or incandescent streets lamps is scattered back from the troposphere. The sodium line at 589 nm (5890 Angstroms) in Figure 2.3 is an example of how emission from street lamps can contribute to the NSB level.

Figure 2.3 shows a spectrum of the NSB and a table that compares the contributions from different sources. The spectrum shows that the NSB is stronger at longer wavelengths than at shorter wavelengths, with strong contribution from

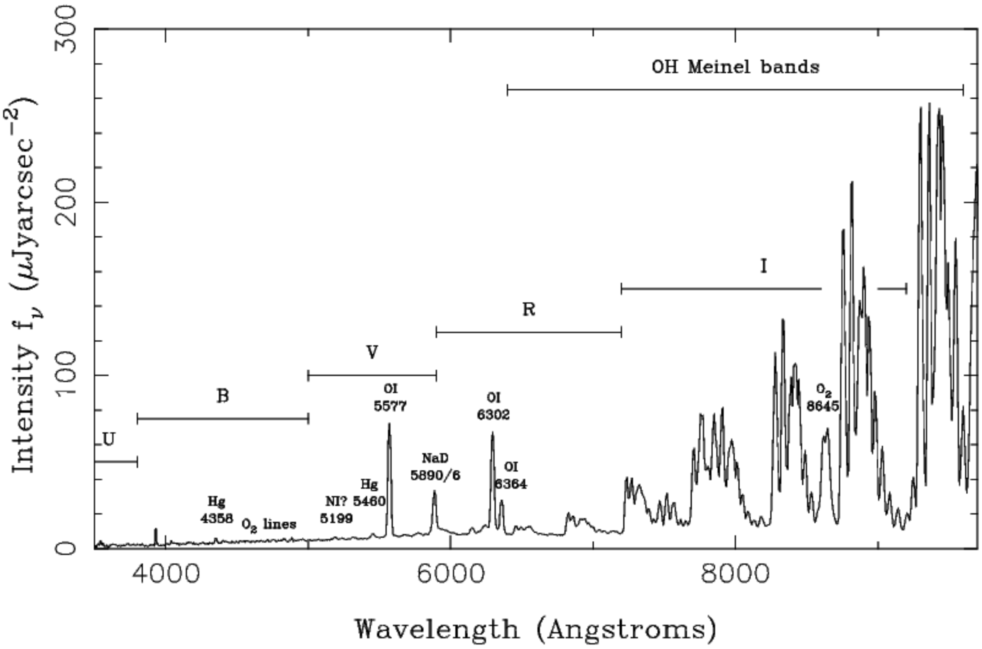

(a)

Contribution	Surface brightness V (S_{10} units)	Typical V_{zenith} (sunspot minimum)
Airglow	$\approx 145 + 130(S_{\odot} - 0.8)/1.2$	145
Aurora	negligible at |latitude| $< 40^o$	0
Zodiacal light	$\approx 140 - 90 sin(\|\beta\|)$ ($\|\beta\| < 60^o$) ≈ 60 ($\|\beta\| > 60^o$) (when $> 90^o$ from the sun)	60
Stars ($V > 20$, integ. light)		< 5
Starlight scattered by interstellar dust	≈ 100 exp(-($\|b\|/10^o$))	10
Extragalactic light		~ 1
Light pollution	< 20 at a ‘dark’ site (Smith 1979)	
Total		220

(b)

Figure 2.3: (a) Typical NSB spectrum taken at La Palma, Canary Islands, on a moonless night. From the spectrum, it can be seen that NSB levels drop rapidly from longer wavelengths to shorter wavelengths. (b) A table showing how the contributions from different sources make up the NSB. Surface brightness V and typical V_{zenith} are defined in surface brightness (S_{10}) units, where 1 S_{10} unit corresponds to 27.78 visual magnitudes per arcsec^2. β is defined as the angle from the ecliptic and b is galactic latitude. $S_{\odot}$ is defined as the magnitude of solar activity, with values between ~ 0.8 and 2. Both the image and table were taken from [23].

molecular lines. The table of the NSB shows that the airglow is the largest component, with zodiacal light comparable on the ecliptic plane. The contribution from starlight scattered by interstellar dust is of a similar magnitude to either airglow or zodiacal light, when observing towards the center of our galaxy. The table also shows that the integrated light from bright stars (visible surface brightness > 20 S_{10} units, where 1 S_{10} unit corresponds to 27.78 visual magnitudes per arsec^2) contributes to less than five percent to the total NSB levels. More information can be found in [23].

2.2 Extensive Air Showers (EAS)

An EAS is a cascade of secondary particles, produced when a high energy primary particle interacts with molecules in the Earth's atmosphere. Two main shower types will be discussed, electromagnetic showers and hadronic showers. Electromagnetic showers are initiated by either a photon or an electron/positron and their development is dominated by electromagnetic interactions. Hadronic showers are initiated by hadrons and are dominated by strong and weak interactions with electromagnetic sub-showers.

2.2.1 Electromagnetic Showers

Gamma-rays interact with molecules in the Earth's atmosphere via electromagnetic interactions. The typical first interaction height for a 1 TeV γ-ray is $\sim$ 26 km above sea level ($\sim$ 40 g cm^{-2} from the top of the atmosphere). The initial γ-ray will produce an electron-positron pair in the electric field of an atmospheric nucleus:

$$\gamma \rightarrow e^- + e^+ \tag{2.1}$$

The electron or positron can then further interact with another atmospheric nucleus via Bremsstrahlung to produce a photon:

$$e^- \rightarrow e^{-'} + \gamma \tag{2.2}$$

where $e^{-'}$ is the electron after having lost energy to the photon. These secondary electrons and photons will then interact to produce further particles in a cascading effect. A simple model by Heitler [25] describes this effect. The model assumes alternating pair production and Bremsstrahlung interactions, and equal interaction lengths ($\sim$ 37 g cm^{-2} in air). This means that the number of particles will double with each interaction length. An interaction length (X_0) is defined as the average column density (g cm^{-2}) that a particle will travel between interactions. A graphical outline of the cascade is shown in Figure 2.4. After n interaction lengths, the number of particles, N, in the shower will be:

$$\mathrm{N} = 2^n \tag{2.3}$$

The Heitler model also assumes that the energy of the primary particle is equally distributed amongst all of the shower particles. To obtain the energy E_n of a particle after n interaction lengths:

$$\mathrm{E}_n = \mathrm{E}_0 \, 2^{-n} \tag{2.4}$$

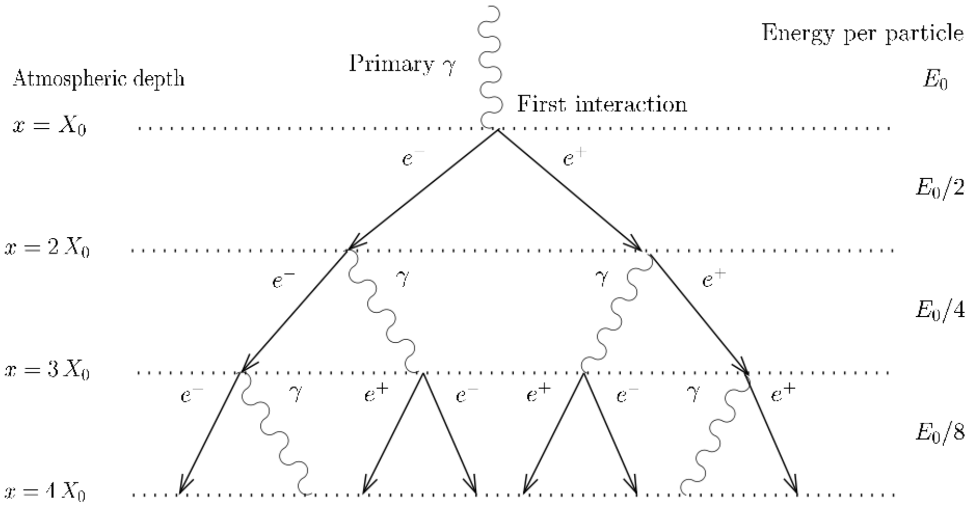

Figure 2.4: A diagrammatic example of the Heitler model [25], which describes the development of an electromagnetic shower. The model shows the interaction of a primary γ-ray photon with successive alternating pair production and Bremsstrahlung interactions. The interaction lengths of the pair production and Bremsstrahlung are assumed to be the same. The energy is assumed to be shared equally amongst all particles produced after each interaction length (X_0.

where E_0 is the energy of the primary particle. As more particles are produced, the average energy per particle decreases. Eventually, the average particle energy will drop below a critical energy (E_C), where ionisation becomes the dominant energy loss process over Bremsstrahlung and pair production. When the average particle energy drops below the critical energy, the total energy and the number of shower particles decreases as shower energy is deposited into the atmosphere. In air, the critical energy is approximately $\sim$ 81 MeV. Combining Equation 2.3 and Equation 2.4, an estimate of the maximum number of particles N_{max} can be obtained (which is achieved when the average particle energy equals E_C):

$$N_{max} = \frac{E_0}{E_C} \tag{2.5}$$

It is also useful to find the atmospheric depth where the maximum number of particles occur. Using the assumption of equal interaction length, a maximum depth (X_{max}) can be defined as:

$$X_{max} = n_{max} \times X_0 \tag{2.6}$$

where n_{max} is the number of interaction lengths to reach N_{max} and X_0 is the interaction length. To see how X_{max} is dependent on energy, Equation 2.4 is substituted into Equation 2.6. X_{max} now becomes:

$$X_{max} = X_0 \ln\left(\frac{E_0}{E_C}\right) \; / \ln(2) \tag{2.7}$$

Thus, according to the Heitler model, the maximum number of particles is proportional to the energy of the primary particle and the atmospheric depth of the maximum number of particles is proportional to the logarithm of the energy. Limitations of this model include the fact that it does not take ionisation or atmospheric scattering into account. The altitude where the particle number maximises is typically 10km above ground level for a 1 TeV γ-ray.

2.2.2 Hadronic Showers

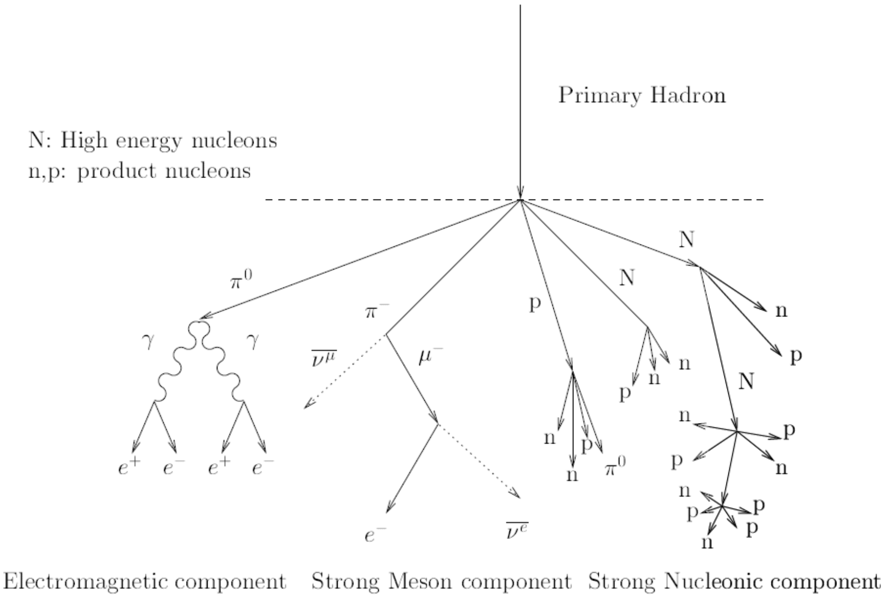

Figure 2.5: This diagram shows three components of the hadronic shower: the electromagnetic component which interacts via the electromagnetic force, the meson component and the strong nucleonic component. The strong component refers to the particles which interact via the strong nuclear force. The hadronic shower is the result of a hadronic particle interacting with an atmospheric nucleus. Note that the length of the arrows does not correspond to the lifetime of the particle. A hadronic sub-cascade is induced by nuclei fragments [26].

Cosmic-rays are proton or complex nuclei that interact with atmospheric nuclei. The cosmic-rays interact via the strong nuclear force. The interaction can lead to fragmentation of the target nucleus into a jet-like cascade of excited nuclei and additional mesons, mainly pions. These secondary components also interact via the strong nuclear force, which can trigger a cascade. A cosmic-ray interaction can produce three distinctive components: a hadronic core, a muonic component and electromagnetic sub-showers [26]. The resultant particle shower produced is called a hadronic shower. A graphical representation is shown in Figure 2.5.

For each hadronic interaction, pions are produced. There is approximately one-third π^0 and two-third $\pi^\pm$ produced for each of these interactions. This occurs for each interaction length until the initial hadron drops below the hadron's decay energy. Once the hadron is below the decay energy, the hadron will decay into a muon. The majority of the EM sub-showers are produced from the photons from the decay of π^0. The production of Cherenkov radiation from the EM component is why hadrons are detected by the IACT telescopes and is a form of background noise. Pions have the largest effect on the horizontal development of the shower as they can have significant transverse momenta [27]. The horizontal development due to the pions is used to discriminate hadronic showers from γ-ray showers. More details on how γ-ray and hadronic showers are separated through data analysis is described in Chapter 3.

2.3 Cherenkov Radiation

A charged particle propagating through a medium at a velocity v will temporarily polarise the medium in the vicinity of its path. After the particle has passed, the polarised molecules oscillate back into their rest position, acting as classical dipoles and thereby emitting electromagnetic radiation. There are two cases to consider, firstly where the charged particle is travelling below the local speed of light in the medium, and secondly where it is travelling faster than the local speed of light. In the first case, the radiation emitted will destructively interfere and no light will be observed a distance away from the source. In the second case, the emitted radiation will constructively interfere and light can be observed. This radiation is known as Cherenkov radiation. Only a brief description will be given here and for more details see [28].

For the case where the particle is emitting Cherenkov radiation, the minimum particle velocity v_{min} that will result in Cherenkov radiation is equal to the local speed of light c_n. The local speed of light is calculated by $c_n = c/n$ where c is the speed of light in a vacuum and n is the refractive index of the medium ($n \simeq 1.00029$ in air at sea level). A particle of rest mass m_0 will emit Cherenkov radiation above a minimum energy (or speed). The minimum energy required can be found in terms of a particle velocity, substituting $v_{min} = c_n = c/n$ into the relativistic energy equation:

$$\mathrm{E}_{min} = \frac{m_0 c^2}{\sqrt{1 - v_{min}^2/c^2}} \tag{2.8}$$

$$\mathrm{E}_{min} = \frac{m_0 c^2}{\sqrt{1 - 1/n^2}} \tag{2.9}$$

Equation 2.9 shows the minimum energy (E_{min}) required to produce Cherenkov radiation. At sea level E_{min} for an electron is $\sim$ 25 MeV, which is below the critical energy for ionisation (discussed in Section 2.2.1). As E_{min} is below the critical energy for ionisation, any charge particles produced from an EAS will be absorbed in the atmosphere before falling below the threshold for Cherenkov radiation.

For individual particles, Cherenkov radiation is emitted at an opening angle Θ_C (shown in Figure 2.6), hence forming a “Cherenkov cone”. Figure 2.6 shows the distance a particle travels from point A to point B compared to a spherical wave travelling from point A to point C. Therefore Θ_C is given by:

$$\cos(\Theta_C) = \frac{c_n \Delta t}{v \Delta t} = \frac{c}{nv} = \frac{1}{n\beta} \tag{2.10}$$

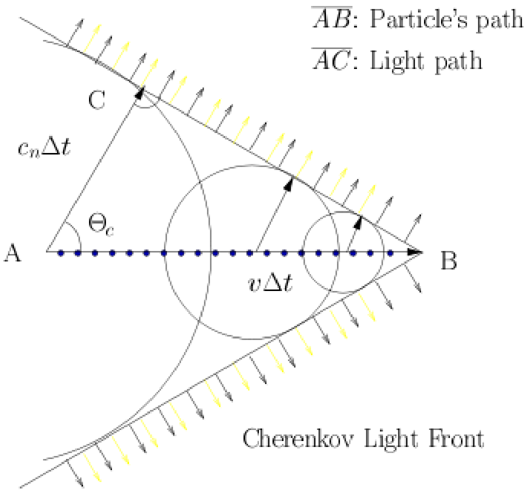

Figure 2.6: The Cherenkov effect showing the production of a coherent light front from a particle moving faster than light in a local medium from point A to point B.

where $\beta = v/c$ refers to the particle velocity. For a particle to emit atmospheric Cherenkov radiation $\beta \to 1$, given that n is close to 1 in air. Equation 2.10 with β and n close to one shows that the cone surrounding the particle trajectory will have a very small opening angle. In air, Θ_C varies between 0.5° and 1.4° [21]. The actual observed light cone angle from an EAS is greater then the opening angle produced from Cherenkov radiation of a single particle, as the increase in emission angle is caused by Coulomb scattering. Coulomb scattering is the process whereby charged particles are deflected by the charges of nuclei. In this case, it is the electrons within the EAS that are Coulomb scattered. This is an elastic scattering process, which just leads to a change in direction and not in energy. More details on Coulomb scattering are given by Molière [29]. The diameter of a Cherenkov light pool can extend up to $\sim$ 1 km for a primary particle with the energy on the order of TeV. This effect is shown in Figure 2.2.

The observed Cherenkov radiation spectrum goes as $1/\lambda^2$, i.e. $\mathrm{d}N/\mathrm{d}\lambda \propto 1/\lambda^2$. In air, Cherenkov radiation produced from EAS peaks in the ultra-violet ($\approx$ 350 nm). A turn-over below 350 nm is caused by atmospheric transmission effects (mainly absorption by ozone). Due to the range of wavelengths in the Cherenkov emission spectrum, an optical telescope can be employed for Cherenkov radiation detection. Cherenkov radiation arrives at ground-level within a time period of a few tens of nano-seconds. So, fast photomultiplier tubes are employed as camera pixels.

Atmospheric effects are important in the propagation of Cherenkov radiation. Rayleigh scattering by molecules and Mie scattering by clouds and atmospheric dust are sources of systematic errors. Atmospheric effects are discussed further in Section 2.4. To more accurately represent the Cherenkov light that is seen at ground level, Monte Carlo simulations that combine both high energy particle physics and atmospheric models are used.

2.4 The Earth's Atmosphere

For IACT, the Earth's atmosphere is used as an interaction medium for cosmic particles, and as a production medium for Cherenkov radiation. The atmospheric composition and transmission play important roles in the propagation of Cherenkov radiation. A brief discussion on the Earth's atmosphere and atmospheric transmission will be given here and for more details see [31, 32, 33].

The Earth's atmosphere is considered to be the collection of gases that surround the planet. The atmosphere is primarily made of nitrogen (∼78%) and oxygen (∼20%) by volume. The atmosphere is split into a variety of layers:

- **Troposphere:** The bottom layer, extending from ground level to an altitiude of ∼ 7 - 17 km. The height of the troposphere is latitude dependent. At the equator, the top of the troposphere will be ∼ 17 km, whilst at the poles, the top of the troposphere will be ∼ 7 km. The temperature within the troposphere decreases with increasing altitude. The troposphere contains a boundary layer that extends from ground level up to ∼ 3 km. The boundary layer contains the majority of aerosol particles. The troposphere is the most dense part of the atmosphere.

- **Stratopshere:** The layer above the troposphere. The stratosphere extends from the top of the thermosphere up to ∼ 50 km. The ozone layer is contained within the stratosphere. The temperature within the stratosphere increases with altitude due to the absorption of ultraviolet light by ozone.

- **Mesosphere:** The layer above the stratosphere. The mesosphere extends from ∼ 50 km to ∼ 80 - 85 km. The temperature within the mesosphere decreases with increasing altitude.

- **Thermosphere:** Extends above the mesosphere. The thermosphere extends from ∼ 80 - 85 km to ∼ 800 km and includes the ionosphere. The ionosphere extends from ∼ 80 km to ∼ 650 km and contains many ions and free electrons. Aurorae occur within the ionosphere.

A diagrammatic example of Earth's atmospheric layers between 0 and 120 km is shown in Figure 2.7.

For energies above 100 GeV (10^{11} eV), particle (e.g. γ-ray and proton) interactions mainly occur within the Stratosphere, with the height of primary interaction above ground-level decreasing as the primary particle energy increases. Cherenkov light is produced and propagates through both the stratosphere and troposphere. The number of Cherenkov photons that reach ground level is dependent on the atmospheric transmission. The atmospheric transmission (T) measured between the observer and the height of the emission for a vertical path can be defined as:

$$\mathrm{T} = \exp(-\tau) \tag{2.11}$$

where τ is the vertical optical depth. The transmission for a non vertical path can be defined as:

$$\mathrm{T} = \exp\left(-\tau \; \sec(\theta)\right) \tag{2.12}$$

where θ is the angle from the vertical.

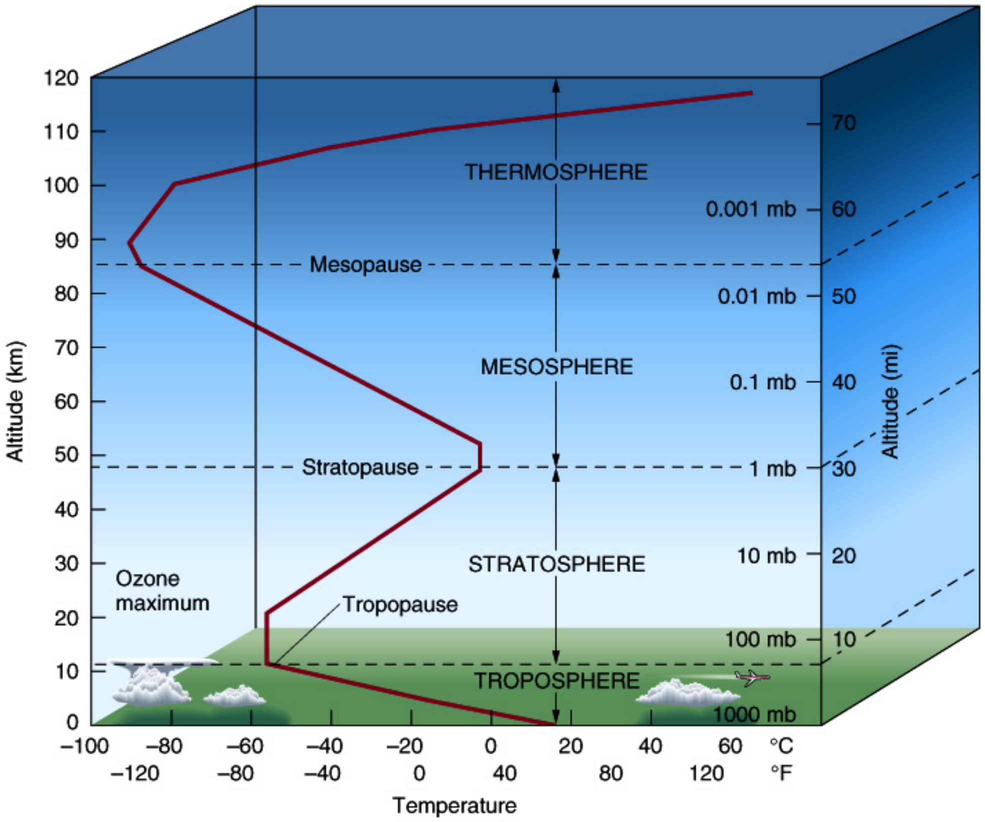

Figure 2.7: A graphical view of the layers within the atmosphere between 0 and 120 km. The red line depicted here shows the average temperature as a function of altitude. Image taken from [30].

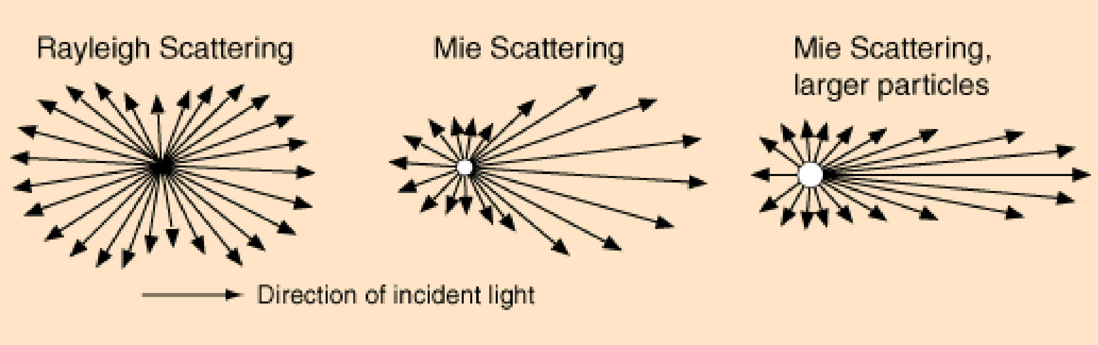

Figure 2.8: The scattering intensity pattern for three different particle sizes. The length of the arrows gives an indication of the relative strength of the scattering. For Rayleigh scattering, the particle size is much smaller then the wavelength of the incident light. When light is Rayleigh scattered, the light is approximately uniformly scattered in all directions. For Mie scattering, the particle size is comparable to or larger than the wavelength of the incident light. When light is Mie scattered, the light is highly forward scattered. Image taken from [31].

The atmospheric transmission is affected by the density of scattering particles contained in the atmosphere. The two main types of scattering are Rayleigh and Mie (or aerosol) scattering. The Rayleigh regime is where the particle size is much smaller then the wavelength of light. Rayleigh scattering has a $1/\lambda^4$ dependence and mainly depends on the number of nitrogen and oxygen molecules along the effective path. Mie scattering is in the regime where the particle size is comparable to the wavelength of light and has a weak wavelength dependence in its effectiveness. Mie scattering is associated with larger particles like dust, salt and smoke. These particles tend to be blown into the atmosphere, so the amount of Mie scattering is highly dependent on local conditions, including wind. Figure 2.8 shows a diagram of the scattering angles and relative strengths. When light is Rayleigh scattered, the light is approximately uniformly scattered in all directions. When light is Mie scattered, the light is strongly forward scattered. As Mie scattering is independent of Rayleigh scattering, the total vertical optical depth, and transmission can found by:

$$\mathrm{T} = \exp\left(-\tau_{\mathrm{T}} \sec(\theta)\right) \tag{2.13}$$

$$\tau_{\mathrm{T}} = \tau_{\mathrm{a}} + \tau_{\mathrm{R}} \tag{2.14}$$

where τ_{T} is the total vertical optical depth, τ_{a} is the vertical Mie (or aerosol) optical depth, τ_{R} is the vertical Rayleigh optical depth, and T is the total vertical transmission. Each of these quantities are measured between the point of transmission and an observer.

The largest source of atmospheric aerosols is dust, mainly comprising of either vegetation or salt from sea spray. There is no real size limit to an aerosol particle. Larger particles (especially around the mm size) tend to quickly settle out of the atmosphere due to their mass. Smaller particles do not settle out this way and require a different mechanism to be removed from the atmosphere. Smaller particles can be removed through rain as they serve as condensation nuclei. The concentration of aerosols decrease rapidly with increased height, as the majority of the aerosols originate at ground level. This explains why most of the aerosols are contained within the boundary layer.

Chapter 3

Simulations of a $\geqslant$ 10 TeV IACT Array

This chapter will outline the method involved in the simulation of an imaging atmospheric Cherenkov technique (IACT) array. A description of an IACT array and how an IACT array uses stereoscopic reconstruction to improve performance over a single telescope is given. Within the performance simulation, I will outline the computer packages used, the array specifications, and how the angular resolution and the ability to reject proton showers are calculated.

3.1 An IACT Array

As a single optical telescope can be used to view an EAS, this process can be extended to using multiple telescopes to view the same EAS. A multiple telescope system is denoted as an IACT array. The benefits of using an array include being able to combine multiple images of the same EAS, to improve the angular resolution and improve the ability to reject proton images from data analysis. The combination of multiple images in the analysis is called stereoscopic reconstruction. The angular resolution and cosmic-ray background rejection are calculated after image parameterisation and stereoscopic reconstruction. The "effective collecting area" (A_{eff}), which was discussed in Chapter 2, can be extended to an array of IACT telescopes. The telescope spacing would also affect the A_{eff}. As a result of these dependencies, A_{eff} is usually estimated from Monte Carlo simulations, rather then by direct calculations.

3.1.1 Image Parameterisation and Stereoscopic Reconstruction

To be able to calculate the angular resolution or to reject proton showers, the Cherenkov images collected must be first parameterised. Image parameterisation is quantified by using so-called Hillas parameters [5]. Such Hillas parameters are known as size, width, length, centre of gravity (CoG) and major axis. These parameters are calculated from an ellipse that is fitted to each image. A graphical description is shown in Figure 3.1. Proton shower images are mainly distinguished from γ-ray shower images by comparison of the mean scale width (discussed later on) of many images. The differences can be seen in the mean scaled width (MSW

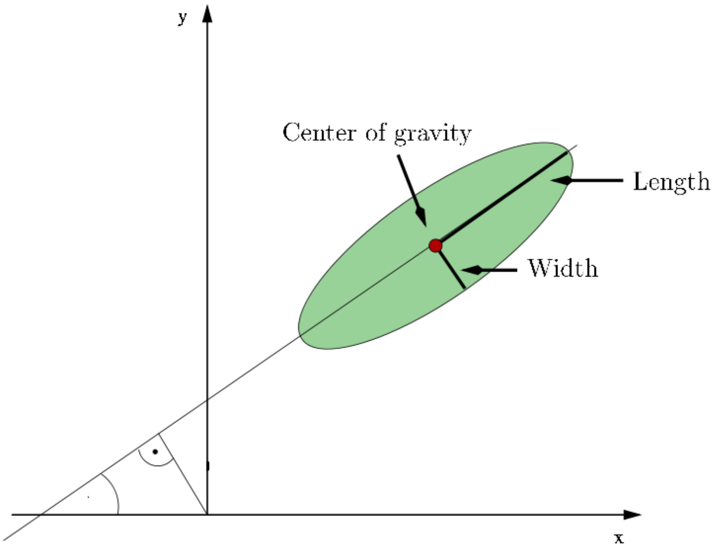

Figure 3.1: A simple graphical view of an ellipse fitted to a Cherenkov image in the camera plane. Some of the Hillas parameters are shown here: Length, which is the semi-major axis of the ellipse; Width, which is the semi-minor axis of the ellipse; and Centre of Gravity, which is the geometric centre of the ellipse and the the major axis. x and y correspond to the coordinates in the camera plane.

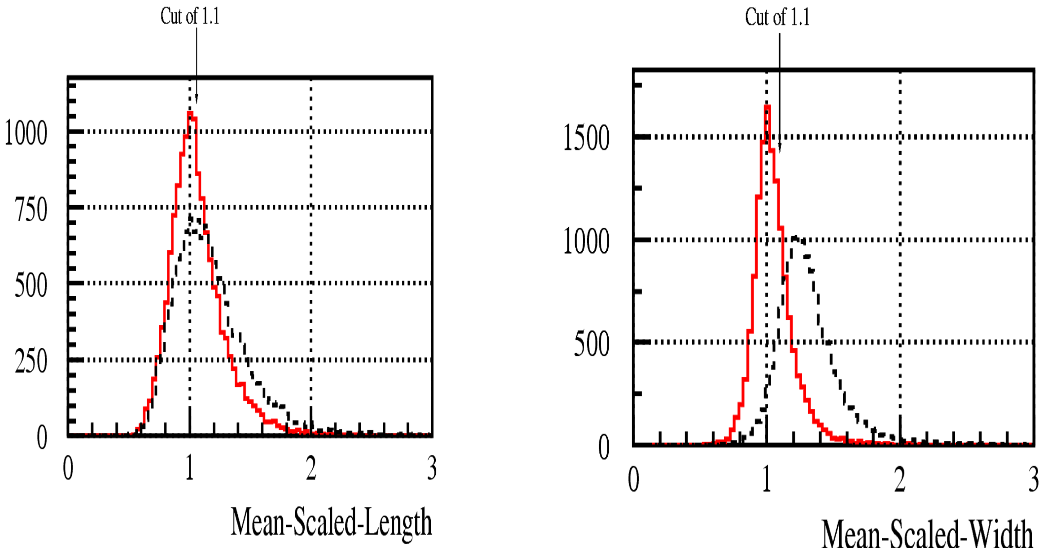

Figure 3.2: Displayed here are histograms of Mean Scaled Length and Mean Scaled Width for a number of showers. The solid red lines represent γ-ray shower events, while the black dashed lines represent proton shower events. The arrow indicates the position of the applied cut of 1.1. When the cut is applied, all events to the right of the arrow are discarded.

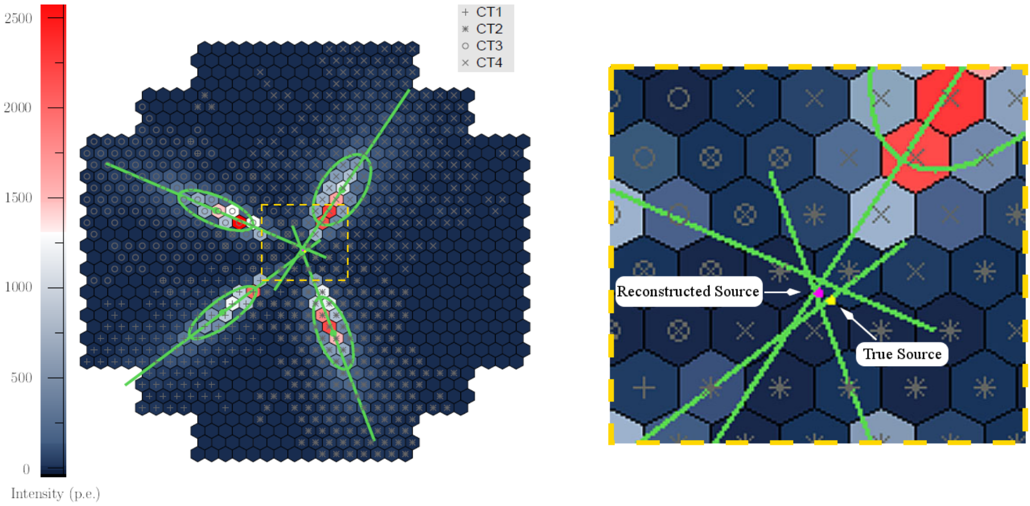

Figure 3.3: The left image shows how Cherenkov images from multiple telescopes, superimposed onto a single camera plane, can be used to find a reconstructed direction. The reconstructed direction is found where the major-axes of each image intersect, weighted and averaged for each pair of axis intersections. The right image shows a zoomed in view of the intersection of the major axes of each image, the reconstructed direction and the true direction. Image taken from [34].

- defined below) calculated from simulated data in Figure 3.2. The change in the mean and width of the MSW distribution of the proton shower images is mainly attributed to the transverse momentum given to pions in strong interactions [27].

Mean scaled width and mean scaled length (MSL) [35] are quantities that are independent of shower energy and core distance. The core distance is defined as the distance between the telescope and the shower axis, calculated in the shower plane. To calculate MSW and MSL, a width and length must first be fitted to each collected image. Length and width correspond to the major and minor axes of the ellipse respectively in the camera plane. To calculate the length and width, the weighted mean in x^2, y^2 and xy must be determined:

$$\langle x^2 \rangle = \frac{\sum_i s_i x_i^2}{\sum_i s_i}, \ \langle y^2 \rangle = \frac{\sum_i s_i y_i^2}{\sum_i s_i}, \ \langle xy \rangle = \frac{\sum_i s_i x_i y_i}{\sum_i s_i} \tag{3.1}$$

where x_i and y_i are the coordinates of the camera plane in degrees and s_i is the signal of the ith pixel. The next step is to find the second order covariance matrix C, which can be calculated from the individual variance σ^2, in each of x, y and xy:

$$\mathbf{C} = \begin{pmatrix} \sigma_x^2 & \sigma_{xy} \\ \sigma_{xy} & \sigma_y^2 \end{pmatrix} \tag{3.2}$$

where:

$$\sigma_x^2 = \langle x^2 \rangle - \langle x \rangle^2, \ \sigma_y^2 = \langle y^2 \rangle - \langle y \rangle^2, \ \sigma_{xy} = \langle xy \rangle - \langle x \rangle \langle y \rangle$$

The parameters of length (L) and width (W) can now be defined:

$$\mathrm{L} = \sqrt{\frac{1}{2}\mathrm{tr(C)} + \sqrt{\frac{1}{2}\mathrm{tr(C)}^2 - \mathrm{det(C)}}} \tag{3.3}$$

$$\mathrm{W} = \sqrt{\frac{1}{2}\mathrm{tr(C)} - \sqrt{\frac{1}{4}\mathrm{tr(C)}^2 - \mathrm{det(C)}}} \tag{3.4}$$

where tr(C) is the trace of the matrix C given by the sum of the diagonal elements and det(C) is the determinant of the matrix C.

In order to remove the dependence of image properties on the shower energy and impact distance and derive the MSW, individual events are divided by the expected mean image width. The mean expected image width is calculated from Monte Carlo simulations. The equation for MSW $\langle\tilde{W}\rangle$ is:

$$\langle\tilde{W}\rangle = \frac{1}{n}\sum_{k=1}^{n}\frac{W_k}{\langle W\rangle_k} \tag{3.5}$$

where n is the number of triggered telescopes, W_k is the width and $\langle W\rangle$ is expected mean image width for the k^{th} image. A similar approach can be applied to derive the MSL. Figure 3.2 shows the MSW and MSL for both simulated γ-ray and proton showers. Within the figure, a cut of $\langle\tilde{W}\rangle < 1.1$ is shown on both MSW and MSL plots. Shower images to the left of the MSW cut are kept, while the rest are removed from the analysis. The cut on the MSW will typically remove $\sim$ 97 % of proton events, while only removing $\sim$ 30 % of γ-ray events for γ-ray showers energies around 1 TeV. A different value cut can be applied on MSL as well and is usually employed after the MSW cut has been applied. The cut on the MSL is applied after the MSW as it removes fewer proton shower images. After the cuts on the MSW and MSL are applied, the ability of the array to reject proton shower images can be determined.

The energy of the viewed shower is found by comparing the size parameter and core distance against Monte Carlo simulations for multiple images of the same shower. The size parameter can be found by summing over the signals produced in all of the photomultiplier tubes (PMTs) in the image:

$$S = \sum_{i} s_i \tag{3.6}$$

where s_i is the signal in the i^{th} PMT and S is the total signal (photoelectrons) across all PMTs. A high energy shower will produce more Cherenkov light than a low energy shower. This is indicated by Equation 2.5, which outlines the relationship between the number of shower particles and the energy of the initial γ-ray. Therefore images from a higher energy shower will be brighter and larger than a lower energy shower at the same core distance. Also, a higher energy shower will propagate deeper into the atmosphere than a lower energy shower. The distance that the telescope is away from the core also affects the size and intensity of the observed image. The centre of gravity is determined from a weighted mean of the $\langle\mathrm{x}\rangle$ and $\langle\mathrm{y}\rangle$ coordinates of the pixels containing signals in the camera plane.

The mean position of the PMTs in the camera is weighted by the signal (photo-electrons) in each PMT. Therefore:

$$\langle \mathrm{x} \rangle = \frac{\sum_i s_i x_i}{\sum_i s_i} \text{ and } \langle \mathrm{y} \rangle = \frac{\sum_i s_i y_i}{\sum_i s_i} \tag{3.7}$$

where x_i and y_i are the coordinates of the camera plane, in degrees, of the i^{th} pixel.

The method of reconstructing the γ-ray arrival direction is to superimpose each of the images of a shower onto one camera plane, and then find the direction from the intersection of the major axis. As a trigger of two or more telescopes is usually required, multiple images of the same shower can be obtained. This is shown in Figure 3.3 with 4 images. In this case, the algorithm employed in the simulation for direction reconstruction was Algorithm 1 [36]. Algorithm 1 involves intersecting the major axes for all pairs of telescopes. For N telescope images, $N(N-1)/2$ intersection points are averaged, with each intersection point being weighted by the sine of the angle between the image axis. This is to give higher weight to image pairs with more orthogonal axis, which provide the most accurate determination of the shower axis. Once many γ-ray shower events have been reconstructed, an angular resolution can be determined.

3.2 Performance Simulation

The performance results of the IACT array were obtained from computer simulations. The computer packages used in the simulation include CORSIKA [37], SIBYLL [38], sim_telarray [39, 40] and MODTRAN [41]. CORSIKA is the computer package used to simulate the EAS and Cherenkov photons of the γ-rays and protons. SIBYLL is the hadronic physics generator used within CORSIKA for hadronic showers. MODTRAN is the computer package used to simulate atmospheric transmission. The simulated Cherenkov photons and generated atmospheres were used as inputs into sim_telarray. Sim_telarray is the computer package used to simulate the telescope array observing a γ-ray source.

- **CORSIKA and SYBILL:** The packages CORSIKA and SYBILL were used to generate the Cherenkov photons produced from the EAS. I used γ-ray and proton showers generated within the energy range of 1 - 500 TeV. The γ-ray showers were simulated with a flat energy spectrum i.e. dN/dE = const. The simulated γ-ray showers where also angled at 30° from the zenith. In each simulation, the source of γ-rays is a point source and the true direction is simulated to be in the centre of the camera. The proton showers were simulated in a view cone of 0.3° radius with an energy spectrum of $\mathrm{dN/dE} \propto \mathrm{E}^{-1}$.

- **MODTRAN:** The atmospheric transmission provided for sim_telarray was simulated through the MODTRAN (MODrerate resolution atmospheric TRANsmission) computer package. MODTRAN solves the Radiative Transfer Equation including the effects of molecular and particulate absorption/emission and scattering, surface reflection and emission, solar/lunar

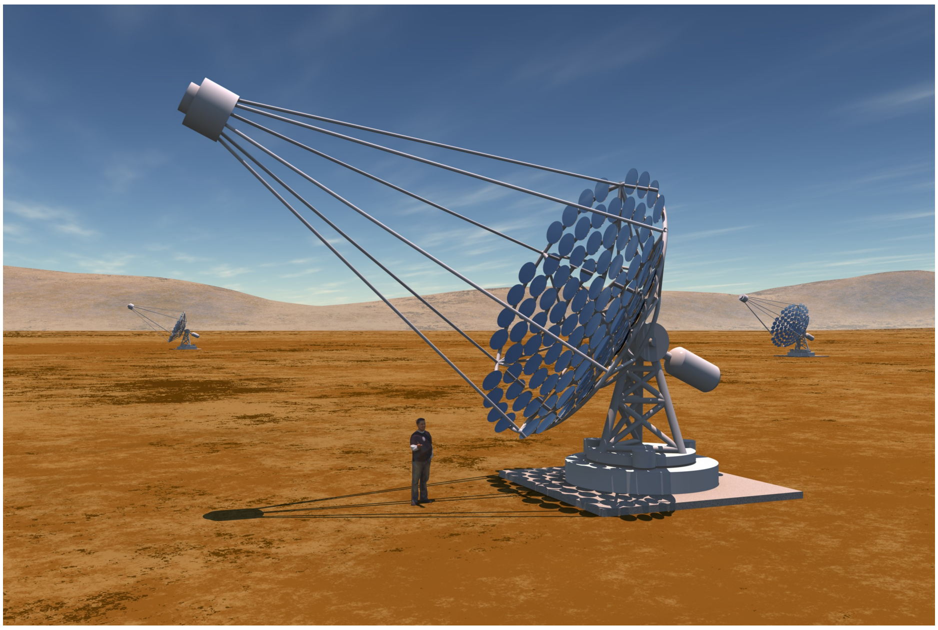

Figure 3.4: A pictorial representation of the simulated telescopes. The size of the telescopes is to scale with the adjacent person but the distance between the telescopes is not an accurate representation of the true distances expected to be employed. The expected distance between telescopes is ∼ 500 meters.

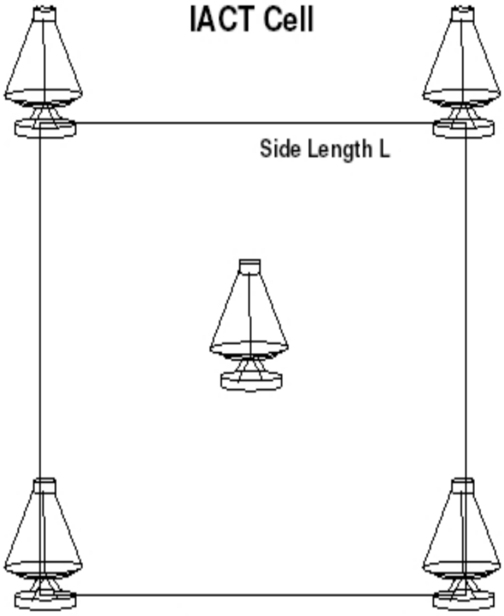

Figure 3.5: Simulated layout of the IACT array of 5 telescope. Side length L of 500 m was used in the simulation

illumination, and spherical refraction. The package contains many different standard Rayleigh models (eg. tropical, mid-latitude, US standard), aerosol models (eg. Maritime, rural, desert) and cloud models (eg. cirrus) to produce a wide range of different simulated atmospheres. I was mainly interested in MODTRAN's capability to generate optical depths from different simulated atmospheres. All the atmospheres were generated between a height of 220 m a.s.l and 100 km. A height of 220 m a.s.l is typical of heights found around Australia. MODTRAN outputs the total optical depth as a function of wavelength between a pair of predetermined altitudes.

- **sim_telarray:** The package sim_telarray is used to simulate how detected photons are dealt with by the telescope electronics, having landed on the telescope mirror. It deals with complete ray tracing, mirror setup, camera setup, triggering, telescope positions, number of telescopes and the parameterisation of images. The mirror setup contains parameters such as dish size, mirror segment size and position, mirror focal length and mirror reflectivity. The camera setup has parameters such as camera size, number of pixels, position and the quantum efficiency of the photomultiplier tubes.

3.2.1 IACT Array Configuration

An individual simulated telescope is based on a tessellated dish with a 9 m focal length. The dish is made up of 84 mirror segments, which are each 60 cm in diameter, with a mirror area of $\sim$ 24 m^2. The mirror optics are based on an elliptical profile [42] with f/1.5 focal ratio. The camera, placed in the focal plane, contains 1024 pixels (32 by 32 pixels), with an 8.2° by 8.2° Field of View (FoV). An 8.2° FoV allows the recording of the full development of $\geqslant$ 10 TeV γ-ray showers in the camera and also detects showers for core distances up to 800 m. Pixels consist of photomultiplier tubes (PMTs), which are 0.25° in angular diameter. A graphical representation of the telescopes is shown in Figure 3.4.

The IACT array used in the simulations consisted of an arrangement of 5 telescopes, with 4 telescopes in a square and a fifth in the centre. This configuration is shown in Figure 3.5. An array side length L of 500 m was simulated to detect the higher energy γ-rays showers (compared with the H.E.S.S. experiment, which has telescopes spaced $\sim$ 120 m apart [43]). Current studies [20] have shown that this layout can achieve an effective collection area (A$_{eff}$) of 1 km^2 with 500 m spacing. To achieve an A$_{eff}$ of 10 km^2, 10 of these arrays would be needed, which would take the total number of telescopes needed towards 50.

3.2.2 Cosmic-ray Background Rejection and Angular Resolution

The angular resolution and the ability to reject proton showers are used to quantify changes in the array performance under different conditions. The ability to reject proton showers is quantified within simulations and is defined as the quality factor (Q) [35]. The quality factor is defined as:

$$\mathrm{Q} = \frac{\kappa_\gamma}{\sqrt{\kappa_p}} \tag{3.8}$$

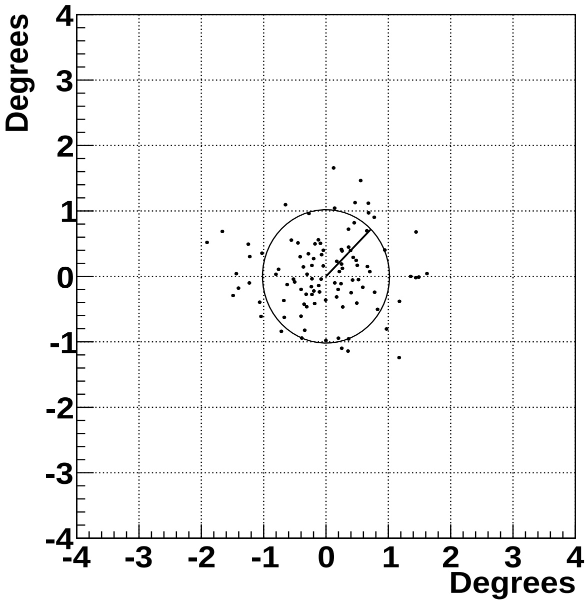

Figure 3.6: This figure gives an example of how reconstructed directions (dots) of many different γ-ray shower events from the same source can be distributed. The drawn circle on the figure represents the radius that contains 68% of events. The radius of the circle is defined as the r68 value. The source is simulated to be at the centre of the camera.

where κ_γ is the fraction of γ-ray shower events and κ_p is the fraction of proton shower events, that are accepted after shape cuts. Shape cuts are cuts on mean scaled width (MSW) and mean scaled length (MSL). The fraction of events are calculated as the number of accepted events after shape cuts divided by the number events before cuts. The quality factor is analogous to the signal-to-noise ratio. The quality factor can only be calculated through simulation as it is necessary to know which events are γ-ray or proton before any cuts are applied.

After each arrival direction is reconstructed for many simulated γ-ray shower events from the same point source, these reconstructed directions can all be placed onto one camera plane. The angular resolution then is determined by calculating the radius that encloses 68% of events from the simulated direction. A diagrammatic example is shown in Figure 3.6. I have defined the radius that contains 68% of events as r68. The smaller the radius that contains these events, the more events were reconstructed closer to the true direction. Angular resolution is important as it describes how well objects, and details of source morphology, can be resolved. This method can only be applied to simulated point sources as the exact location needs to be known. When dealing with an operational experiment, it is commonplace to measure a telescope point spread function (PSF) [44], to determine the angular resolution.

Chapter 4

Performance Simulation of an IACT Array with Differing Atmospheres

This chapter outlines the simulated response of a greater than 10 TeV imaging atmospheric Cherenkov technique (IACT) array to changing atmospheric transmission due to aerosols and to the presence of cirrus clouds. The effects of cirrus clouds were investigated as these clouds occur at a similar height to the maximum emission of Cherenkov photons for γ-ray shower energies around 10 TeV. Before simulating the array's response to cirrus clouds, I compared heights of maximum emission of Cherenkov photons for γ-ray shower energies between 1 TeV and 500 TeV against differing heights of cirrus clouds. The array's performance is quantified through its angular resolution and the ability to reject proton showers. This can then help determine a criteria for selecting Australian sites for future greater than 10 TeV IACT arrays.

4.1 MODTRAN Models

Different atmospheric conditions were simulated in order to quantify the array's simulated response to changing atmospheric transmission. The model atmospheres where produced via the MODTRAN [41] computer package and the different levels of transmission were achieved by using different aerosol models. To produce atmospheres with different transmissions, I combined a Rayleigh atmosphere with three standard MODTRAN aerosol models: a desert model with wind speed equal to 5 m/s, a maritime model and a rural model. Each of these models were chosen to produce different levels of atmospheric transmission. The Rayleigh scattering atmosphere used was the MODTRAN tropical model. This choice was based on [47], as they used this Rayleigh scattering model within their simulated Australian atmosphere. The effects of Rayleigh and aerosol scattering on atmospheric transmission were discussed in Chapter 2. The array's response to a pure Rayleigh atmosphere was used as a base-line. Any Rayleigh scattering atmosphere could have been used, as I am interested in the relative changes in the array's performance due to different aerosol profiles.

I will show the effects of the different aerosol models on the transmission through the vertical optical depth. Figure 4.1 shows the total vertical optical

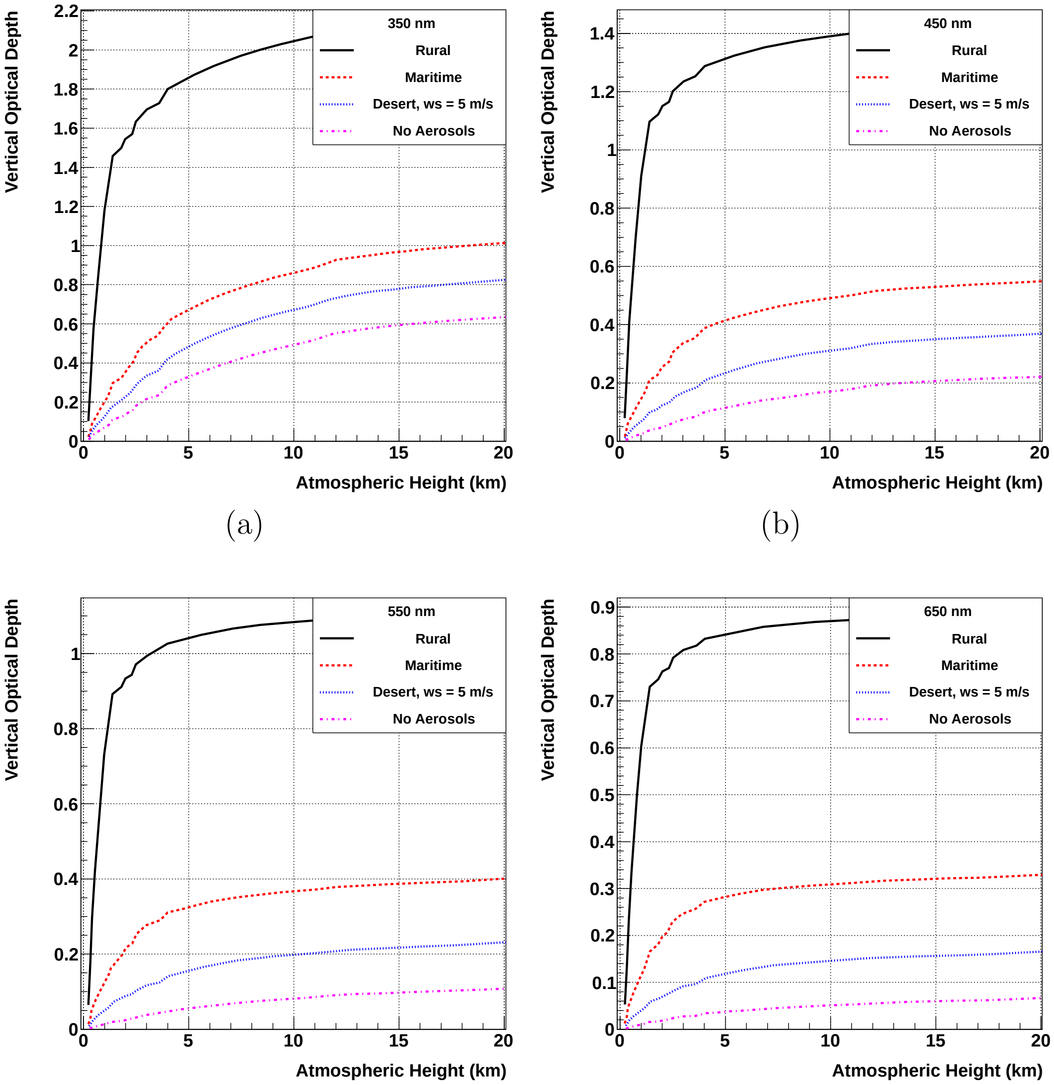

(a) (b)

(c) (d)

Figure 4.1: The total vertical optical depth for tropical Rayleigh atmospheric models with different aerosol content. The vertical optical depth is calculated from the ground to different atmospheric heights. The vertical optical depths were generated by MODTRAN [41]. Ground level was chosen to be 220 m a.s.l., which is typical of many Australian sites. The vertical optical depth profiles for four wavelengths are shown here: (a) 350 nm, (b) 450 nm, (c) 550 nm and (d) 650 nm. For the desert model, WS stands for wind speed and is set to 5 m s^{-1}. Over all wavelengths, the model containing no aerosols has the largest optical transmission (as expected), while the rural model exhibits the smallest optical transmission. This is due to the transmission being inversely proportional to the exponential of the vertical optical depth.

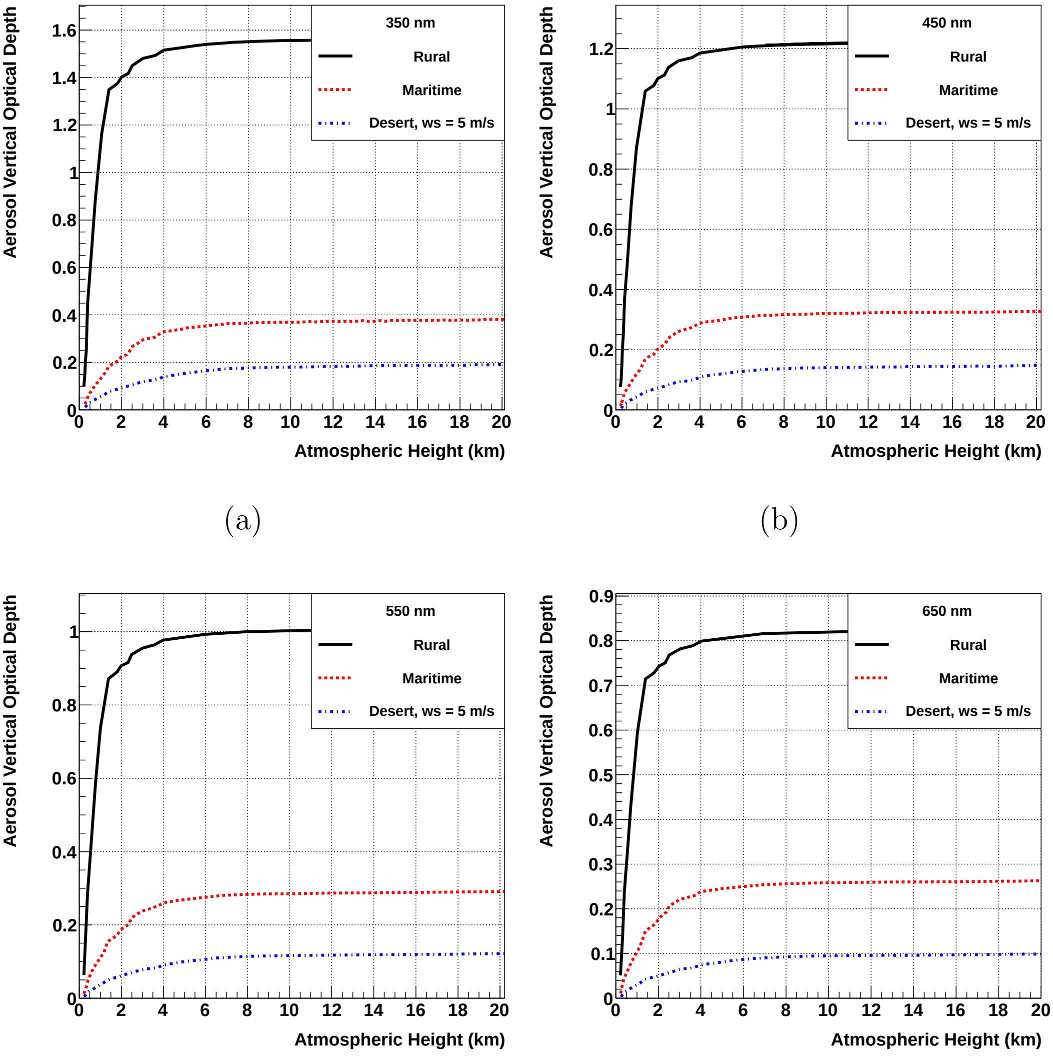

(a)

(b)

(c)

(d)

Figure 4.2: The vertical aerosol optical depth shown for different aerosol models. These vertical aerosol optical depths are calculated from the ground to different atmospheric heights. The aerosol optical depths were generated by MODTRAN [41]. Ground level was chosen to be 220 m a.s.l., which is typical of many Australian sites. The vertical aerosol optical depth profiles for four wavelengths are shown here: (a) 350 nm, (b) 450 nm, (c) 550 nm and (d) 650 nm. The majority of aerosols are contained below an atmospheric height of 4 km. The effect of the containment on the vertical aerosol optical depth can be seen in all of the aerosol models shown. For the desert model, WS stands for wind speed and is set to 5 m s^{-1}. In comparison, the measured vertical aerosol optical depth at the Pierre Auger [45] experiment or HiRes [46] from ground level to an atmospheric height of 3.5 km at 355 nm is 0.04. The aerosol optical depth of the desert aerosol model from MODTRAN comes closest to this value but is still two to three times larger.

depth (aerosol scattering plus Rayleigh scattering) for a pure Rayleigh atmosphere and three atmospheres using the standard MODTRAN aerosol models. The vertical optical depth is shown for an atmospheric height between ground level to an altitude of 20 km. An atmospheric height up to 20 km is shown since the majority of the vertical optical depth is evident below this altitude. The wavelengths 350, 450, 550 and 650 nm are shown to illustrate how the vertical optical depth changes as a function of wavelength. These wavelengths are contained within the wavelength range of a typical photomultiplier tube used in an IACT telescope. The vertical optical depth (τ) between the point of transmission and an observer is related to the transmission via:

$$\mathrm{T} = \exp\left(-\tau \sec(\theta)\right) \tag{4.1}$$

where T is the transmission, and θ is the angle from the vertical. From Figure 4.1, it can be seen that the Rayleigh (no aerosol) model contains the lowest optical depth and the rural model contains the highest optical depth. Therefore, these models demonstrate the highest and lowest transmission respectively.

To demonstrate the effects of aerosols on the optical depth, the total vertical aerosol optical depth for four different atmospheric models is shown in Figure 4.2. The total vertical aerosol optical depth was calculated by subtracting a vertical optical depth for a pure Rayleigh atmosphere from a vertical optical depth for an atmosphere containing both Rayleigh and aerosol particles at the same atmospheric height and wavelength. It can be seen that the majority of the aerosol optical depth is evident below an atmospheric height of 4 km. This effect is seen in all of the aerosol models shown. As a point of reference, the average vertical aerosol optical depth measured by both the Pierre Auger Observatory [45] and HiRes [46] (both employ optical telescopes and fast photomultiplier tubes) from ground level to an atmospheric height of 3.5 km at 355 nm is 0.04. The aerosol optical depth of the desert aerosol model from MODTRAN comes closest to this value but is still two to three times larger than the measured aerosol optical depth from these experiments.

4.2 Aerosol Simulation Result

This section presents the results of the simulated response of the IACT array to detecting γ-ray showers angled 30° to the zenith when atmospheres containing different aerosol profiles are introduced. I quantify the array response to detecting proton and γ-ray events, between 1 to 500 TeV, by measuring the angular resolution (r68) and the ability to reject proton events (Q). The simulated shower events were reconstructed knowing the atmospheric transmission the Cherenkov light had propagated through. The details of the simulation, the IACT array, angular resolution and the method to reject proton events was given in Chapter 3. The results of the r68 and Q are plotted for different core distances and arranged in equal bins of log(energy) from 1 to 500 TeV. These results are arranged in this manner to observe how the array is effected by the energy of the primary particle, and by the telescope to shower axis distance.

The results of the measured r68 for the simulated array are shown in Figure 4.3. Even with increasing the level of aerosols, the r68 profile is mostly not

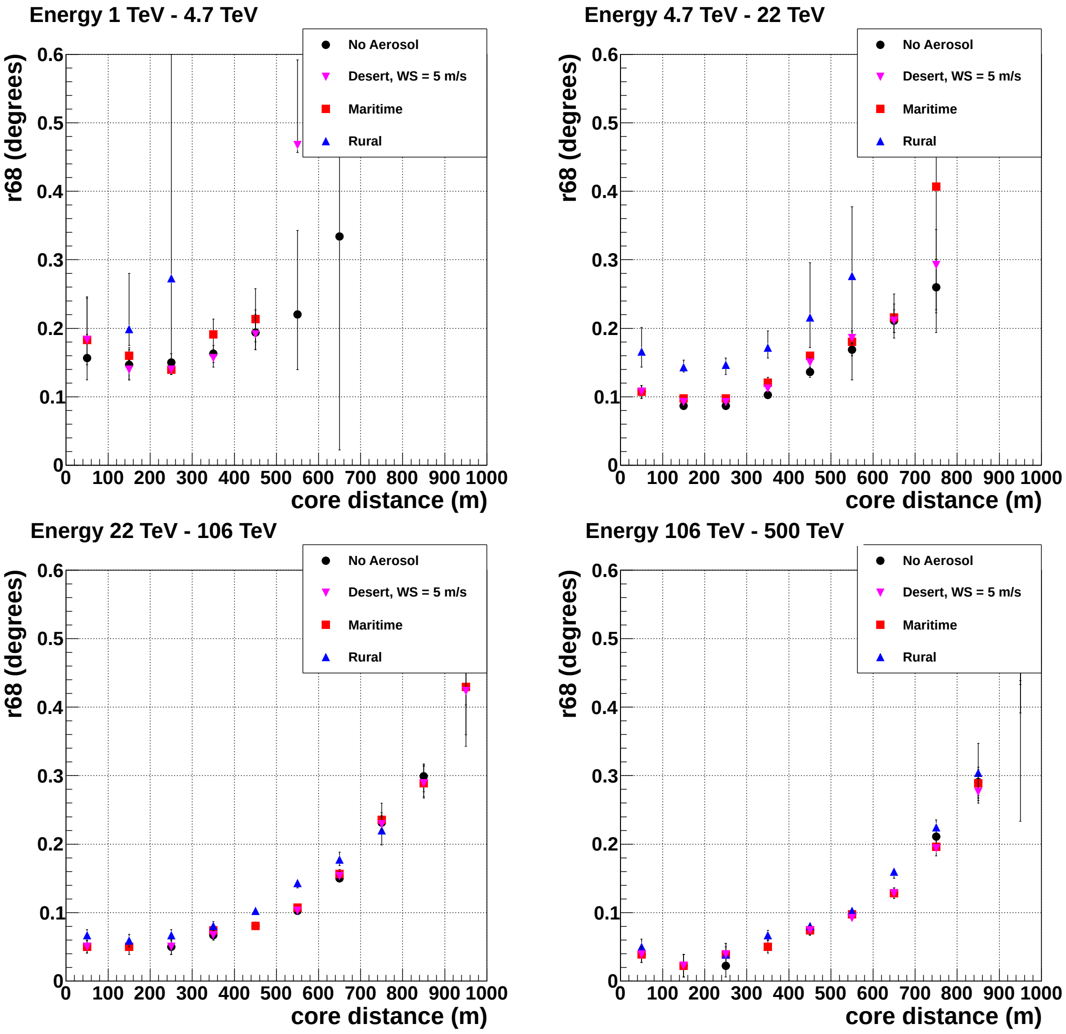

Figure 4.3: The simulated IACT array's angular resolution (r68) for no aerosols (black circles), desert model with wind speed (WS) = 5 m/s (pink triangles point down), maritime model (red square) and rural model (blue triangles point up) as a function of shower core distance from the telescopes. The plots are split into four equal log(energy) bins over the energy range of 1 to 500 TeV. Even with increasing the level of aerosols, the r68 profile is mostly not effected. The explanation for this result is that, even as more light is scattered out (due to the increasing presence of aerosols), the image gets fainter, but an ellipse can still be easily fitted. However, in extreme cases, the images can be very faint and can appear circular in shape. These faint images can have incorrect axis fitted or even be undetected. This effect can be seen on the r68 in the two energy bins of 1 - 4 TeV and 4 - 22 TeV for the rural aerosol model. For each of the aerosol models used, the shower events were reconstructed knowing the atmospheric transmission the Cherenkov light had propagation through. The simulated shower events were reconstructed knowing the atmospheric transmission the Cherenkov light had propagated through. All atmospheres were generated by MODTRAN [41].

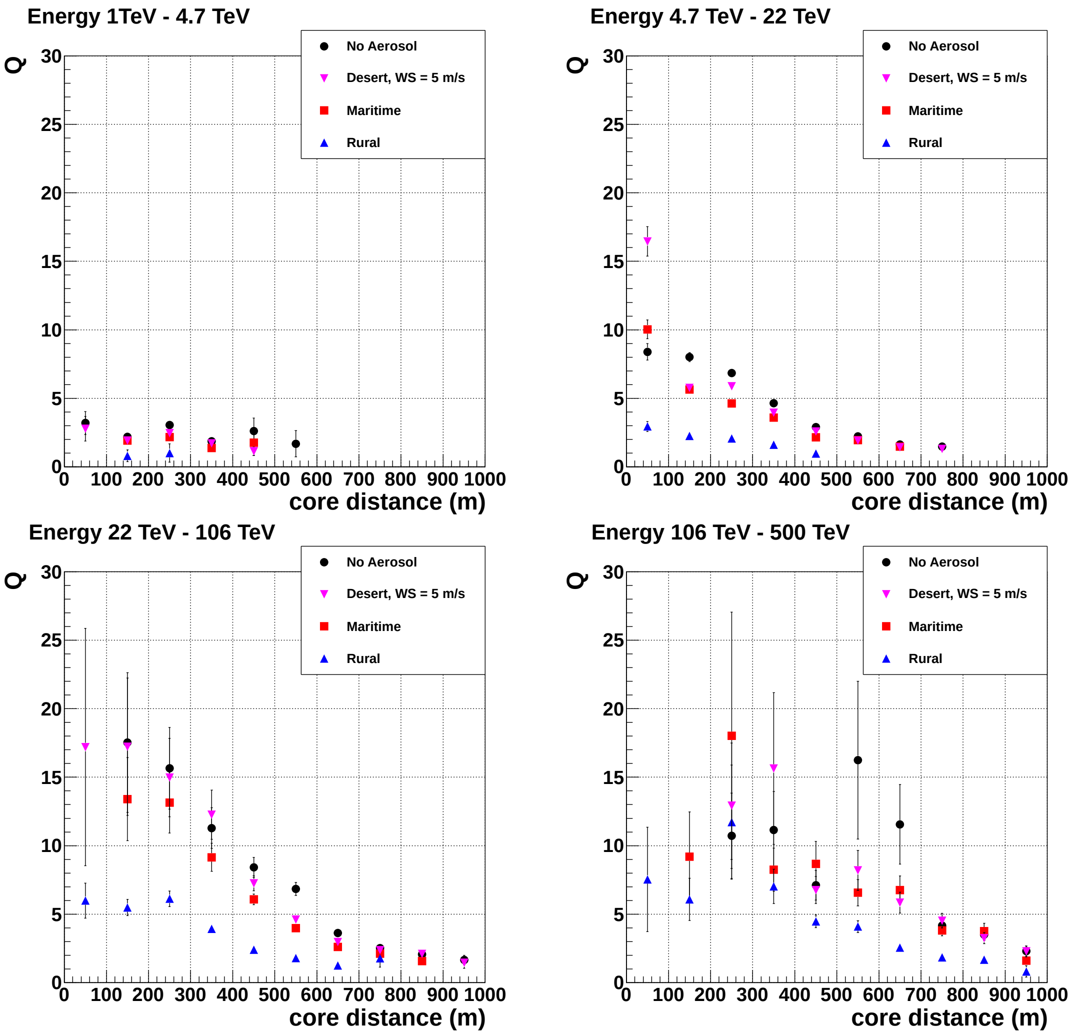

Figure 4.4: The simulated IACT array's ability to reject proton events (Q) for no aerosol model (black circles), desert model with wind speed (WS) = 5 m/s (pink triangles point down), maritime model (red square) and rural model (blue triangles point up) as a function of shower core distance from the telescopes. The plots are split into four equal log(energy) bins over the energy range of 1 to 500 TeV. Over all energy bins, it can be seen that the rural aerosol model consistently produced the worst Q, with the no aerosol model giving the best. The desert aerosol model and maritime aerosol model performed nearly as well as the no aerosol model. These showed that the performance of the array can tolerate some change in aerosol conditions. A higher Q denotes a greater ability to reject proton shower events. The large error bars in the 100 to 500 TeV energy bin is due to low number of proton events passing the image shape cuts. The simulated shower events were reconstructed knowing the atmospheric transmission the Cherenkov light had propagated through. All atmospheres were generated by MODTRAN [41].

effected. The explanation for this result is that, even as more light is scattered out (due to the increasing presence of aerosols), the image gets fainter but an ellipse can still be easily fitted. An image can be too faint, appearing more circular in shape, and can have an incorrect axis fitted or even be undetected. This effect can be seen on the r68 in the two energy bins of 1 - 4 TeV and 4 - 22 TeV for the rural aerosol model. The r68 value increases for a core distance greater than 200 metres for all energy bins. The number of Cherenkov photons reaching ground-level decreases rapidly as a function of core distance (this effect is shown in [48]).

The results for the Q of the simulated array are shown in Figure 4.4. When comparing the results, a higher Q is deemed better as it shows a greater ability to reject proton shower events. Across all energy bins, this shows that an atmosphere containing no aerosols allows the best separation between γ-ray and proton showers. Also across all energy bins, as the concentration of aerosols increases, the Q decreases. This result was expected, as when the optical depth is increased fewer Cherenkov photons can reach ground level. The decreasing levels of photons remove fine structure from images of both γ-ray and photon showers. Removal of the fine structure could allow protons showers to be characterised as γ-ray showers.

From Figure 4.3 and Figure 4.4, it can be seen that the Q is more sensitive to changes in the concentration of aerosols than the r68 value. This is not surprising as the r68 value relies on only fitting a major axis to an ellipse and this process works well on either a bright or dull image. The Q is a more complicated parameter. Discrimination of proton showers from γ-ray showers relies on the differences in fitted ellipse lengths and widths (discussed within Chapter 3). As the aerosol level increases, images can be blurred or dulled which means more proton showers can be misidentified as γ-ray showers.

This simulation helps with the site survey by showing the array's performance under a range of atmospheric conditions. For the array best performance to occur, sites with atmospheres close to containing no aerosols should be consisted.

4.3 Effects of Cirrus Cloud

This section investigates whether the introduction of cirrus clouds effects the simulated performance of the IACT array. The effects of cirrus clouds were investigated, as the height of these clouds is similar to the height to the maximum emission of Cherenkov photons for γ-ray shower energies around 10 TeV. Cirrus clouds are high clouds, forming 5 km to 12 km above the ground for a mid-latitude region [49]. Figure 4.5 gives an overview of of parameters of cirrus clouds and other types of cloud found in the atmosphere. Middle or low clouds were not investigated, because their atmospheric height of formation was typically below the height of maximum emission of Cherenkov photons for 500 TeV γ-ray showers.

The effects of cirrus clouds on γ-ray showers between 1 TeV and 500 TeV were first investigated by comparing the height of cirrus clouds against the height of maximum Cherenkov photon emission. The height of maximum Cherenkov photon emission was found by the use of the CORSIKA [37] computer package. An average atmospheric depth of maximum Cherenkov emission was found for 0.1, 1, 3, 10, 30, 100 and 300 TeV. The average height of maximum Cherenkov emis-

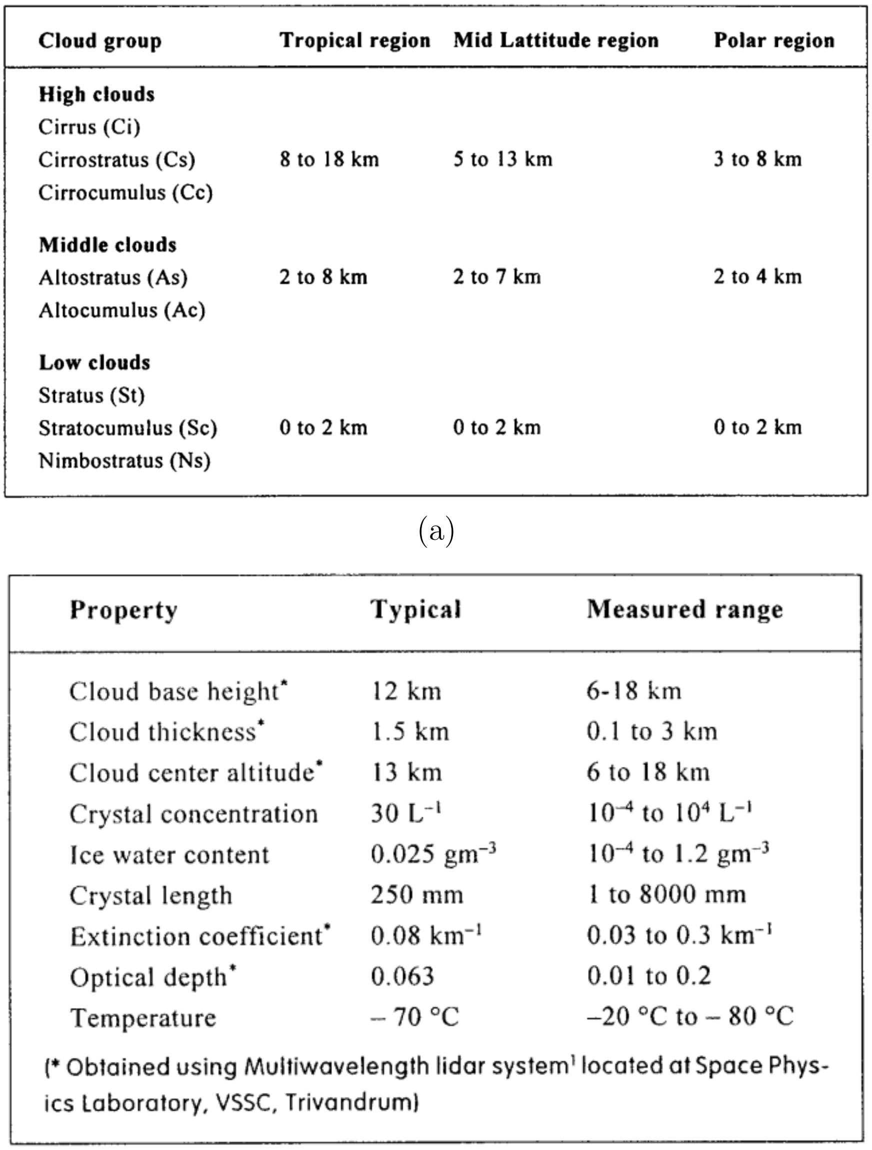

Cloud group	Tropical region	Mid Lattitude region	Polar region
High clouds			
Cirrus (Ci)			
Cirrostratus (Cs)	8 to 18 km	5 to 13 km	3 to 8 km
Cirrocumulus (Cc)			
Middle clouds			
Altostratus (As)	2 to 8 km	2 to 7 km	2 to 4 km
Altocumulus (Ac)			
Low clouds			
Stratus (St)			
Stratocumulus (Sc)	0 to 2 km	0 to 2 km	0 to 2 km
Nimbostratus (Ns)			

(a)

Property	Typical	Measured range
Cloud base height*	12 km	6-18 km
Cloud thickness*	1.5 km	0.1 to 3 km
Cloud center altitude*	13 km	6 to 18 km
Crystal concentration	30 L^{-1}	10^{-4} to 10^{4} L^{-1}
Ice water content	0.025 gm^{-3}	10^{-4} to 1.2 gm^{-3}
Crystal length	250 mm	1 to 8000 mm
Extinction coefficient*	0.08 km^{-1}	0.03 to 0.3 km^{-1}
Optical depth*	0.063	0.01 to 0.2
Temperature	– 70 °C	–20 °C to – 80 °C

(* Obtained using Multiwavelength lidar system[1] located at Space Physics Laboratory, VSSC, Trivandrum)

(b)

Figure 4.5: (a) Types of clouds and their typical altitudes for different regions. For the IACT array simulations, mid-latitude values for the cirrus clouds were chosen. (b) Typical values and measured ranges of the physical and optical properties of cirrus clouds at 532 nm. Tables from [49].

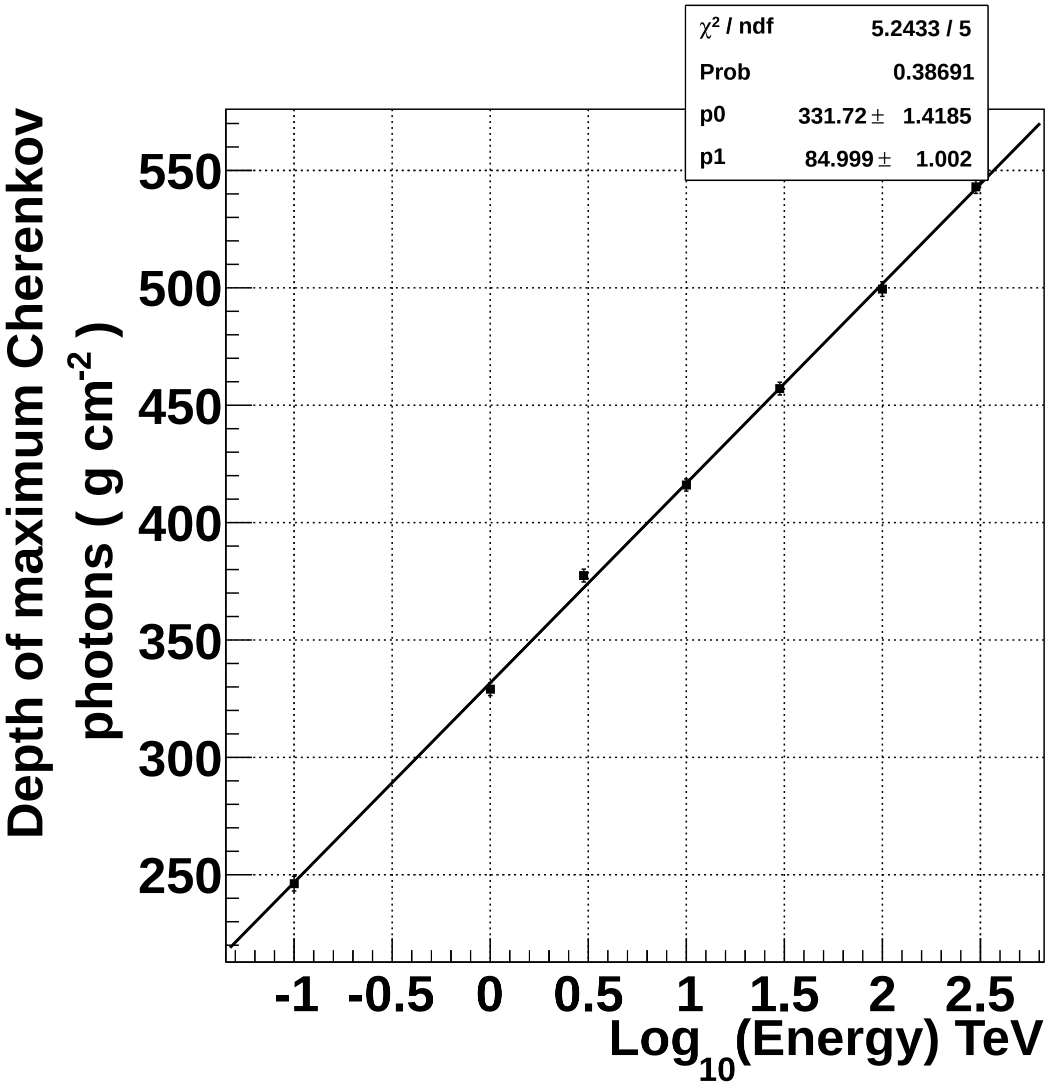

Figure 4.6: Atmospheric depth of maximum Cherenkov emission plotted against log(energy) for vertical γ-ray events simulated with CORSIKA [37]. Each point represents the mean depth found from 1000 simulated shower events. The slope of this plot is similar to the elongation rate of electromagnetic showers in air [50]. This is expected as the Cherenkov emission is closely linked to the evolution of electromagnetic showers. An elongation rate describes how the depth of maximum particle number changes with energy.

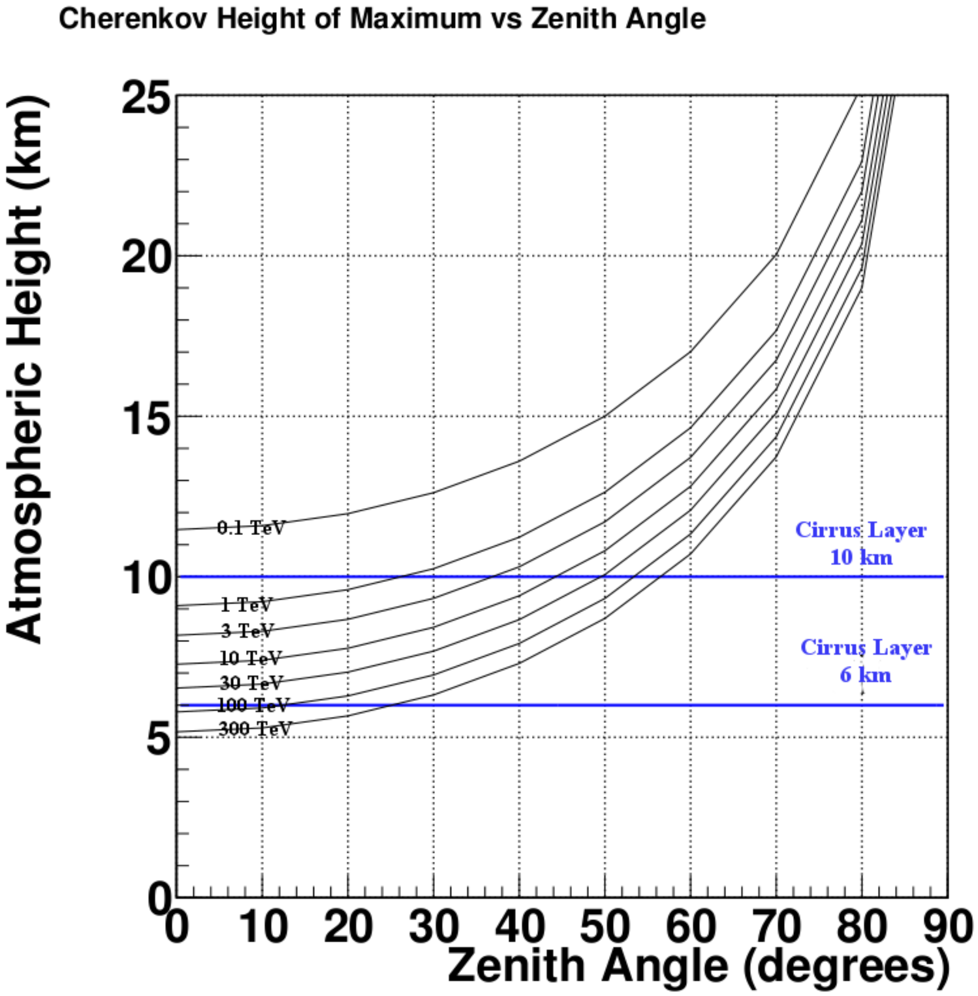

Figure 4.7: A plot showing how the height of maximum emission of Cherenkov photons is effected as the γ-ray showers are angled away from vertical. The (blue) horizontal lines at 6 km and 10 km are examples of where the base of cirrus clouds would occur. A cirrus cloud base at 6 km would mean that, on average, for vertical γ-ray showers with energy below 100 TeV, the majority of the Cherenkov photons produced would travel through the cirrus cloud. For a cirrus cloud base at 10 km, on average, vertical γ-ray showers with energy above 1 TeV, the majority of the Cherenkov photons produced would be below the cirrus cloud base. This plot gives an indication of the range of cloud heights and γ-ray shower energies where the maximum Cherenkov photon number could be below the cirrus cloud base.

sion was determined from the simulation of 1000 vertical γ-ray showers for each of these energies. Next, the average atmospheric depth of maximum Cherenkov emission was plotted against log(energy), shown in Figure 4.6. Atmospheric depth (G) can be converted into an atmospheric height (H) via the formula:

$$\mathrm{H} = \mathrm{H}_0 \times \ln\left(\frac{\mathrm{P}_0}{\mathrm{g} \times \mathrm{G}}\right) \tag{4.2}$$

where H_0 is the atmospheric scale height, P_0 is the atmospheric pressure at ground level, and g is the gravitational acceleration. The values used to convert atmospheric depth into atmospheric height in Figure 4.7 were:

$$\begin{aligned}\mathrm{H}_0 &= 8.0 \text{ km}\\ \mathrm{P}_0 &= 1.014 \times 10^6 \text{ mbar}\\ \mathrm{g} &= 980 \text{ cm s}^{-2}\end{aligned}$$

The height of maximum Cherenkov photon emission is plotted against zenith angles (the angle away from vertical). The result is shown in Figure 4.7. Within this figure are horizontal (blue) lines representing the base of the cirrus clouds at heights of 6 and 10 km. The lines representing the base of cirrus clouds give an indication of which energy or zenith angle for γ-ray showers the clouds are most likely to effect. A cirrus cloud base at 6 km could effect the observation of vertical γ-ray showers with a primary energy below 100 TeV, whilst for a cirrus cloud base at 10 km, it could only effect the the observation of vertical γ-ray showers with primary energy below 1 TeV. This allows for the possibility that between 1 TeV and 500 TeV, vertical γ-ray showers could be observed under such cloud. The height of the cirrus cloud and shower angle would influence the energy threshold and observable zenith range.

4.4 Summary

We have seen that an atmosphere that contains no aerosols gives the best performance for the array. The difference in performance when aerosols are introduced is mainly seen through the ability to reject proton images (Q). The best Q was seen with an atmosphere containing no aerosols. The Qs for desert and maritime aerosol models were comparable to a model with no aerosols. Comparing the angular resolution (r68) between the different aerosol models showed few differences. This shows, at these energies, the array's performance is not greatly effected by changes in the optical depth, up to ~ 0.4 (at 550 nm). I showed which TeV γ-ray showers could be effect by a cirrus cloud base at either 6 or 10 km. The next step would be to simulation the effect on the array performance by adding cirrus cloud into atmospheric models used.

Chapter 5

Photometry with a Pentax K10D DSLR Camera

In this chapter, I determine whether a Pentax K10D digital single lens reflex (DSLR) camera can be used for photometry. Photometry is the technique of measuring the flux of light (typically measuring wavelengths from near infra-red to ultra-violet) emitted from objects. A DSLR camera was chosen as a photometric instrument as it contains a photo-sensitive device that can measure optical light. A photo-sensitive device can be used for photometry if it contains a suitable region of linearity, and can be successfully flat and dark fielded. In the Pentax K10D DSLR camera it is also necessary to check the effect that the filter pattern on top of the photo-sensitive device has on measurements, and to calculate the gain of individual pixels for incorporation into error calculations and determination of absolute fluxes. In this experiment, the success of the flat- and dark-field procedures was checked through the photometric techniques of measuring star extinction coefficients and night sky background (NSB) levels.

5.1 Background

This section gives background details on the equipment and photometry methods used. The Pentax K10D DSLR camera is the main focus when discussing the equipment used for photometry techniques. The two photometry techniques used within the camera suitability test were measuring star extinction coefficients and night sky background (NSB) levels.

5.1.1 Equipment

The equipment used to take images of the night sky for photometric purposes was a Pentax K10D DSLR camera and a tripod. The Pentax K10D camera specifications are:

- 23.5 mm by 15.7 mm charged couple device (CCD)
- 10 Mega-pixels (3896 × 2616 pixels)
- Internal battery supply
- An ISO setting (measure of a camera sensitivity to light) of up to 1600

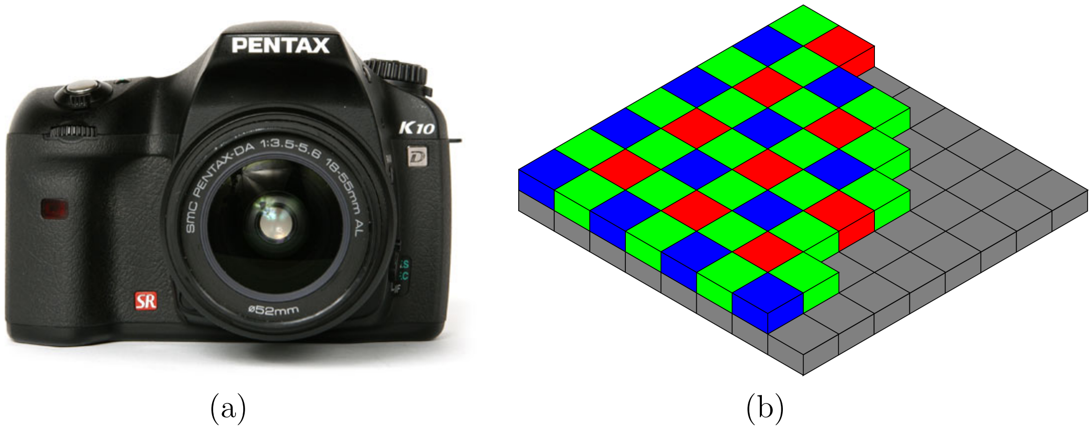
(a) (b)

Figure 5.1: (a) An image of a Pentax K10D digital single lens reflex (DSLR) camera. (b) A diagram of how the Bayer filter pattern is applied to the top of the CCD sensor. The diagram of the Bayer filter pattern shows that within a two by two grid of pixels, there are two green, one red and one blue pixel.

- f-stop 22 to 3.5 (aperture setting)
- Uses JPEG and DNG (ADOBE raw) formats
- 12-bit digital output
- Bayer filter pattern on pixels (further detail in this section)
- Sigma 18 mm - 200 mm lens
- With Sigma lens, can achieve a 70° by 50° maximum field of view

A Pentax K10D camera is example of an off the shelf DSLR camera and containing a charge coupled device (CCD) makes it a suitable candidate to used as photometric device. Other notable features are an internal power source, is easily transportable and has a minimal set up time. Transportability is an important issue as the locations that are of interest for the site surveys can be remote. The remoteness of locations restricts the amount of equipment that can be taken on each site survey. Other DSLR cameras could have been used for testing but the Pentax K10D camera was the one that available to me at the time.

The CCD is the main reason the Pentax K10D camera was tested as a device to be used for photometry. A CCD is a device which converts an incoming photon flux into stored electron charge. As an object is viewed, the pixels fill up with the converted electrons. The electrons in each pixel are then shifted to an adjacent pixel, column by column. As each column reaches the edge of the CCD it is read out, pixel by pixel. The electron counts are converted to a digital value, expressed in analogue-to-digital units (ADU). An ADU is the number of electrons within the pixel multiplied by the gain. As the Pentax K10D camera has a 12-bit output, the ADU values can only range between 0 and 4096. When the maximum capacity of a pixel is reached, one of two scenarios can occur in CCD chips. Either the excess electrons spill over into neighbouring pixels or excess electrons are drained away. In the Pentax K10D camera, excess charge is drained away from the pixel.

The consequence of electrons being drained away, is that a signal larger than the pixel capacity is capped to the maximum capacity of the pixel. The capping of capacity has the potential to impact analysis of data, the implications of which are discussed further in Chapter 6. For further information on CCDs see [51].

Pentax K10D camera options effecting the detection of light include the ISO, aperture size and exposure length. ISO stands for the International Organisation for Standardisation (ISO) and the ISO setting is the measure of a camera's sensitivity to light. An increase in the ISO setting means an increase in the gain. The aperture setting deals with the size of the opening through which light is shone onto the CCD. The aperture setting (defined in the camera settings as f-stop) is defined as:

$$\text{f-stop} = \frac{\mathrm{f}}{\mathrm{D}} \tag{5.1}$$

where f is the focal length and D is aperture diameter. Another way to change the amount of measured light is to change the exposure length. The exposure length is the amount of time that the CCD is exposed to a light source. For further information about the specifications and operation of the Pentax K10D camera, see the manual [52].

The CCD on the Pentax K10D camera is monochromatic, but to get different coloured channels, filters have been applied directly on top of each pixel. The coloured filters have been arranged in a Bayer pattern. Within a grid of two by two pixels, the Bayer pattern includes one red, one blue and two green pixels. Each colour channel refers to a different wavelength window. A diagram of the Bayer pattern is shown in Figure 5.1. A side-effect of the Bayer pattern is that when analysing single colour channels, pixels related to other colour channels are considered dead space. The effects of the Bayer pattern are discussed later in this chapter.

Images used for analysis must contain the raw digital values that each Pentax K10D camera pixel observed. For the Pentax K10D camera this is achieved by using the digital negative (DNG) [53] format option. The other format that the Pentax K10D camera can use is JPEG. JPEG is a lossy format, where some information is lost to reduce the amount of memory needed to store the images.

5.1.2 Method of Photometry

The method of photometry used in astronomy is concerned with measuring the flux of astronomical objects. Raw data taken by a CCD camera needs to be processed before any photometric measurements can be made. A raw image will contain the signal of interest, dark noise, and the effects from optical vignetting. Vignetting is the optical effect which sees less light measured towards the edge of an image compared with the centre. If a camera were to image a uniform coloured and lit surface, the resultant image would have darker edges compared with the center. Vignetting is generally caused by lens limitations, where rays that enter at large angles observe a smaller effective area of the lens. Dark noise is any electronic or thermal noise within a camera.

The raw image is corrected by use of a flat-field and dark-field image. A flat-field image is used to correct for vignetting and any variations in pixel by pixel gain. The process of flat-fielding is to divide the raw image by a flat-field image and then multiply by a normalising constant. The normalising constant can be calculated by averaging all values within the flat-field image. Flat-field images are images taken of uniform illuminated surfaces. Dark-field images correct for any electronic or thermal noise within a camera. Dark noise is corrected by subtracting a dark-field image from the raw image. A dark-field is produced via recording an image while no light is illuminating the CCD in a camera. A dark-field and flat-field image is applied to a raw image via:

$$\mathrm{S}(x,y) = \frac{\mathrm{k} \times (\mathrm{R}(x,y) - \mathrm{D}(x,y))}{\mathrm{F}(x,y) - \mathrm{D}(x,y)} \tag{5.2}$$

where S is the processed signal value, R is the raw value, D is the dark-field value, F is the flat-field value, k is the normalising constant and (x,y) is pixel position within the image. This method can be applied to each of the different coloured channels, with the normalising constant k being calculated for each channel. To calculate the uncertainty in the processed signal value from Equation 5.2, propagation of errors is performed. The uncertainty formula becomes:

$$\sigma_S^2 = \sigma_R^2 \times \left(\frac{\partial \mathrm{S}}{\partial \mathrm{R}}\right)^2 + \sigma_D^2 \times \left(\frac{\partial \mathrm{S}}{\partial \mathrm{D}}\right)^2 + \sigma_F^2 \times \left(\frac{\partial \mathrm{S}}{\partial \mathrm{F}}\right)^2 \tag{5.3}$$

$$\begin{aligned} \sigma_S^2 &= \sigma_R^2 \times \left(\frac{\mathrm{k}}{\mathrm{F}(x,y) - \mathrm{D}(x,y)}\right)^2 \\ &+ \sigma_D^2 \times \left(\frac{\mathrm{k}(\mathrm{R}(x,y) - \mathrm{F}(x,y))}{(\mathrm{F}(x,y) - \mathrm{D}(x,y))^2}\right)^2 \\ &+ \sigma_F^2 \times \left(\frac{\mathrm{k}(\mathrm{R}(x,y) - \mathrm{D}(x,y))}{(\mathrm{F}(x,y) - \mathrm{D}(x,y))^2}\right)^2 \end{aligned} \tag{5.4}$$

where σ_S is the uncertainty in the processed signal, σ_R is the uncertainty in the raw value, σ_D is the uncertainty in the dark-field value and σ_F is the uncertainty in the flat-field value. After the images have been flat and dark fielded, the values can be used for a number of analysis techniques. I will describe two techniques that can be employed: measuring star extinction coefficients and measuring night sky background (NSB) levels. Within the explanation of these techniques, I outline why I chose these two methods. For further information on photometry see [54, 55].

5.1.3 Photometry: Star Extinction Coefficient

Star extinction coefficients are a measure of how stars' magnitudes change as a function of airmass. The star extinction coefficient was chosen as a quantity for measurement as it can be directly related to atmospheric transmission. To find a star magnitude at a given airmass, a circle is first placed around all the pixels containing signal from a star in an image. The summed pixel values within the circle gives Count_{star}. All the light from the star must be contained within the circle and will also contain a level of NSB noise. The average NSB level per pixel is found by placing a larger circle around the star and averaging the summed pixel count of the area contained by the outer circle, minus the area contained

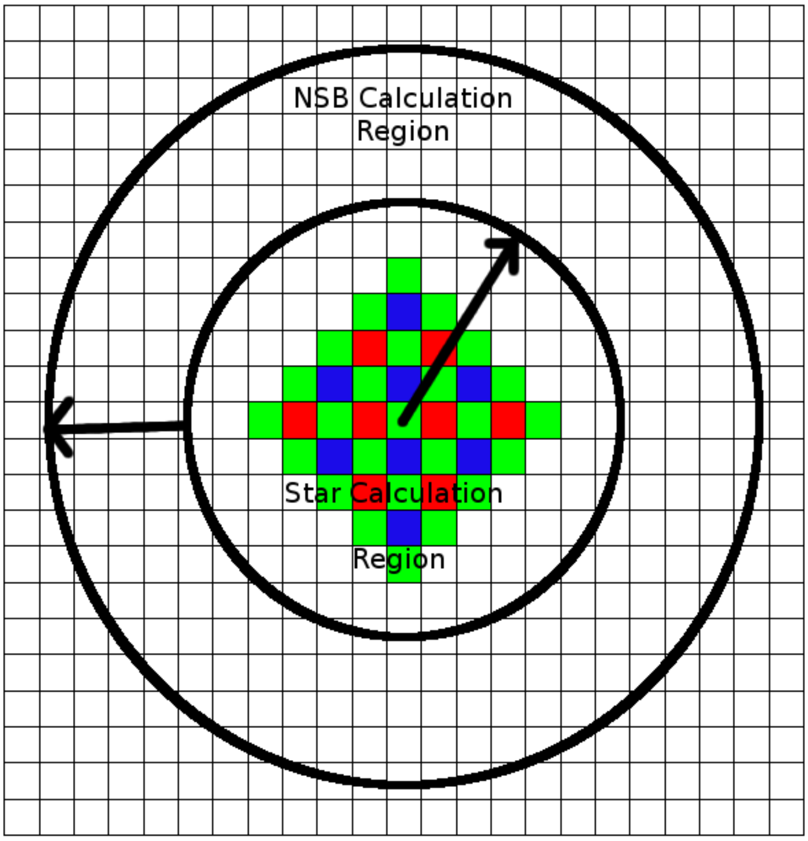

Figure 5.2: A diagram of how star counts within a picture are calculated. Count$_{star}$ is calculated by summing up all the pixels within the star calculation region. The coloured pixels give an indication of what a star would look like when viewed by a Pentax K10D camera's CCD employing the Bayer filter pattern. The average NSB per pixel is found by summing up the pixel counts within the NSB calculation region, and dividing by the number of pixels within the region. Count$_{star}$ and the average NSB per pixel are calculated separately for each colour channel.

by the inner circle. A diagrammatic example is shown in Figure 5.2. If there are N pixels used for Count_{star}, an estimation of the NSB contained with inner circle (Count_{NSB}) can be found:

$$\text{Count}_{NSB} = \text{N} \times (\text{average NSB per pixel}) \tag{5.5}$$

To find the “magnitude” of the star in terms of the instrument:

$$\text{magnitude} = -2.5 \times \log_{10}(\text{Count}_{star} - \text{Count}_{NSB}) \tag{5.6}$$

where both count_{star} and count_{NSB} are in ADU. The magnitude calculated from ADU measured by a camera in Equation 5.6 will be referred to as the instrumental magnitude.

To calculate the star extinction coefficient (k), the instrumental magnitude is plotted against airmass (X). An airmass is defined as the number of atmospheres that light would pass through from the top of the atmosphere to ground level at an angle θ, taken from the vertical. An approximate formula for calculating airmass is:

$$\text{X} = \sec(\theta) \tag{5.7}$$

This formula works to approximately 80° from the zenith. The relationship between instrumental magnitude and airmass is linear. The form of the linear fit is:

$$\text{magnitude} = \text{magnitude}_0 + \text{k X} \tag{5.8}$$

where magnitude is the instrumental magnitude observed through X airmass, magnitude_0 is the instrumental magnitude that would be recorded if the atmosphere was absent and the k is the star extinction coefficient.

To calculate the atmospheric transmission, the star extinction coefficient is first related to the vertical atmospheric optical depth (τ) by:

$$\frac{\text{I}}{\text{I}_0} = \exp(-\tau \text{X}) \tag{5.9}$$

$$\text{magnitude} - \text{magnitude}_0 = -2.5 \times \log_{10}\left(\frac{\text{I}}{\text{I}_0}\right) \tag{5.10}$$

where I is the reduced intensity after passing through the atmosphere, I_0 is the intensity at the top of the atmosphere, τ is the vertical optical depth, and X is the airmass. Substituting Equation 5.8 and Equation 5.9 into Equation 5.10 gives:

$$\text{kX} = -2.5 \times \log_{10}(\exp(-\tau\text{X}) = -2.5 \times 0.434 \times \ln(\exp(-\tau\text{X}) \tag{5.11}$$

$$\text{k} = 1.086 \times \tau \tag{5.12}$$

Then the vertical optical depth measured between the top of the atmosphere and an observer can be related to the atmospheric transmission (T) by:

$$\text{T} = \exp\left(-\tau \sec(\theta)\right) \tag{5.13}$$

where θ is the angle from the vertical. Given the presence of the Bayer filter with the Pentax K10D camera, this method must be applied to each colour channel separately. The atmospheric transmission measured by a camera is the quantity that is important to an imaging atmospheric Cherenkov technique (IACT) array. A decreasing atmospheric transmission means a decreasing atmospheric quality. The results of observed star extinction coefficients will be discussed in Chapter 6.

5.1.4 Photometry: Night Sky Background (NSB)

This section deals with the detection and processing of NSB signals by the Pentax K10D camera. As seen in Chapter 2, NSB is the signal a device would measure directed at an area of the night sky containing no discernible light sources, e.g. stars or galaxies. The most useful unit for the measured NSB, when dealing with IACT arrays, is in units of photons per steradian per square centimetre per second. Before we can get to this point, the magnitude per viewing angle of the NSB must be calculated. The reason for finding magnitude per viewing angle stems from the formulae used (Equation 5.15 and Equation 5.16). The method involves splitting the image into grids. Grids contain many pixels which define the area of the average NSB count. First the pixels within the grid are split into their respective colour channels. Within the grid, pixels for each colour channel are summed, then divided by the area of the sky that is viewed by the grid in units of arc-seconds^2. The next step is to find the instrumental magnitude per arcsec^2 for each of the colour channels:

$$\text{magnitude per arcsec}^2 = -2.5 \times \log_{10}(\text{counts per arcsec}^2) \tag{5.14}$$

To find an absolute NSB value, the instrumental magnitudes need to be calibrated against equivalent catalogue apparent magnitudes for each colour channel. The catalogue magnitudes used for calibration were taken from the SIMBAD Astronomical Database [56]. The relationship between the instrumental magnitudes and the catalogue magnitudes is linear.

In this study only the NSB for the green and blue channels were calculated. The red colour channel was omitted due to the absence of red colour magnitudes within the SIMBAD Astronomical Database. The measurement of the red NSB is of less importance for an IACT array. The green channel magnitudes are calibrated against the visible (V) catalogue magnitudes, while the blue channel magnitudes are calibrated against the blue (B) catalogue magnitudes. For the Visible band (or Green Channel), the equation to convert the catalogue magnitude of the NSB is:

$$\mathrm{b}_V = \exp\left(\frac{41.438 - \mathrm{Mag}_V}{1.0857}\right) \tag{5.15}$$

where b_V is the number of photons / (sr cm^2 s) and Mag_V is the calibrated catalogue magnitude of the NSB in the Visible band. For the Blue band, the equation is:

$$\mathrm{b}_B = \exp\left(\frac{41.965 - \mathrm{Mag}_B}{1.0857}\right) \tag{5.16}$$

where b_B is the number of photons / (sr cm^2 s) and Mag_B is the calibrated catalogue magnitude of the NSB in the Blue band. Equation. 5.15 and Equation. 5.16 were both taken from [57]. The results of this analysis will be discussed in Chapter 6.

5.1.5 Gain: Method

The gain is the ratio between the number of electrons that the CCD measures and the number of ADU that are displayed. The Pentax K10D camera sets the gain via the ISO setting. The main reason that the gain needs to be calculated is that Poisson statistics can only be applied to the number of electrons counted to calculate the errors, not on the analogue-to-digital units (ADUs) recorded by the Pentax K10D camera (see Section. 5.1.2 for further detail). To measure the gain of individual pixels, I used 100 images uniformly illuminated at the same ISO, aperture and exposure setting. For each pixel, the data is collated across the 100 images. The collated data for a single pixel is then used to work out a mean and RMS. The pixel gain can then be determined using:

$$\mathrm{G} = \frac{\mathrm{Mean}}{(\mathrm{RMS})^2} \text{ electrons / ADU} \tag{5.17}$$

This equation assumes that the RMS of the pixel values is simply the result of Poisson fluctuations of the electron number. The gain was determined for individual pixels, as there was an expected variation in the gain from pixel to pixel. The method that I used to calculate the gain takes advantage of Poisson statistics. Below is the equation for the gain and how a calculated RMS and mean in ADUs relate to the fluctuation in the electron counts:

$$\mathrm{G} = \mathrm{N} \ / \ \mathrm{Mean} \text{ (electrons per ADU)} \tag{5.18}$$

$$\frac{\mathrm{RMS}}{\mathrm{Mean}} = \frac{\sqrt{\mathrm{N}}}{\mathrm{N}} \tag{5.19}$$

where N is the number of electrons observed by the CCD, and G is the gain. The RMS and the mean are both in ADU. Equation 5.19 shows how the relative uncertainty in the ADU is related the uncertainty in the electron numbers.

5.2 Camera Suitability Results

Five tests were applied to determine the suitability of a Pentax K10D camera. These were: linearity, ability to dark-field, gain, ability to flat-field and impact of the Bayer filter. The test for linearity is necessary to check that a linear increase in a light source intensity is matched by a linear increase in the measured signal. Next the dark-field was investigated for its ability to measure and correct for the dark noise. The ability to dark-field was tested with real data and through simulation. The gain was found in order to calculate the uncertainties in the measurements. I quantified the effects of different flat-field methods on measuring star extinction coefficients. Lastly, I investigated the effects the Bayer filter pattern had on measuring the star instrumental magnitudes.

5.2.1 Linearity

A linear region of a CCD is the range of flux where the pixel counts are in direct proportion to an observed changing photon flux. If there is a non-linear region present, it becomes much more difficult to compare differences in the recorded signal from different light sources. Two ways are described here to measure the linearity of a CCD. One way is to use a fixed exposure time and vary the intensity of a light source. The other way is to use a constant intensity light source and to vary the exposure time. Both these methods should produce the same results, as

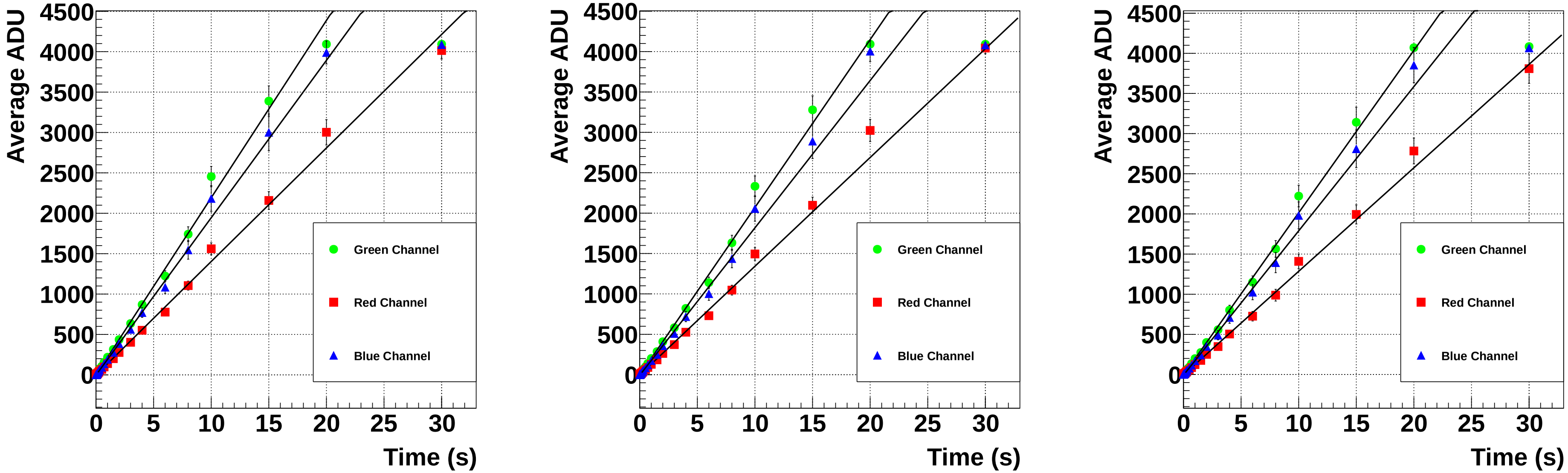

(a)

(b)

(c)

Figure 5.3: These plots show the average ADU against exposure time for (a) 400 ISO (b) 800 ISO and (c) 1600 ISO. The green channel is indicated by the (green) circles, the red channel by the (red) squares and the blue channel by (blue) triangles. A constant intensity light source was used for each measurement. The line fitted to each of the channels is a by 'eye indication' of the linearity. The average ADU reaches the limit of digitisation (12-bit range) before demonstrating any non-linear characteristics. Each dot represents an average of 1050^2 pixels taken at different exposure times.The f-stop (or aperture setting) was different for each of the ISO settings, so the maximum ADU count could be reached for exposure times between 15 and 30 seconds.

increasing the exposure time has a similar effect to increasing the flux from the light source. I measured the linearity of the Pentax K10D camera via the second method.

As the method of varying the exposure of the Pentax K10D camera was used to find the linearity, a series of images with different exposure times were taken. The images taken were of a white surface, illuminated by indirect sunlight. Next, the mean and RMS of the signal was calculated from a 1050 by 1050 square of pixels, centred on the middle of the image, for each of the different exposure times. A separate mean and RMS was calculated for each of the different colour channels. By plotting the mean against exposure time, the linearity of the CCD was tested. The results of this method is shown in Figure 5.3. The figure shows that the Pentax K10D camera is linear up to ~ 4000 ADU for each of the measured ISO settings of 400, 800 & 1600. The linearity cannot be tested past ~ 4000 ADU as this is the limit of the digital output, which is only 12-bit. Therefore I have shown that the Pentax K10D camera reaches the limit of digitisation before any non-linear behaviour is observed. Also, the figure shows that the Pentax K10D camera's CCD is linear in each of the different colour channels. Each point in Figure 5.3 represents a single exposure time. The f-stop (or aperture setting) was different for each of the ISO settings, so the maximum ADU count could be reached for exposure times between 15 and 30 seconds.

5.2.2 Dark-Field

The dark noise is a signal present in any picture taken, and its effect on different analysis processes needs to be quantified. The dark noise within the Pentax K10D camera can be measured by taking dark-field images. A dark-field image can be produced by the CCD taking an image exposed to no light. Examples of dark-field images for 400, 800 and 1600 ISO are shown in Figure 5.4. Each image was taken with an exposure length of 20 seconds. Within these images, there are some features of note: the regular striping and the bright areas. The bright areas could be caused by electronics near the chip which produce thermal noise. The striping could be caused either by gain variations or by the electronic read-out.

To see whether the Pentax K10D camera could observe the night sky background (NSB) over the dark noise, I compared an image containing both NSB and dark noise against a dark-field image. The purpose of this test was to see if there was any separation between the average signal per pixel from the star-field image and the dark-field image. Each of the images was split into grids, 52 by 52 pixels in size. Next, pixels that contain signal from stars were removed. The average pixel value was found for each grid and was placed into a histogram. The same pixels were also excluded from the dark-field to keep the comparison areas the same for when finding the average pixel value. This was done for each image used in the analysis. The same dark-field image was used for the comparison to the five images taken, each with different aperture settings (or f-stop): f11, f8.0, f6.7, f5.6 and f3.5. The results for different aperture settings for the 400 ISO green channel are shown in Figure 5.5. The best separation, when using the 400 ISO green channel, came from using the largest aperture setting (or smallest f-stop) of 3.5, and the separation occurred when the NSB image had an average pixel signal larger then 5 ADU. This method was extended to the other colour

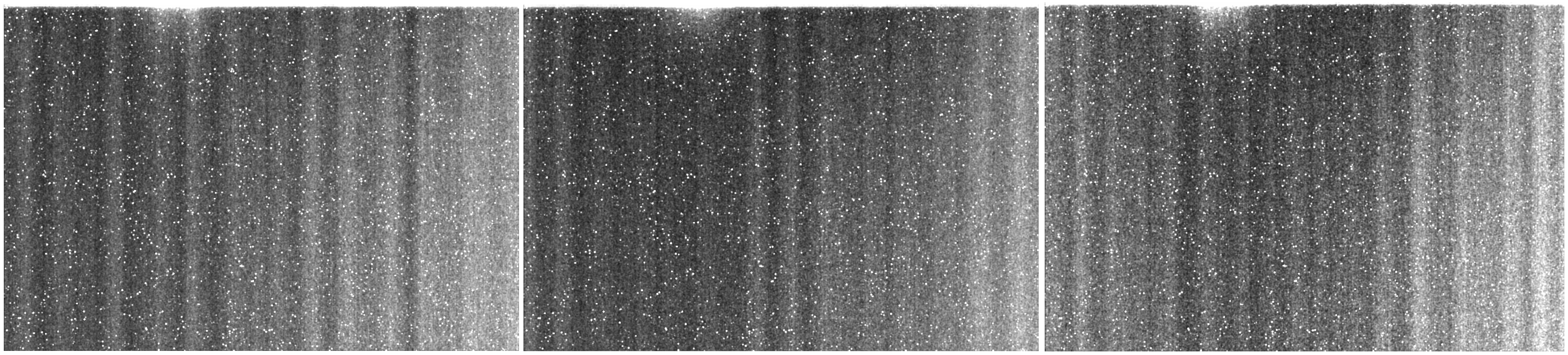
(a) (b) (c)

Figure 5.4: Examples of dark-field pictures, each with 20 sec exposure. (a) is set at 400 ISO and shown with a threshold between 0 and 5 ADU, (b) is set at 800 ISO and shown with a range between 0 and 10 ADU, and (c) is set at 1600 ISO and shown with a range between 0 and 15 ADU. Each image has been Gaussian blurred to accentuate the low level structure. Within the images, a striping and bright area are visible for each of the different ISO. An explanation for the striping could be caused by variations in gain or electronic read-out. The bright areas could be caused by thermal noise from nearby electronics.

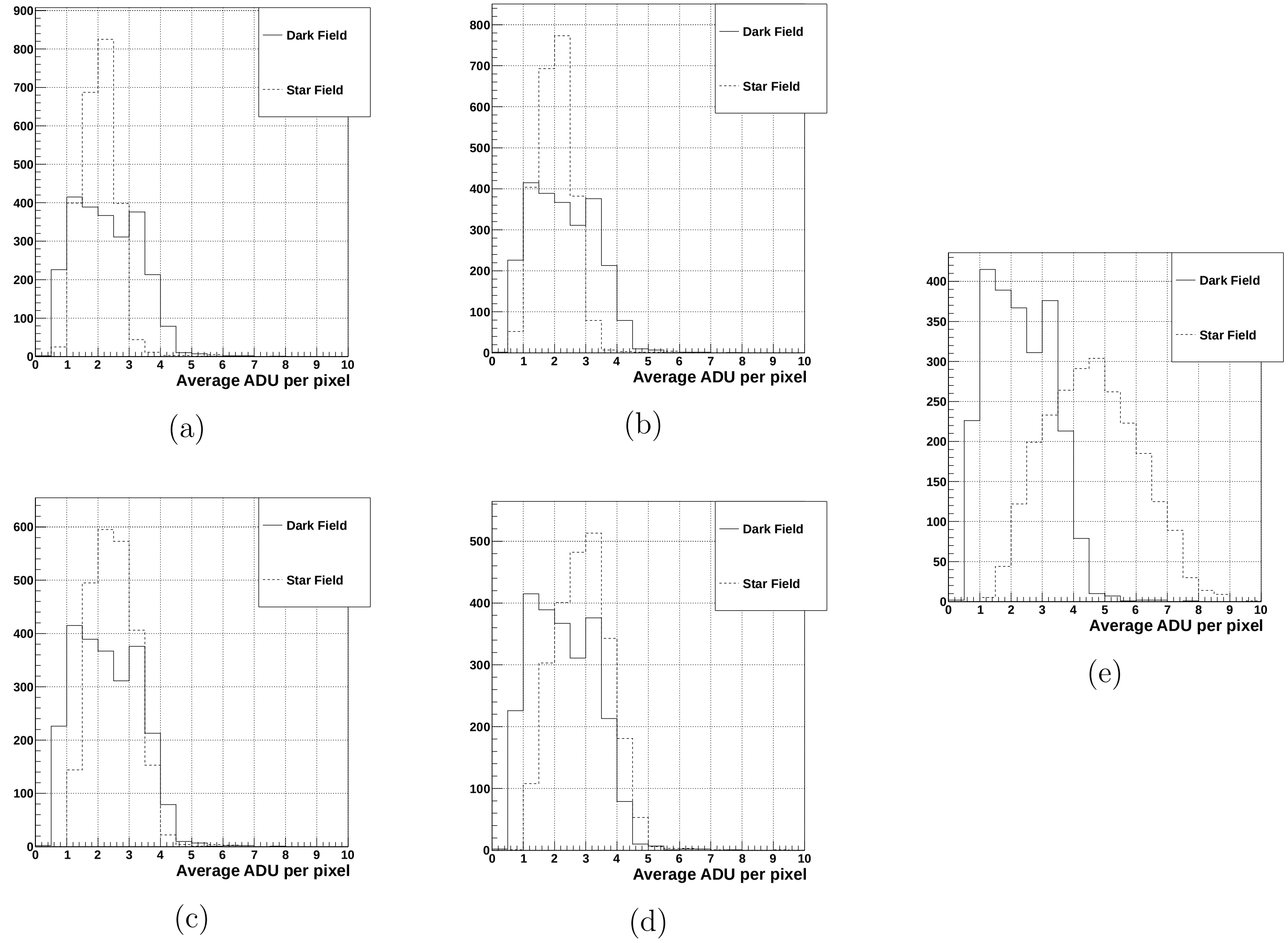

(a) (b) (c) (d) (e)

Figure 5.5: Plots of average dark-field counts per pixel and average signal counts per pixels from a night sky image for just the Green Channel. Average ADU per pixel from the dark-field is denoted by the solid line, while average counts per pixel from the night sky image are denoted by the dash line. Counts due to Stars and “hot” dark pixels were removed. All pixels have been taken with the Pentax K10D camera settings of 400 ISO, exposure length of 20 sec and f-stop (or aperture setting) of (a) 11, (b) 8.0, (c) 6.7, (d) 5.6 and (e) 3.5. The f-stop of 3.5 shows the only evidence of a signal level above the noise, which indicates an ability to measure the NSB.

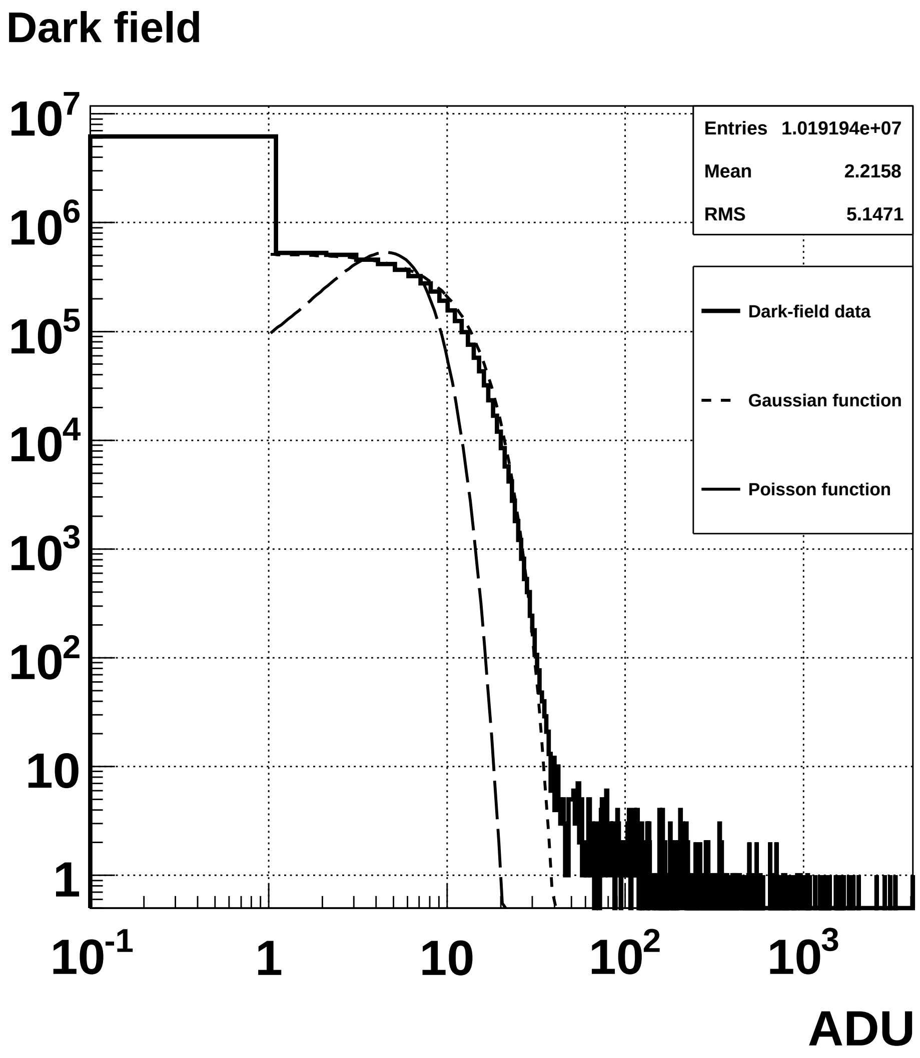

Figure 5.6: An example of a histogram of a dark-field image. The dark-field image was taken at 400 ISO with an exposure time of 0.25 seconds. Notable features are a large peak at zero ADU, with the counts between 1 and 100 ADU being described by the Gaussian function. Both a Gaussian function and Poisson function are fitted for comparison. It can be seen that the Gaussian function fits the best.

Exposure (sec)	**Data**	**Fitted Gaussian**
0.100	1.02e+07	1.03e+07
0.125	1.02e+07	1.06e+07
0.167	1.02e+07	1.02e+07
0.250	1.02e+07	0.97e+07
0.333	1.02e+07	1.03e+07
0.500	1.02e+07	1.00e+07
0.700	1.02e+07	0.99e+07
1.0	1.02e+07	1.01e+07
1.5	1.02e+07	1.02e+07
2.0	1.02e+07	1.01e+07
3.0	1.02e+07	0.96e+07
4.0	1.02e+07	0.94e+07
6.0	1.02e+07	0.99e+07
8.0	1.02e+07	0.98e+07
10	1.02e+07	0.99e+07
15	1.02e+07	0.97e+07
20	1.02e+07	1.00e+07
30	1.02e+07	0.99e+07
Mean	1.02e+07	1.00e+07
RMS	0.001e+07	0.03e+07

Table 5.1: Table of values comparing the integrated histogram of dark-field images against the integrated value of a fitted Gaussian. A Gaussian was fitted for ADU $\geqslant 1$ and was integrated from -100 ADU to 100 ADU, while the histogram of dark-field values were integrated from 0 to 100 ADU. The table shows two different effects: that the integration of dark-field values from 0 to 100 ADU is equivalent to the integration of the fitted Guassian from -100 to 100 ADU, and that the noise is not dependent on exposure time. As the noise is not dependent on time, it is most likely to be mainly read-out noise.

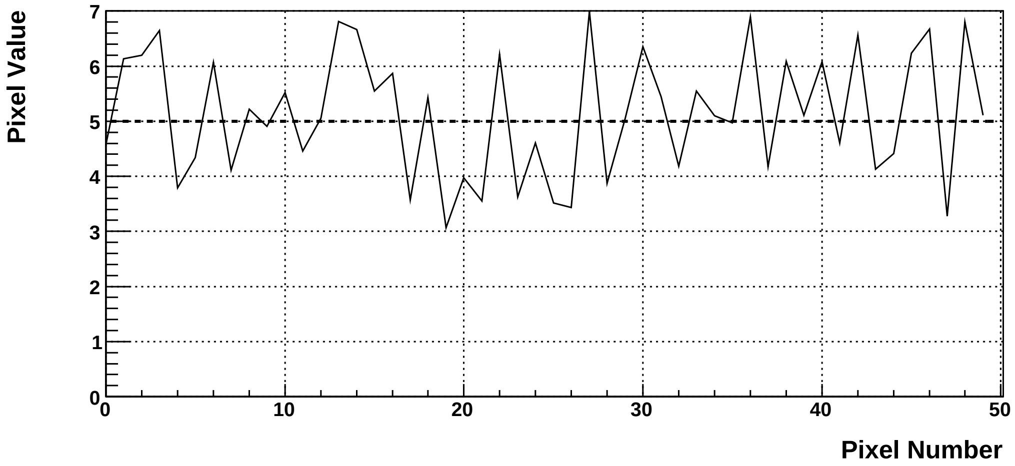

(a)

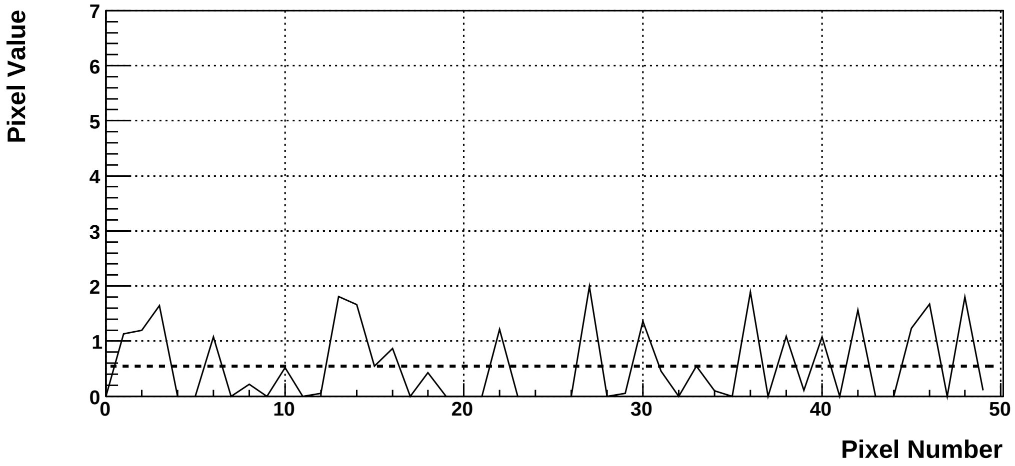

(b)

Figure 5.7: Simulated data of the noise expected from (a) electronic device containing a pedestal and (b) Pentax K10D camera. A dark-field image from a Pentax K10D camera displays no pedestal and has all negative values set to zero. The dashed lines represent the average value of noise. In the case of the device containing a pedestal, the mean value would be used to remove the pedestal. Using the mean in a similar manner is not quite right for the Pentax K10D camera as there is no pedestal and would also over-correct for the noise.

channels and different ISO, all showing that an f-stop of 3.5 gave the best separation. The comparison plots for the 400 ISO red and blue channels, 800 ISO all colour channels, and 1600 ISO all colour channels are shown in Appendix A.1.

To further understand the dark noise signal that the Pentax K10D camera recorded, I placed the pixel data from single dark-field images into histograms. An example using a single dark-field image taken at 400 ISO with an exposure time of 0.25 seconds is shown in Figure 5.6. This figure has a couple of interesting features: there is a large number of counts at zero ADU and what looks like a half Gaussian shape extending from 1 ADU outwards. The shape of a half Gaussian and the large spike of zero counts led to the investigation of whether the integration of a fitted Gaussian would match the area under the histogram from 0 ADU to 100 ADU. To see if this was the case, I fitted both a Gaussian and Poisson function to the histogram in Figure 5.6 for pixel values greater than or equal to one ADU. This showed that the Gaussian function fitted the best. Next, I compared the total area under the Gaussian (integrated from -100 ADU to 100 ADU) to the area under the histogram from 0 ADU to 100 ADU. I found that the area under the histogram is on a similar order of magnitude to the area under the fitted Gaussian. In Table 5.1, I confirm this for a range of exposure times between 0.1 and 30 seconds. All the images were taken with an ISO setting of 400. From that table, it can be seen that the majority of the noise is independent of exposure time. An explanation for this effect is that the noise is probably mainly comprised of electronic read-out noise.

An explanation for the spike of counts at zero ADU could be either that the CCD is unable to record the full variation in dark noise, or that the mean dark noise value has been used as the zero point. This means that any values less than zero ADU are recorded as zero by the Pentax K10D camera. In contrast, other electronic instrument can operate with an electronic pedestal (e.g. a CCD designed for scientific purposes), which would allow the full range of noise to be observed. These two cases are illustrated in Figure 5.7. The figure shows an example how a pedestal within an instrument displays the full range of dark noise and an example of how the absence of a pedestal effects the recorded dark noise. To remove a pedestal, the mean value is subtracted from the dark-field image. As the Pentax K10D camera does not contain a pedestal, subtracting the mean noise value would over estimate the dark noise present. In the case of the Pentax K10D camera, it might be possible not to subtract anything but this does not deal with noisy pixels. I decided to use the dark-field image from the Pentax K10D camera to subtract the dark noise and quantify any systematic uncertainty through the use of simulations.

5.2.2.1 Simulation

The effect of using dark-field images from the Pentax K10D camera for the dark noise correction is investigated through simulation. This is investigated as the dark-field images from the Pentax K10D camera are used to analyse the collected data in this chapter and Chapter 6. The simulations explore the method of measuring signal from the sky, the method of measuring star extinction coefficient, and measuring the Pentax K10D camera pixel gain. These methods are outlined in Section 5.1. For each of the methods, the dark noise and NSB values were generated by random sampling from separate Gaussian functions and the signal

Input Mean (ADU)	**Output Mean (ADU)**	**Error in the Mean (ADU)**
2	1.193	0.003
4	2.631	0.003
6	4.271	0.004
8	6.054	0.004
10	7.946	0.004
15	12.865	0.004
20	17.857	0.004
30	27.850	0.004
50	47.848	0.004
100	97.851	0.004
1000	997.854	0.004

Table 5.2: The result of simulating the process of using the Pentax K10D camera dark-field image to process different sky signals observed by the camera. The input mean set the mean sky signal value and the Pentax K10D camera noise is added by sampling from random Gaussian with mean of 0 ADU and standard deviation of 6 ADU. A simulated Pentax camera dark-field value is subtracted to reconstruct the input mean value to produce the output mean. The table shows the result of the simulation for selected ADU from 2 to 1000. From the table it can be seen that all of the output means are smaller than the input mean which indicates that the Pentax K10D camera dark-field value could be removing signal as well as noise. This could be an issue for measuring the NSB values and dull stars as most of their signal is on the similar order of magnitude as the noise.

Input k_{mag}	**m_0**	**Uncertainty**	**Output k_{mag}**	**Uncertainty**
0.16	-6	2	0.2	0.6
	-7.8	0.2	0.26	0.08
	-8.99	0.07	0.19	0.02
	-10.07	0.03	0.17	0.01
	-11.10	0.02	0.16	0.005
	-12.12	0.001	0.16	0.001
0.24	-6.3	0.8	0.3	0.3
	-8.3	0.2	0.39	0.08
	-9.38	0.07	0.29	0.02
	-10.41	0.03	0.26	0.01
	-11.43	0.01	0.25	0.005
	-12.44	0.001	0.24	0.001
0.32	-6.9	0.8	0.4	0.3
	-8.8	0.2	0.50	0.07
	-9.74	0.06	0.38	0.02
	-10.75	0.03	0.34	0.01
	-11.76	0.01	0.33	0.005
	-12.76	0.001	0.32	0.001

Table 5.3: Table displaying the results of simulating star extinction plots for stars with different magnitudes when using the Pentax K10D camera dark-field image as the dark noise correction. m_0 defines the "reconstructed" instrumental magnitude that the Pentax K10D camera would observe for a star without the atmosphere present after the dark-field correction. The "reconstructed" m_0 is shown here as this quantity can only be observed by the Pentax K10D camera. k_{mag} denotes the star extinction coefficient. A larger negative number for m_0 denotes a brighter simulated star. The star extinction coefficients were produced by simulating the star signal with a Gaussian function containing Poisson fluctuations with the addition of the night sky background noise. The night sky background is simulated via sampling from a Gaussian function containing Poisson fluctuations. The stars within the star extinction coefficient plots were simulated from 2 airmass to 4 airmass. The results of the simulation seem to indicate that stars with m_0 less than -9 give more accurate measurements than stars with m_0 greater than -9. The uncertainties are large for m_0 great than -7 as the star counts are on the same order of magnitude as the Pentax K10D camera noise.

Input Gain (ADU/electron)	**Input Mean (ADU)**	**Resultant Gain (ADU/electron)**		
		Mean	**RMS**	**Error in the Mean**
0.5	100	0.62	0.09	2.8×10^{-3}
	1000	0.51	0.07	2.2×10^{-3}
1	100	1.23	0.18	5.6×10^{-3}
	1000	1.01	0.14	4.49×10^{-3}
2	100	2.48	0.35	1.1×10^{-2}
	1000	2.04	0.28	8.9×10^{-3}
4	100	4.78	0.60	1.9×10^{-2}
	1000	4.04	0.57	1.8×10^{-2}

Table 5.4: The results of the Pentax K10D camera pixel gain simulating using the Pentax camera dark-field image as the dark noise correction. The method involves calculating the gain from 100 simulated pixel values containing both signal and dark noise. The signal is produced by adding a random Poisson fluctuation and a random dark noise value to the input mean. The dark noise is produced by sample from a Gaussian distribution with mean of zero ADU and a standard deviation of 6 ADU. The complete method is explained in Section 5.1.5. For each input mean ADU, the mean gain was simulated 1000 times. The table shows a couple of interesting results. Firstly, the resultant gain calculated for an input mean equal to 1000 ADU matches the input input gain within uncertainties, in contrast with the case of an input mean of 100 ADU. Secondly, there is a spread in the resultant gain that is seen in all of the RMS values. This can be attributed to the fact that only 100 values are used in calculating the gain.

from a star was generated by a Gaussian spatial function with random Poisson variations to simulate photon fluctuations from a counting device. For all the simulations discussed in this subsection, the Gaussian distribution used to simulate the dark noise had a mean of 0 ADU and standard deviation of 6 ADU. The Gaussian spatial function is used to represent the signal from a star, as it models the point spread function (PSF) of the Pentax K10D camera lens [58]. To simulate the signal recorded by the Pentax K10D camera (e.g. dark noise and counts from a star), any signal that is negative is set to zero.

The first method investigated was the effect of using the Pentax K10D camera dark-field image to process different sky signal strengths. Different sky signal strengths were investigated as the NSB and some star signals are on the same order of magnitude as the Pentax K10D camera dark noise. The dark noise and signal were simulated by random sampling from separate Gaussian distributions. The process involves adding the simulated Pentax K10D camera dark noise and signal then subtracting a simulated Pentax K10D camera dark-field value. This process was repeated to simulate different signal levels by changing the mean for the signal Gaussian distribution. The mean of the Gaussian distribution for the dark noise was kept fixed through out the simulation. For each of the different mean signal values, the simulation was run 1000 times. The result of the simulation is shown in Table 5.2. From the table, it can be seen that there is a significant difference between the expected value (the Input mean signal value) when compared to the simulated Output mean signal value. For all Input Mean values used, the simulated Output Mean value after subtracting the simulated dark field value is less than the expected signal value. The gap between the expected signal value and the simulated is reduced for 100 ADU and reduced even further for 1000 ADU. This result is expected as the mean signal value is now very much larger than the simulated dark noise from the Pentax K10D camera.

The second method simulated was measuring the star extinction coefficient. The method of measuring star extinction coefficients is explained in Subsection 5.1.3. These simulations were used to investigate the effects of the dark noise on measuring different star extinction coefficients with stars of differing m_0 magnitudes (the magnitude that the Pentax K10D camera would observe if the atmosphere was absent). The star was simulated by a Gaussian spatial function and the noise was added by random sampling from a Gaussian distribution. The results of the simulation are shown in Table 5.3. The table shows that for brighter stars (m_0 magnitudes less than -9), the star extinction coefficient can be more accurately found. This effect was seen across the three different star extinction coefficients simulated.

The last method that was simulated was a measurement of the Pentax K10D camera pixel gain. The method of calculating the Pentax K10D camera pixel gain is explained in Section 5.1.5. For each input mean ADU, the mean and RMS were calculated from a 1000 simulated pixel values. Each simulated pixel value was produced by taking the mean and adding both a random Poisson fluctuation and a random noise value. The results of the simulation that calculated the gain of individual pixels are shown in Table 5.4. The result includes two different scenarios: no dark noise subtracted, and subtracting the dark noise measured by the CCD. The table shows that subtracting either a simulated mean CCD dark noise value or no dark noise at all resulted in almost no difference in the resultant gain. The resultant gain calculated with an input mean ADU of 1000 matches the input gain better than the resultant gain calculated with an input mean ADU of 100. There is a spread in the resultant gain that is seen in all of the RMS values. This can be attributed to the fact that only 100 values are used in calculating the gain.

In summary, the Pentax K10D camera does not contain a pedestal so is not able to record the full dark noise fluctuations. The implication of this undesired effect when measuring the pixel gain, star extinction coefficient and signal from the sky was investigated through simulation. The simulation showed that there is a significant under estimation of the sky signal value after subtracting the Pentax K10D camera dark-field value. This effect was reduced once the measured ADU value was much greater than the average dark noise value. Using a dark-field from the Pentax K10D camera when measuring the star extinction coefficient only had a significant effect when measuring stars with a m_0 value greater than -9. This effect was seen across the three different star extinction coefficients simulated. This is an issue as there are a large proportion of measured star extinction coefficient at Fowlers Gap (seen in Chapter 6) with m_0 value greater than or equal to -9. For the pixel gain simulation, I showed that the dark field has little to no effect on the pixel gain measurement when the mean ADU is around 1000 ADU. A significant difference between the expected gain and the simulated gain was observed when the mean ADU was around 100.

5.2.3 Gain

The definition of the pixel gain and the method used to calculate it is described in Subsection 5.1.5. This subsection deals with the measurement of average gain and uncertainty for different ISO and aperture settings. The Pentax K10D camera settings investigated were 400 ISO (f-stop 3.5 and f-stop 8.0), 800 ISO (f-stop 8.0), and 1600 ISO (f-stop 8.0). For each of the different Pentax K10D camera settings and across each set of 100 images, the mean ADU was kept above 1000 ADU to help reduce variations from dark noise (explained in Section 5.2.2).

The results of the pixel gain measurements for the different Pentax K10D camera settings are shown in Table 5.5. From the table, it can be seen that the gain only roughly halves as the ISO setting is doubled. This was expected as the gain should only depend on ISO setting. Figure 5.8 shows the one-dimensional histograms of the gains for the green channel with Pentax K10D camera settings of 400 ISO (f-stop 8.0), 800 ISO (f-stop 8.0) and 1600 ISO (f-stop 8.0). The one-dimensional histograms for the red and blue channel for each of the ISO settings are shown in Appendix A.1. The histograms show the variations from the mean. The RMS of the measured gain is similar to the simulated results in Section 5.2.2. Therefore, the RMS is most likely an artefact of the method for measuring the pixel gain, and is related to the statistics of using only 100 images. The values found for RMS were not an issue as I was only interested in the mean gains and due to the large number of individual pixel gains measured, each mean is well defined.

5.2.4 Flat-Field

Flat-field images are used to correct vignetting and gain variation within an image taken by the Pentax K10D camera. The process of how a flat-field image is applied to the analysis is explained in Section 5.1.2. There are many methods to produce a flat-field image but I will only discuss a few. The Pentax K10D camera focus was setting to infinity when used to produce each of the different flat-field images. The different flat-field images are tested by comparing how uniformly illuminated each of the images are, and the effectiveness of the flat-field images to produce star extinction coefficient plots. I used five different methods to produce flat-field images:

- **Computer Screen Flat-field:** This is an image taken of a computer screen, while displaying a white image. The Pentax K10D camera was placed less than 20 cm away from the screen.

- **Projector Screen Flat-field:** This is an image taken of a white projector screen, illuminated by sunlight. The Pentax K10D camera was placed ~ 1 m away from the screen.

- **Clear Sky Flat-field:** This is an image taken of the clear sky, with the sun below the horizon. The Pentax K10D camera was pointed vertically and the image taken as the sun set.

- **Rotated Clear Sky Flat-field:** This is an image produced by taking an average of two clear sky images. The two clear sky images are taken with the second image taken with the Pentax K10D camera rotated 180 degrees with respect to the first image. The Pentax K10D camera was pointed vertically and images were taken as the sun set. I explored this method due to the results gained from the test of how uniformly illuminated each flat-field image appeared. These results are shown later on in this section.

For each of the different flat-field methods, the Pentax K10D camera had the same settings as the star field images, that were analysed for the effectiveness to produce the star extinction coefficient plots. The Pentax K10D camera settings for all the flat-field images were: an aperture setting of f-stop 3.5, 400 ISO, exposure length of 20 seconds, and focused at infinity.

The results of the uniform illumination test on each flat-field method will now be discussed. The test was conducted by splitting an image up into four quadrants and comparing the average ADU versus pixel radius from the centre of the Pentax K10D camera CCD for each of the quadrants. Figure 5.9 gives a diagrammatic example of how the images are split up into the four quadrants. If the Pentax K10D camera has been illuminated evenly, then each of the quadrants should display the same trends. Figure 5.10 shows the quadrant test applied to the five different flat-field images. From the figure, it can be seen that projector or computer screen flat-fields produced more consistent quadrants than either the clear sky or rotated clear sky flat-fields. Another observed difference was the amount of measured vignetting within the different flat-field images. The amount of vignetting can be seen through the ratio of maximum ADU to the

ISO	**f-stop**	**Red Channel (electrons/ADU)**		
		Gain	**RMS**	**Error in the Mean Gain**
400	3.5	1.458	0.3352	2.01×10^{-4}
400	8.0	1.489	0.2212	1.37×10^{-4}
800	8.0	0.7565	0.1222	7.66×10^{-5}
1600	8.0	0.3606	0.0629	3.94×10^{-5}

ISO	**f-stop**	**Green Channel (electrons/ADU)**		
		Gain	**RMS**	**Error in the Mean Gain**
400	3.5	2.244	0.4187	1.86×10^{-4}
400	8.0	2.059	0.3011	1.33×10^{-4}
800	8.0	1.053	0.1706	7.56×10^{-5}
1600	8.0	0.5572	0.0940	4.16×10^{-5}

ISO	**f-stop**	**Blue Channel (electrons/ADU)**		
		Gain	**RMS**	**Error in the Mean Gain**
400	3.5	1.813	0.3840	2.41×10^{-4}
400	8.0	1.881	0.2840	1.78×10^{-4}
800	8.0	1.015	0.1632	1.02×10^{-4}
1600	8.0	0.5028	0.0870	5.45×10^{-5}

Table 5.5: Shown here is the mean, RMS and the error in the mean gain from the histogram (shown in Figure 5.8 and Appendix A.1) of all the pixel gains (electrons/ADU) for each of the colour channels. The gain was calculated for Pentax K10D camera settings of 400 ISO (f-stop 3.5 and 8.0), 800 ISO (f-stop 8.0) and 1600 ISO (f-stop 8.0). The exposure length was set to 20 seconds. It can be seen that gain halves as the ISO value is doubled. It can also be seen that changes in the f-stop caused no significant change in the mean gain value, which was expected. Calculating the pixel gain at different f-stops was used to make sure that the method was working.

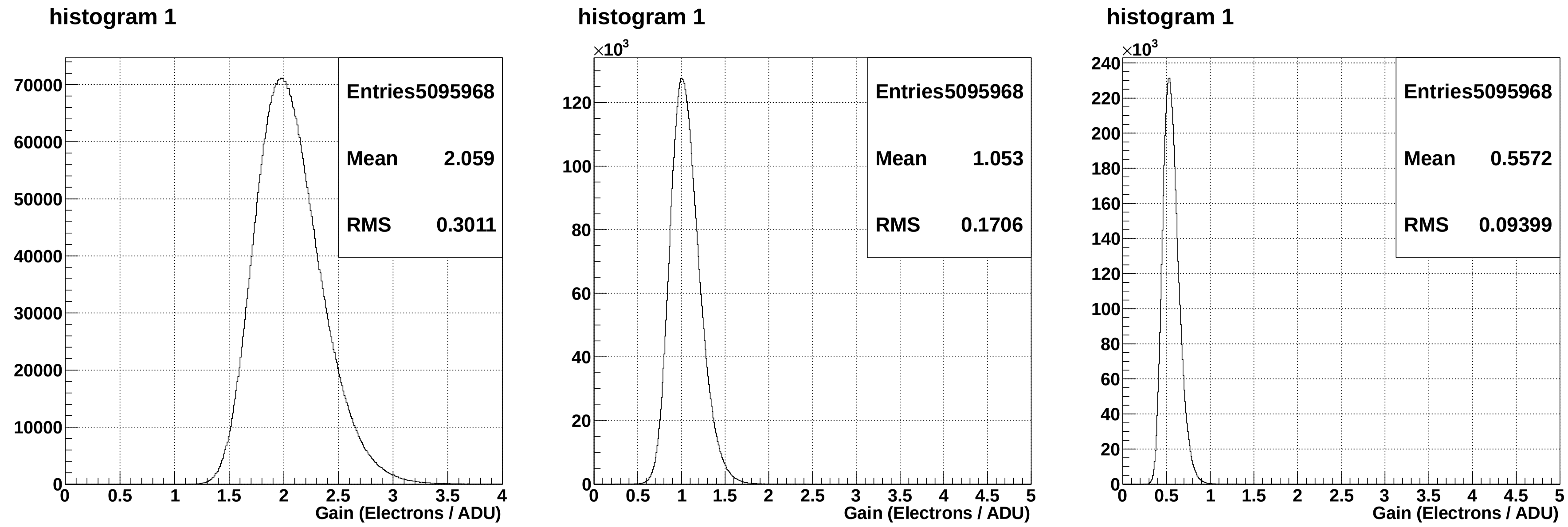

(a) (b) (c)

Figure 5.8: Histograms displaying the distribution of gains for all the green pixels within the Pentax K10D camera. (a) 400 ISO, (b) 800 ISO, and (c) 1600 ISO. It can be seen that there is a fluctuation in gains which can be attributed to either differences in pixel to pixel gains, or from a lack of statistics when calculating the mean and RMS. As only 100 images were used to find individual pixel mean and RMS to calculate the pixel gains, this is probably the largest contributing factor to the RMS in the histograms.

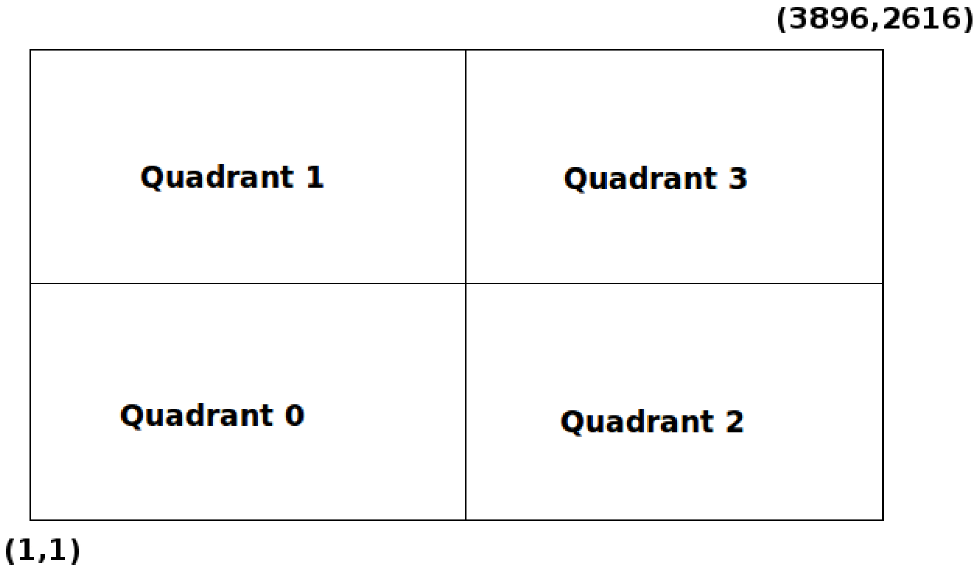

Figure 5.9: A diagram showing how an image was split for the quadrant test. The coordinates of pixels for an image are given at the bottom-left and top-right corners. The quadrants are split into equal area.

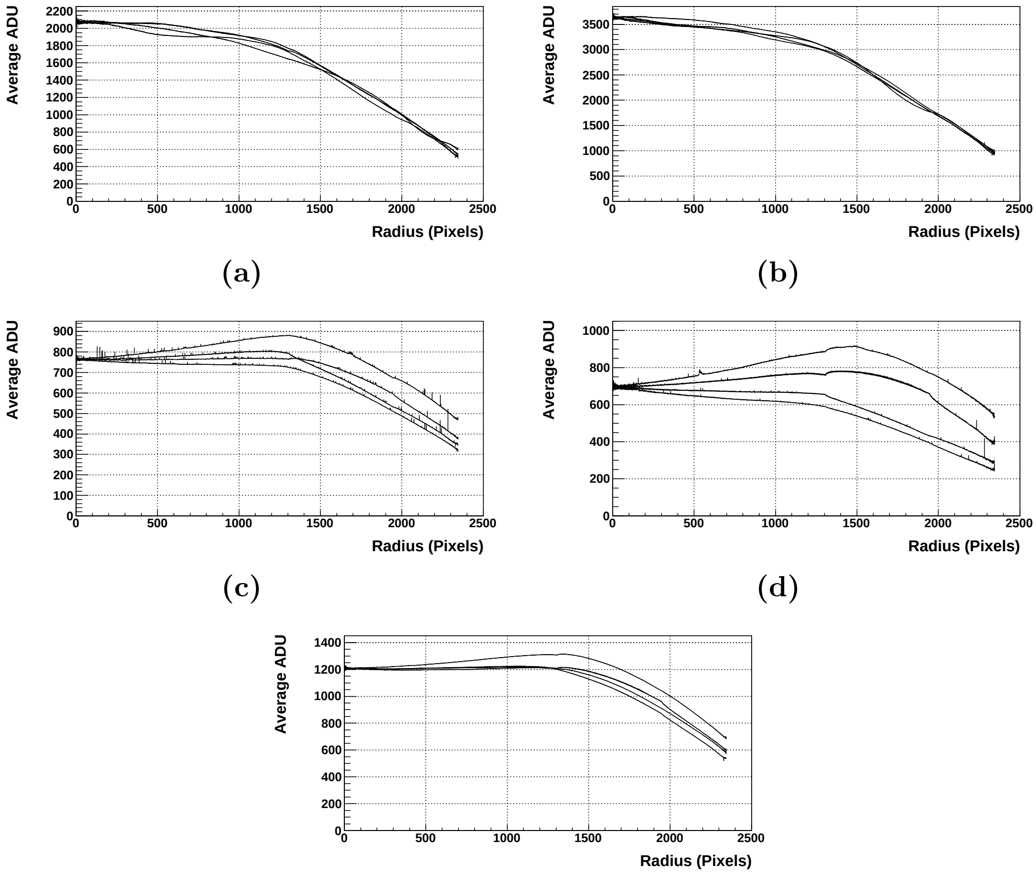

(a) (b) (c) (d) (e)

Figure 5.10: Comparison of four quadrants for different methods of producing flat-field images: (a) an image taken of a white projector screen, (b) an image of a computer screen displaying a white image, (c) averaged clear sky image taken in the Adelaide Hills on 8/5/2010, (d) single image taken in Adelaide on 4/4/2011, and (e) an image produced by using the rotated clear sky method. The Pentax K10D camera setting used was 400 ISO, aperture settings of f-stop 3.5, exposure length of 20 seconds and the focus set to infinity. The radius is defined as the number of pixels from the centre of the Pentax K10D camera. Only the Green Channel for each flat-field method is shown here.

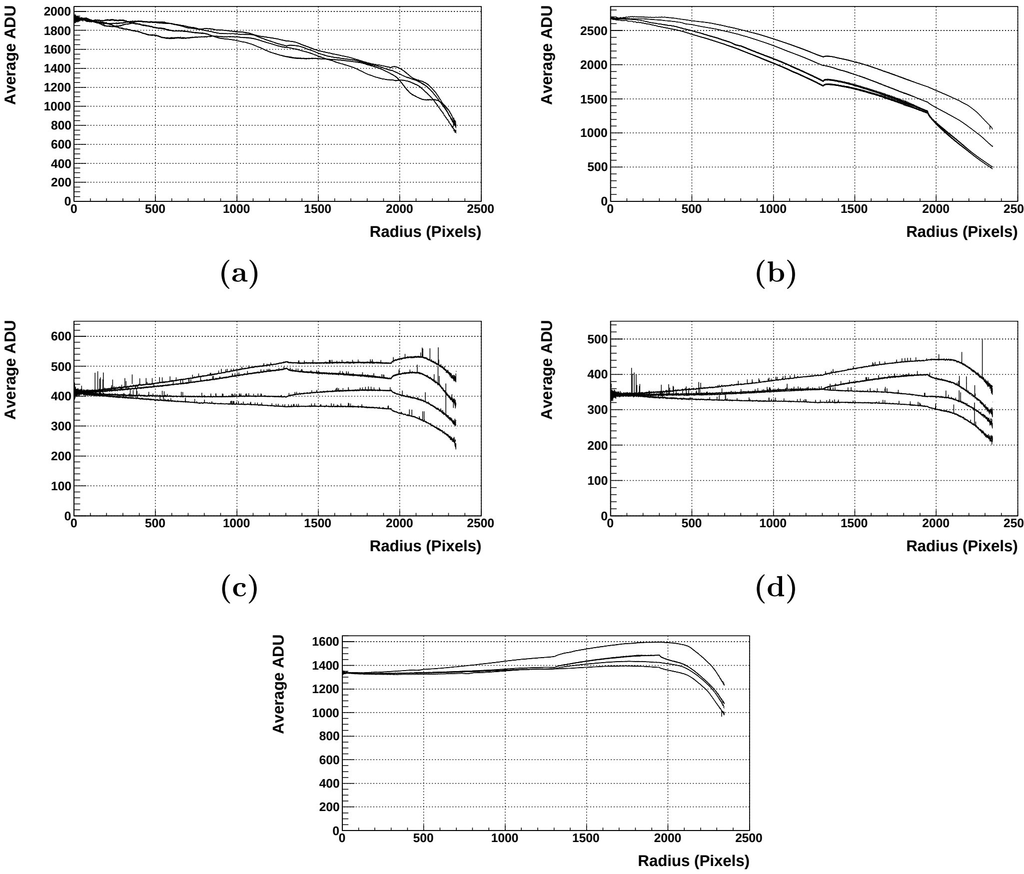

(a)

(b)

(c)

(d)

(e)

Figure 5.11: Comparison of four quadrants for different methods of producing flat-field images: (a) an image of a white projector screen, (b) an image of a computer screen displaying a white image, (c) averaged clear sky image taken at Fowlers Gap on 13/12/2010, (d) a single clear sky image taken in Adelaide on 4/4/2011, and (e) an image produced by using the rotated clear sky method. The Pentax K10D camera setting used was 400 ISO, aperture settings of f-stop 8.0, exposure length of 20 seconds and the focus set to infinity. The radius is defined as the number of pixels from the centre of the Pentax K10D camera. Only the Green Channel for each flat-field method is shown here.

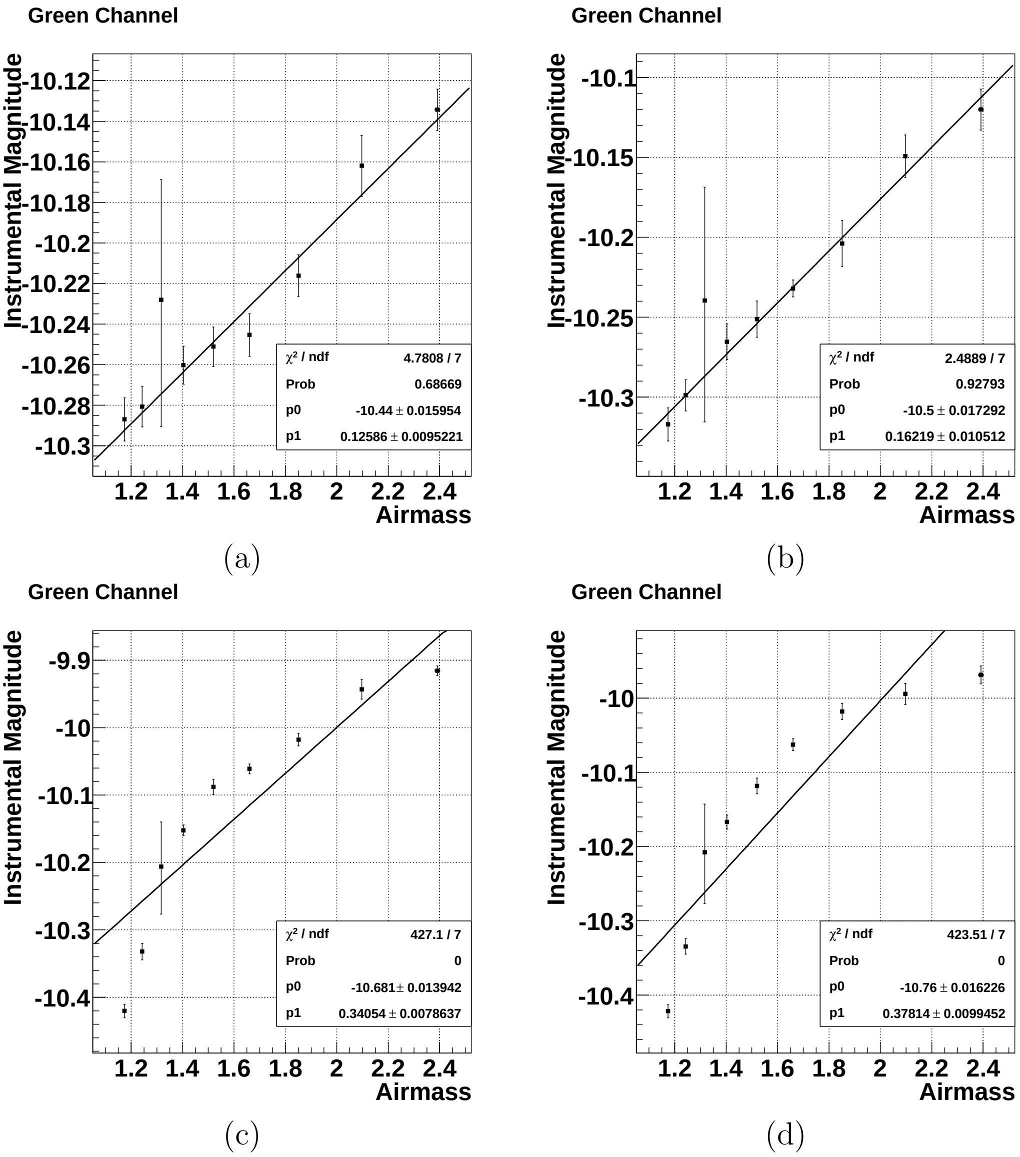

(a) (b)

(c) (d)

Figure 5.12: Examples of the effect on measuring star extinction coefficients using flat-field images produced from different methods. Shown here the instrumental magnitude versus airmass for the green channel for a star on the night of 11/08/2010. The different flat-field methods used were (a) the rotated clear sky method, (b) a single clear sky image, (c) imaging a white projector screen, and (d) imaging a white computer screen. The star extinction coefficient is the slope of the fit and is denoted p1 within the fit box. The Pentax K10D camera setting used was 400 ISO, 20 second exposure length and aperture setting of f-stop 3.5. In each of the plots, the more negative the instrumental magnitude is, the brighter the object is. For the projector screen and white screen, it can be seen that the Pentax K10D camera's vignetting has been over-corrected as the points form an convex curve instead of the expected straight line.

minimum ADU. Projector or computer screen flat-fields had the ratio of maximum to minimum ADU of approximately 3.5, while the clear sky or rotated clear sky flat-fields only has a ratio of approximately 2. The difference in the ratio between the different flat-field images is still present if the same test is applied to flat-field images taken with an aperture setting of 8.0, as shown in Figure 5.11. The quadrant test showed a disparity within the single clear sky flat-field for both aperture settings. Out of the four quadrants, one quadrant demonstrated a higher than average ADU count and one a lower average ADU count, when compared with the other two quadrants. This result was expected. When using the large FoV to take the star field images, the clear sky flat-field image will observe a brightening of the image towards the direction of the setting sun, while it will be dimmer in the opposite direction.

Next, I compared the different flat-field methods for their effectiveness to produce star extinction coefficient plots. The result I was looking for was a linear relationship between instrumental magnitude and airmass. Figure 5.12 shows the star extinction coefficient plots for a star taken on 11/08/2010. The effects of the different flat-fields can be seen in the figure. The Pentax K10D camera was stationary, and the star of interest moved from the edge of the Pentax K10D camera FoV towards the center. The star was measured while it was setting, so it moved from a low to high airmass. The computer screen and projector screen flat-field images produced results showing over-corrected star extinction coefficient plots. The over-corrected magnitudes can be seen by their deviation from the linear fit. The clear sky and rotated clear sky flat-field images produced star extinction coefficient plots that contained magnitudes with little to no discernible deviation from a linear fit. This result shows that, to effectively flat-field the observed star field image, the ratio of maximum to minimum ADU within the flat-field image must be no more then 2.

In summary, the results of the two methods showed that the best test to determine which flat-field image to use was by comparing different star extinction coefficient plots. The clear sky and rotated clear sky flat-field images corrected for the vignetting better than the computer and projector flat-field images within the plots. The computer and projector flat-field images were discounted as they produced non linear star extinction plots. This behaviour indicates that the amount of vignetting observed was not correctly accounted for by these flat-field images. The quadrant test gave an indication of how evenly illuminated the flat-field images were. The computer and projector flat-field images showed that the four different quadrants where consistently illuminated but had a different ratio of maximum to minimum ADU compared to the clear sky flat-field images. This ratio was probably because the white screens imaged were a short distance away from the Pentax K10D camera (around 1 metre), so did not have an isotropic distribution of incoming light rays. The white screens were a short distance away so the white screens completely filled the Pentax K10D camera field of view, while keeping the desired Pentax K10D camera settings.

5.2.5 Bayer Filter

One of the features of the Pentax K10D camera is the use of a Bayer filter pattern located on top of the CCD. An example of the Bayer filter pattern is shown in Figure 5.1. The main feature of the Bayer pattern is that within a two by two

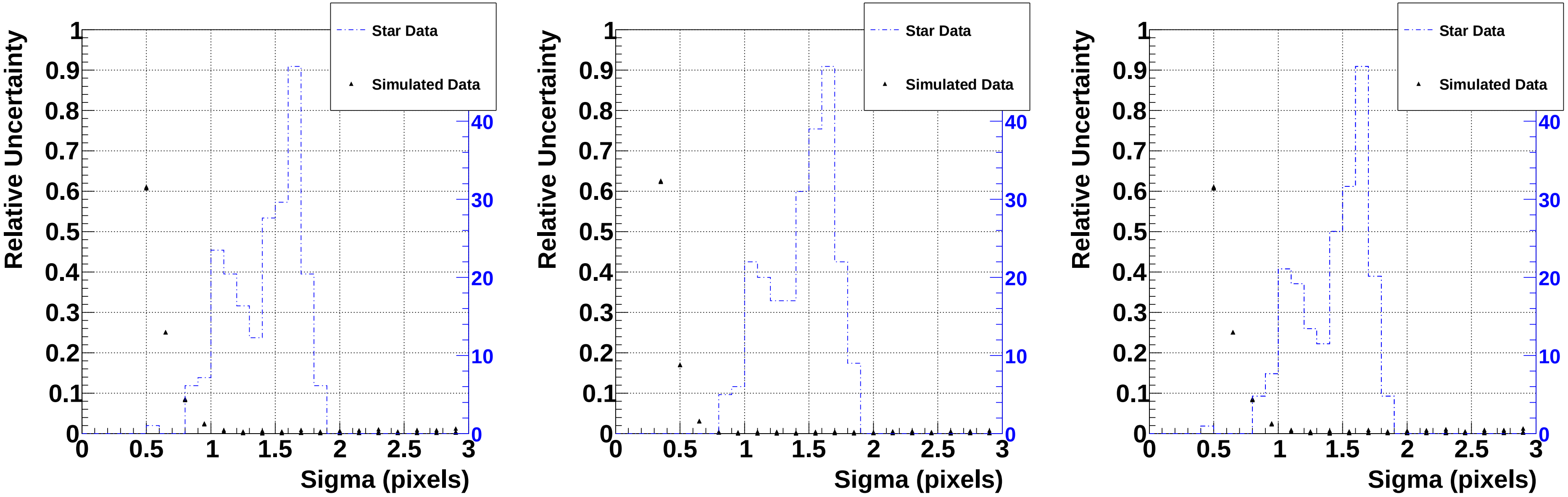

(a)

(b)

(c)

Figure 5.13: Shown here is the relative uncertainty in the star brightness (the RMS of the distribution of the Gaussian integrals divided by its mean) versus the standard deviation (sigma) of the Gaussian used in the simulation (y-axis on the left) and the distribution of standard deviation (denoted as sigma) of stars observed at Fowlers Gap (dashed blue plot, y-axis on the right), for (a) the red channel profile, (b) the green channel profile, and (c) the blue channel profile. The Gaussian is used to model the point spread function (PSF) [58]. Sigma is used to define the width of the Gaussian. The star data within the distribution were observed over three different nights with Pentax K10D camera settings of 400 ISO, f-stop 8.0, and 20 sec exposure. The nights of observation were 15/02/2010, 11/08/2010, and 13/12/2010. These plots show that the Bayer filter pattern has negligible contribution to the uncertainty across all colour channels when the sigma of the Gaussian is greater then 1.1 pixels. The star data shows that most of the observed stars have a sigma above this threshold. The simulation was repeated for different star brightness and it was shown that the effect of the Bayer filter is independent of star brightness.

grid of pixels, there are one red, one blue and two green pixels. Image analysis is done on individual colour channels so the pixels related to the other colour channels are considered dead space. I investigated the effect of the Bayer filter on simulated star instrumental magnitudes as stars cover a small number of pixels (e.g. around ten). I modelled the star signal that a Pentax K10D camera would see as a Gaussian function, as it is a good approximation for a point spread function (PSF) [58]. The Gaussian equation used in the simulation was:

$$G(x,y) = A \times \exp\left(\frac{(x-B)^2}{2\sigma_x^2} + \frac{(y-C)^2}{2\sigma_y^2}\right) \tag{5.20}$$

where A is the amplitude, B and C are the central position of the star, σ_x^2 and σ_y^2 are the standard deviations, and x and y are the pixel coordinates. The mean values are used to set the location of the peak of the Gaussian and the standard deviations are used to set the width. No Poisson fluctuation was added as I was only interested in how a star signal is effected by the Bayer filter.

The method used to simulate a star on different locations on the Bayer filter pattern was to move the Gaussian central position 1000 times. The different Gaussian positions were evenly spaced throughout a two by two pixel grid. This was done to cover the different colour combinations within the Bayer filter (one red pixel, one blue pixel and two green pixels). At each move, the Gaussian was integrated for each pixel within a 13 by 13 grid. For each colour channel, the pixel values are summed up and added to a histogram. The relative spread of the integrated Gaussians (RMS divided by the mean value) was plotted against the standard deviation of the Gaussian. The process of moving the Gaussian and adding the result to a histogram was repeated for different standard deviations and different star magnitudes.

The result of the simulation is shown in Figure 5.13. The main result is that the Bayer filter only has an effect on simulated star counts when the Gaussian standard deviation is smaller than one pixel. The same trend was found when the simulation was repeated for star of different magnitudes. Figure 5.13 also shows the distributions of the standard deviation of stars observed at Fowlers Gap. The standard deviation of stars gives an indication of the PSF of the Pentax K10D camera. The star data within the distribution were obtained over three different nights with Pentax K10D camera settings of 400 ISO, f-stop 8.0, and 20 sec exposure, and with stars of differing brightnesses. The nights of observation were 15/02/2010, 11/08/2010, and 13/12/2010. The star data shows that most of the observed stars have a standard deviation larger than one pixel.

5.3 Summary

The key conclusion was that the Pentax K10D camera CCD can be used as a photometric device. The linearity, dark-field, and flat-field results were used to demonstrate this.

The linearity results show that the CCD had a linear range up to its maximum digital output of 12-bits, satisfying the criterion of containing a region of linearity.

Another point satisfying the criteria for using the Pentax K10D camera CCD as a photometric device was demonstrating that the dark-field can be used to separate the signal from an observed object from the dark noise within the Pentax K10D camera. Several key results supporting this ability have been demonstrated. Firstly, all the pixel values from a dark-field image were placed into a histogram. This showed two interesting features: a spike of counts at zero ADU and a feature that could be fitted by a half Gaussian extending from 1 ADU. Comparing the integration of the full Gaussian (using the parameters from the half Gaussian) to the integration of the histogram showed that the dark-field image only displays half of the dark noise present within the CCD. Secondly, the Pentax K10D camera was shown to only be able to measure NSB when using a Pentax K10D camera aperture setting of f-stop 3.5. This was shown by looking for separation between average pixel counts from an image containing NSB and a dark-field image for different aperture settings. For the 400 ISO green channel, this occurs when the NSB signal is above an average pixel count of 5 ADU.

The impact of using the dark-field images produced by the Pentax K10D camera on the gain, star extinction coefficient plots, and measuring the NSB were shown through simulation. The results of the simulated gain show that using the dark-field images had a significant impact on measuring the true gain when using images containing a mean ADU count of 100. The impact of using the dark-field images was greatly reduced when the mean ADU count within the images was increased to 1000. The results of the simulated star extinction coefficients showed that using the Pentax K10D camera dark-field image on star extinction plots with star m_0 (the magnitude the Pentax K10D camera would observe with no atmosphere) less than -9 had no significant effect. This result was observed over three different star extinction coefficients. The results of the simulated NSB showed that using the Pentax K10D camera dark-field image would underestimate the expected NSB value. The effect was reduced when the mean ADU per pixel for the NSB was much larger than the average ADU per pixel for the dark noise. The dark-field images are still used throughout my analysis even knowing these impacts. The step of subtracting the dark noise might be skipped in some cases but this leaves ”hot“ and noisy pixels that are easily removed by dark-field images.

Satisfying the criteria for the Pentax K10D camera being used as a photometric device required the identification of flat-field methods suitable for use on star extinction coefficient plots. It was seen that using either clear sky or rotated clear sky flat-field methods gave the best results. In comparison, projector screen or computer screen flat-field methods produced plots that were over corrected. Even though computer screen, and projector screen flat-field methods produced more consistent quadrants, using these flat-field images did not correctly account for the vignetting pattern within the star field images. The discrepancies in these flat-field images could have arisen from taking an image of a surface that was quite close ($\sim$ 1 m away), while using a camera setting that was focused at infinity.

The results of the Bayer filter test showed that the Bayer filter had no effect on measuring signals from a star when the standard deviation of it PSF was greater than one pixel. It was also shown that the majority of the standard deviations of observed stars were greater than one pixel as well.

Chapter 6

Study of Fowlers Gap and its Night Sky

In this chapter, I show the star extinction coefficients and night sky background (NSB) levels measured by a Pentax K10D digital single lens reflex (DSLR) camera, at the Fowlers Gap research station. Data was collected from three different trips. I show the results of the measured star extinction coefficient from the nights of 15/02/2010, 11/08/2010 and 13/12/2010, including the results of the measured NSB levels for the nights of 11/08/2010 and 13/12/2010. The star extinction coefficient was measured as it is an indication of the atmospheric transmission, which impacts on the detection of the Cherenkov photons by an imaging atmospheric Cherenkov technique (IACT) array. A star extinction coefficient for different atmospheric transmissions was simulated, to use as a comparison to the measured star extinction coefficients found at Fowlers Gap. The NSB level was measured as it is a source of background noise that an IACT array can observe (as discussed in Chapter 2).

6.1 Location

(a) (b)

Figure 6.1: Examples of the layout of the terrain at Fowlers Gap. (a) shows the sandy soil of the plains. (b) shows the rocky surface and some of the hills.

Fowlers Gap research station [59] is the first Australian site to be surveyed as a possible location for a greater than 10 TeV γ-ray array. Located 100 km north of Broken Hill, New South Wales, Fowlers Gap is currently owned by the University of New South Wales. A satellite cloud study [60] showed that a region containing Fowlers Gap has one of the lowest average annual cloud coverage levels in Australia. The low cloud coverage was one of the main factors leading to Fowlers Gap being considered for the survey. Due to Fowlers Gap's remoteness and its existing infrastructure, it is an ideal place to begin investigating the suitability of Australian sites. The remoteness is a key quality as the bright lights of cities can increase the area's NSB levels. Fowlers Gap's closest source of city light is Broken Hill. The existing infrastructure consists of living quarters, access to power and the Internet. The terrain at Fowlers Gap comprises of a combination of hills and flat plains. The hilly terrain consists of rocky surfaces, while the flat plains are covered in sandy soil. Pictures of the terrain taken at Fowlers Gap are shown in Figure 6.1. The hilly terrain was noted to be a suitable site for locating telescopes as the hills provide some buffering from dust that can be blown across the flat plains.

6.2 Star Extinction Coefficients Results

The results of the measured star extinction coefficients from the night-time observations at Fowlers Gap are discussed in this section. The method for measuring the star extinction coefficients was described in Chapter 5. In addition to the method outlined in Chapter 5, a weighted mean of the instrumental magnitude was found for each group of images taken, and a cut was used on the data to remove any pixels that are at a distance greater than 1500 pixels from the centre of the Pentax K10D camera CCD. Each night of observation saw clear and cloudless skies with a new moon on the nights of the 15/02/2010 and 11/08/2010 and a first quarter moon on the 13/12/2010. The star extinction coefficient plots for each observation night are shown in Appendix B. Each star extinction plot was fitted with the equation y = p1*x + p0, where p1 is the k_{mag} and p0 is the m_0. k_{mag} is the star extinction coefficient, m_0 is the instrumental magnitude the Pentax K10D camera would observe if no atmosphere was present, and data that had a χ^2 greater than 2 for the star extinction coefficient fits has been omitted. The χ^2 gives an indication of how good the fit is.

The Pentax K10D camera settings used, number of images taken, and the star field chosen are described below:

- **15/02/2010 (Southern Cross) :** Pictures were taken of stars within and near the constellation of the Southern Cross. The Pentax K10D camera settings used were 20 second exposures, f-stop of 8.0, and both 400 ISO and 800 ISO. Nine groups of images were taken 20 minutes apart, for each of the ISO settings. Each group contained three images. The results of the measured star extinction coefficients for ten stars are shown in Table 6.1.

- **11/08/2010 (Scorpio) :** Pictures were taken of stars within the constellation of Scorpio. The Pentax K10D camera settings used were 20 second exposures, 400 ISO, and both f-stop of 8.0 and 3.5. Nine groups of images were taken 20 minutes apart, for each of the f-stop settings. Each

Star Name	ISO	Visible Magnitude	Spectral Type	Red Channel		Green Channel		Blue Channel	
				m_0	k_{mag}	m_0	k_{mag}	m_0	k_{mag}
β - Cru	400	1.3	B0.5	- ± -	- ± -	- ± -	- ± -	-9.89 ± 0.07	0.10 ± 0.04
	800			-9.60 ± 0.02	0.11 ± 0.01	- ± -	- ± -	- ± -	- ± -
β - Cen	400	0.6	B0.5	-9.64 ± 0.04	0.17 ± 0.01	-11.4 ± 0.1	0.22 ± 0.03	- ± -	- ± -
δ - Cru	400	2.78	B2	- ± -	- ± -	- ± -	- ± -	-8.79 ± 0.09	0.30 ± 0.04
	800			-7.93 ± 0.09	0.09 ± 0.01	-9.51 ± 0.04	0.05 ± 0.02	-9.5 ± 0.2	0.22 ± 0.09
δ - Cen	400	2.56	B2	-7.94 ± 0.06	0.22 ± 0.04	- ± -	- ± -	-9.02 ± 0.06	0.25 ± 0.04
	800			-8.63 ± 0.05	0.19 ± 0.02	-10.0 ± 0.02	0.11 ± 0.01	-9.80 ± 0.04	0.26 ± 0.02
γ - Cen	400	2.18	A1	-7.96 ± 0.03	0.12 ± 0.01	-9.52 ± 0.01	0.13 ± 0.01	-9.00 ± 0.02	0.19 ± 0.06
	800			-8.72 ± 0.03	0.14 ± 0.01	- ± -	- ± -	-9.95 ± 0.02	0.26 ± 0.01
γ - TrA	400	2.88	A1	-7.4 ± 0.1	0.19 ± 0.03	- ± -	- ± -	- ± -	- ± -
	800			-8.2 ± 0.2	0.21 ± 0.04	-9.81 ± 0.05	0.22 ± 0.01	-8.5 ± 0.1	0.09 ± 0.03
β - TrA	400	2.85	F2	-7.49 ± 0.06	0.18 ± 0.01	- ± -	- ± -	-8.33 ± 0.09	0.29 ± 0.02
	800			- ± -	- ± -	- ± -	- ± -	-8.91 ± 0.06	0.26 ± 0.01
α - Cen	400	-0.1	G2	-10.8 ± 0.03	0.17 ± 0.01	- ± -	- ± -	- ± -	- ± -
α - TrA	400	1.92	K2	- ± -	- ± -	- ± -	- ± -	-8.5 ± 0.2	0.27 ± 0.05
ε - Cru	400	3.59	K3/K4	-6.92 ± 0.09	0.12 ± 0.05	-7.79 ± 0.04	0.07 ± 0.02	- ± -	- ± -
	800			-7.78 ± 0.05	0.18 ± 0.03	-8.52 ± 0.05	0.08 ± 0.03	-7.5 ± 0.2	0.33 ± 0.09
γ - Cru	400	1.63	M4	-8.78 ± 0.05	0.05 ± 0.02	- ± -	- ± -	-8.47 ± 0.09	0.21 ± 0.04
	800			-9.60 ± 0.06	0.08 ± 0.03	- ± -	- ± -	-9.1 ± 0.1	0.17 ± 0.05

Table 6.1: Star extinction coefficients measured on 15/02/2010 at Fowlers Gap. Pentax K10D camera settings used were f-stop of 8.0 and exposure length of 20 sec. Nine groups of three images were taken, with each group taken 20 minutes apart. The star extinction coefficient plots are shown in Appendix B.1, with each point a weighted average of each group of images. k_{mag} is the star extinction coefficient and m_0 is the instrumental magnitude the Pentax K10D camera would observe if no atmosphere was present. The gaps in the tables are from star extinction plots that did not pass the χ^2 cut and were not included. An interesting feature of the table is that observing the same star using different ISO settings had no significant effect on the measured k_{mag}. This is expected as the k_{mag} depends on the relative difference in magnitudes. There are a couple of interesting features that can be seen within this table of observed star extinction coefficients. The green channel k_{mag} were lower than the ones in the red channels, and the k_{mag} show a dependence on the star spectral type. This is not expected behaviour as it implies that there is a higher atmospheric transmission within the green channel than the red channel, and star spectral type should have no impact. Both these behaviours are caused by colour leakage within the different colour channels. This is explained further in Section 6.3.

Star Name	f-stop	Visible Magnitude	Spectral Type	Red Channel		Green Channel		Blue Channel	
				m_0	k_{mag}	m_0	k_{mag}	m_0	k_{mag}
δ - Sco	3.5	2.29	B0.2	- ± -	- ± -	-11.7 ± 0.02	0.18 ± 0.01	- ± -	- ± -
β - Sco	3.5	2.50	B0.5	-9.43 ± 0.02	0.20 ± 0.01	-10.9 ± 0.02	0.16 ± 0.01	-10.6 ± 0.02	0.28 ± 0.02
π - Sco	3.5	2.89	B1	-8.99 ± 0.03	0.20 ± 0.02	- ± -	- ± -	-10.3 ± 0.02	0.27 ± 0.01
	8.0			-7.56 ± 0.06	0.28 ± 0.03	- ± -	- ± -	- ± -	- ± -
σ - Sco	3.5	2.91	B1	-9.03 ± 0.05	0.15 ± 0.03	-10.4 ± 0.02	0.13 ± 0.01	-10.0 ± 0.03	0.27 ± 0.02
	8.0			-7.61 ± 0.09	0.28 ± 0.06	- ± -	- ± -	-8.54 ± 0.05	0.33 ± 0.02
ρ - Sco	3.5	3.86	B2	-8.05 ± 0.08	0.26 ± 0.05	-9.54 ± 0.04	0.18 ± 0.02	-9.34 ± 0.05	0.31 ± 0.03
	8.0			- ± -	- ± -	- ± -	- ± -	-7.90 ± 0.08	0.39 ± 0.04
α - Sco	3.5	1.09	M1	- ± -	- ± -	- ± -	- ± -	-10.6 ± 0.02	0.20 ± 0.01

Table 6.2: Star Extinction Coefficients taken on 11/08/2010 at Fowlers Gap. Pentax K10D camera setting used were 400 ISO and an exposure time of 20 sec. Nine groups of five images were taken, with each group taken 20 minutes apart. The star extinction coefficient plots are shown in Appendix B.2, with each point a weighted average of each group of images. k_{mag} is the star extinction coefficient and m_0 is the instrumental magnitude the Pentax K10D camera would observe if no atmosphere was present. The gaps in the tables are from star extinction plots that did not pass the χ^2 cut and were not included. An interesting feature of the table is that observing the same star using different f-stop settings measured different star extinction coefficients. This was unexpected as the star extinction coefficient depends only on change in magnitude per airmass, which is only atmospheric dependent. The difference was observed due to large difference in m_0 between the different f-stop settings. This different was expected as it is a side effect of the dark field produced by the Pentax K10D camera. This effect was shown through simulation in Section 5.2.2. Another interesting feature was that for some observed star extinction coefficients, the green channel star extinction coefficients were lower than the ones in the red channels. This is not expected behaviour as it implies that there is a higher transmission within the green channel than the red channel.

Star Name	ISO	Visible Magnitude	Spectral Type	Red Channel		Green Channel		Blue Channel	
				$\mathbf{m_0}$	$\mathbf{k}_{mag}$	$\mathbf{m_0}$	$\mathbf{k}_{mag}$	$\mathbf{m_0}$	$\mathbf{k}_{mag}$
β - Cru	1600	1.30	B0.5	-10.7 ± 0.04	0.23 ± 0.01	- ± -	- ± -	-12.2 ± 0.1	0.37 ± 0.03
α - Cru	1600	0.81	B0.5	-11.1 ± 0.06	0.22 ± 0.02	- ± -	- ± -	- ± -	- ± -
β - Cen	1600	0.60	B1	-11.1 ± 0.02	0.19 ± 0.01	- ± -	- ± -	-12.2 ± 0.1	0.26 ± 0.01
δ - Cru	1600	2.78	B2	-9.0 ± 0.1	0.24 ± 0.03	- ± -	- ± -	-10.3 ± 0.1	0.31 ± 0.02
δ - Cen	1600	2.56	B2	-8.0 ± 0.1	0.19 ± 0.03	-9.16 ± 0.04	0.06 ± 0.01	-8.82 ± 0.05	0.13 ± 0.01
γ - TrA	1600	2.88	A1	-8.8 ± 0.2	0.19 ± 0.04	-10.5 ± 0.1	0.21 ± 0.02	-9.57 ± 0.07	0.20 ± 0.02
α - Cir	1600	3.19	F1	-8.5 ± 0.1	0.20 ± 0.02	-10.2 ± 0.1	0.21 ± 0.01	-9.02 ± 0.03	0.21 ± 0.01
α - Cen	1600	-0.1	G2	- ± -	- ± -	- ± -	- ± -	-12.4 ± 0.4	0.25 ± 0.04
ε - Cru	1600	3.59	K3/K4	-9.65 ± 0.10	0.24 ± 0.04	-9.65 ± 0.08	0.22 ± 0.03	- ± -	- ± -
γ - Cru	1600	1.63	M4	-10.7 ± 0.1	0.19 ± 0.01	-11.7 ± 0.02	0.21 ± 0.01	-10.3 ± 0.06	0.31 ± 0.02

Table 6.3: Star Extinction Coefficients taken on 13/12/2010 at Fowlers Gap. Pentax K10D camera settings used for each star was an f-stop of 8.0, an exposure time of 20 sec and the ISO setting given in the table. Sixteen groups of four images were taken, with each group taken 20 minutes apart. The star extinction coefficient plots are shown in Appendix B.3, with each point a weighted average of each group of images. k_{mag} is the star extinction coefficient and m_0 is the instrumental magnitude the Pentax K10D camera would observe if no atmosphere was present. The gaps in the tables are from star extinction plots that did not pass the χ^2 cut and were not included. An interesting feature was that for some observed star extinction coefficients, the green channel star extinction coefficients were lower than the ones in the red channels. This is not expected behaviour as it implies that there is a higher transmission within the green channel than the red channel.

Star Name	**ISO**	**Visible Magnitude**	**Spectral Type**	**Red Channel**		**Green Channel**		**Blue Channel**	
				$\mathbf{m_0}$	$\mathbf{k_{mag}}$	$\mathbf{m_0}$	$\mathbf{k_{mag}}$	$\mathbf{m_0}$	$\mathbf{k_{mag}}$
ζ - Tau	800	3.03	B2	-8.11 ± 0.07	0.28 ± 0.03	- ± -	- ± -	-9.70 ± 0.07	0.37 ± 0.03
	1600			-9.26 ± 0.09	0.36 ± 0.05	-10.6 ± 0.1	0.20 ± 0.01	-10.4 ± 0.1	0.37 ± 0.04
γ - Ori	400	1.64	B2	-8.70 ± 0.03	0.18 ± 0.01	-10.3 ± 0.1	0.17 ± 0.03	-10.0 ± 0.1	0.27 ± 0.02
o - Tau	800	4.87	B2.5	- ± -	- ± -	- ± -	- ± -	-7.5 ± 0.5	0.2 ± 0.2
λ - Tau	800	3.41	B3	-8.2 ± 0.2	0.49 ± 0.09	-9.2 ± 0.1	0.18 ± 0.05	-9.2 ± 0.2	0.45 ± 0.06
	1600			-8.8 ± 0.1	0.43 ± 0.04	- ± -	- ± -	- ± -	- ± -
β - Tau	800	1.68	B7	-9.52 ± 0.03	0.21 ± 0.01	-11.1 ± 0.1	0.19 ± 0.01	-10.7 ± 0.1	0.29 ± 0.01
	1600			-10.3 ± 0.1	0.24 ± 0.02	- ± -	- ± -	- ± -	- ± -
	400			-8.71 ± 0.02	0.19 ± 0.01	-10.3 ± 0.1	0.18 ± 0.01	-9.96 ± 0.04	0.28 ± 0.01
ξ - Tau	800	3.73	B9	-7.5 ± 0.6	0.3 ± 0.2	-8.9 ± 0.1	0.19 ± 0.03	-8.58 ± 0.09	0.34 ± 0.03
ε - Tau	800	3.53	K0	-8.2 ± 0.1	0.38 ± 0.04	-9.0 ± 0.1	0.20 ± 0.04	-8.3 ± 0.2	0.50 ± 0.07
	1600			-8.78 ± 0.08	0.32 ± 0.02	-9.74 ± 0.05	0.20 ± 0.02	-9.1 ± 0.1	0.49 ± 0.04
f - Tau	800	4.14	K0	- ± -	- ± -	-8.15 ± 0.09	0.15 ± 0.03	- ± -	- ± -
	1600			-8.2 ± 0.6	0.4 ± 0.2	-8.9 ± 0.2	0.14 ± 0.05	-8 ± 1	0.6 ± 0.4
ι - Aur	800	2.69	K3	-9.2 ± 0.2	0.30 ± 0.07	-10.0 ± 0.2	0.24 ± 0.05	-8.3 ± 0.2	0.27 ± 0.08
	1600			-9.8 ± 0.1	0.27 ± 0.03	-10.5 ± 0.05	0.17 ± 0.02	-9.3 ± 0.2	0.36 ± 0.07
α - Tau	400	0.99	K5	-9.90 ± 0.03	0.15 ± 0.01	-10.9 ± 0.1	0.17 ± 0.01	-9.50 ± 0.03	0.27 ± 0.01

Table 6.4: Star Extinction Coefficients taken on the 13/12/2010 at Fowlers Gap. Pentax K10D camera settings used for each star were an f-stop of 8.0, an exposure time of 20 sec and the ISO setting given in the table. Seven groups of four images were taken, with each group taken 20 minutes apart. The star extinction coefficient plots are shown in Appendix B.4, with each point a weighted average of each group of images. k_{mag} is the star extinction coefficient and m_0 is the instrumental magnitude the Pentax K10D camera would observe if no atmosphere was present. The gaps in the tables are from star extinction plots that did not pass the χ^2 cut and were not included. An interesting feature of the table is that observing the same star using different f-stop settings had no significant effect on the measured star extinction coefficient. This is expected as the star extinction coefficient depends on the relative difference in magnitudes. Another interesting feature was that for some observed star extinction coefficients, the green channel star extinction coefficients were lower than the ones in the red channels. This is not expected behaviour as it implies that there is a higher transmission within the green channel than the red channel.

group contained five images. The results of the measured star extinction coefficients for six stars are shown in Table 6.2.

- **13/12/2010 (Southern Cross) :** Pictures were taken of stars within and near the constellation of the Southern Cross. The Pentax K10D camera settings used were 15 second exposures, f-stop of 3.5, and 1600 ISO. The groups of images were taken while the moon was setting. The moon had dropped below the horizon before all of the groups of images had been taken. Sixteen groups of images where taken, 15 minutes apart. Each group contained five images. The results of the measured star extinction coefficients for nine stars are shown in Table 6.3.

- **13/12/2010 (Taurus) :** Pictures were taken of stars within and near the constellation of Taurus. The Pentax K10D camera settings used were 20 second exposures, f-stop of 8.0, and ISO settings of 400, 800 and 1600. Seven groups of images where taken for ISO settings of 800 and 1600, while there were eight groups for ISO setting of 400. Each group was taken 20 minutes apart and contained four images. The results of the measured star extinction coefficients for nine stars are shown in Table 6.4.

Gaps in the tables of results are from data that has been removed by the χ^2 cut.

Atmospheric quality had not been observed at the site before, so to check to see if my method was working, I compared extinction coefficients at different ISO and f-stop settings. I compared the effect of using different ISO settings within Table 6.1 and Table 6.4 and the effect of using different f-stop settings within Table 6.2. In Table 6.3, the observations were taken to see if the star extinction coefficients can be measured while the moon is above the horizon. The results of Table 6.3 can be compared to Table 6.4 to see if there is any significant difference in the measured star extinction coefficient. The data in both tables were taken on the same night.

Looking through all the tables of results, some interesting features can be seen. Firstly, the star extinction coefficient across the three different colour bands was expected to be smallest for the red channel, larger for the green, than largest for the blue channel. This was expected as atmospheric attenuation via Rayleigh scattering is proportional to $1/\lambda^4$. Within the tables, it can be seen that for most of the B-type stars observed, the star extinction coefficient is larger in the red channel than the green channel. This implies a lower transmission in the red channel than the blue as star extinction coefficient (k_{mag}) is related to the vertical optical depth (τ) by:

$$\mathrm{k}_{mag} = 1.086 \times \tau \tag{6.1}$$

and the vertical optical depth is related to the transmission (T) by:

$$\mathrm{T} = \exp(-\tau) \tag{6.2}$$

Secondly, there is a slight trend for the star extinction coefficient to be higher for B-type (blue) stars than M-type (red) stars within a given colour channel. This was unexpected as the star extinction extinction coefficient should be constant for each night of observation. These trends are investigated through simulation and the cause was from leakage within the different colour bands. Full detail of the simulations is discussed within Section 6.3.

Lastly, within Table 6.2, it can be seen that the measured star extinction coefficients were significantly different when observing the same star with different f-stops. This is unexpected behaviour as the same star, measured with different Pentax K10D camera settings, should produce the same star extinction coefficient. This effect is from using the Pentax K10D camera dark-field image and when analysing star measurements of different brightness. The star extinction coefficient was shown to be different when comparing stars with observed star m_0 value above and below an instrumental magnitude of -9. The effect of observed star brightness and using the Pentax K10D camera dark-field image was investigated through simulation in Section 5.2.2.

6.3 Star Extinction Coefficient Simulation

To understand the interesting features that were seen in the measured star extinction coefficients in Section 6.2, simulations were used. The simulations involved modelling the atmospheric transmission and optic depth that the Pentax K10D camera would observe. To find the atmospheric transmission for each of the Pentax K10D camera different colour channels, atmospheric models from MODTRAN [41], the Pentax K10D camera wavelength response [61], and star spectral data [62] are used. The Pentax K10D camera wavelength response is shown in Figure 6.2. The simulated transmission observed by the Pentax K10D camera was found by combining the atmospheric models, the Pentax K10D camera wavelength response, and the star spectral data in the following equation:

$$\mathrm{T}_C = \sum_{\lambda=i}^{n} \frac{\mathrm{S}(\lambda)\mathrm{C}(\lambda)\mathrm{T}_M(\lambda)}{\mathrm{S}(\lambda)\mathrm{C}(\lambda)} \tag{6.3}$$

where $\mathrm{S}(\lambda)$ is the star spectral distribution, $\mathrm{C}(\lambda)$ is the Pentax K10D camera wavelength response for a specific colour channel, $\mathrm{T}_M(\lambda)$ is the atmospheric transmission from MODTRAN, T_C is the transmission observed by the Pentax K10D camera for a specific colour channel, i is the starting wavelength, and n is the final wavelength. Each atmospheric transmission was simulated with the observer looking vertically, to find a vertical transmission. The different MODTRAN aerosol models used were no aerosols, a desert model with a wind speed of 5 m/s, a maritime model and a rural model. These different aerosol models produced atmospheres that contained different levels of transmission. Of the different star spectral profiles available, I used an O-type, K-type and M-type. An O-type star is blue in colour, a K-type star is orange in colour, and an M-type star is red in colour.

The results of combining the star spectrum data and the Pentax K10D camera response were investigated first. I found that there was colour leakage within the Pentax K10D camera wavelength response. The overall effect of the colour leakage was dependent on the star spectral type observed, which effects the measured star extinction coefficient. Combining the Pentax K10D camera wavelength response with an O-type star showed up a blue leakage into the red filter. The combination of the Pentax K10D camera response and an O-type spectrum is shown in Figure

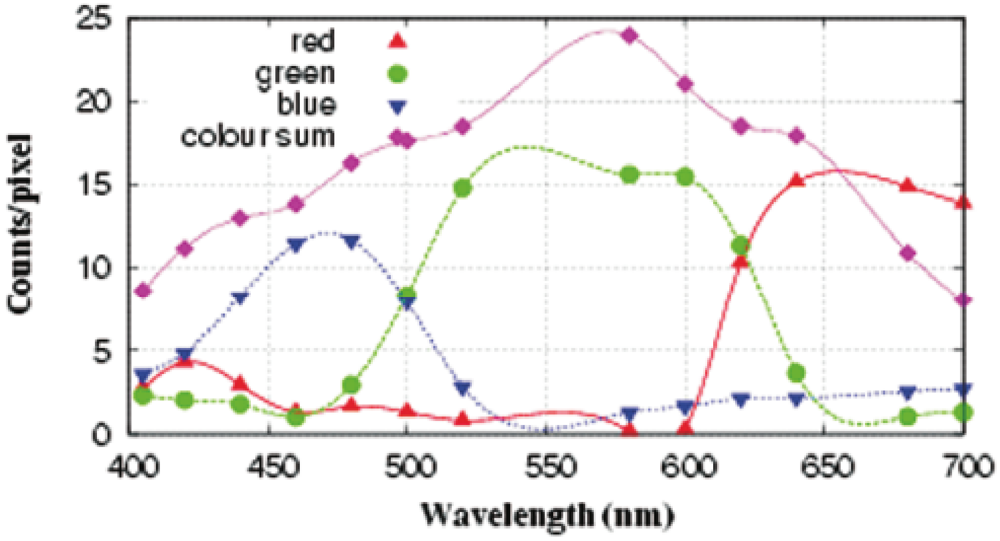

Figure 6.2: A plot of wavelength versus counts per pixel for a Pentax K10D camera [61]. This plot shows indications of colour leakage in the red and blue channels. The colour leakage is seen through the presence of an unexpected secondary peak. The area under the curve of the secondary peaks are approximately 30 percent of the area under the curve of the main peaks. The leakage in the filters becomes a major factor when measuring star extinction coefficients.

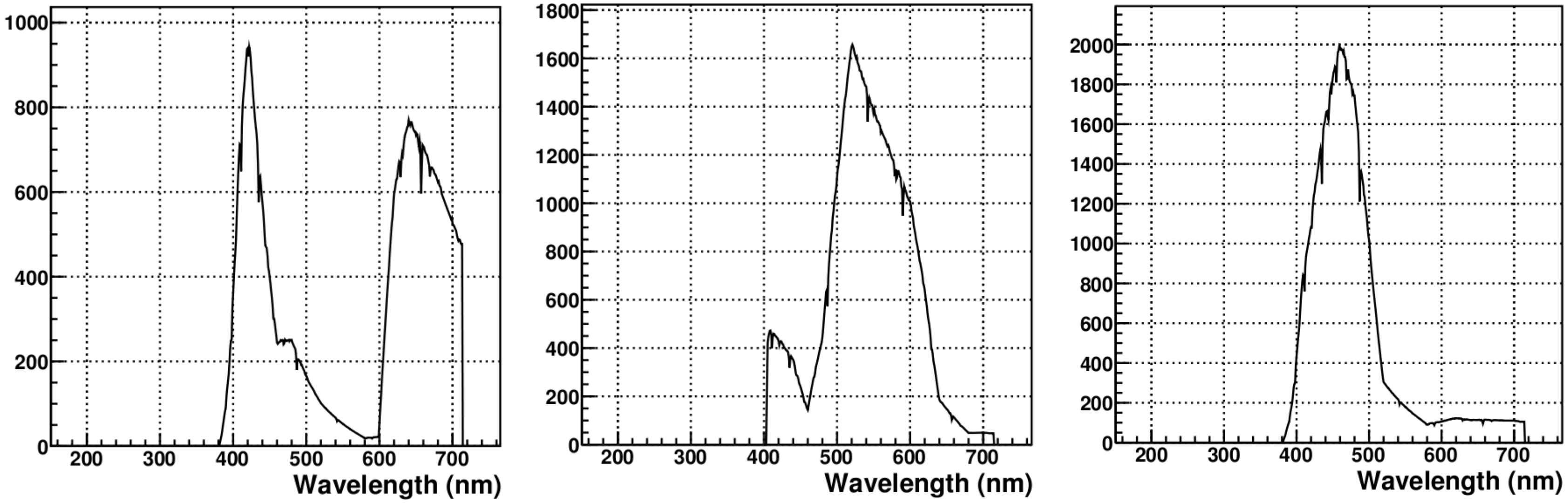

(a) (b) (c)

Figure 6.3: Combination of the Pentax K10D camera wavelength response [61] and an O-type star spectrum [62]. (a) Red Channel, (b) Green Channel and (c) Blue Channel. Within the red channel, a blue leakage is very evident. Within each of the different colour channels, there should be a single peak. For the red channel, there is a peak within the blue and red wavelengths. It has been amplified because an O-type star spectrum peaks around the blue band. This double peak has an effect on the comparison of measured red-channel star extinction coefficients to other star extinction coefficients from different spectral types.

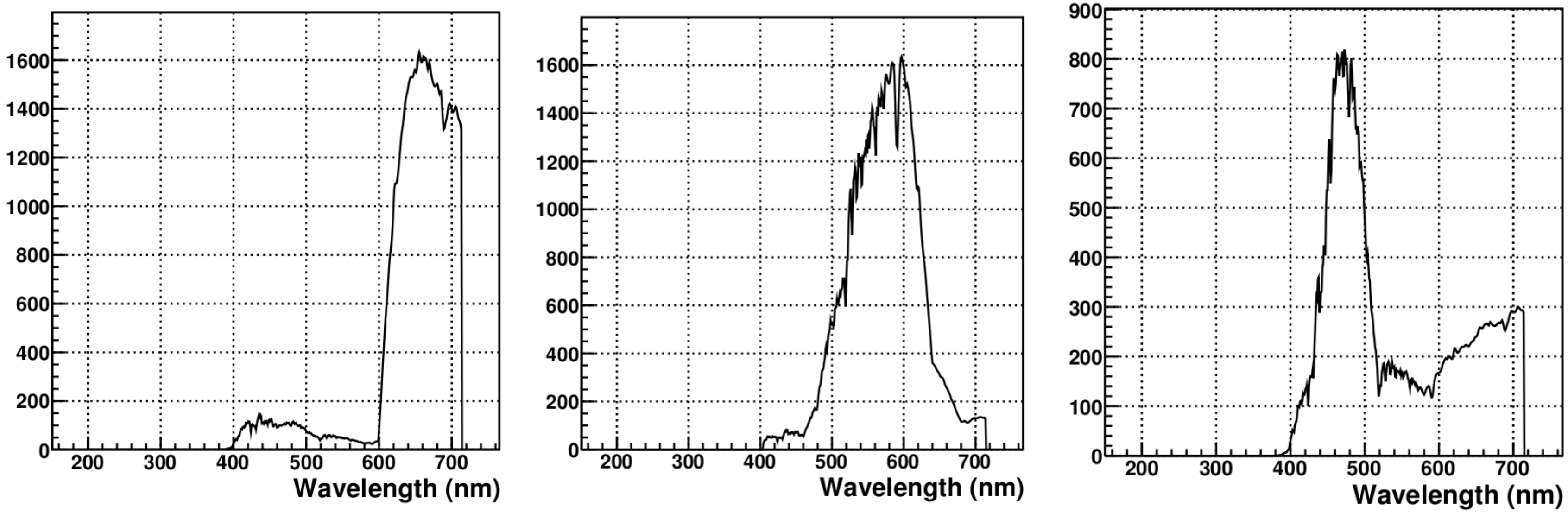

(a)

(b)

(c)

Figure 6.4: Combination of the Pentax K10D camera wavelength response [61] and an K-type star spectrum [62]. (a) Red Channel, (b) Green Channel and (c) Blue Channel. Within the blue channel, a red leakage is partially evident. Within each of the different colour channels, there should be a single peak. For the blue channel, there is a peak within the blue and red wavelengths. This double peak has an effect on the comparison of measured blue-channel star extinction coefficient to other star extinction coefficients from different spectral types.

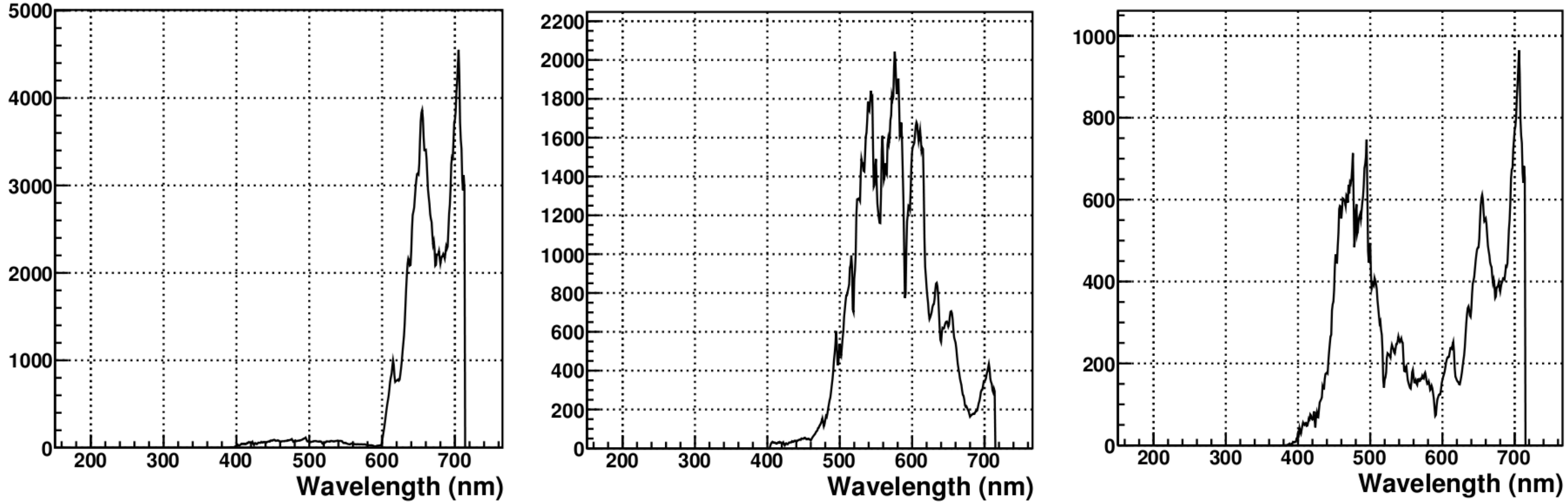

(a) (b) (c)

Figure 6.5: Combination of the Pentax K10D camera wavelength response [61] and an M-type star spectrum [62]. (a) Red Channel, (b) Green Channel and (c) Blue Channel. Within the blue channel, a red leakage is very evident. Within each of the different colour channels, there should be a single peak. For the blue channel, there is a peak within the blue and red wavelengths. This double peak has an effect on the comparison of the measured blue-channel star extinction coefficient to other star extinction coefficient from different spectral types.

Aerosol Model	Star Type	Red Channel			Green Channel			Blue Channel		
		VOD	**VAOD**	**k_{mag}**	**VOD**	**VAOD**	**k_{mag}**	**VOD**	**VAOD**	**k_{mag}**
No Aerosols	O	0.16	0	0.17	0.14	0	0.15	0.20	0	0.22
	F	0.12	0	0.13	0.13	0	0.14	0.18	0	0.19
	M	0.10	0	0.10	0.12	0	0.13	0.13	0	0.15
Desert, wss = 5 m/s	O	0.28	0.12	0.30	0.27	0.12	0.29	0.34	0.14	0.37
	F	0.22	0.11	0.24	0.25	0.12	0.27	0.31	0.13	0.34
	M	0.19	0.10	0.21	0.24	0.12	0.26	0.25	0.12	0.27
Maritime	O	0.45	0.29	0.48	0.44	0.29	0.47	0.52	0.32	0.56
	K	0.39	0.27	0.42	0.42	0.29	0.46	0.49	0.31	0.53
	M	0.36	0.26	0.39	0.40	0.28	0.44	0.42	0.28	0.45
Rural	O	1.1	0.96	1.2	1.2	1.0	1.3	1.3	1.1	1.5
	K	1.0	0.87	1.1	1.1	0.98	1.2	1.3	1.1	1.4
	M	0.90	0.80	0.97	1.1	0.94	1.2	1.1	0.94	1.2

Table 6.5: Results of simulating vertical optical depth (VOD), vertical aerosol optical depth (VAOD), star extinction coefficients (k_{mag}) that the Pentax K10D camera would observe through different MODTRAN [41] aerosol models and star spectral types [62]. The vertical optical depths are produced from the combination of the Pentax K10D camera response for each colour channel, the star spectrum and the MODTRAN atmospheric transmission for each aerosol model. The VAOD is calculated by subtracting the VOD of the no aerosol MODTRAN model away from the other aerosol model's VOD. The star extinction coefficient is calculated by $k_{mag} = 1.086 \times \text{VOD}$. Star spectral type is displayed from the hottest star (O-type) to coldest (M-type). Comparing the star type, the optical depth observed by the Pentax K10D camera changes depending on what spectral type of star is observed. Also the blue leakage into the red channel can be observed here as well, as the optical depth in the red channel for a O-type star is larger than the green channel.

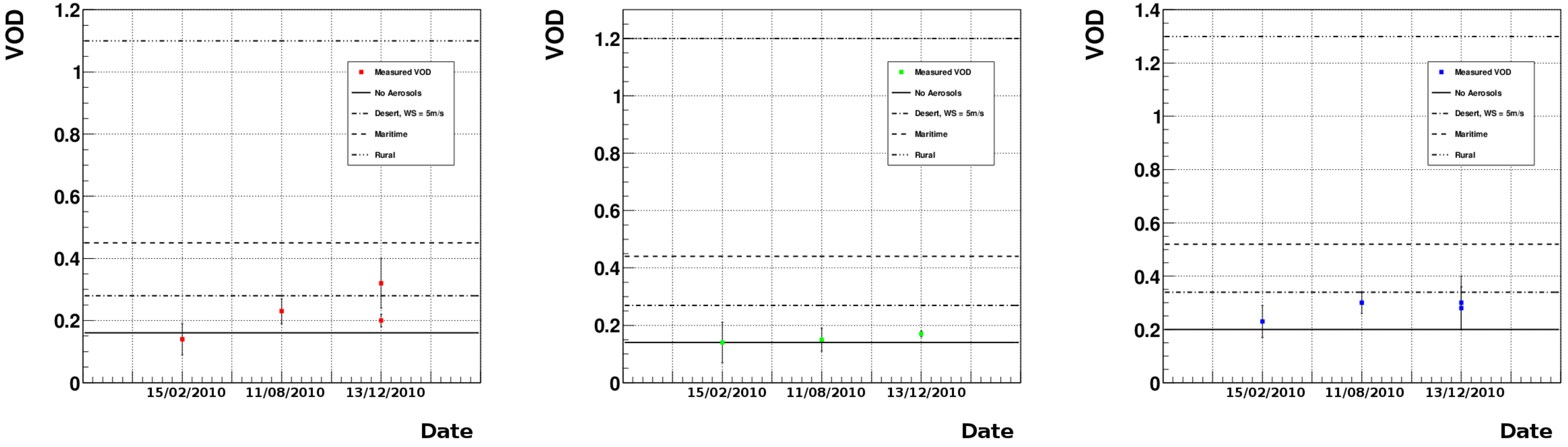

(a) (b) (c)

Figure 6.6: Shown here are graphical representations of the vertical optical depth (VOD) data from Table 6.6 and the results of simulations from Table 6.5. The simulated VODs are from observing O-type stars with the Pentax K10D camera seen through the atmosphere containing either no aerosols, desert (WS stands for wind speed), maritime or rural aerosol models. The simulated VOD's are represented as horizontal lines on the graphs. The measured VOD is the weighted mean and standard deviation of the VOD from the three different nights at Fowlers Gap for B-type stars only and are represented as dots. (a) VOD's seen through the red channel of the Pentax K10D camera, (b) VODs seen through the green channel of the Pentax K10D camera, and (c) VODs seen through the blue channel of the Pentax K10D camera. These graphs show that the data, across the three different colour bands, are best represented by the desert aerosol model and discount the maritime and rural aerosol models.

Night	**Colour Channel**					
	Red		**Green**		**Blue**	
	k$_{mag}$	**VOD**	**k**$_{mag}$	**VOD**	**k**$_{mag}$	**VOD**
15/02/2010: Southern Cross	0.15 ± 0.05	0.14 ± 0.05	0.15 ± 0.08	0.14 ± 0.07	0.23 ± 0.06	0.21 ± 0.06
11/08/2010: Scorpio	0.25 ± 0.05	0.23 ± 0.04	0.16 ± 0.05	0.15 ± 0.04	0.33 ± 0.05	0.30 ± 0.04
13/12/2010: Southern Cross	0.22 ± 0.02	0.20 ± 0.02	N/A	N/A	0.30 ± 0.08	0.28 ± 0.08
13/12/2010: Taurus	0.35 ± 0.09	0.32 ± 0.08	0.18 ± 0.01	0.17 ± 0.01	0.3 ± 0.1	0.3 ± 0.1

Table 6.6: Shown here are the weighted means and standard deviations of the star extinction coefficient (k$_{mag}$) from the three different nights at Fowlers Gap for B-type stars only. The vertical optical depths (VOD) are shown, where k$_{mag} = 1.086 \times$ VOD. The VOD is the addition of both Rayleigh and aerosol optical depths. These values are compared against the simulated star extinction coefficient for O-type stars for an atmosphere containing no aerosols that the Pentax K10D camera would observe and is shown in Figure 6.6. The table shows that the star extinction coefficient over the three different nights was not significantly from each other.

Aerosol Model	Star Type	Colour Channel								
		Red			Green			Blue		
		VOD	**VAOD**	**k_{mag}**	**VOD**	**VAOD**	**k_{mag}**	**VOD**	**VAOD**	**k_{mag}**
No Aerosols	O	0.082	0	0.089	0.120	0	0.130	0.273	0	0.297
	K	0.082	0	0.089	0.116	0	0.126	0.264	0	0.287
	M	0.083	0	0.090	0.116	0	0.126	0.254	0	0.276
Desert, 5 m/s	O	0.167	0.094	0.183	0.227	0.116	0.246	0.410	0.148	0.445
	K	0.168	0.093	0.182	0.221	0.114	0.240	0.401	0.148	0.435
	M	0.167	0.091	0.181	0.222	0.117	0.241	0.389	0.146	0.422
Maritime	O	0.323	0.262	0.351	0.390	0.293	0.423	0.585	0.338	0.635
	K	0.322	0.261	0.350	0.382	0.289	0.415	0.575	0.337	0.624
	M	0.321	0.259	0.349	0.383	0.290	0.416	0.562	0.334	0.610
Rural	O	0.831	0.813	0.902	1.046	1.006	1.136	1.460	1.289	1.586
	K	0.824	0.806	0.895	1.019	0.981	1.107	1.441	1.268	1.565
	M	0.815	0.795	0.885	1.026	0.988	1.114	1.418	1.243	1.540

Table 6.7: The results of the simulations of the star extinction coefficient observed by the Pentax K10D camera combined with the use of Johnson filters [63]. The VOD is the vertical optical depth and the VAOD is the vertical aerosol optical depth. The VOD is the addition of the Rayleigh and aerosol optical depths. The results of the simulation show that the application of the filters produces star extinction coefficient from stars of different spectral type that are more consistent with each other. The use of the Johnson filters in further measurements of star extinction coefficients with the Pentax K10D camera would remove the inconsistencies produced by the colour leakage within the red and blue colour filters.

6.3. The leakage can be seen through the double peak within the wavelength response. The combination of the Pentax K10D camera response and an K-type spectrum showed little to no colour leakage in any of the channels. The result of this combination is shown in Figure 6.4. Another leakage is seen through the combination of the Pentax K10D camera response and an M-type spectrum. This time there is a leakage of red wavelengths into the blue channel. The result of this combination is shown in Figure 6.5.

Next, the combination of star spectrum data, the Pentax K10D camera response and different MODTRAN atmospheric models were simulated. The results of the simulation are shown in Table 6.5. The table shows the total vertical optical depth (VOD), the vertical aerosol optical depth (VAOD) and the star extinction coefficient. The VOD (τ_{Tot}) for a specific colour channel is calculated from the simulated transmission observed by the Pentax K10D camera by:

$$\tau_{\mathrm{Tot}} = -lnT \tag{6.4}$$

The vertical aerosol optical depth (τ_{A}) was calculated:

$$\tau_{\mathrm{A}} = \tau_{\mathrm{Tot}} - \tau_{\mathrm{R}} \tag{6.5}$$

where τ_{R} is the Rayleigh optical depth. The Rayleigh optical depth is calculated from the MODTRAN model that contained no aerosols. When I compared the results of the simulation to the measured star extinction coefficient at Fowlers Gap both sets of data display a similar trend where, for blue stars, the star extinction coefficient is larger in the red channel than the green channel.

Now I can compare the results of the simulation to the measured values of star extinction coefficient found on the different nights of observation at Fowlers Gap. Only B-type stars were used for comparison as they were the only star type observed across the three nights. I show this comparison in Figure 6.6 for each of the three different colour bands. It can be seen from the figure that all the average star extinction coefficients rule out the MODTRAN rural model and most of the star extinction coefficients rule out the MODTRAN maritime model. The model that best describes the measured results is the MODTRAN desert model. The results of the measurements of B-type stars for each of the three nights are summarized in Table 6.6. To decrease the uncertainty, more nights of observation are needed.

In an ideal experiment, the measured star extinction coefficient would not depend on the spectral type of the star. To remove the unwanted wavelength leakage, the Pentax K10D camera could be fitted with different coloured filters in front of the lens. The disadvantage of this would be that one could then only observe a single colour channel at the one time, whereas with the original set-up, all three channels are used at once. I simulated this setup, where the Pentax K10D camera could be fitted with a set of Johnson filters [63] via:

$$\mathrm{T}_{JC} = \sum_{\lambda=i}^{n} \frac{\mathrm{S}(\lambda)\mathrm{C}(\lambda)\mathrm{J}(\lambda)\mathrm{T}_{M}(\lambda)}{\mathrm{S}(\lambda)\mathrm{J}(\lambda)\mathrm{C}(\lambda)} \tag{6.6}$$

where S(λ) is the star spectral data, C(λ) is the Pentax K10D camera wavelength response, $\mathrm{T}_M(\lambda)$ is the simulated atmospheric transmission, J(λ) is the Johnson filter response, , and i is the starting wavelength and n is the final wavelength. I simulated using a red, visual and blue filter. The results are shown in Table 6.7. The simulation showed that the application of the filters removes any dependence on star spectral type from measuring star extinction coefficients. The Johnson filters would remove the unexpected behaviour produced by using the Pentax K10D camera red and blue colour filters. This shows that the colour leakage in the Pentax K10D camera's filters was the cause of the trend where the star extinction coefficient in the red channel could be larger than the one within the green channel for the same star.

6.4 Night Sky Background Results

The results of the measured night sky background (NSB) levels at Fowlers Gap on 11/08/2010 and 13/12/2010 are outlined in this section. Images used for calculating the NSB levels at Fowlers Gap were taken with Pentax K10D camera settings of 400 ISO, f-stop of 3.5, and exposure length of 20 seconds. The raw images used in the analysis are shown in Figure 6.7. The method that I used to measure the NSB levels was described in Chapter 5, with the addition that calculated magnitudes are scaled to one airmass and a cut was used on the data to remove any pixels that are at a distance greater than 1500 pixels from the centre of the Pentax K10D camera CCD. The scaling to one airmass involves the use of a plate constant and assignment of celestial coordinates. Plate constants allow the conversion from image pixel coordinates to equatorial coordinates. The formula for the plate constant and celestial coordinates are shown in Appendix C. I used the star extinction coefficients measured in Table 6.6 to convert both the star instrumental magnitudes and the NSB to one airmass. Before the NSB levels can be measured, the instrumental magnitudes observed by the Pentax K10D camera had to be calibrated against the catalogue magnitudes. The result of this calibration is shown in Figure 6.8. The figure shows two green calibration plots using different star fields and one blue calibration plot. The equation fitted to each of the plots in the figure is of the form $y = mx + c$, where $m = 1$ and $c = p0$. By comparing the two green calibration plots it can be seen that, even using different sets of stars, there is a similar relationship between the instrumental magnitude and the catalogue magnitude. This comparison was used to check that the calibration was calculated consistently.

The Galactic Plane was included in both images as I am interested in comparing the NSB levels on the Galactic Plane and away from it. The result of the measured NSB levels taken on 11/08/2010 is shown in Figure 6.9 and Figure 6.10, and the NSB levels for 13/12/2010 are shown in Figure 6.11 and Figure 6.12. The images of the NSB photon counts are circular as pixel values located greater than 1500 pixels away from the center of the Pentax K10D camera were discarded. The pixels within Figure 6.9 and Figure 6.11 are equivalent to 52 by 52 pixels within an image taken by the Pentax K10D camera. 52 by 52 pixels were chosen as this area approximately covers 1° by 1° of the night sky. The on-Galactic Plane NSB value was classified as near zero galactic latitude, whereas the off plane NSB values are considered to be galactic latitudes away from the Galactic Plane. Off-Galactic Plane is defined as $|b| > 20°$, where b is the galactic latitude. The NSB plots are given in galactic coordinates to show the location of the Galactic Plane, which runs along zero galactic latitude. Both Figure 6.10 and

(a)

(b)

Figure 6.7: Unprocessed images of the Galactic Plane taken with the Pentax K10D camera. Image (a) taken on 11/8/2010, and is looking towards the centre of the Galactic Plane, with the plane running vertically through the centre. Image (b) taken on 12/13/2010, and is looking towards the edge of the Galactic Plane, with the plane running from horizontally through the bottom. Each image was taken with the Pentax K10D camera settings of 400 ISO, f-stop of 3.5 and exposure time of 20 seconds. Images cover approximately 50° by 70° of night sky.

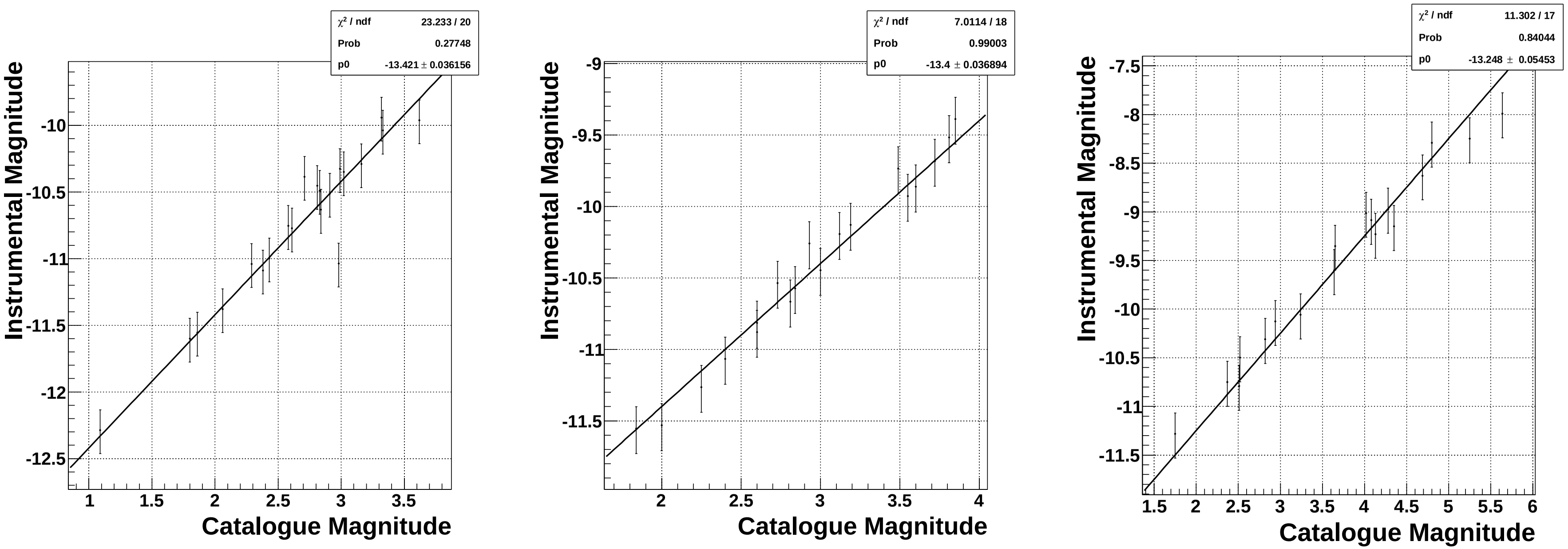

(a) (b) (c)

Figure 6.8: Calibration plot of instrumental magnitudes against catalogue magnitudes for (a) green channel taken on the night of 11-08-2010 against visual catalogue magnitudes, (b) green channel taken on the night of 13-12-2010 against visual catalogue magnitudes and (c) blue channel taken on the night of 13-12-2010 against blue catalogue magnitudes. The equation fitted to each of the plots is of the form y = mx + c, where m = 1 and c = p0. The blue channel calibration plot taken on the night of 11-08-2010 was discarded due to a poor χ^2. The catalogue magnitudes where taken from [56].

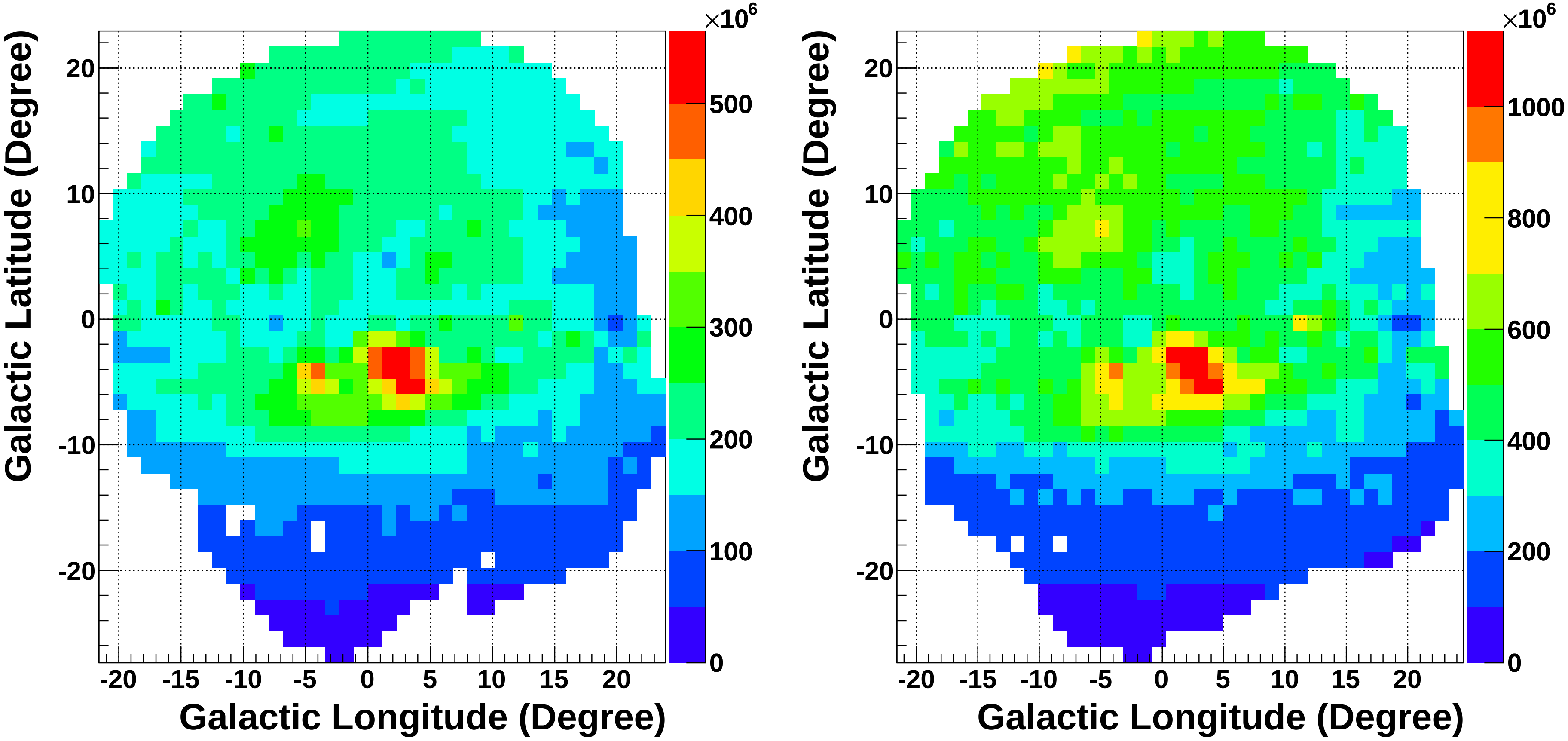

(a)

(b)

Figure 6.9: A NSB map produced from an image taken on 11/08/2010 from Folwers Gap, where (a) Green Channel and (b) Blue Channel. Units of the colour scale are in photons sr^{-1} s^{-1} cm^{-2}. This map is in galactic coordinates, looking towards the galactic centre. The images are circular in shape as I removed pixel counts that were greater than 1500 pixels away from the center of the image.

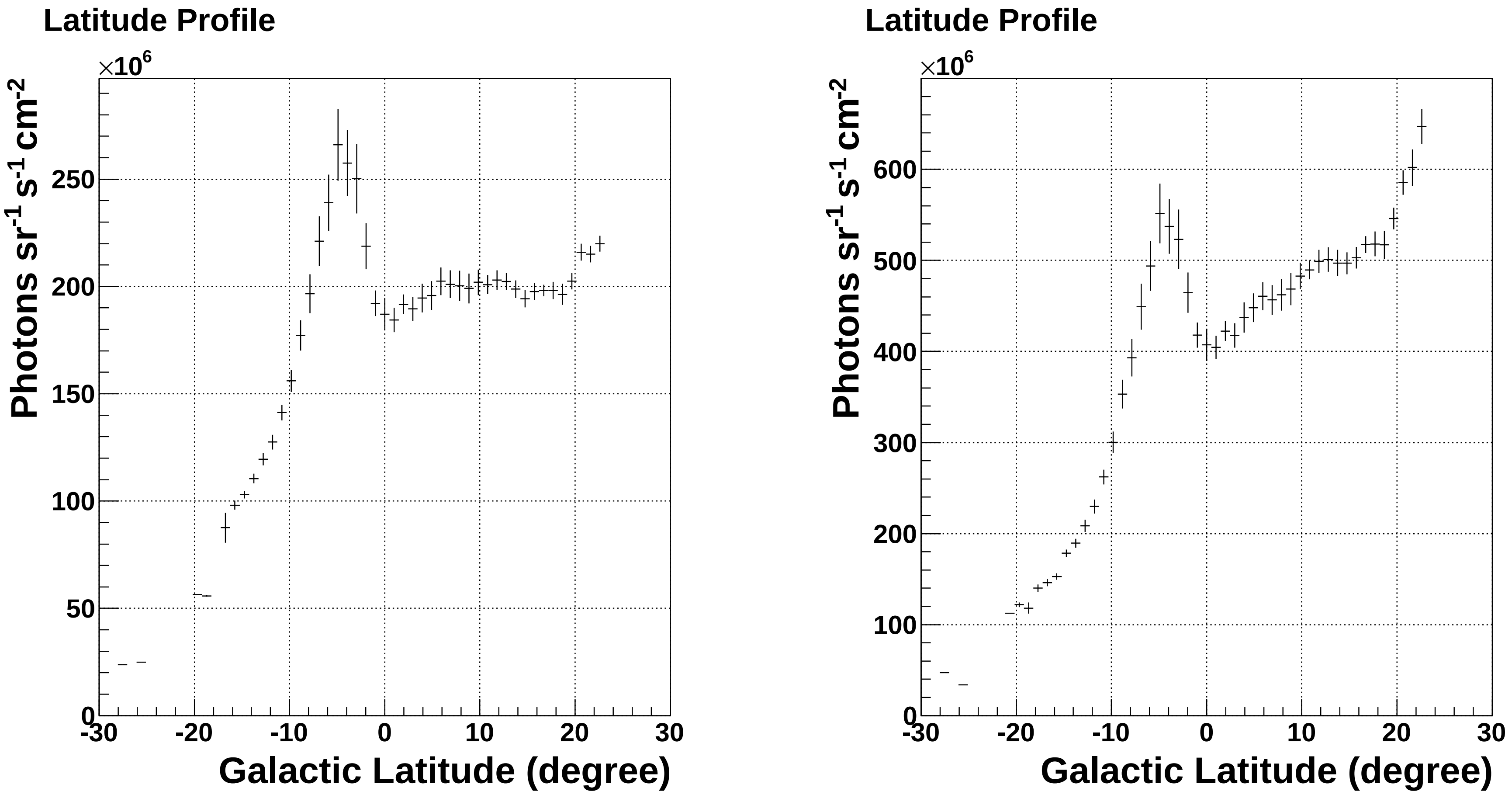

(a)

(b)

Figure 6.10: Profile of NSB photons $\mathrm{sr}^{-1}\ \mathrm{s}^{-1}\ \mathrm{cm}^{-2}$ versus galactic latitude taken on 11-08-2010 at Fowlers Gap of the data shown in Figure 6.9. The profiles sums the values over all the galactic longitudes available for each galactic latitude and then displays the mean and the error in the mean. Each bin covers one degree. (a) is the green channel profile and (b) is the blue channel profile. The profile shows how NSB values drop off for galactic latitudes $> |0°|$. The plateau within the profile is from the bright area observed from observing the galactic center and can be seen within Figure 6.7a. The increase in number of NSB photons in the blue channel profile at greater than 20° latitude could be from lack of data near the edge of pixel radius cut applied to the image.

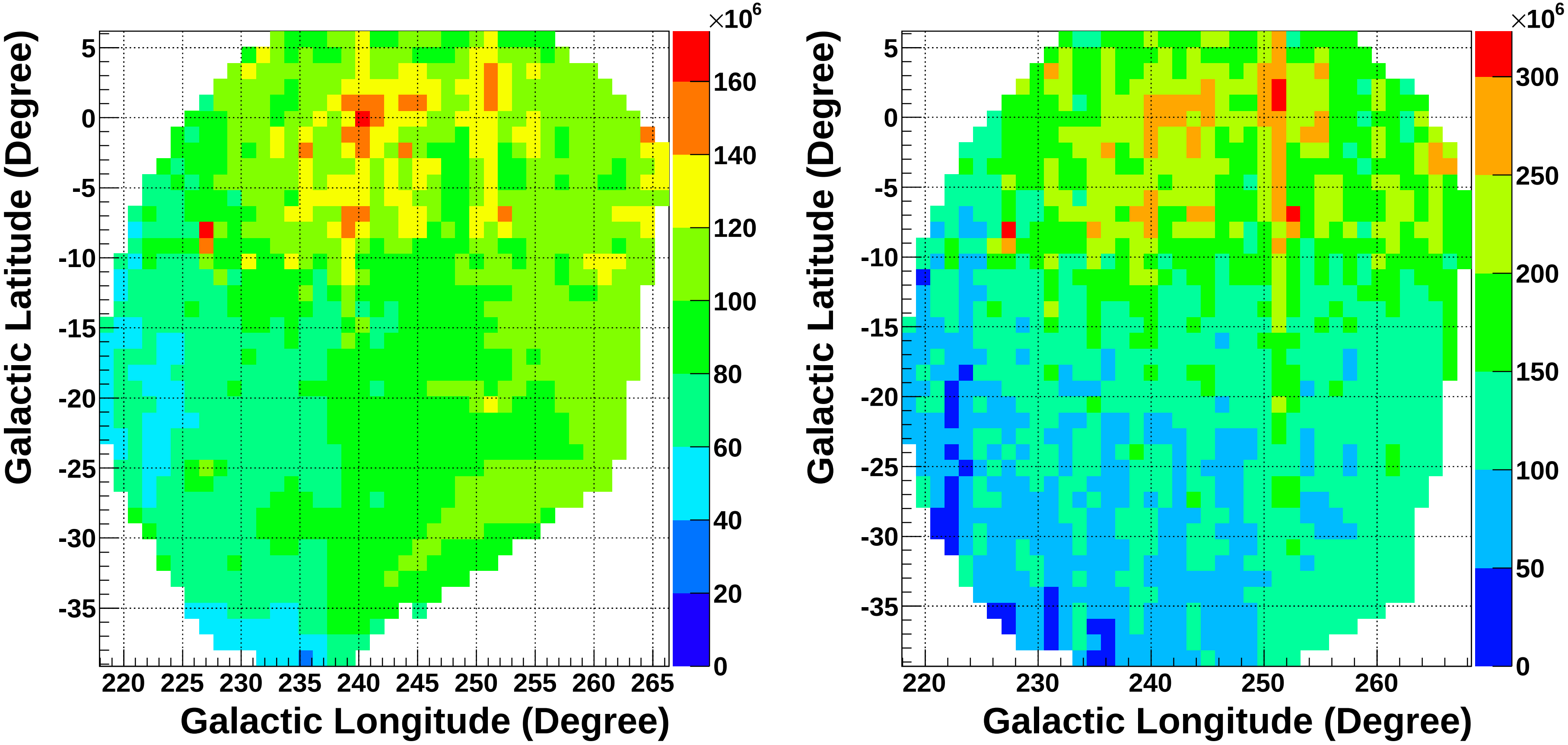

(a) (b)

Figure 6.11: A NSB map produced from an image taken on 13/12/2010 from Folwers Gap, where (a) Green Channel and (b) Blue Channel. Units of the colour scale are in photons sr^{-1} s^{-1} cm^{-2}. This map is in galactic coordinates, looking towards the edge of the Galactic Plane. The images are circular in shape as I removed pixel counts that were greater than 1500 pixels away from the center of the image.

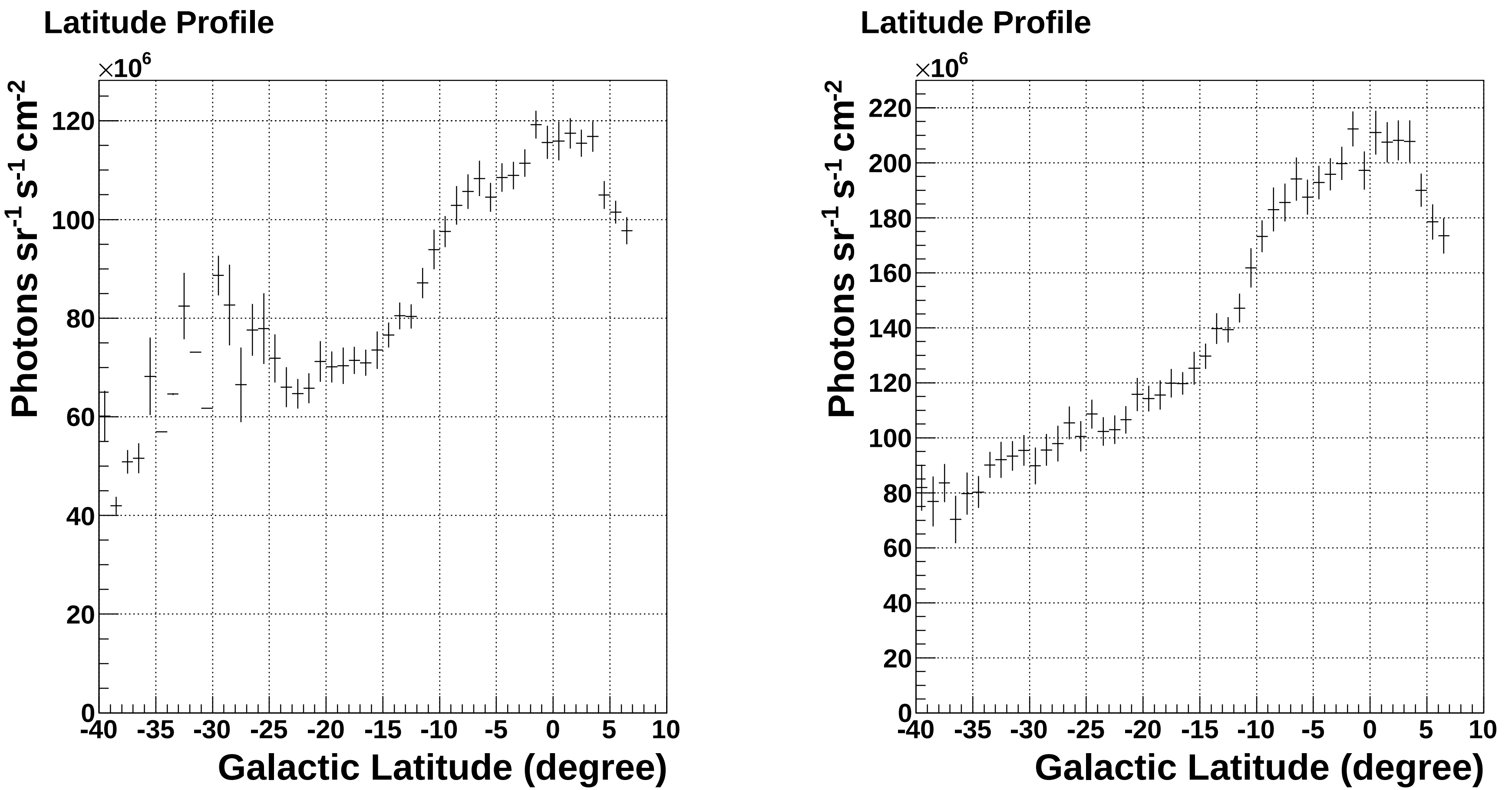

(a) (b)

Figure 6.12: Profile of NSB photons sr^{-1} s^{-1} cm^{-2} versus galactic latitude taken on 13-12-2010 at Fowlers Gap of the data shown in Figure 6.11. The profiles sums the values over all the galactic longitudes available for each galactic latitude and than displays the mean and the error in the mean. Each bin covers one degree. (a) is the green channel profile and (b) is the blue channel profile. The scatter and small uncertainty bars on the left-hand side of the green channel profile is due to a lack of statistics as this is near the edge of the pixel radius cut applied to the image.

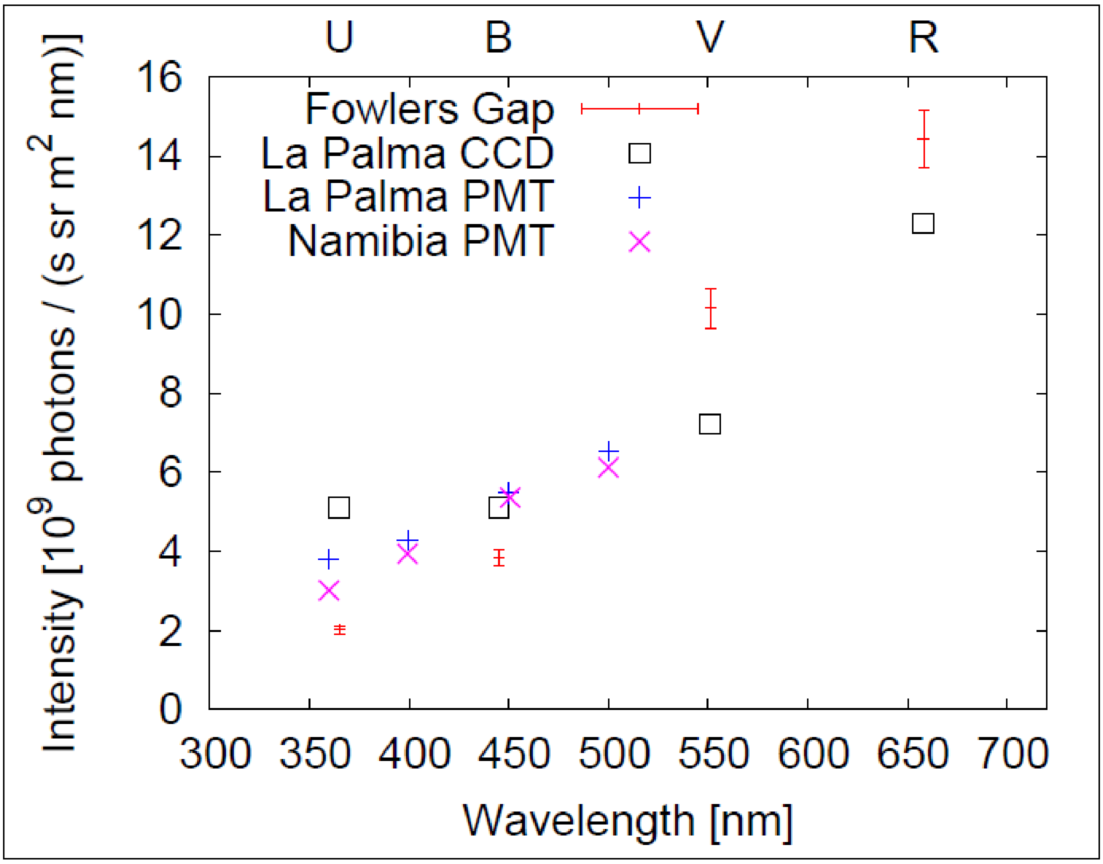

Figure 6.13: NSB measurements taken of a series of dark regions within the Galactic Plane from "Fowlers Gap" [64], "La Palma PMT" and "Namibia PMT" [65], and "La Palma CCD" [66]. Image taken from [64]. These values are shown to give an indication of the lower limit of expected observed NSB photons.

Figure 6.12 show the NSB values are greater around 0° latitude, with the NSB values decreasing when moving off the Galactic Plane. The figures show how the NSB values are two to three times larger around zero degrees galactic latitude than for galactic latitudes $> |20°|$, except within Figure 6.10 where the measured NSB values increases for positive galactic latitudes. The increase in brightness for positive galactic latitudes is from the brighter area of the galactic centre extending to these latitude, as seen in Figure 6.7a. The uncertainty profiles from fluctuations in measured NSB values within the 52 by 52 pixel grid are shown in Appendix D, with an estimation of the systematic uncertainty from using the dark field image taken from the Pentax K10D camera is shown in Figure 5.2.

Figure 6.13 shows other NSB measurements from Fowlers Gap [64], La Palma [65, 66] and Namibia [65]. These measurements were of dark regions within the Galactic plane, and give an indication of the lower limits of the observable NSB. The measurements are in photons sr^{-1} s^{-1} m^{-2} nm^{-1}. To convert these units into a measurement that can be used as a comparison to the measurements taken by the Pentax K10D camera, they needed to be converted from square metres to square centimetres and multiplied by the wavelength width of the filter. In this case, the blue and green wavelength windows were assumed to be 100 nm wide. This the approximate width of the wavelength window of the Pentax K10D camera that can be seen in Figure 6.2. The approximate average photon flux from dark regions from Figure 6.13 are:

- **Green Filter :** 70×10^6 photons sr^{-1} s^{-1} cm^{-2}
- **Blue Filter :** 45×10^6 photons sr^{-1} s^{-1} cm^{-2}

It can be seen from the NSB measurements taken by the Pentax K10D camera within Figure 6.10 and Figure 6.12, that these values are greater than the values measured from the average dark regions when scaled to the colour filter wavelength windows. These differences are to be expected, given the measurements were taken from different size sky areas and the night sky image taken by the Pentax K10D camera contained brighter regions of the sky.

6.5 Summary

The analysis of three nights of measuring star extinction coefficients at Fowlers Gap showed that the aerosol levels are best described by the MODTRAN desert model with wind speed 5 m/s. Both MODTRAN maritime and rural aerosol model were ruled out by the measurements taken. This conclusion was made from the comparison of B-type stars as they were the only star type measured over all three nights of observations. Out of the different Pentax K10D camera settings used, there was no observable difference on measuring the star extinction coefficients where the star m_0 was < -9. If the star's measured m_0 was > -9, then the results were affected by the use of the Pentax K10D camera's dark-field image. A set of observations measured on 13/11/2010, the images were taken while the moon was above the horizon but not within the target area. These measured star extinction coefficients was not significantly different to the measured star extinctions coefficients measured while the moon was below the horizon.

Differences between measured star extinction coefficients on the same night were found: a larger measured red channel star extinction coefficient than the one measured by the green channel, and a star spectral type dependence even within the same colour channel. It was found that a colour leakage within the red and blue channel explained these effects. A solution to these problems could be the use of coloured filters placed in front of the Pentax K10D camera's lens. The effectiveness of Johnson filters at fixing these problems was simulated and the simulation showed this could be an effective fix. The side-effect of using filters in front of the lens is that the ability to measure three colour channels at once is lost.

The night sky background (NSB) measurements towards the centre and towards the edge of the Galactic Plane gave expected results. The expected results were that the NSB levels are higher towards the centre of the Galactic Plane than the edge and that the NSB levels dropped off the further the measurements were taken away from 0° galactic latitude. The difference between measured NSB levels between centre and edge of the Galactic Plane is approximately a factor of 2 to 3. The measured on and off plane values (off plane values are defined as galactic latitudes greater than 20°). The results showed that the on-off plane values differed by a factor of between two to three times.

Chapter 7

Conclusion

The results of this work were related to an Australian site survey to catalogue atmospheric conditions effecting the performance of proposed greater than 10 TeV γ-ray astronomy arrays such as CTA [19] and TenTen [20]. An assessment was made of the viability of using a Pentax K10D camera for measuring the atmospheric conditions, and to determine the effect atmospheric conditions might have on the γ-ray array.

The effects of different atmospheric conditions on the performance of a γ-ray array were assessed through simulation. Models of atmospheric conditions with different levels of aerosols were generated by MODTRAN for investigation. The array's performance was quantified through its angular resolution and its ability to reject images from proton events. The effect of cirrus clouds on the array's performance was also investigated through simulation. My findings showed that the simulated array had the best performance when the atmosphere contained no aerosols. This was seen through the array's ability to reject proton images. The angular resolution was not effected until quite high level of aerosols were introduced (aerosol levels contained in the rural model). The effect of cirrus cloud at either 6 km or 10 km on the propagation of Cherenkov radiation from γ-ray showers was briefly investigated. I showed that it may be possible to observe TeV γ-ray showers by the array in the presence of cirrus cloud. The next step would be to quantify the effect of cirrus cloud on the array's performance through simulation.

A suitability study was conducted to find out if the Pentax K10D camera could be used as a photometric device. The Pentax K10D camera was tested because photometric methods can be used to infer information about atmospheric conditions, such as night sky background (NSB) and optical depth. The tests were related to linearity, flat-fields and dark-fields. These tests determined that the Pentax K10D camera could be used as a photometric device. The effects of the Bayer filter and the gain were also calculated to help determine the uncertainties. A linearity test showed that the Pentax K10D camera was linear over the whole digitisation range (12-bit). The dark-field test showed that the Pentax K10D camera could only record half of the full dark noise variation. This had a significant effect only where the measured signal was on a similar order of magnitude to the dark noise. The flat-field test showed that using either a clear sky flat-field image or the rotated clear sky flat-field method corrected for the effects of vignetting within star extinction coefficient plots. The pixel gain of the Pentax K10D camera for 400, 800 and 1600 ISO settings was found. The Bayer filter was shown, through simulation, to have a minimal impact on measuring star's instrumental magnitudes where the star image half-width is greater than one pixel.

Star extinction coefficients were measured for three nights at Fowlers Gap research station. This was done to find information about the vertical optical depth and the vertical aerosol optical depth. I found the weighted mean for the vertical optical depth and vertical aerosol optical depth for the three different different nights and compared them to the vertical optical depth of the simulated atmosphere with no aerosols. The MODTRAN desert aerosol model with 5 m/s wind speed best describes the aerosol levels across the three nights of observations. The measurements taken at Fowlers Gap exclude the MODTRAN maritime and rural aerosol models.

In the process of measuring star extinction coefficients, I found that star spectral types effect the observed star extinction coefficient. This led to the realisation that there was colour leakage within the Pentax K10D camera colour filters. The effects of the colour leakage were investigated through simulation. When observing an O-type star, there is significant blue wavelength leakage into the red channel. A similar effect was observed when viewing M-type stars where a red wavelength leak is observed in the blue channel. The star spectral type thus effected the observed optical depth measured by a single colour channel, and when observing an O-type star, the red channel optical depth was higher than the optical depth seen in the green channel. The effect of the colour leakage could be removed by the use of Johnson filters [63] placed in front of the Pentax K10D camera lens. The reduction of this effect by the use of Johnson filters is shown through simulations.

I measured the night sky background (NSB) with the Pentax K10D camera for 2 nights at Fowlers Gap. This showed that the NSB is two to three times higher on the galactic plane, compared with the NSB off the plane. Also, on the galactic plane the NSB was two to three times greater on the night of 13/12/2010, compared with the night of 11/08/2010. The difference between the two nights was caused by comparing different parts of the galactic plane. Off galactic plane values are defined as galactic latitudes greater than 20°. This was expected as the observations were looking at different parts of the Galactic plane.

7.1 Future Work

Future investigation could be done to look at the performance of a γ-ray array when shower images are reconstructed with incorrect atmospheric profiles. For example, the showers may travel through a "dirty" atmosphere but the shower images are reconstructed assuming a clean atmospheric profile. This investigation would be done to look at the precision needed to measure the atmospheric quality. For the cirrus cloud investigation, simulations can be done on quantifying the effects of the clouds on an IACT array. The performance can be quantified through studying angular resolution and the ability to reject photon events, and also on energy reconstruction and trigger rates.

The atmospheric quality monitoring for both the aerosol optical depth and NSB can be extended to more nights and different sites around Australia. This can be done to develop a better average and understanding of long term observations of sites of interest. Extending the atmospheric monitoring to different sites would assist in finding an optimal site in Australia. It was shown through simulation that a proposed γ-ray array would have the best performance when the atmosphere viewed through contained no aerosols. Therefore the optimal site would be the one containing the lowest average atmospheric aerosol levels.

To reduce the effects of colour leakage, the use of external colour filters on the Pentax K10D camera when measuring star extinction coefficients could be investigated. Even though an improvement was shown through simulation, this still needs to be verified through experiment. This would help with decreasing the uncertainty on the average star extinction coefficients and improve the comparison of different sites.

Appendix A

Extra Camera Suitability Plots

In this chapter I display the extra plots that were unable to be shown in the main body of this thesis. There are extra plots for the dark-field and star-field image separation, gain and flat-field method tests. The extra plots are mainly for the red and blue channel that have displayed a similar trend to the green channel that was shown.

A.1 Dark-field and Star-field image separation

Shown here are the extra dark-field and star-field image separation plots. Chapter 5.2.2 has the method involved for why these plots were produced. Each set of images show different colour channels and ISO settings, containing images taken with different aperture settings. The different aperture settings use are: f11, f8.0, f6.7, f5.6, and f3.5. The order is:

- 400 ISO Blue Channel
- 400 ISO Red Channel
- 800 ISO Green Channel
- 800 ISO Blue Channel
- 800 ISO Red Channel
- 1600 ISO Green Channel
- 1600 ISO Blue Channel
- 1600 ISO Red Channel

The main trend is that the f-stop of 3.5 gives the largest separation between average signal from an unprocessed star field image and a dark-field image. This result is independent of ISO setting and colour channel.

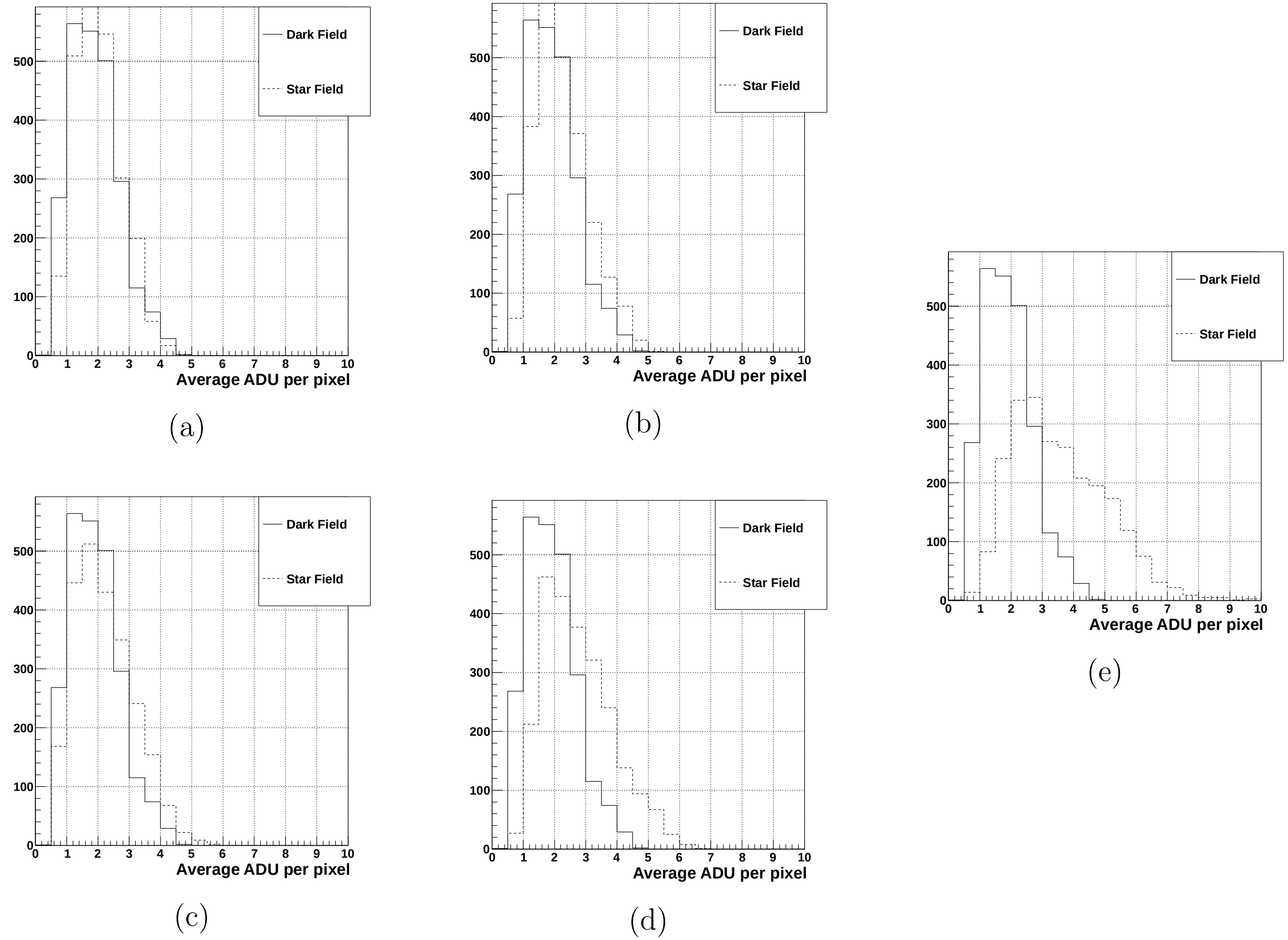

(a) (b) (c) (d) (e)

Figure A.1: Plots of average dark field counts per pixel and average signal counts per pixels from a star field image for just the Blue Channel. Average ADU per pixel from the dark field is denoted by the solid line, while average counts per pixel from the star field image is denoted by the dash line. Counts due to Stars and “hot” dark pixels were removed. All pixels have been taken with the camera settings of 400 ISO, exposure length of 20 sec and f-stop of (a) 11, (b) 8.0, (c) 6.7, (d) 5.6 and (e) 3.5. The f-stop of 3.5 shows the only evidence of a signal level above the noise, which indicates an ability to measure the NSB.

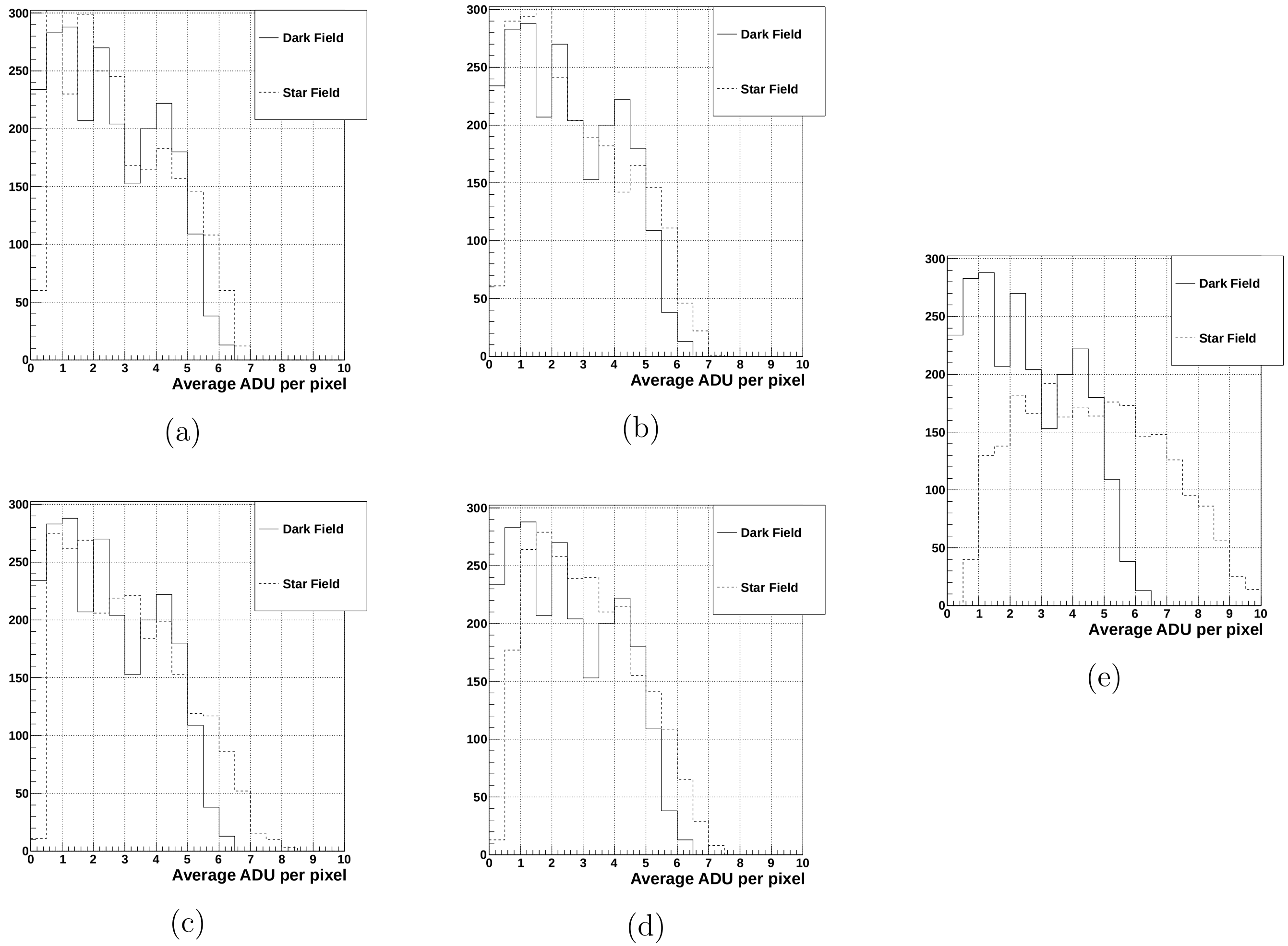

(a) (b) (c) (d) (e)

Figure A.2: Plots of average dark field counts per pixel and average signal counts per pixels from a star field image for just the Red Channel. Average ADU per pixel from the dark field is denoted by the solid line, while average counts per pixel from the star field image is denoted by the dash line. Counts due to Stars and "hot" dark pixels were removed. All pixels have been taken with the camera settings of 400 ISO, exposure length of 20 sec and f-stop of (a) 11, (b) 8.0, (c) 6.7, (d) 5.6 and (e) 3.5. The f-stop of 3.5 shows the only evidence of a signal level above the noise, which indicates an ability to measure the NSB.

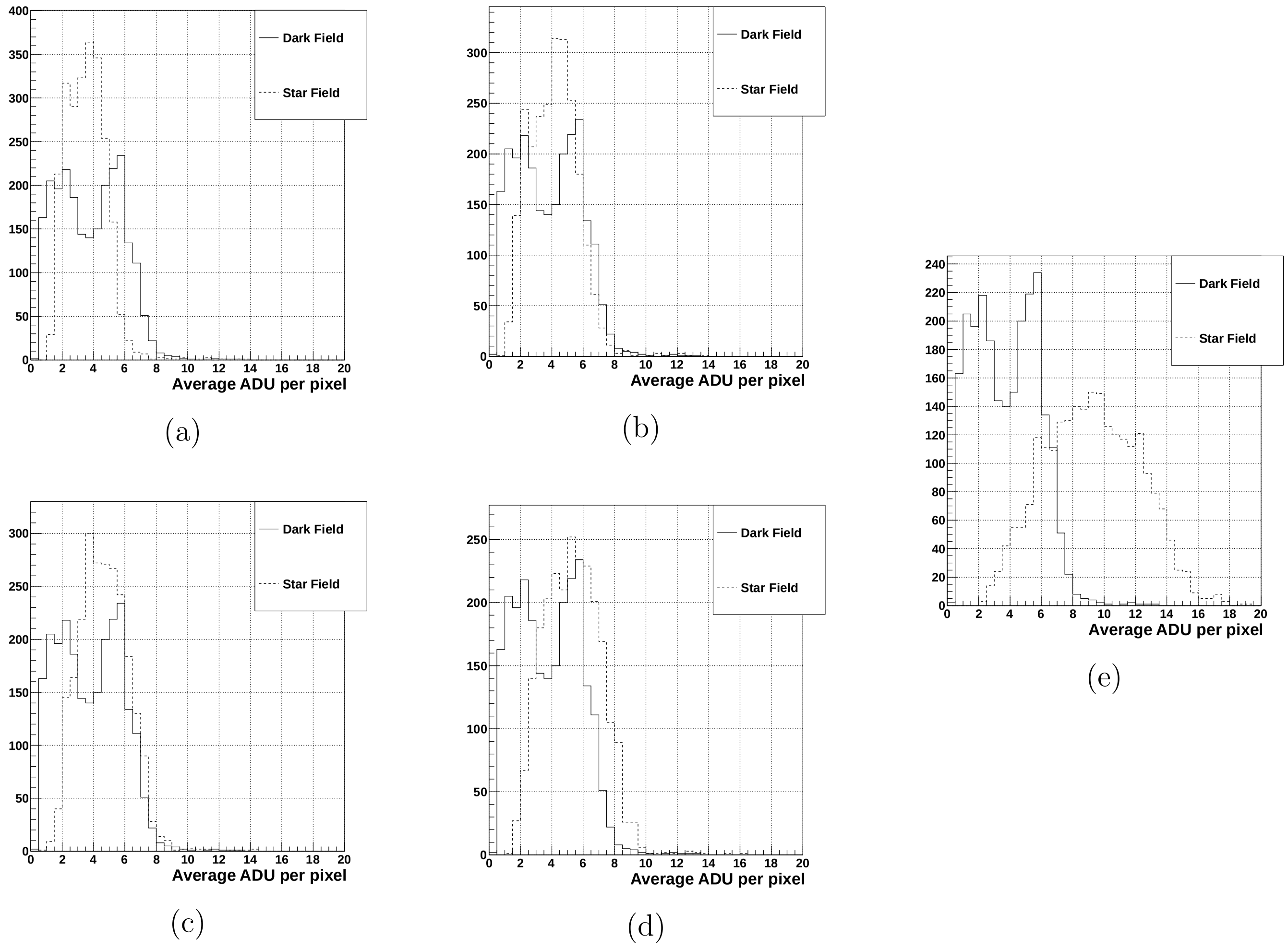

(a) (b) (c) (d) (e)

Figure A.3: Plots of average dark field counts per pixel and average signal counts per pixels from a star field image for just the Green Channel. Average ADU per pixel from the dark field is denoted by the solid line, while average counts per pixel from the star field image is denoted by the dash line. Counts due to Stars and “hot” dark pixels were removed. All pixels have been taken with the camera settings of 800 ISO, exposure length of 20 sec and f-stop of (a) 11, (b) 8.0, (c) 6.7, (d) 5.6 and (e) 3.5. The f-stop of 3.5 shows the only evidence of a signal level above the noise, which indicates an ability to measure the NSB.

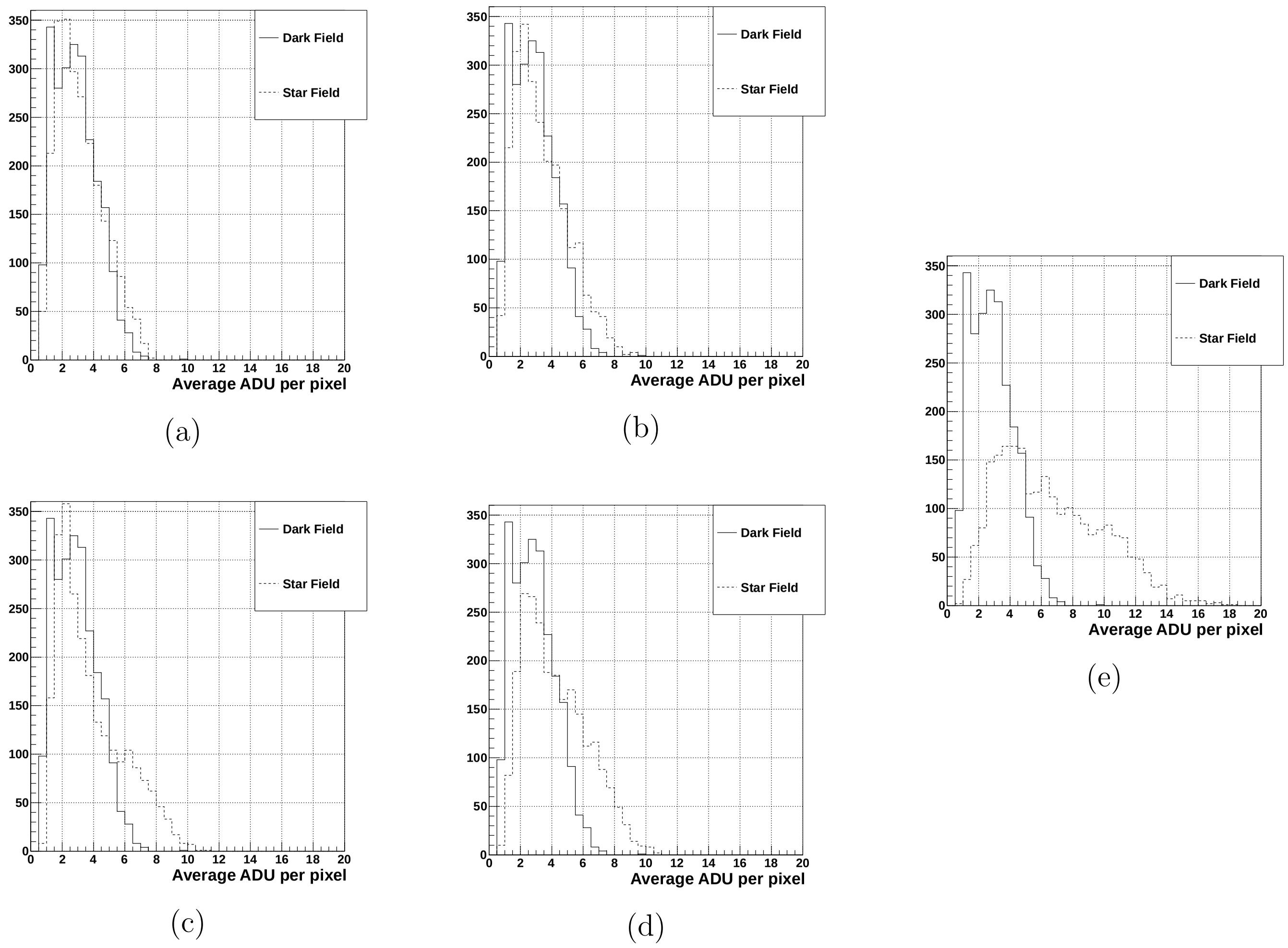

(a) (b) (c) (d) (e)

Figure A.4: Plots of average dark field counts per pixel and average signal counts per pixels from a star field image for just the Blue Channel. Average ADU per pixel from the dark field is denoted by the solid line, while average counts per pixel from the star field image is denoted by the dash line. Counts due to Stars and “hot” dark pixels were removed. All pixels have been taken with the camera settings of 800 ISO, exposure length of 20 sec and f-stop of (a) 11, (b) 8.0, (c) 6.7, (d) 5.6 and (e) 3.5. The f-stop of 3.5 shows the only evidence of a signal level above the noise, which indicates an ability to measure the NSB.

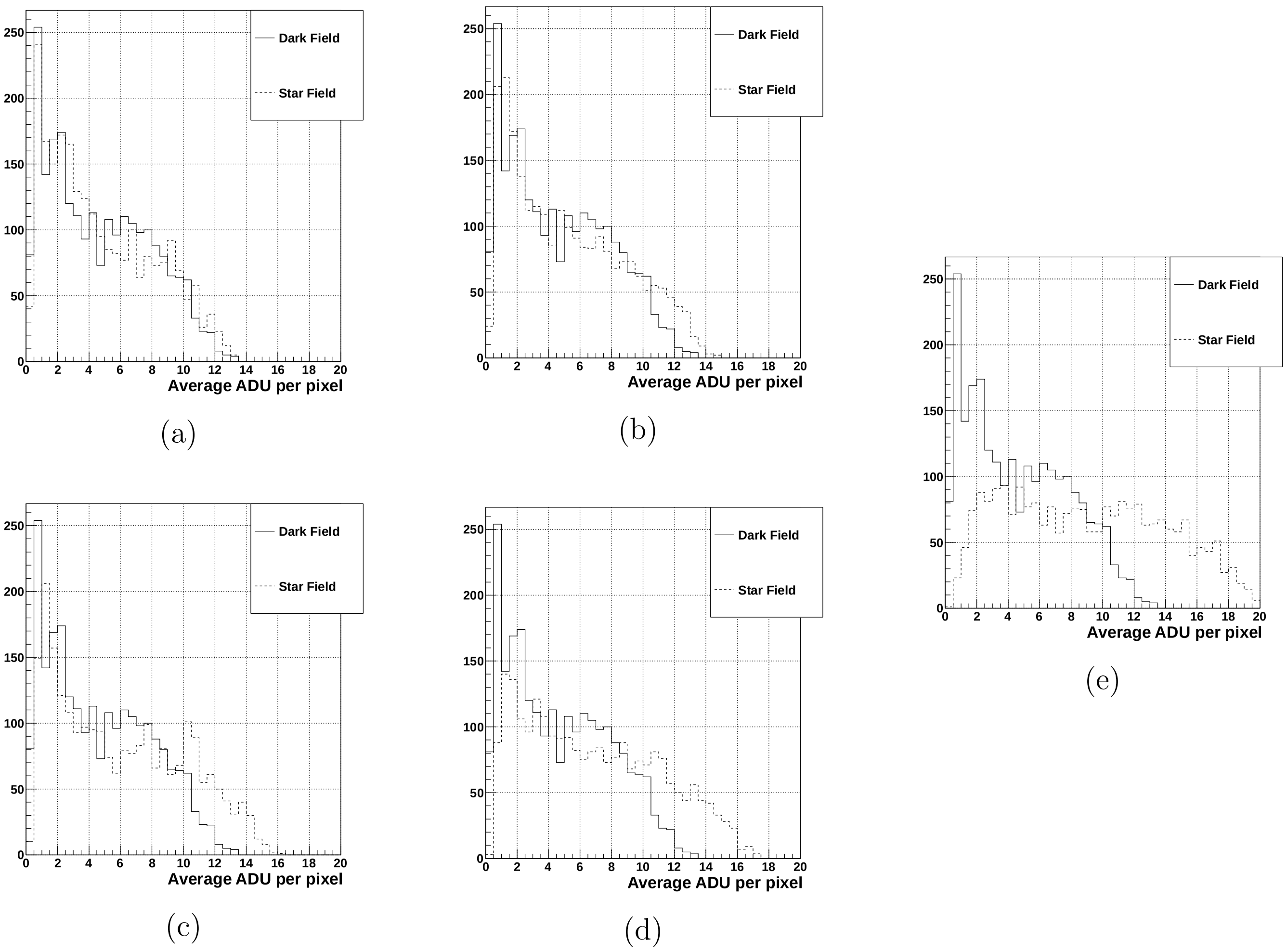

Figure A.5: Plots of average dark field counts per pixel and average signal counts per pixels from a star field image for just the Red Channel. Average ADU per pixel from the dark field is denoted by the solid line, while average counts per pixel from the star field image is denoted by the dash line. Counts due to Stars and “hot” dark pixels were removed. All pixels have been taken with the camera settings of 800 ISO, exposure length of 20 sec and f-stop of (a) 11, (b) 8.0, (c) 6.7, (d) 5.6 and (e) 3.5. The f-stop of 3.5 shows the only evidence of a signal level above the noise, which indicates an ability to measure the NSB.

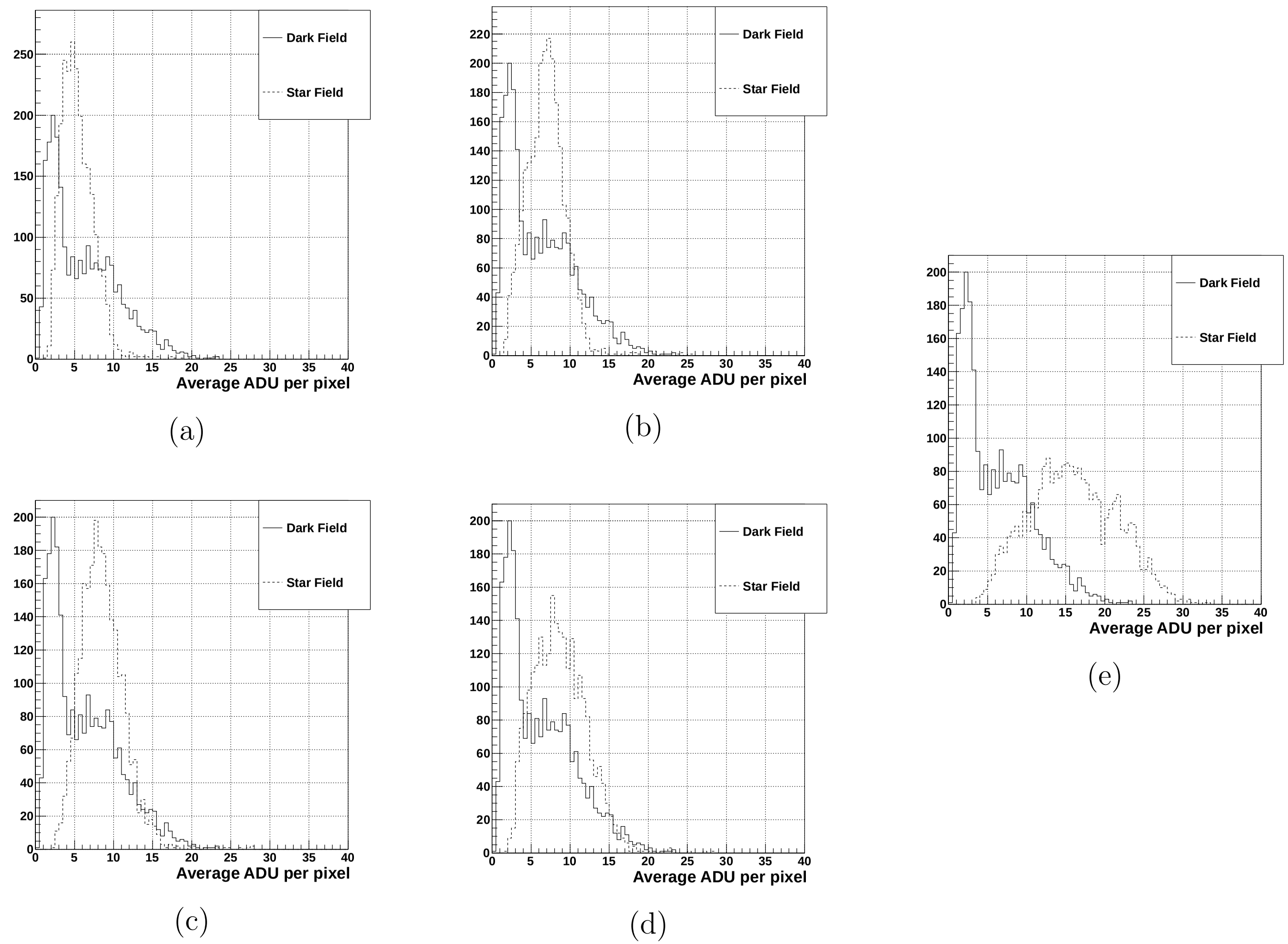

Figure A.6: Plots of average dark field counts per pixel and average signal counts per pixels from a star field image for just the Green Channel. Average ADU per pixel from the dark field is denoted by the solid line, while average counts per pixel from the star field image is denoted by the dash line. Counts due to Stars and “hot” dark pixels were removed. All pixels have been taken with the camera settings of 1600 ISO, exposure length of 20 sec and f-stop of (a) 11, (b) 8.0, (c) 6.7, (d) 5.6 and (e) 3.5. The f-stop of 3.5 shows the only evidence of a signal level above the noise, which indicates an ability to measure the NSB.

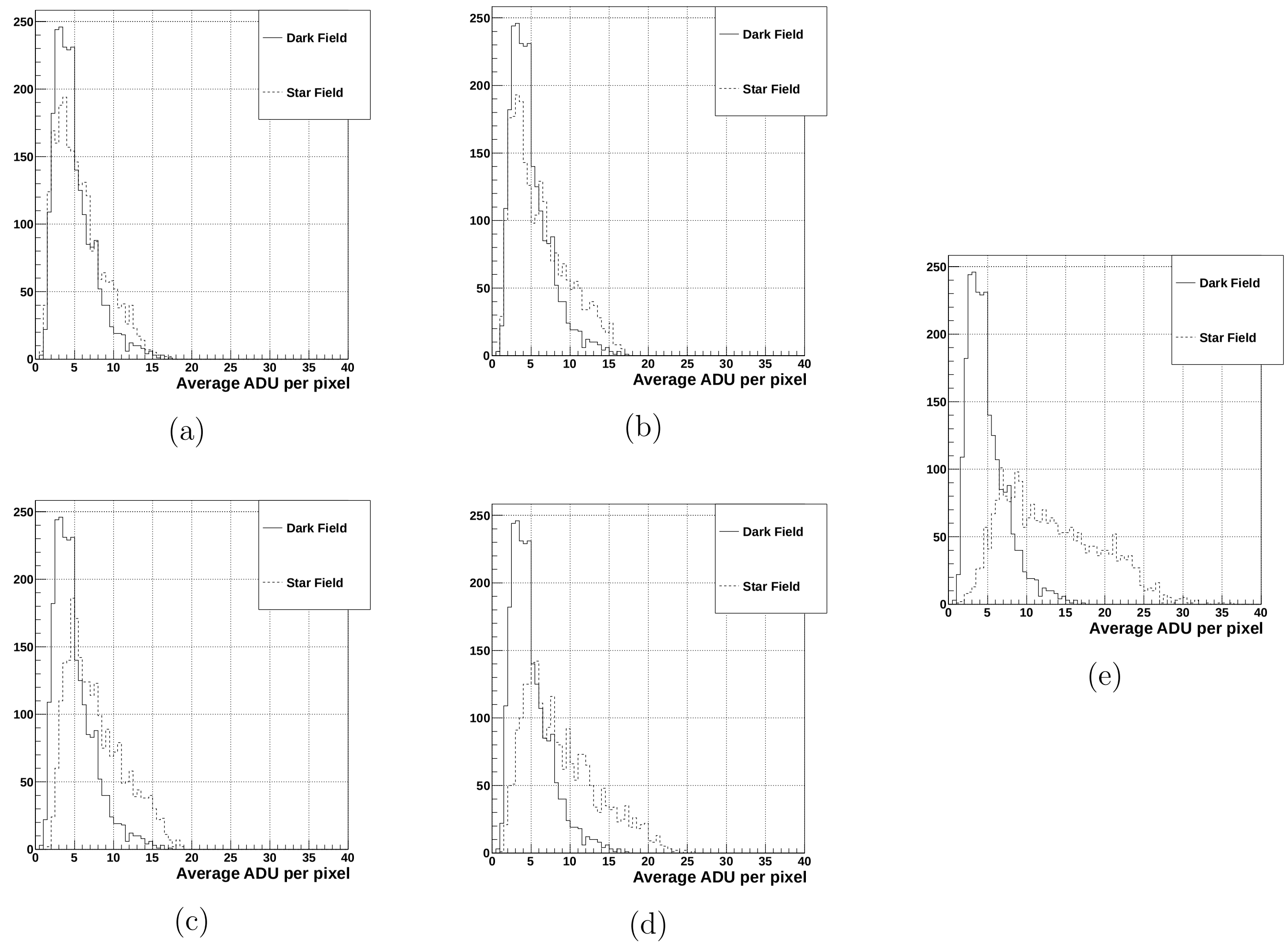

(a) (b) (c) (d) (e)

Figure A.7: Plots of average dark field counts per pixel and average signal counts per pixels from a star field image for just the Blue Channel. Average ADU per pixel from the dark field is denoted by the solid line, while average counts per pixel from the star field image is denoted by the dash line. Counts due to Stars and "hot" dark pixels were removed. All pixels have been taken with the camera settings of 1600 ISO, exposure length of 20 sec and f-stop of (a) 11, (b) 8.0, (c) 6.7, (d) 5.6 and (e) 3.5. The f-stop of 3.5 shows the only evidence of a signal level above the noise, which indicates an ability to measure the NSB.

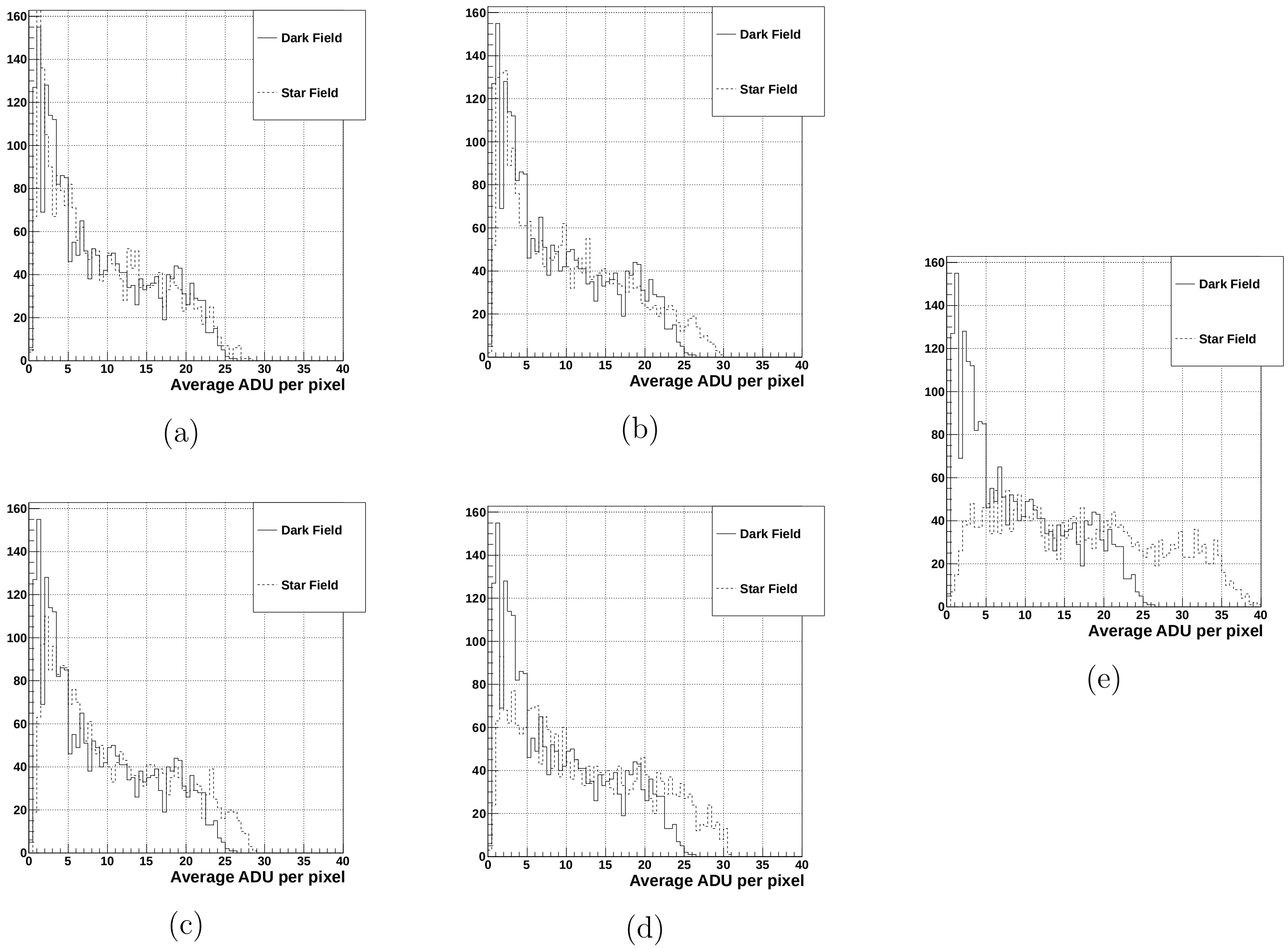

(a)

(b)

(c)

(d)

(e)

Figure A.8: Plots of average dark field counts per pixel and average signal counts per pixels from a star field image for just the Red Channel. Average ADU per pixel from the dark field is denoted by the solid line, while average counts per pixel from the star field image is denoted by the dash line. Counts due to Stars and “hot” dark pixels were removed. All pixels have been taken with the camera settings of 1600 ISO, exposure length of 20 sec and f-stop of (a) 11, (b) 8.0, (c) 6.7, (d) 5.6 and (e) 3.5. The f-stop of 3.5 shows the only evidence of a signal level above the noise, which indicates an ability to measure the NSB.

A.2 Extra Gain Histograms

Shown here are the extra gain plots. The plots show the one-dimensional histograms of all the pixel gains for the red and blue channel. Each figure contains histograms for:

- Red channel, 20 secend exposure, f-stop 8.0 for 400, 800, and 1600 ISO
- Blue channel, 20 secend exposure, f-stop 8.0 for 400, 800, and 1600 ISO
- 400 ISO, 20 second exposure, f-stop 3.5 for red, green, and blue channel

The extra plots are for Chapter 5.2.3.

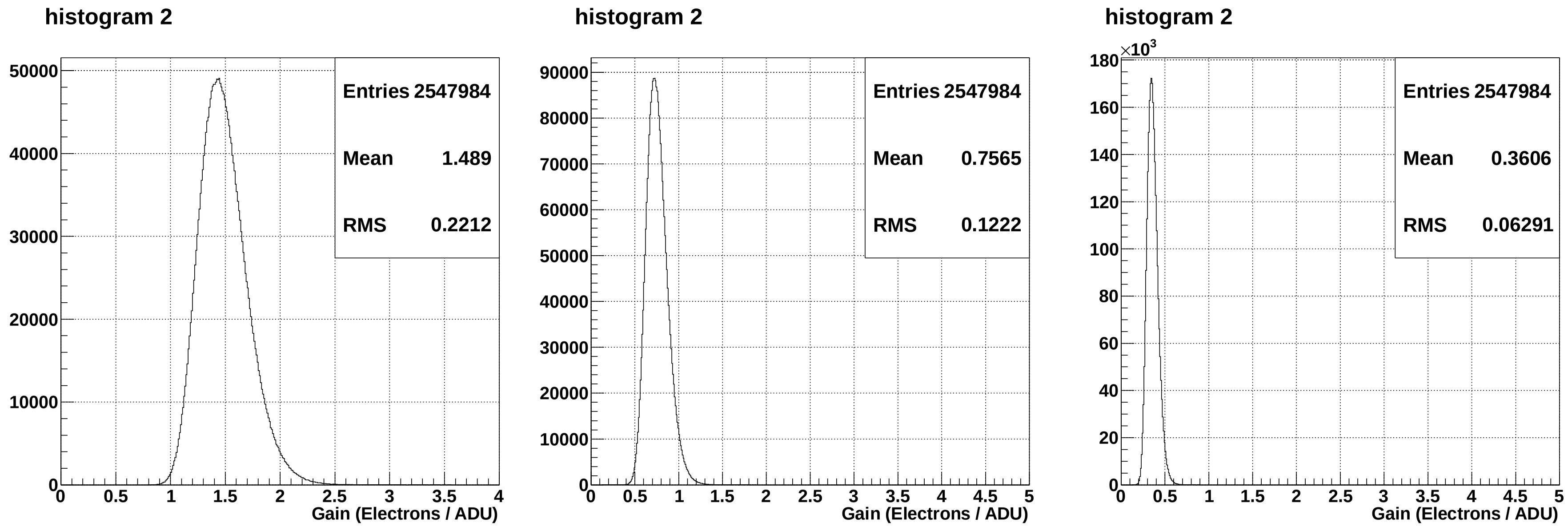

(a) (b) (c)

Figure A.9: Histograms displaying the distribution of gains for all the red pixels within the camera. (a) 400 ISO, (b) 800 ISO, and (c) 1600 ISO. The camera f-stop was set to 8.0. It can be seen that there is a fluctuation in gains which can be attributed to either differences in pixel to pixel gains, or from a lack of statistics when calculating the mean and RMS. Only a 100 images where used to find individual pixel mean and RMS.

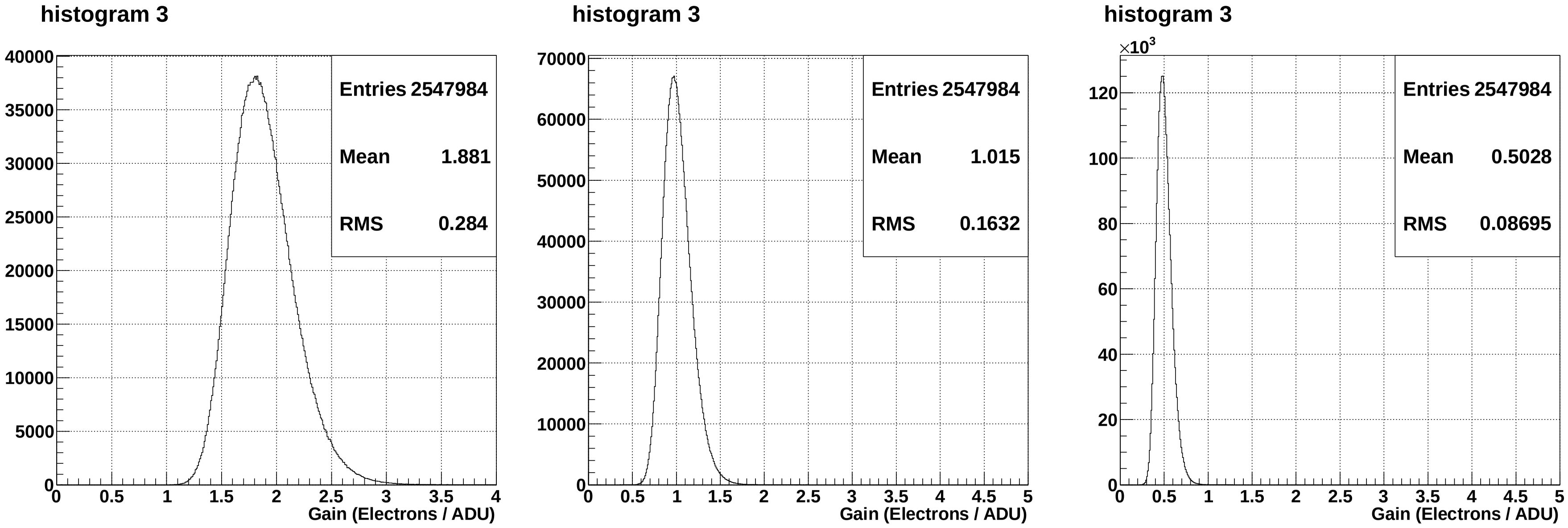

(a) (b) (c)

Figure A.10: Histograms displaying the distribution of gains for all the blue pixels within the camera. (a) 400 ISO, (b) 800 ISO, and (c) 1600 ISO. The camera f-stop was set to 8.0. It can be seen that there is a fluctuation in gains which can be attributed to either differences in pixel to pixel gains, or from a lack of statistics when calculating the mean and RMS. Only a 100 images where used to find individual pixel mean and RMS.

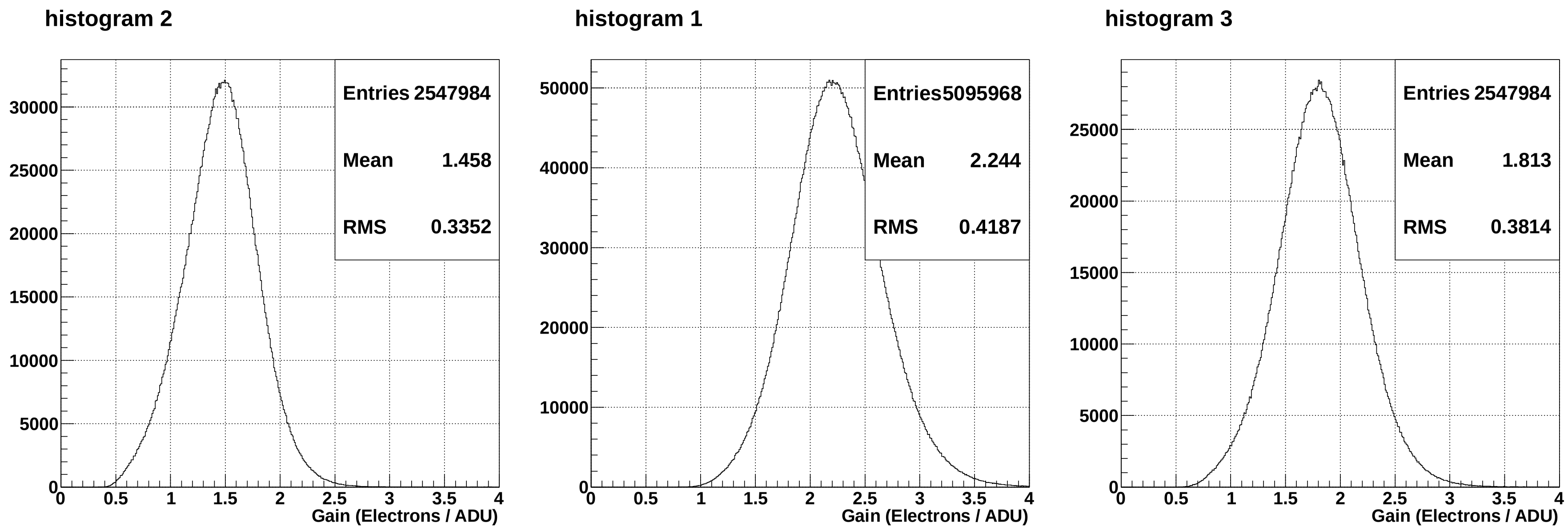

(a) (b) (c)

Figure A.11: Histograms displaying the distribution of gains for all the pixels within the camera. The camera settings used was 400 ISO, f-stop of 3.5. (a) red channel, (b) green channel, and (c) blue channel. It can be seen that there is a fluctuation in gains which can be attributed to either differences in pixel to pixel gains, or from a lack of statistics when calculating the mean and RMS. Only a 100 images where used to find individual pixel mean and RMS.

A.3 Extra Flat-field Plots

Extra flat-field plots for the red and blue channel. The camera setting used was 400 ISO, 20 second exposure length and aperture setting of 3.5. The extra plots are for Chapter 5.2.4.

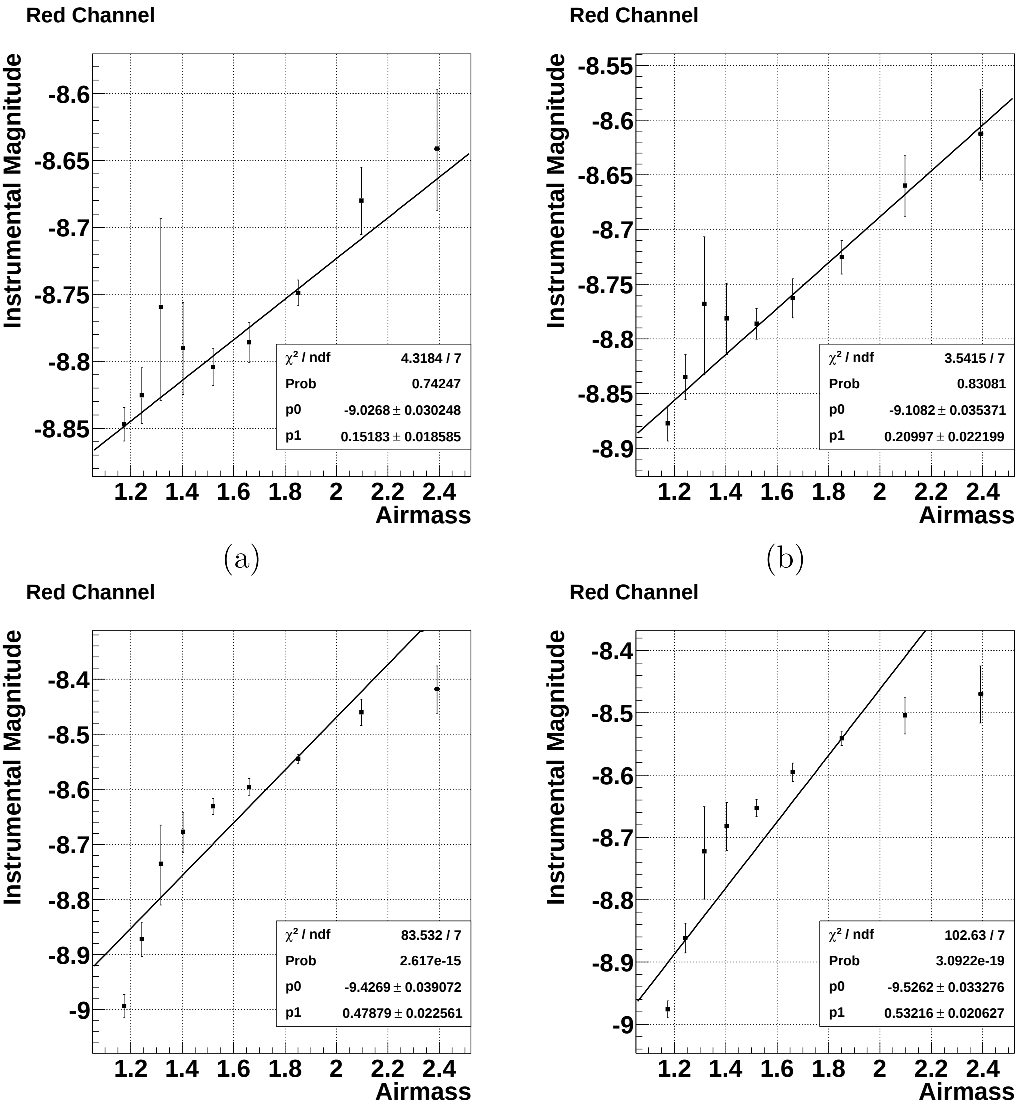

(a) (b)

(c) (d)

Figure A.12: Examples of using flat field produced from different methods on measuring star extinction coefficients. Shown here the instrumental magnitude versus airmass the red channel for a star on the night of the 11/08/2010. The flat fields were produce using (a) the "rotation" method, (b) a single clear sky image, (c) imaging a white project screen, and (d) imaging a white computer screen. The star extinction coefficient is the slope of the fit and is denoted p1 within the fit box. The camera setting used was 400 ISO, 20 second exposure length and aperture setting of 3.5. In each of the plots, more negative the instrumental magnitude is, brighter the object is. For the projector screen and white screen, it can be seen that the camera's vignetting has been over corrected for as the points form an upturned curve instead of the expected straight line.

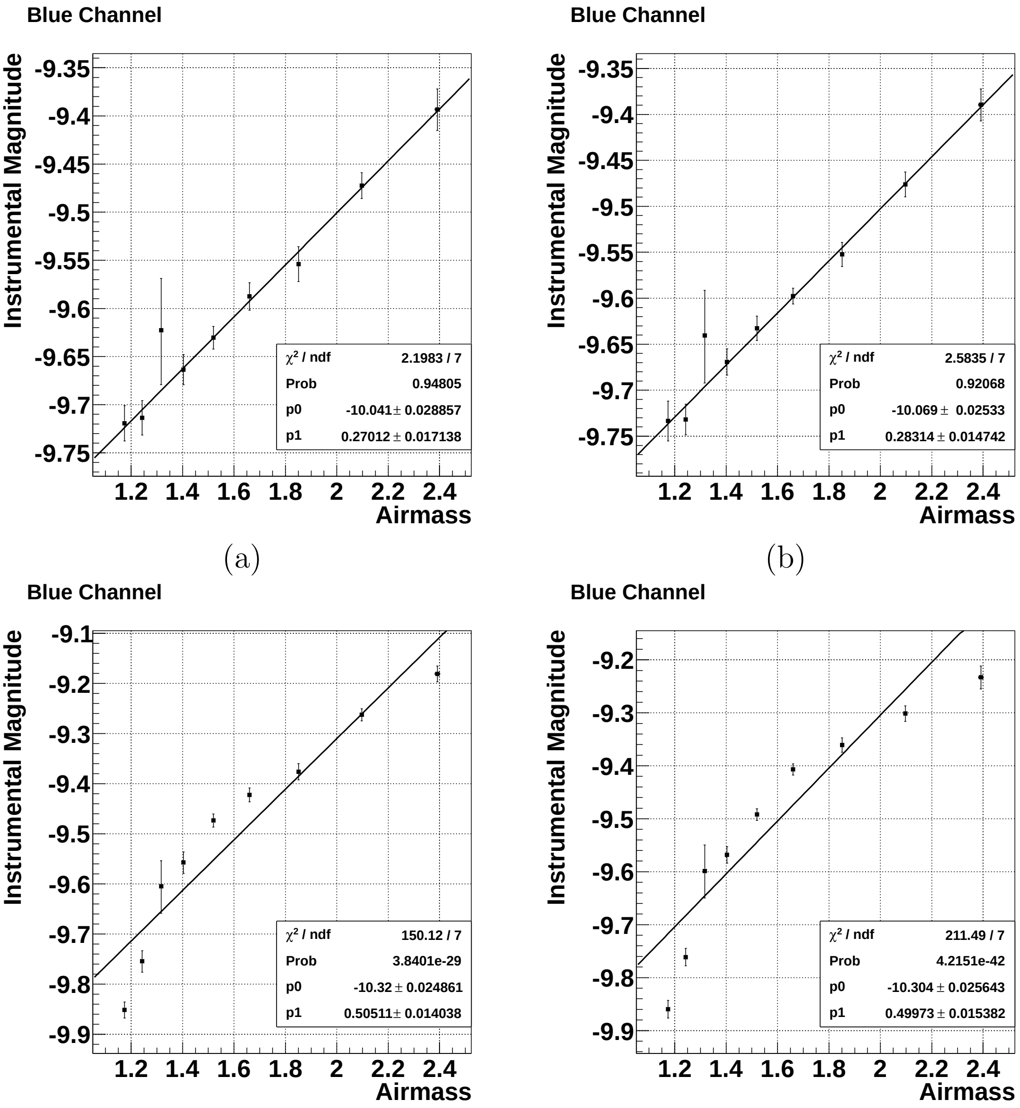

(a) (b)

(c) (d)

Figure A.13: Examples of using flat field produced from different methods on measuring star extinction coefficients. Shown here the instrumental magnitude versus airmass the blue channel for a star on the night of the 11/08/2010. The flat fields were produce using (a) the "rotation" method, (b) a single clear sky image, (c) imaging a white project screen, and (d) imaging a white computer screen. The star extinction coefficient is the slope of the fit and is denoted p1 within the fit box. The camera setting used was 400 ISO, 20 second exposure length and aperture setting of 3.5. In each of the plots, more negative the instrumental magnitude is, brighter the object is. For the projector screen and white screen, it can be seen that the camera's vignetting has been over corrected for as the points form an upturned curve instead of the expected straight line.

Appendix B

Star Extinction Coefficient Plots

Here are all the star extinction plots for the data shown in Chapter 6.2. The star extinction coefficient plots are shown for all of the nights that data was taken from Fowlers Gap.

B.1 15/02/2010: Southern Cross

Star extinction coefficient plots shown here for the camera settings of f-stop 8.0, and ISO setting of 400 and 800. Each plot is fitted with the linear line in the form of y = p1 × x + p0, where p1 is the extinction coefficient, x is the airmass, and p0 is the instrumental magnitude the Pentax camera would observe if no atmosphere was present. Order of the figures is:

Star Name	**ISO Setting**	**Channel**		
		Red	**Green**	**Blue**
γ - Centauri	400	√	√	√
δ - Centauri	400	√		√
γ - Crucis	400	√		√
δ - Crucis	400			√
ε - Crucis	400	√	√	
β - Crucis	400			√
β - Centauri	400	√	√	
α - Centauri	400	√		
γ - Trianguli Australis	400	√		
β - Trianguli Australis	400	√		√
α - Trianguli Australis	400	√		√
γ - Centauri	800	√		√
δ - Centauri	800	√	√	√
δ - Crucis	800	√	√	√
ε - Crucis	800	√	√	√
β - Crucis	800	√		
γ - Trianguli Australis	800	√	√	√
β - Trianguli Australis	800			√

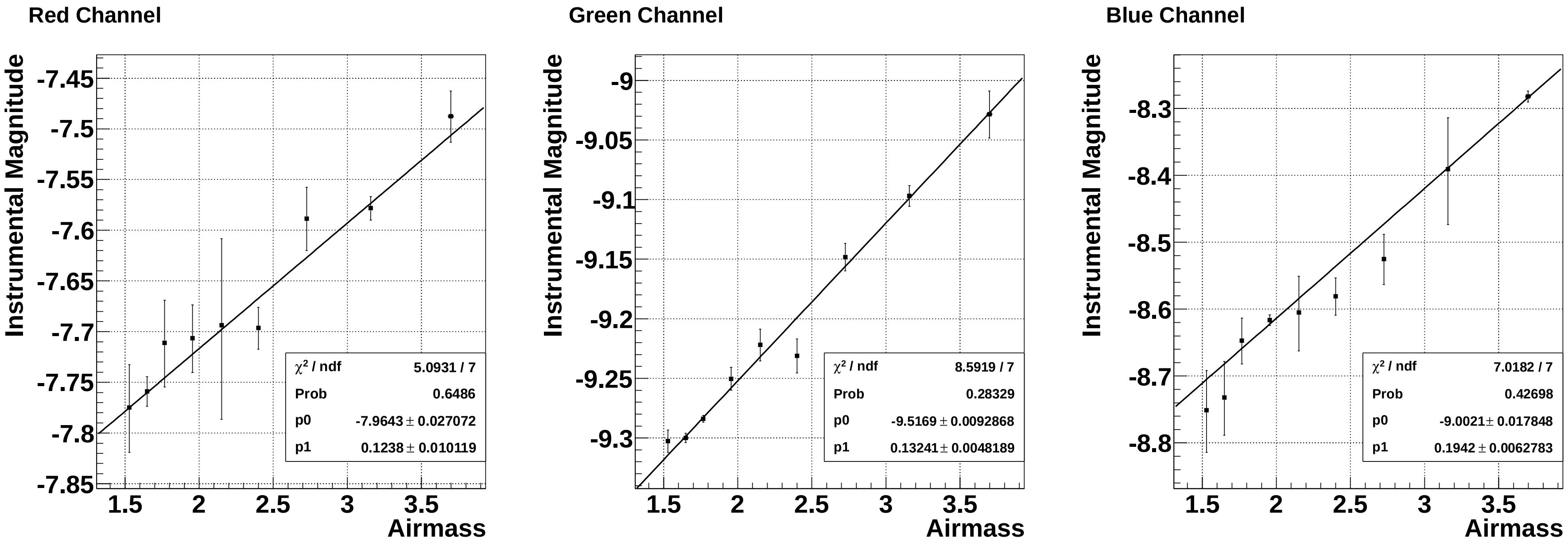

Figure B.1: Star extinction coefficient plots for γ - Centauri. Images used in plots were taken on the 15-02-2010 with camera settings of 400 ISO, f-stop of 8.0 and exposure length of 20 seconds. The variable p1 is the value for the star extinction coefficient, where p0 is the instrumental magnitude that the Pentax camera would observe if no atmosphere was present.

Figure B.2: Star extinction coefficient plots for δ - Centauri. Images used in plot were taken on the 15-02-2010 with camera settings of 400 ISO, f-stop of 8.0 and exposure length of 20 seconds. The variable p1 is the value for the star extinction coefficient, where p0 is the instrumental magnitude that the Pentax camera would observe if no atmosphere was present.

Figure B.3: Star extinction coefficient plots for γ - Crucis. Images used in plots were taken on the 15-02-2010 with camera settings of 400 ISO, f-stop of 8.0 and exposure length of 20 seconds. The variable p1 is the value for the star extinction coefficient, where p0 is the instrumental magnitude that the Pentax camera would observe if no atmosphere was present.

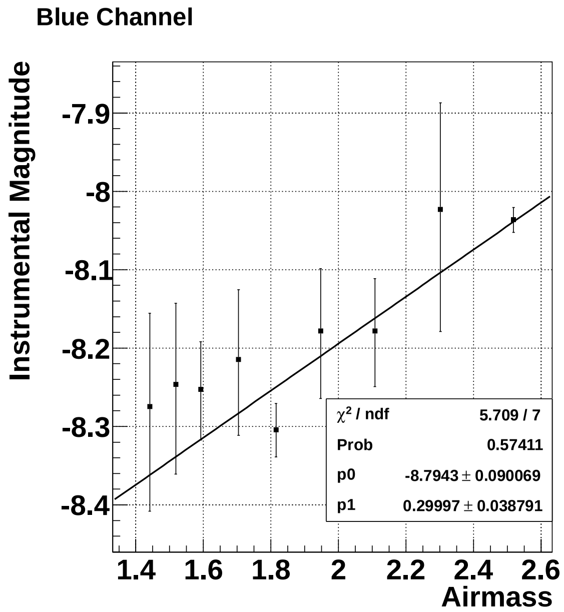

Figure B.4: Star extinction coefficient plot for δ - Crucis. Images used in plot were taken on the 15-02-2010 with camera settings of 400 ISO, f-stop of 8.0 and exposure length of 20 seconds. The variable p1 is the value for the star extinction coefficient, where p0 is the instrumental magnitude that the Pentax camera would observe if no atmosphere was present.

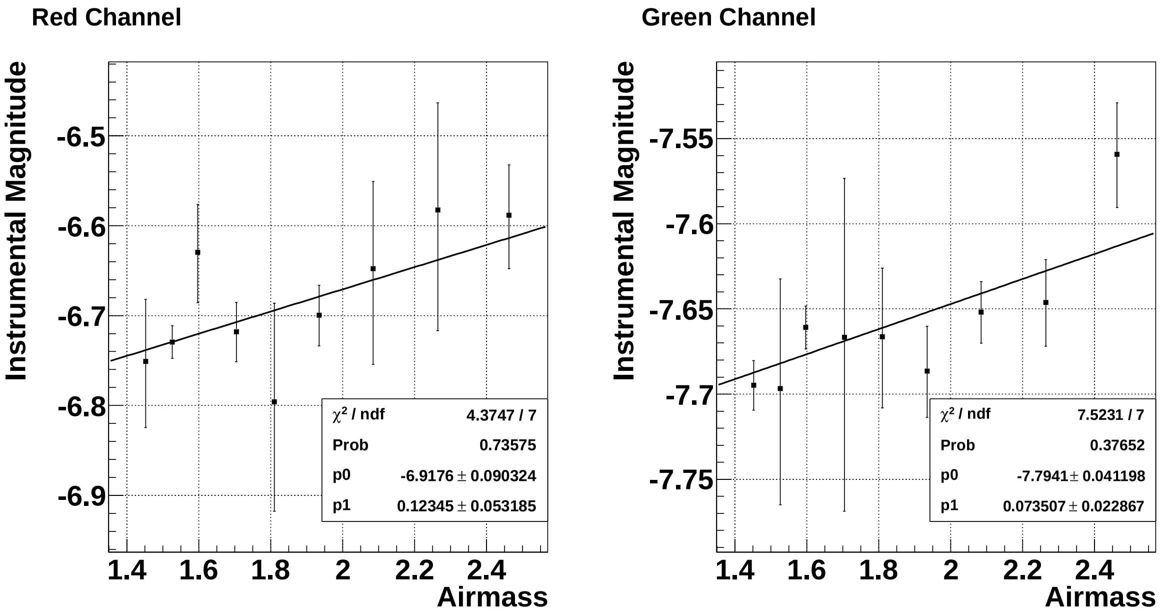

Figure B.5: Star extinction coefficient plots for ε - Crucis. Images used in plots were taken on the 15-02-2010 with camera settings of 400 ISO, f-stop of 8.0 and exposure length of 20 seconds. The variable p1 is the value for the star extinction coefficient, where p0 is the instrumental magnitude that the Pentax camera would observe if no atmosphere was present.

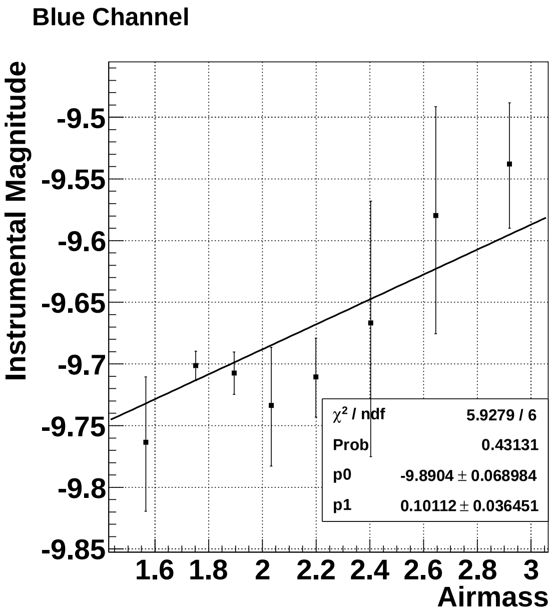

Figure B.6: Star extinction coefficient plot for β - Crucis. Images used in plot were taken on the 15-02-2010 with camera settings of 400 ISO, f-stop of 8.0 and exposure length of 20 seconds. The variable p1 is the value for the star extinction coefficient, where p0 is the instrumental magnitude that the Pentax camera would observe if no atmosphere was present.

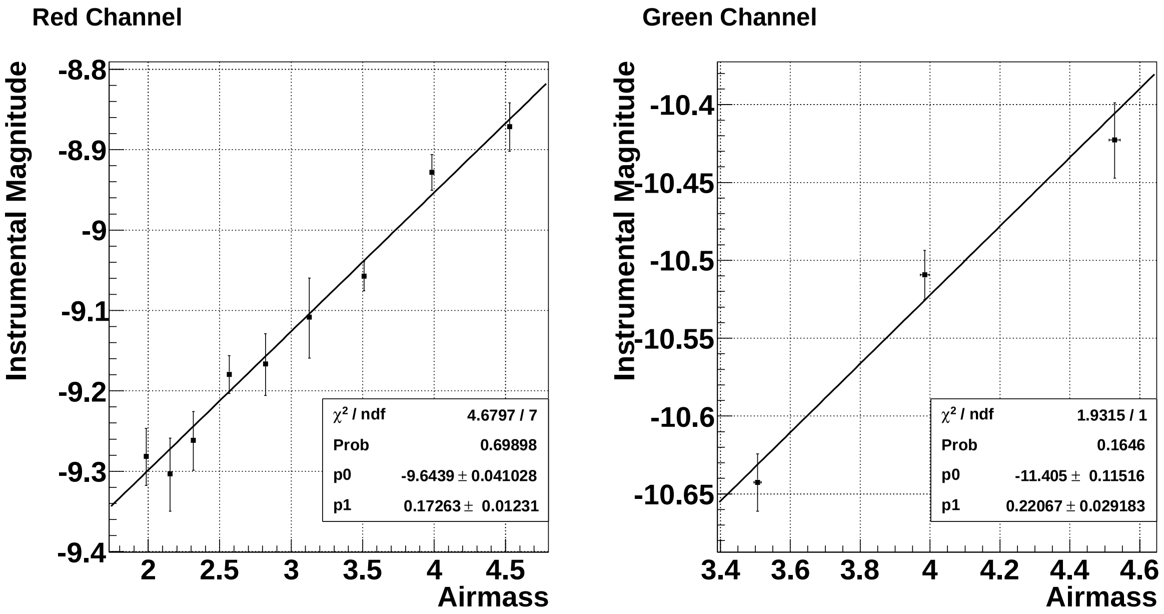

Figure B.7: Star extinction coefficient plots for β - Centauri. Images used in plots were taken on the 15-02-2010 with camera settings of 400 ISO, f-stop of 8.0 and exposure length of 20 seconds. The variable p1 is the value for the star extinction coefficient, where p0 is the instrumental magnitude that the Pentax camera would observe if no atmosphere was present.

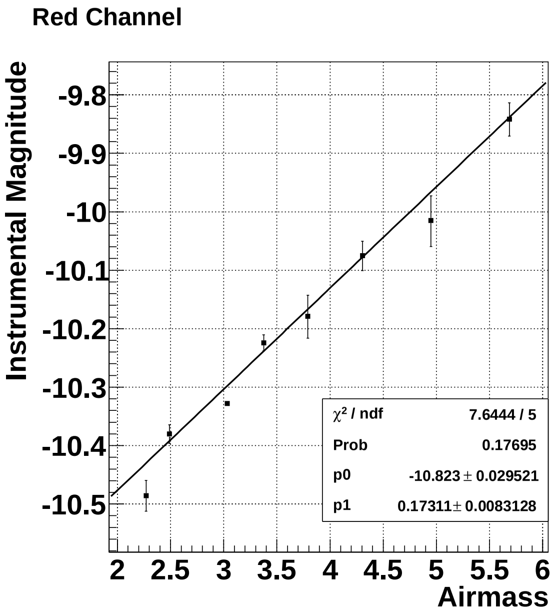

Figure B.8: Star extinction coefficient plots for α - Centauri. Images used in plots were taken on the 15-02-2010 with camera settings of 400 ISO, f-stop of 8.0 and exposure length of 20 seconds. The variable p1 is the value for the star extinction coefficient, where p0 is the instrumental magnitude that the Pentax camera would observe if no atmosphere was present.

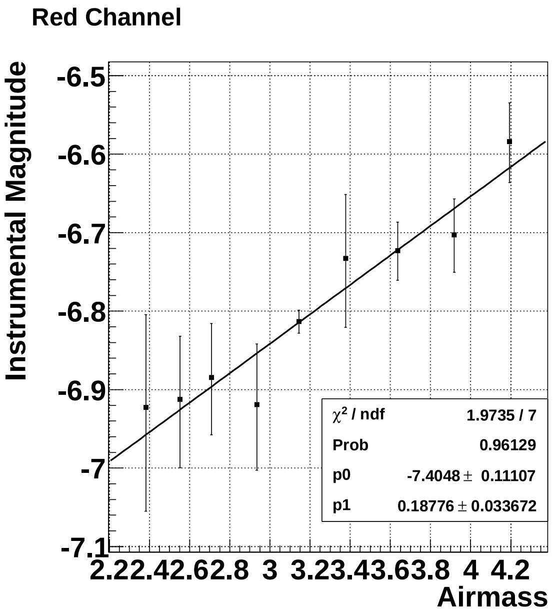

Figure B.9: Star extinction coefficient plots for γ - Trianguli Australis. Images used in plots were taken on the 15-02-2010 with camera settings of 400 ISO, f-stop of 8.0 and exposure length of 20 seconds. The variable p1 is the value for the star extinction coefficient, where p0 is the instrumental magnitude that the Pentax camera would observe if no atmosphere was present.

Figure B.10: Star extinction coefficient plots for β - Trianguli Australis. Images used in plots were taken on the 15-02-2010 with camera settings of 400 ISO, f-stop of 8.0 and exposure length of 20 seconds. The variable p1 is the value for the star extinction coefficient, where p0 is the instrumental magnitude that the Pentax camera would observe if no atmosphere was present.

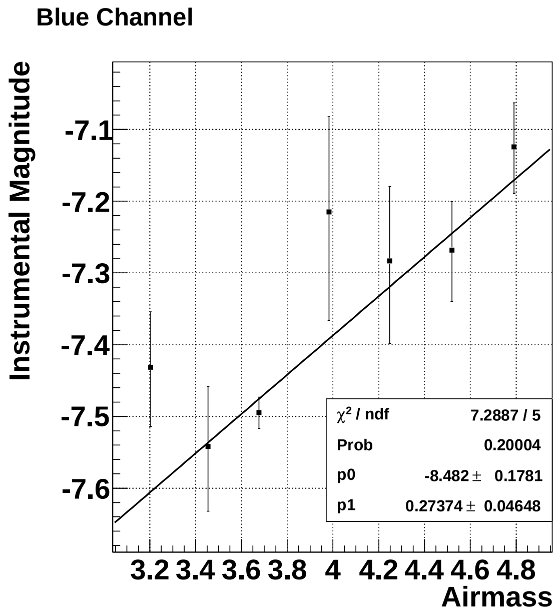

Figure B.11: Star extinction coefficient plots for α - Trianguli Australis. Images used in plots were taken on the 15-02-2010 with camera settings of 400 ISO, f-stop of 8.0 and exposure length of 20 seconds. The variable p1 is the value for the star extinction coefficient, where p0 is the instrumental magnitude that the Pentax camera would observe if no atmosphere was present.

Figure B.12: Star extinction coefficient plots for γ - Centauri. Images used in plots were taken on the 15-02-2010 with camera settings of 800 ISO, f-stop of 8.0 and exposure length of 20 seconds. The variable p1 is the value for the star extinction coefficient, where p0 is the instrumental magnitude that the Pentax camera would observe if no atmosphere was present.

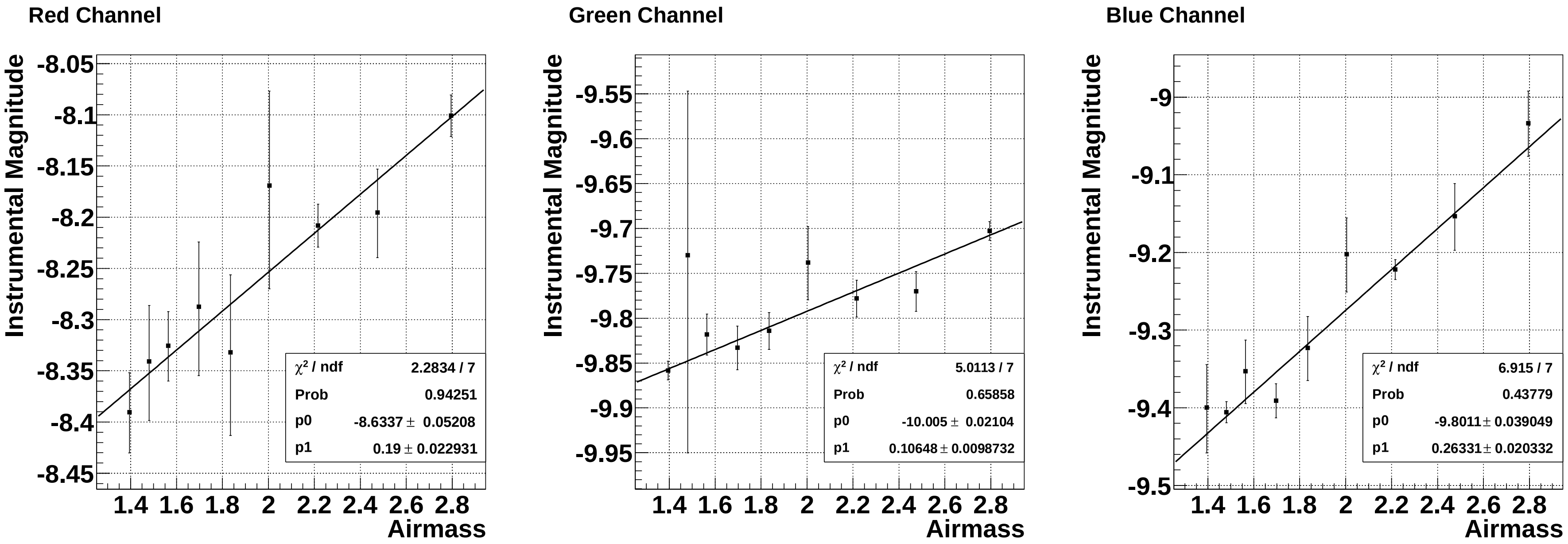

Figure B.13: Star extinction coefficient plots for δ - Centauri. Images used in plots were taken on the 15-02-2010 with camera settings of 800 ISO, f-stop of 8.0 and exposure length of 20 seconds. The variable p1 is the value for the star extinction coefficient, where p0 is the instrumental magnitude that the Pentax camera would observe if no atmosphere was present.

Figure B.14: Star extinction coefficient plots for γ - Crucis. Images used in plots were taken on the 15-02-2010 with camera settings of 800 ISO, f-stop of 8.0 and exposure length of 20 seconds. The variable p1 is the value for the star extinction coefficient, where p0 is the instrumental magnitude that the Pentax camera would observe if no atmosphere was present.

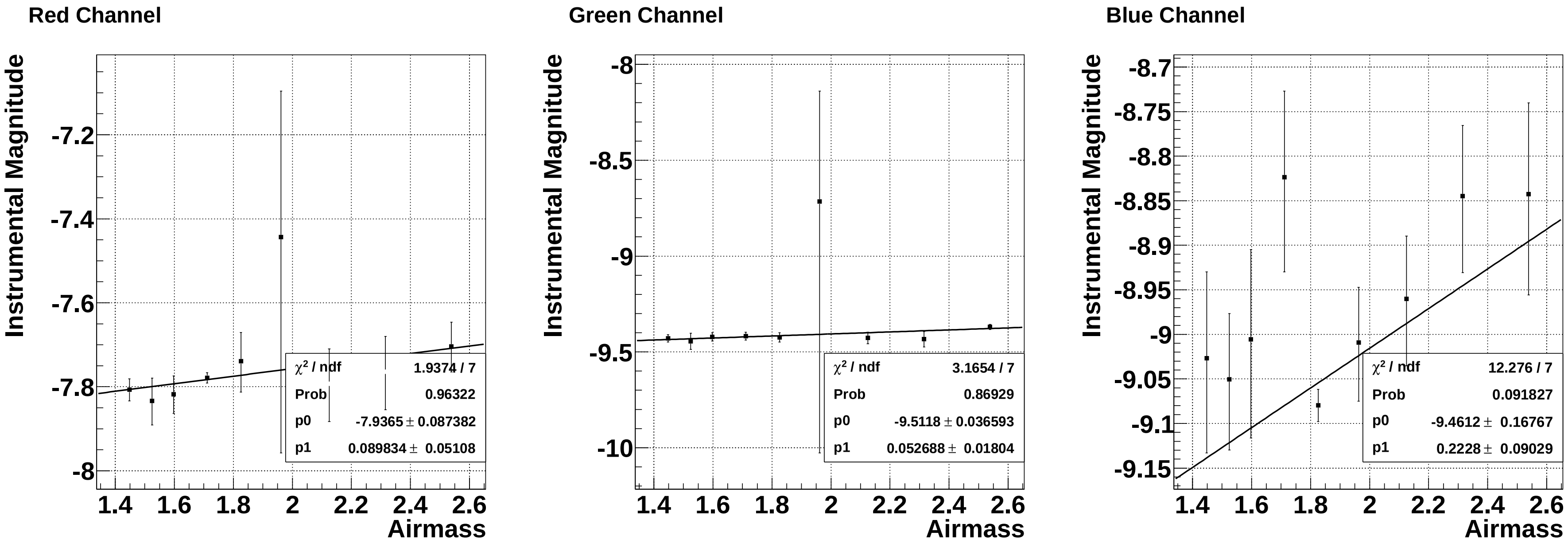

Figure B.15: Star extinction coefficient plots for δ - Crucis. Images used in plots were taken on the 15-02-2010 with camera settings of 800 ISO, f-stop of 8.0 and exposure length of 20 seconds. The variable p1 is the value for the star extinction coefficient, where p0 is the instrumental magnitude that the Pentax camera would observe if no atmosphere was present.

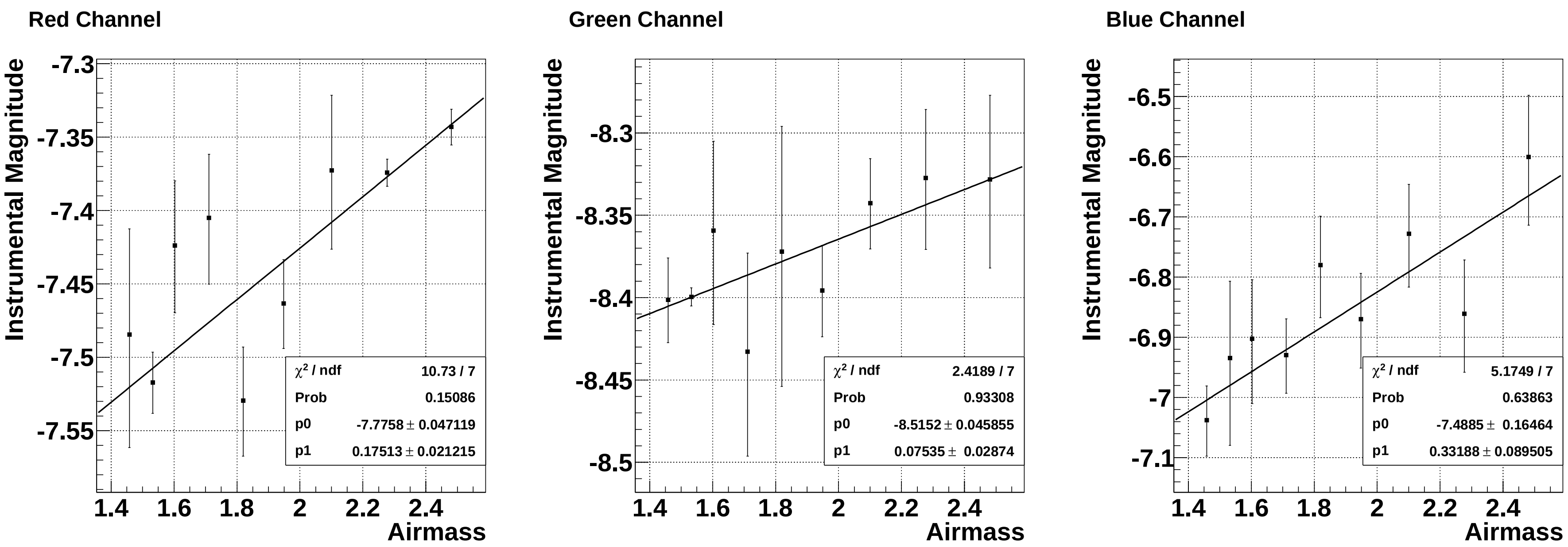

Figure B.16: Star extinction coefficient plots for ε - Crucis. Images used in plots were taken on the 15-02-2010 with camera settings of 800 ISO, f-stop of 8.0 and exposure length of 20 seconds. The variable p1 is the value for the star extinction coefficient, where p0 is the instrumental magnitude that the Pentax camera would observe if no atmosphere was present.

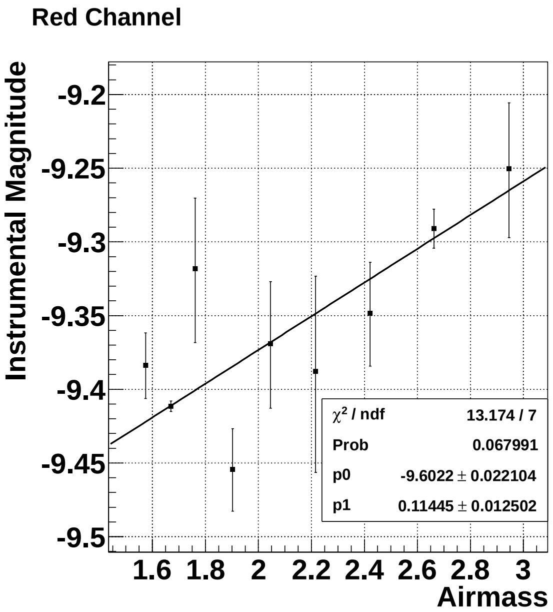

Figure B.17: Star extinction coefficient plots for β - Crucis. Images used in plots were taken on the 15-02-2010 with camera settings of 800 ISO, f-stop of 8.0 and exposure length of 20 seconds. The variable p1 is the value for the star extinction coefficient, where p0 is the instrumental magnitude that the Pentax camera would observe if no atmosphere was present.

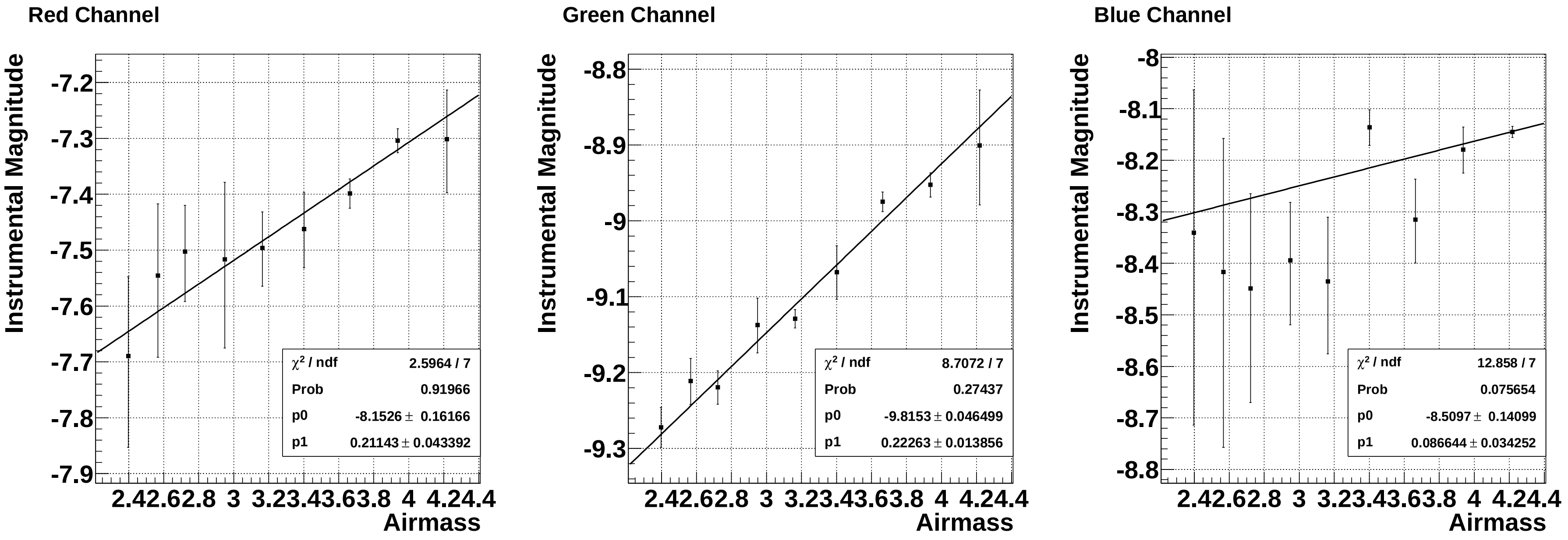

Figure B.18: Star extinction coefficient plots for γ - Trianguli Australis. Images used in plots were taken on the 15-02-2010 with camera settings of 800 ISO, f-stop of 8.0 and exposure length of 20 seconds. The variable p1 is the value for the star extinction coefficient, where p0 is the instrumental magnitude that the Pentax camera would observe if no atmosphere was present.

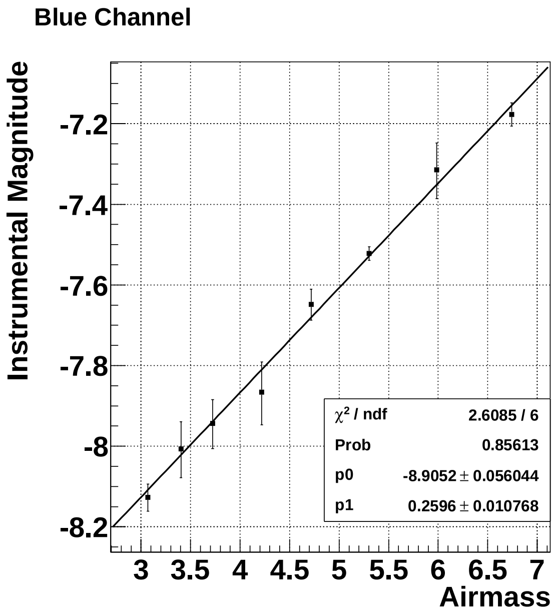

Figure B.19: Star extinction coefficient plots for β - Trianguli Australis. Images used in plots were taken on the 15-02-2010 with camera settings of 800 ISO, f-stop of 8.0 and exposure length of 20 seconds. The variable p1 is the value for the star extinction coefficient, where p0 is the instrumental magnitude that the Pentax camera would observe if no atmosphere was present.

B.2 11/08/2010: Scorpio

Star extinction coefficient plots shown here for the camera settings of 400 ISO, exposure length of 20 seconds, and f-stop settings of 3.5 and 8.0. Each plot is fitted with the linear line in the form of y = p1 × x + p0, where p1 is the extinction coefficient, x is the airmass, and p0 is the instrumental magnitude the Pentax camera would observe if no atmosphere was present. Order of the figures is:

Star Name	**f-stop Setting**	**Channel**		
		Red	**Green**	**Blue**
σ - Scorpio	8.0	√		√
ρ - Scorpio	8.0			√
π - Scorpio	8.0	√		
α - Scorpio	3.5			√
σ - Scorpio	3.5	√	√	√
ρ - Scorpio	3.5	√	√	√
π - Scorpio	3.5	√		√
δ - Scorpio	3.5		√	
β - Scorpio	3.5	√	√	√

Figure B.20: Star extinction coefficient plots for σ - Scorpio. Images used in plots were taken on the 11-08-2010 with camera settings of 400 ISO, f-stop of 8.0 and exposure length of 20 seconds. The variable p1 is the value for the star extinction coefficient, where p0 is the instrumental magnitude that the Pentax camera would observe if no atmosphere was present.

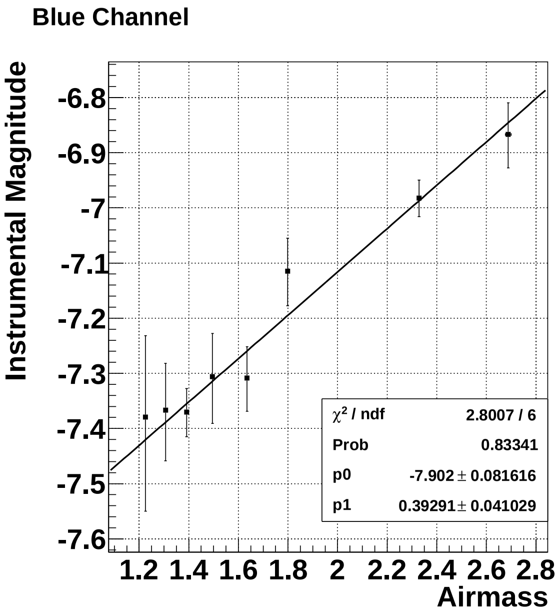

Figure B.21: Star extinction coefficient plots for ρ - Scorpio. Images used in plots were taken on the 11-08-2010 with camera settings of 400 ISO, f-stop of 8.0 and exposure length of 20 seconds. The variable p1 is the value for the star extinction coefficient, where p0 is the instrumental magnitude that the Pentax camera would observe if no atmosphere was present.

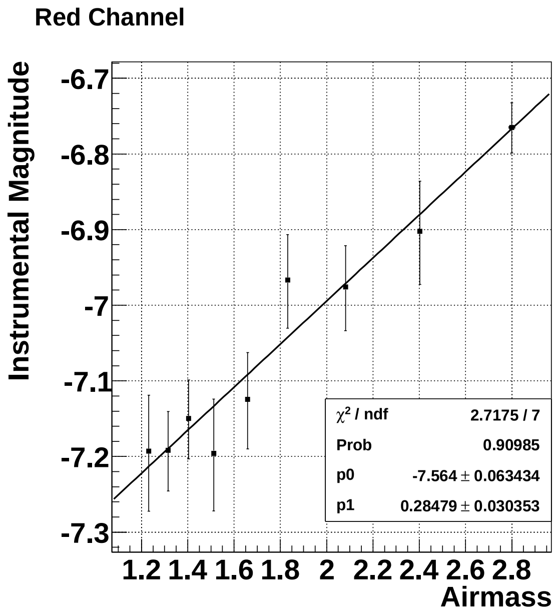

Figure B.22: Star extinction coefficient plots for π - Scorpio. Images used in plots were taken on the 11-08-2010 with camera settings of 400 ISO, f-stop of 8.0 and exposure length of 20 seconds. The variable p1 is the value for the star extinction coefficient, where p0 is the instrumental magnitude that the Pentax camera would observe if no atmosphere was present.

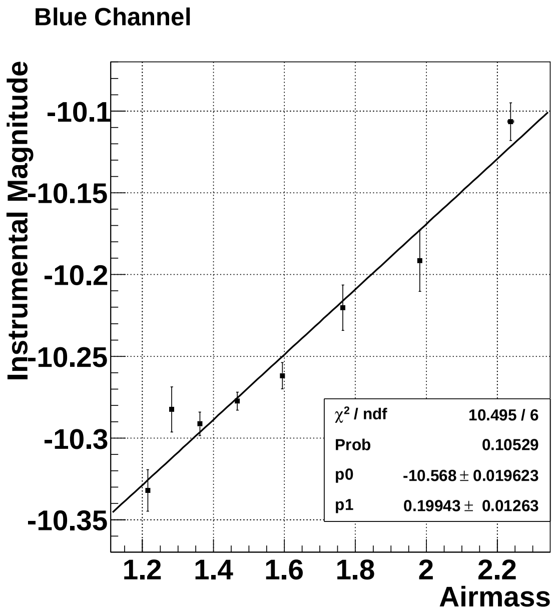

Figure B.23: Star extinction coefficient plots for α - Scorpio. Images used in plots were taken on the 11-08-2010 with camera settings of 400 ISO, f-stop of 3.5 and exposure length of 20 seconds. The variable p1 is the value for the star extinction coefficient, where p0 is the instrumental magnitude that the Pentax camera would observe if no atmosphere was present.

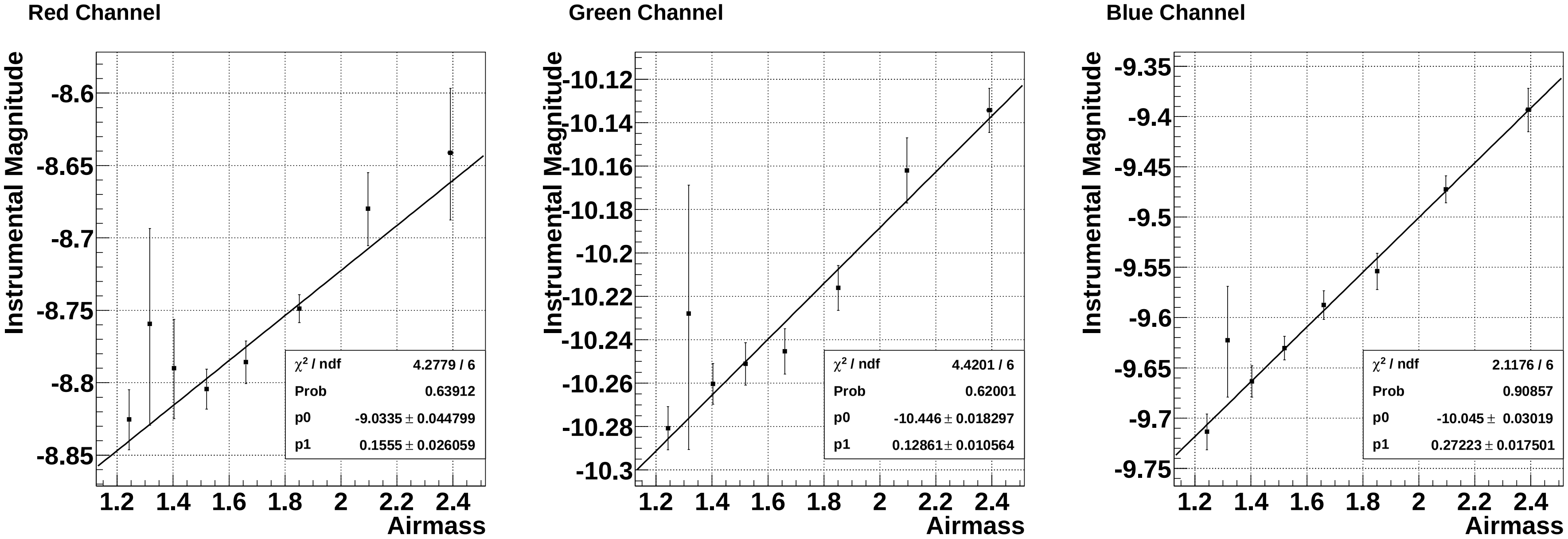

Figure B.24: Star extinction coefficient plots for σ - Scorpio. Images used in plots were taken on the 11-08-2010 with camera settings of 400 ISO, f-stop of 3.5 and exposure length of 20 seconds. The variable p1 is the value for the star extinction coefficient, where p0 is the instrumental magnitude that the Pentax camera would observe if no atmosphere was present.

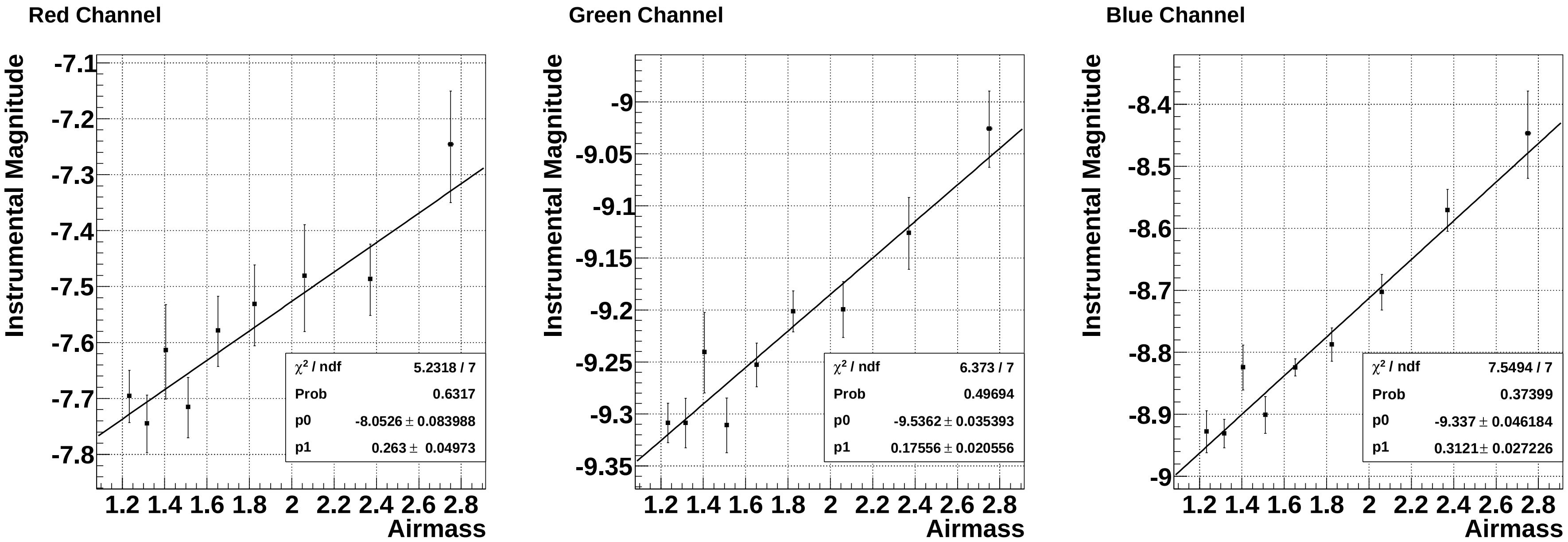

Figure B.25: Star extinction coefficient plots for ρ - Scorpio. Images used in plots were taken on the 11-08-2010 with camera settings of 400 ISO, f-stop of 3.5 and exposure length of 20 seconds. The variable p1 is the value for the star extinction coefficient, where p0 is the instrumental magnitude that the Pentax camera would observe if no atmosphere was present.

Figure B.26: Star extinction coefficient plots for π - Scorpio. Images used in plots were taken on the 11-08-2010 with camera settings of 400 ISO, f-stop of 3.5 and exposure length of 20 seconds. The variable p1 is the value for the star extinction coefficient, where p0 is the instrumental magnitude that the Pentax camera would observe if no atmosphere was present.

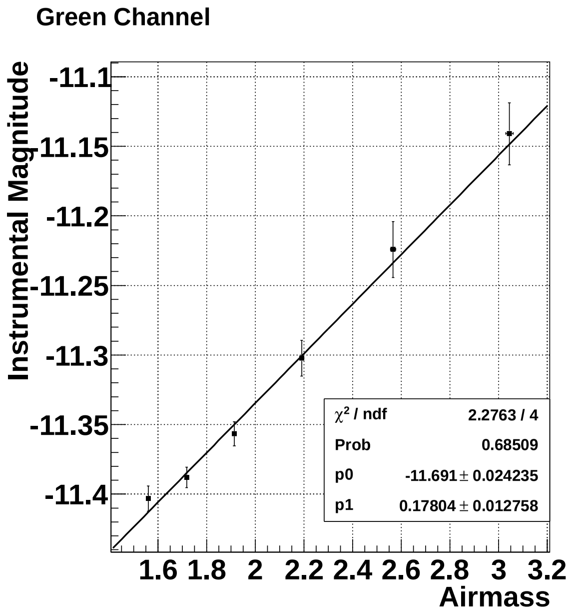

Figure B.27: Star extinction coefficient plots for δ - Scorpio. Images used in plots were taken on the 11-08-2010 with camera settings of 400 ISO, f-stop of 3.5 and exposure length of 20 seconds. The variable p1 is the value for the star extinction coefficient, where p0 is the instrumental magnitude that the Pentax camera would observe if no atmosphere was present.

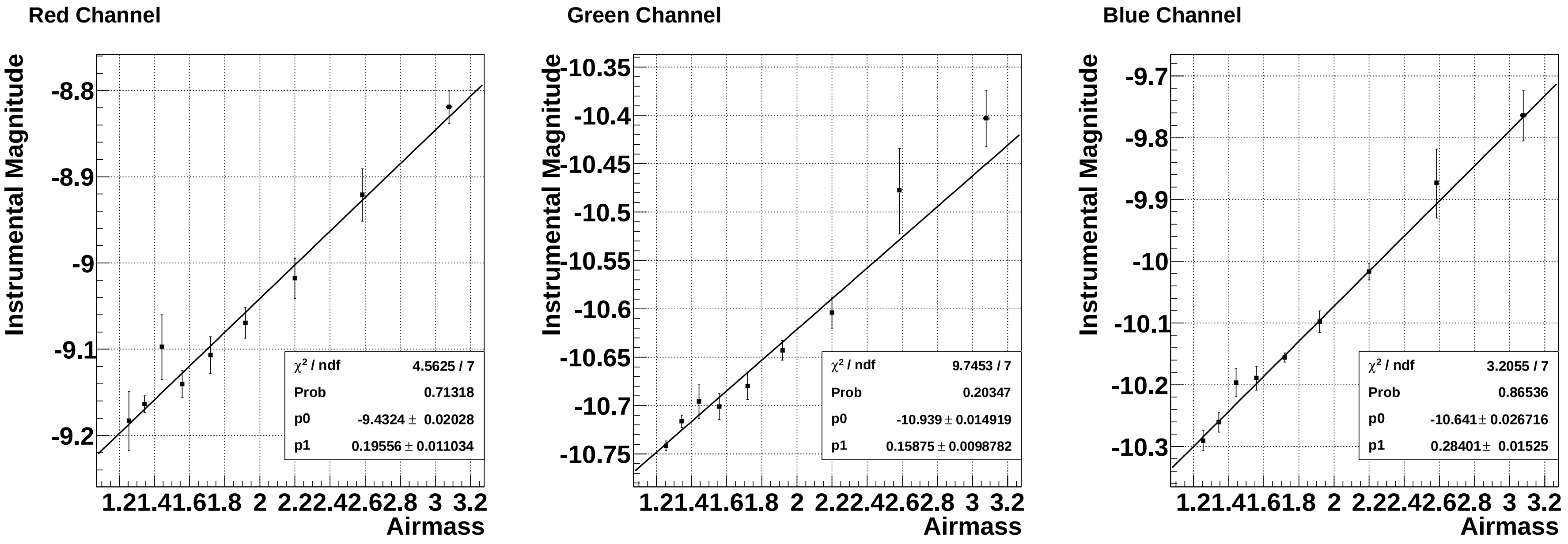

Figure B.28: Star extinction coefficient plots for β - Scorpio. Images used in plots were taken on the 11-08-2010 with camera settings of 400 ISO, f-stop of 3.5 and exposure length of 20 seconds. The variable p1 is the value for the star extinction coefficient, where p0 is the instrumental magnitude that the Pentax camera would observe if no atmosphere was present.

B.3 13/12/2010: Southern Cross

Star extinction coefficient plots shown here for the camera settings of 1600 ISO, exposure length of 20 seconds, and f-stop settings of 8.0. Each plot is fitted with the linear line in the form of y = p1 × x + p0, where p1 is the extinction coefficient, x is the airmass, and p0 is the instrumental magnitude the Pentax camera would observe if no atmosphere was present. Order of the figures is:

Star Name	**ISO Setting**	**Channel**		
		Red	**Green**	**Blue**
γ - Trianguli Australis	1600	√	√	√
α - Circinus	1600	√	√	√
α - Centauri	1600			√
β - Centauri	1600	√		√
β - Crucis	1600	√		√
α - Crucis	1600	√		
ε - Crucis	1600	√	√	
δ - Crucis	1600	√		√
γ - Crucis	1600	√	√	√
δ - Centauri	1600	√	√	√

The images taken to produce the star extinction coefficient were taken while the moon was setting. Therefore for a proportion of the images, the moon was above the horizon but not within the field of view of the camera.

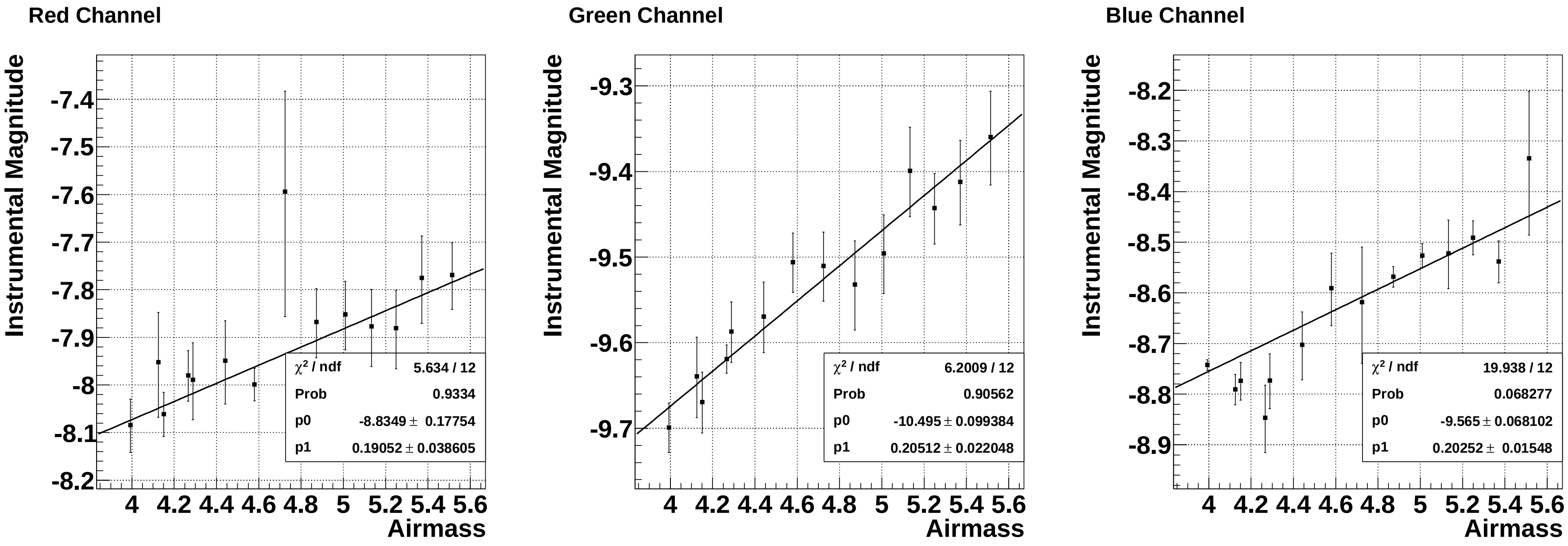

Figure B.29: Star extinction coefficient plots for γ - Trianguli Australis. Images used in plots were taken on the 13-12-2010 with camera settings of 1600 ISO, f-stop of 8.0 and exposure length of 20 seconds. The variable p1 is the value for the star extinction coefficient, where p0 is the instrumental magnitude that the Pentax camera would observe if no atmosphere was present. For a proportion of images, the moon was above the horizon but not within the field of view of the camera.

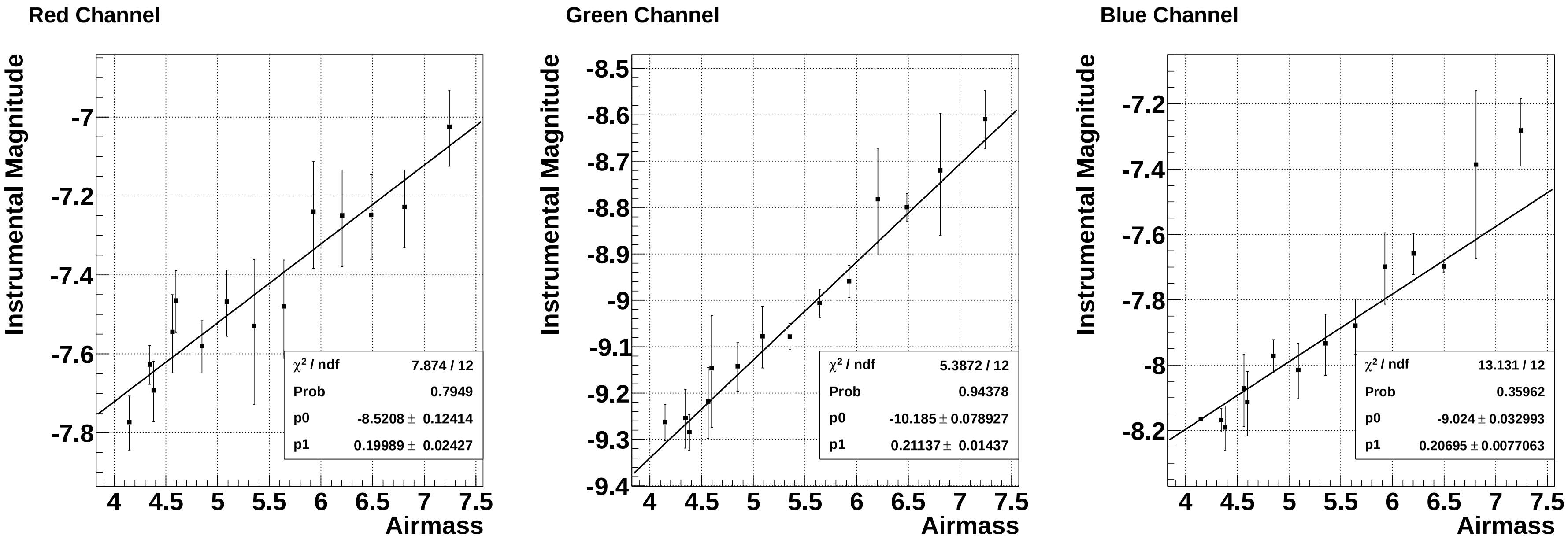

Figure B.30: Star extinction coefficient plots for α - Circinus. Images used in plots were taken on the 13-12-2010 with camera settings of 1600 ISO, f-stop of 8.0 and exposure length of 20 seconds. The variable p1 is the value for the star extinction coefficient, where p0 is the instrumental magnitude that the Pentax camera would observe if no atmosphere was present. For a proportion of images, the moon was above the horizon but not within the field of view of the camera.

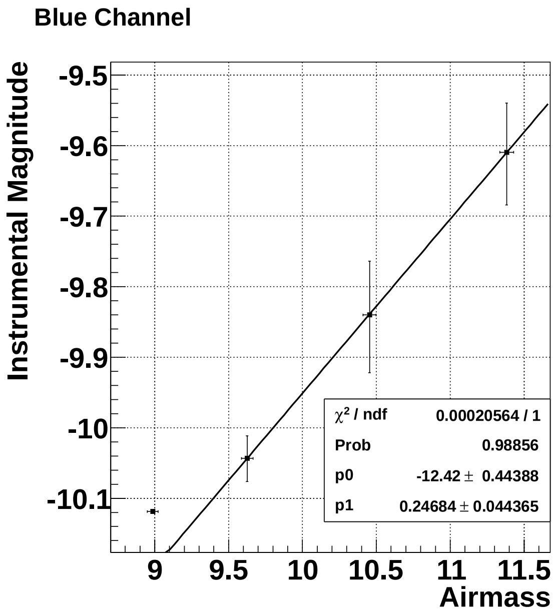

Figure B.31: Star extinction coefficient plots for α - Centauri. Images used in plots were taken on the 13-12-2010 with camera settings of 1600 ISO, f-stop of 8.0 and exposure length of 20 seconds. The variable p1 is the value for the star extinction coefficient, where p0 is the instrumental magnitude that the Pentax camera would observe if no atmosphere was present. For a proportion of images, the moon was above the horizon but not within the field of view of the camera.

Figure B.32: Star extinction coefficient plots for β - Centauri. Images used in plots were taken on the 13-12-2010 with camera settings of 1600 ISO, f-stop of 8.0 and exposure length of 20 seconds. The variable p1 is the value for the star extinction coefficient, where p0 is the instrumental magnitude that the Pentax camera would observe if no atmosphere was present. For a proportion of images, the moon was above the horizon but not within the field of view of the camera.

Figure B.33: Star extinction coefficient plots for β - Crucis. Images used in plots were taken on the 13-12-2010 with camera settings of 1600 ISO, f-stop of 8.0 and exposure length of 20 seconds. The variable p1 is the value for the star extinction coefficient, where p0 is the instrumental magnitude that the Pentax camera would observe if no atmosphere was present. For a proportion of images, the moon was above the horizon but not within the field of view of the camera.

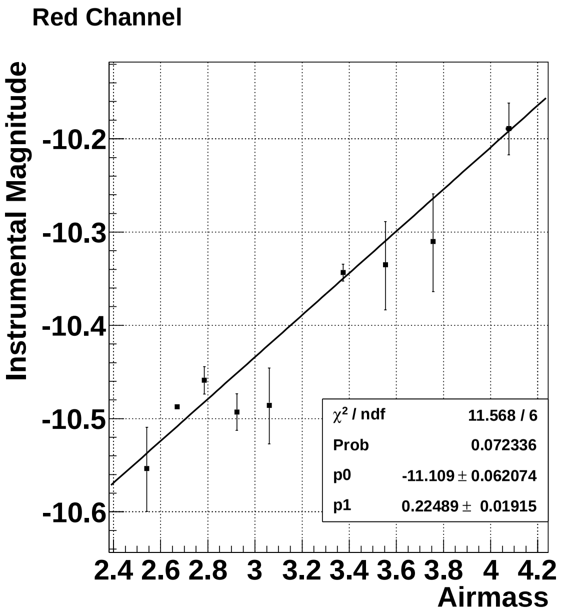

Figure B.34: Star extinction coefficient plots for α - Crucis. Images used in plots were taken on the 13-12-2010 with camera settings of 1600 ISO, f-stop of 8.0 and exposure length of 20 seconds. The variable p1 is the value for the star extinction coefficient, where p0 is the instrumental magnitude that the Pentax camera would observe if no atmosphere was present. For a proportion of images, the moon was above the horizon but not within the field of view of the camera.

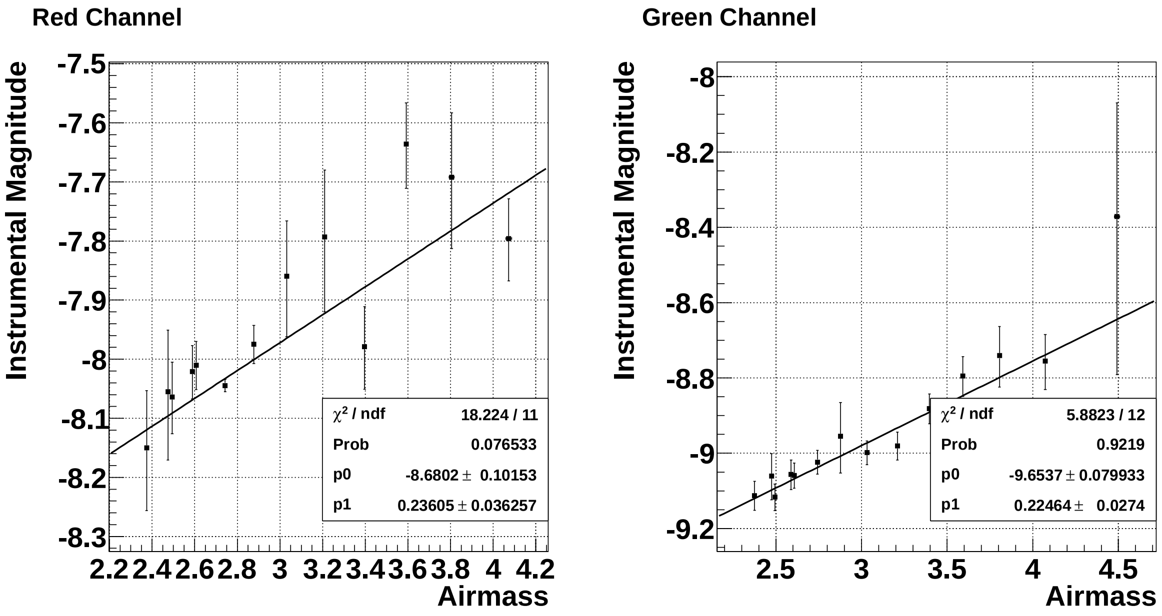

Figure B.35: Star extinction coefficient plots for ε - Crucis. Images used in plots were taken on the 13-12-2010 with camera settings of 1600 ISO, f-stop of 8.0 and exposure length of 20 seconds. The variable p1 is the value for the star extinction coefficient, where p0 is the instrumental magnitude that the Pentax camera would observe if no atmosphere was present. For a proportion of images, the moon was above the horizon but not within the field of view of the camera.

Figure B.36: Star extinction coefficient plots for δ - Crucis. Images used in plots were taken on the 13-12-2010 with camera settings of 1600 ISO, f-stop of 8.0 and exposure length of 20 seconds. The variable p1 is the value for the star extinction coefficient, where p0 is the instrumental magnitude that the Pentax camera would observe if no atmosphere was present. For a proportion of images, the moon was above the horizon but not within the field of view of the camera.

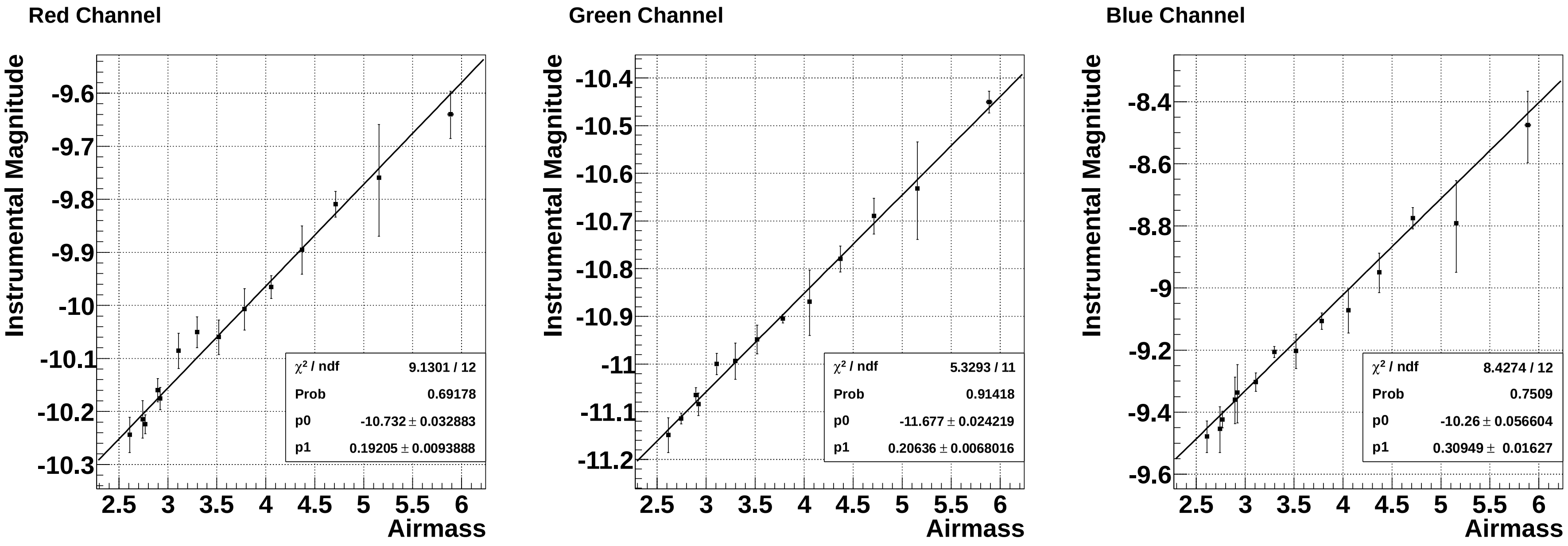

Figure B.37: Star extinction coefficient plots for γ - Crucis. Images used in plots were taken on the 13-12-2010 with camera settings of 1600 ISO, f-stop of 8.0 and exposure length of 20 seconds. The variable p1 is the value for the star extinction coefficient, where p0 is the instrumental magnitude that the Pentax camera would observe if no atmosphere was present. For a proportion of images, the moon was above the horizon but not within the field of view of the camera.

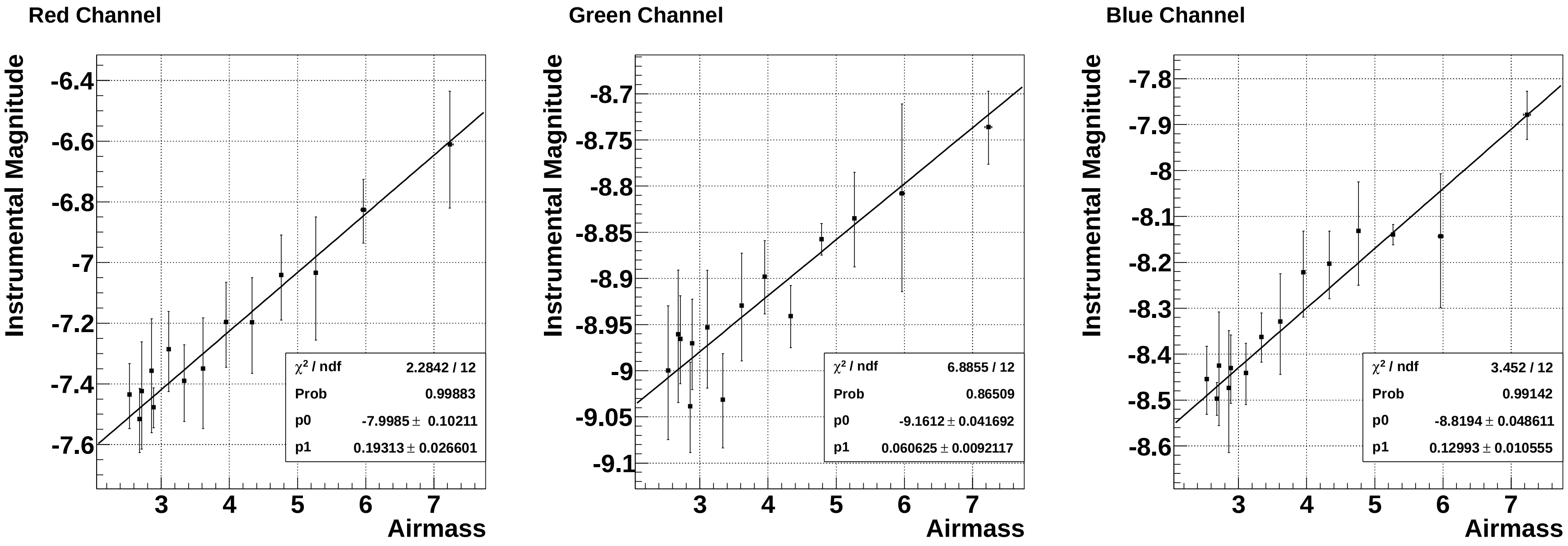

Figure B.38: Star extinction coefficient plots for δ - Centauri. Images used in plots were taken on the 13-12-2010 with camera settings of 1600 ISO, f-stop of 8.0 and exposure length of 20 seconds. The variable p1 is the value for the star extinction coefficient, where p0 is the instrumental magnitude that the Pentax camera would observe if no atmosphere was present. For a proportion of images, the moon was above the horizon but not within the field of view of the camera.

B.4 13/12/2010: Taurus

Star extinction coefficient plots shown here for the camera settings of 400, 800, and 1600 ISO, exposure length of 20 seconds, and f-stop settings of 8.0. Each plot is fitted with the linear line in the form of y = p1 × x + p0, where p1 is the extinction coefficient, x is the airmass, and p0 is the instrumental magnitude the Pentax camera would observe if no atmosphere was present. Order of the figures is:

Star Name	**ISO Setting**	**Channel**		
		Red	**Green**	**Blue**
γ - Orionis	400	√	√	√
α - Tauri	400	√	√	√
β - Tauri	400	√	√	√
o - Tauri	800			√
ξ - Tauri	400	√	√	√
f - Tauri	800		√	
λ - Tauri	800	√	√	√
ε - Tauri	800	√	√	√
ζ - Tauri	800	√		√
β - Tauri	800	√	√	√
ι - Aurigae	800	√	√	√
f - Tauri	1600	√	√	√
λ - Tauri	1600	√		
ε - Tauri	1600	√	√	√
ζ - Tauri	1600	√	√	√
β - Tauri	1600	√		
ι - Aurigae	1600	√	√	√

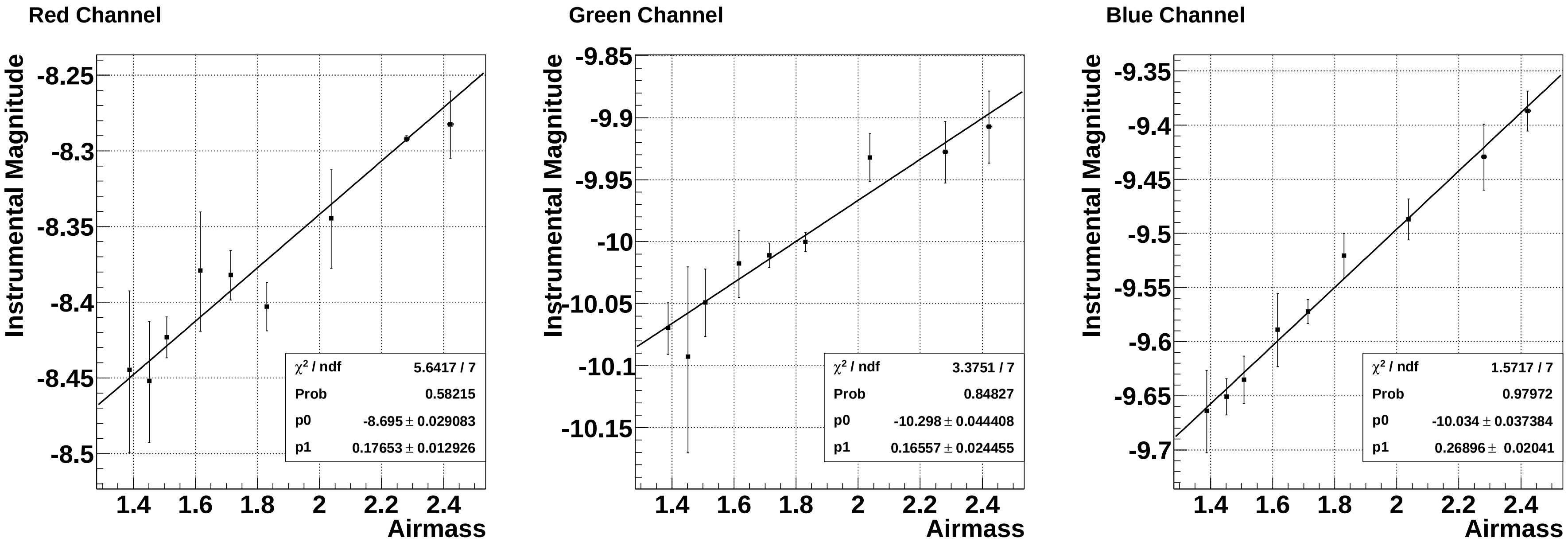

Figure B.39: Star extinction coefficient plots for γ - Orionis. Images used in plots were taken on the 13-12-2010 with camera settings of 400 ISO, f-stop of 8.0 and exposure length of 20 seconds. The variable p1 is the value for the star extinction coefficient, where p0 is the instrumental magnitude that the Pentax camera would observe if no atmosphere was present.

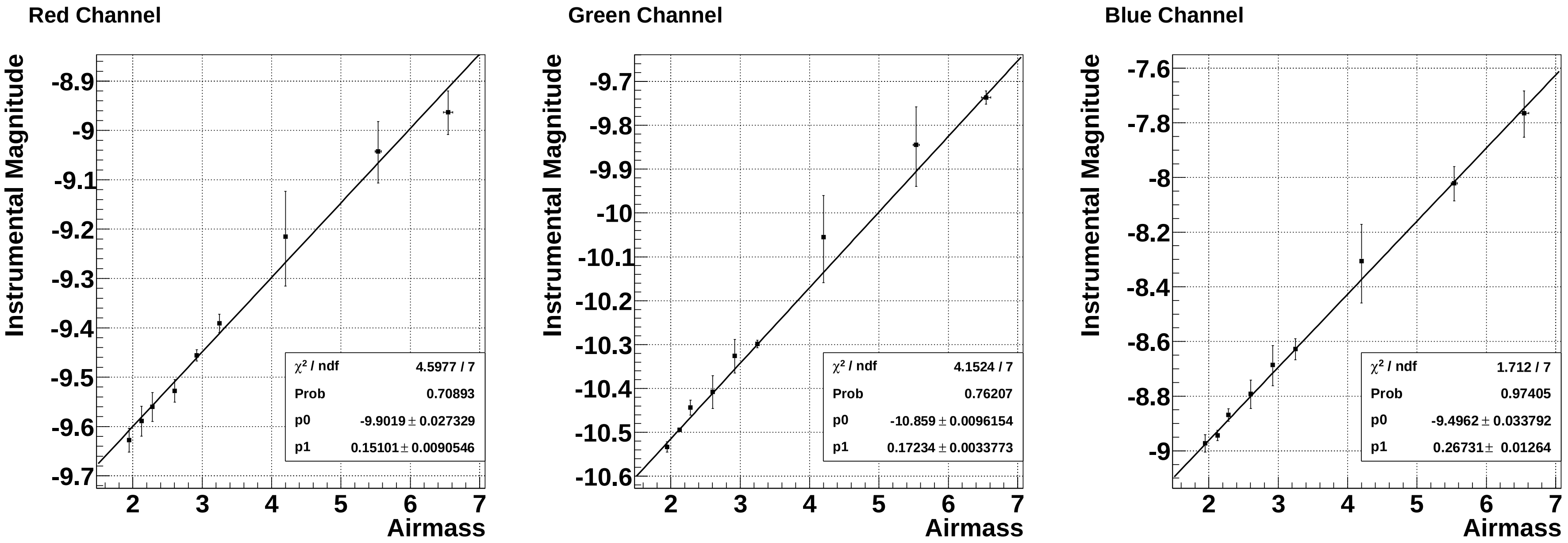

Figure B.40: Star extinction coefficient plots for α - Tauri. Images used in plots were taken on the 13-12-2010 with camera settings of 400 ISO, f-stop of 8.0 and exposure length of 20 seconds. The variable p1 is the value for the star extinction coefficient, where p0 is the instrumental magnitude that the Pentax camera would observe if no atmosphere was present.

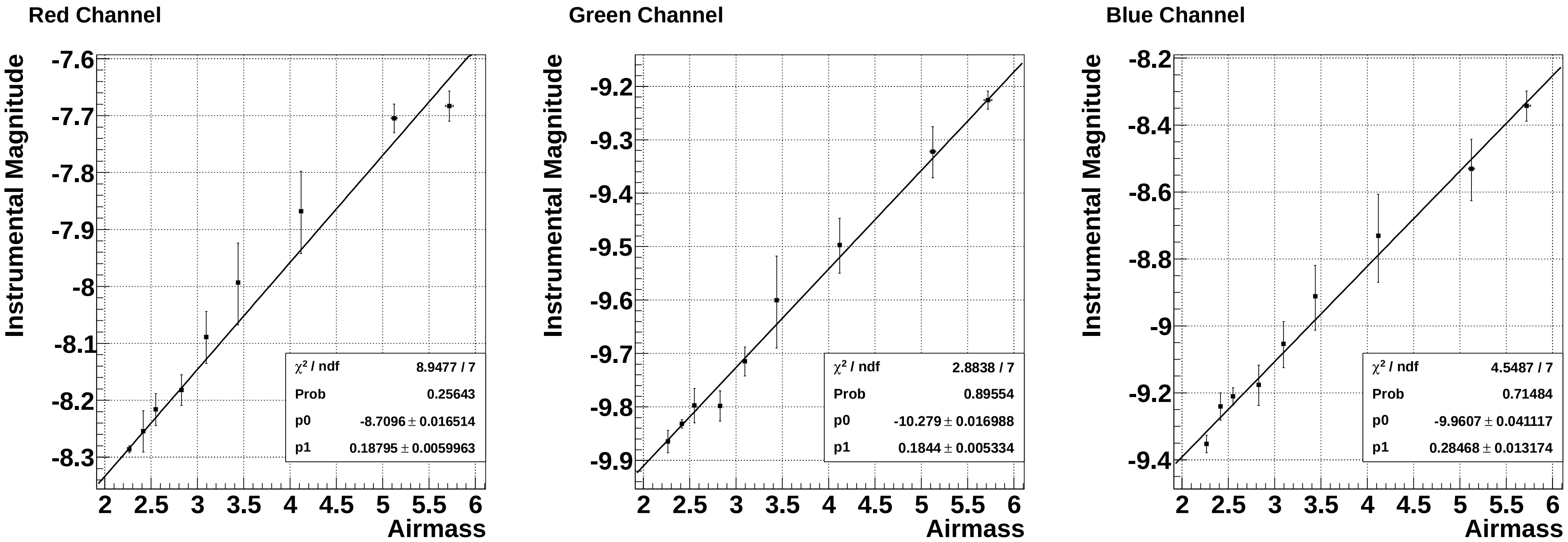

Figure B.41: Star extinction coefficient plots for β - Tauri. Images used in plots were taken on the 13-12-2010 with camera settings of 400 ISO, f-stop of 8.0 and exposure length of 20 seconds. The variable p1 is the value for the star extinction coefficient, where p0 is the instrumental magnitude that the Pentax camera would observe if no atmosphere was present.

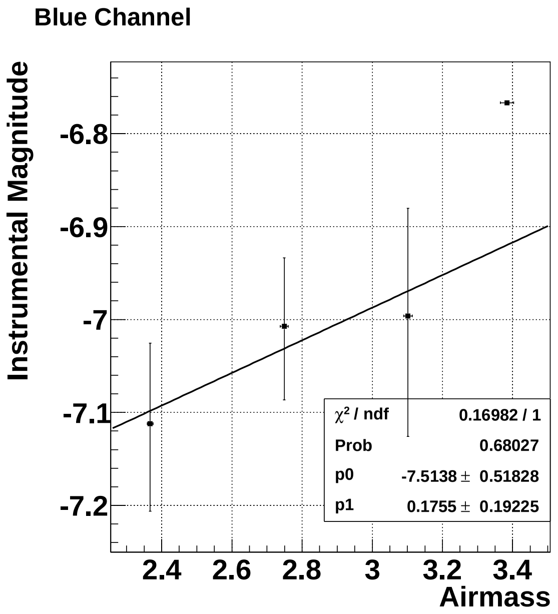

Figure B.42: Star extinction coefficient plots for o - Tauri. Images used in plots were taken on the 13-12-2010 with camera settings of 800 ISO, f-stop of 8.0 and exposure length of 20 seconds. The variable p1 is the value for the star extinction coefficient, where p0 is the instrumental magnitude that the Pentax camera would observe if no atmosphere was present.

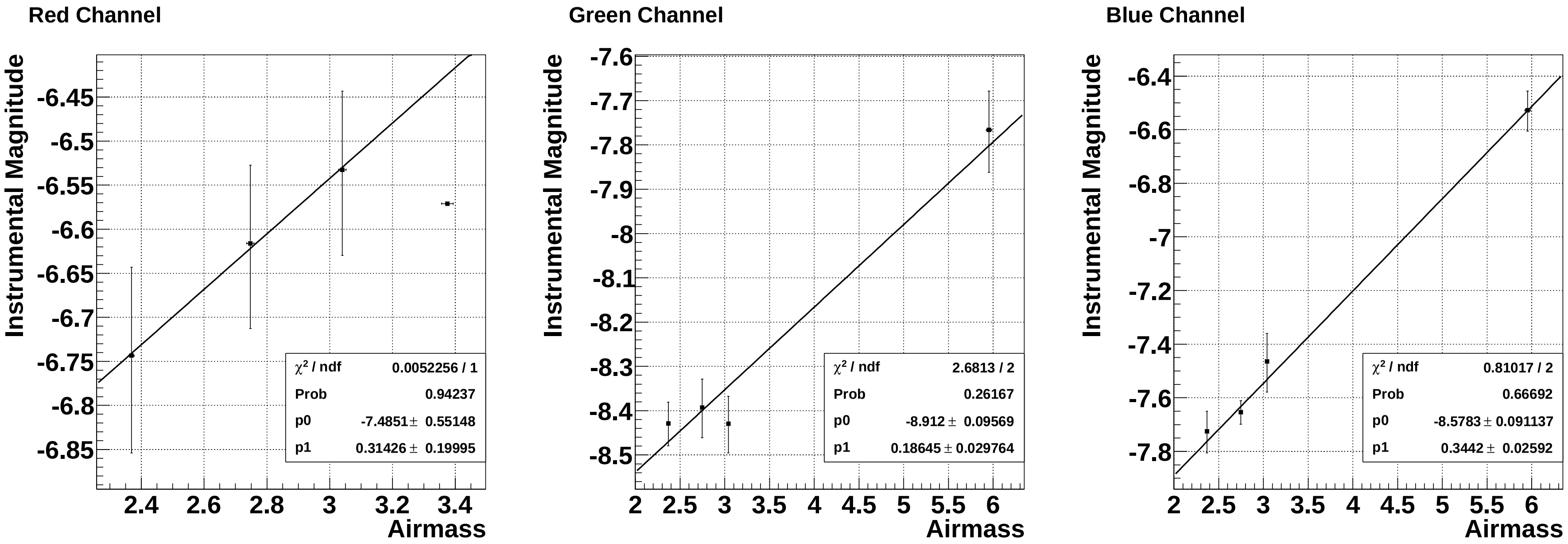

Figure B.43: Star extinction coefficient plots for ξ - Tauri. Images used in plots were taken on the 13-12-2010 with camera settings of 800 ISO, f-stop of 8.0 and exposure length of 20 seconds. The variable p1 is the value for the star extinction coefficient, where p0 is the instrumental magnitude that the Pentax camera would observe if no atmosphere was present.

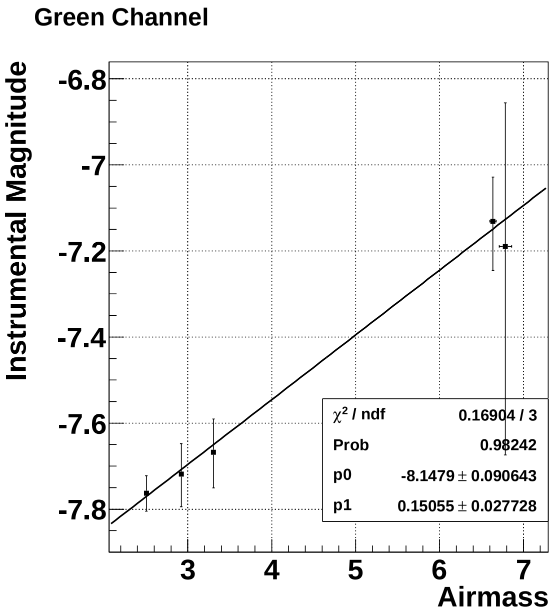

Figure B.44: Star extinction coefficient plots for f - Tauri. Images used in plots were taken on the 13-12-2010 with camera settings of 800 ISO, f-stop of 8.0 and exposure length of 20 seconds. The variable p1 is the value for the star extinction coefficient, where p0 is the instrumental magnitude that the Pentax camera would observe if no atmosphere was present.

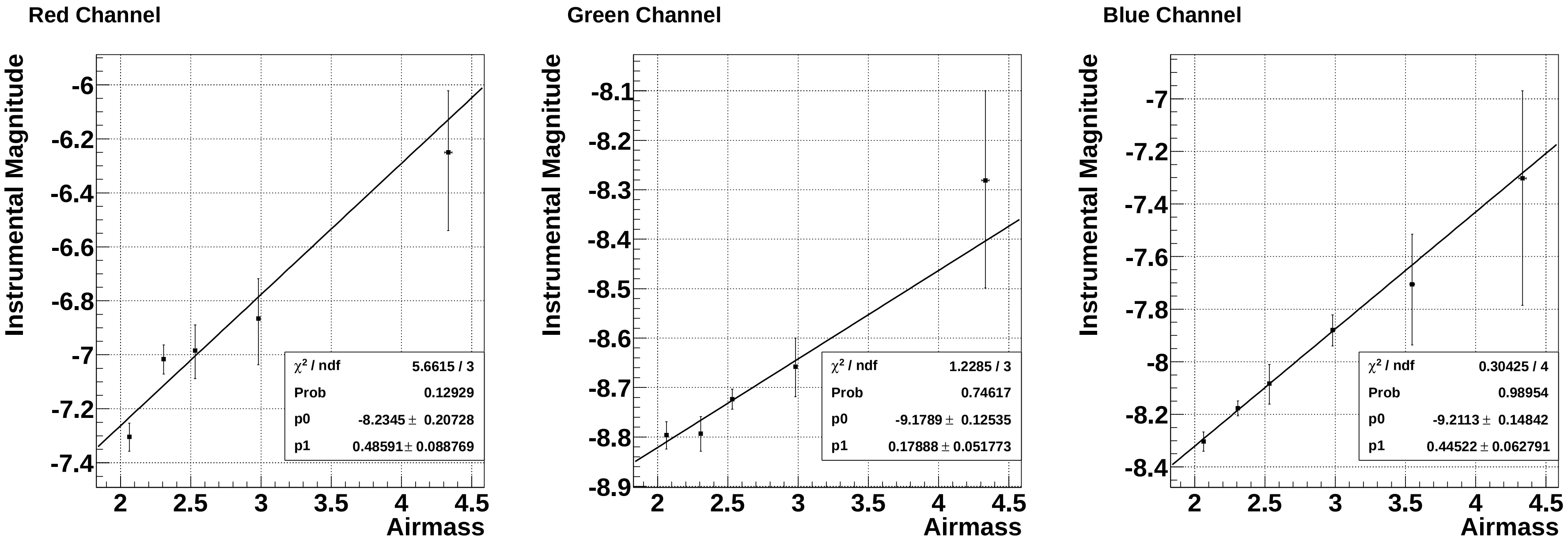

Figure B.45: Star extinction coefficient plots for λ - Tauri. Images used in plots were taken on the 13-12-2010 with camera settings of 800 ISO, f-stop of 8.0 and exposure length of 20 seconds. The variable p1 is the value for the star extinction coefficient, where p0 is the instrumental magnitude that the Pentax camera would observe if no atmosphere was present.

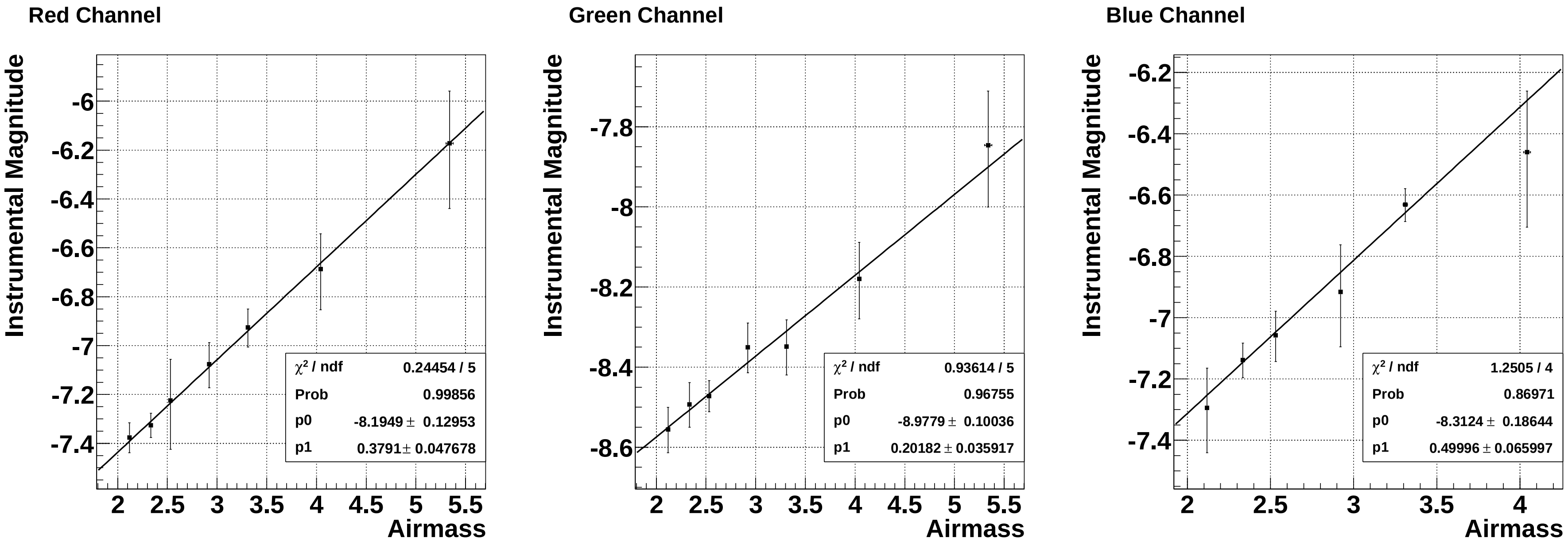

Figure B.46: Star extinction coefficient plots for ε - Tauri. Images used in plots were taken on the 13-12-2010 with camera settings of 800 ISO, f-stop of 8.0 and exposure length of 20 seconds. The variable p1 is the value for the star extinction coefficient, where p0 is the instrumental magnitude that the Pentax camera would observe if no atmosphere was present.

Figure B.47: Star extinction coefficient plots for ζ - Tauri. Images used in plots were taken on the 13-12-2010 with camera settings of 800 ISO, f-stop of 8.0 and exposure length of 20 seconds. The variable p1 is the value for the star extinction coefficient, where p0 is the instrumental magnitude that the Pentax camera would observe if no atmosphere was present.

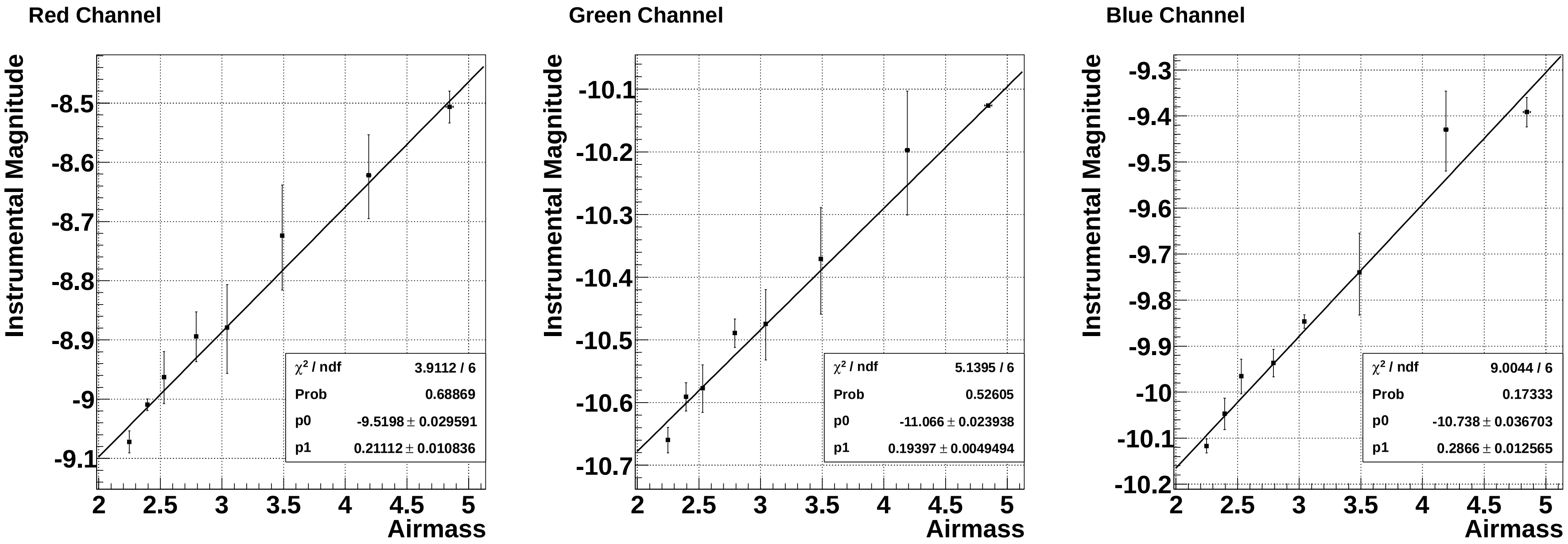

Figure B.48: Star extinction coefficient plots for β - Tauri. Images used in plots were taken on the 13-12-2010 with camera settings of 800 ISO, f-stop of 8.0 and exposure length of 20 seconds. The variable p1 is the value for the star extinction coefficient, where p0 is the instrumental magnitude that the Pentax camera would observe if no atmosphere was present.

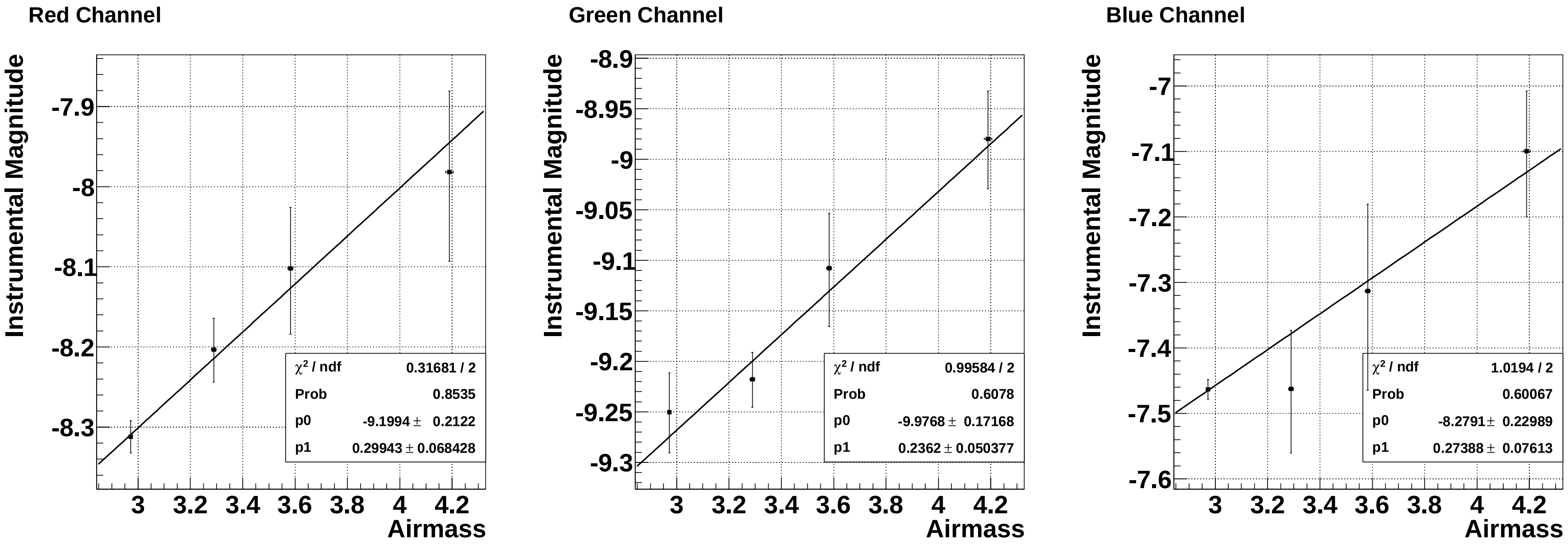

Figure B.49: Star extinction coefficient plots for ι - Aurigae. Images used in plots were taken on the 13-12-2010 with camera settings of 800 ISO, f-stop of 8.0 and exposure length of 20 seconds. The variable p1 is the value for the star extinction coefficient, where p0 is the instrumental magnitude that the Pentax camera would observe if no atmosphere was present.

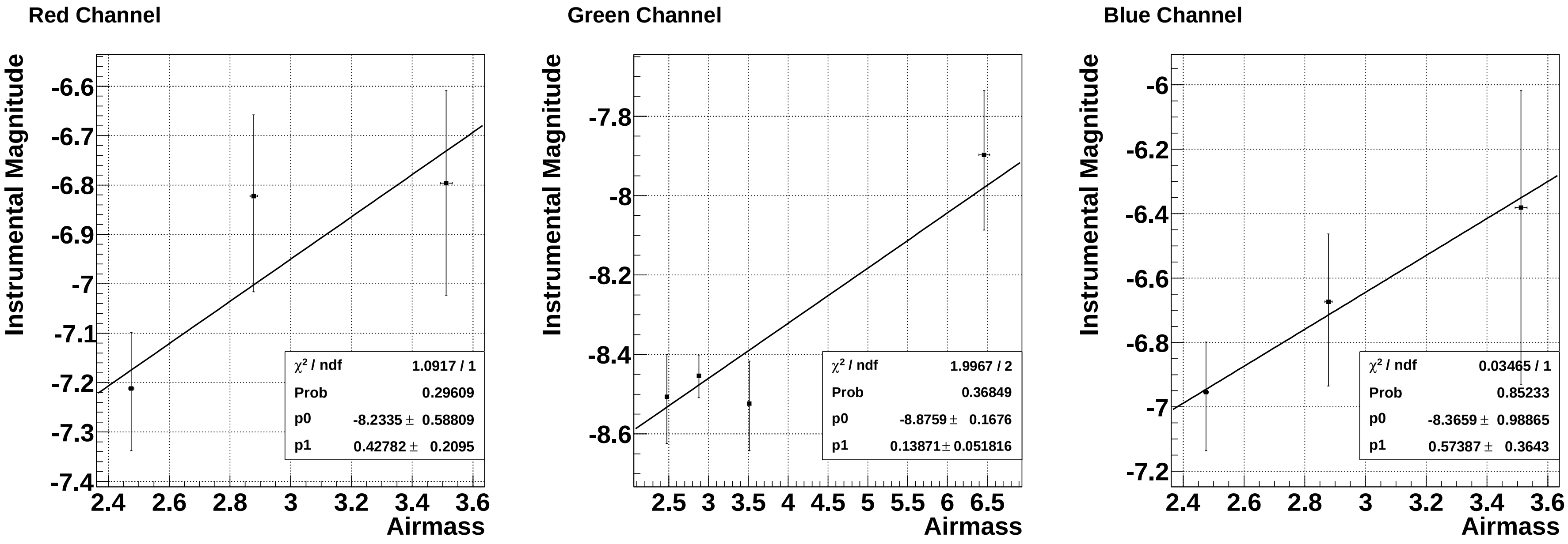

Figure B.50: Star extinction coefficient plots for f - Tauri. Images used in plots were taken on the 13-12-2010 with camera settings of 1600 ISO, f-stop of 8.0 and exposure length of 20 seconds. The variable p1 is the value for the star extinction coefficient, where p0 is the instrumental magnitude that the Pentax camera would observe if no atmosphere was present.

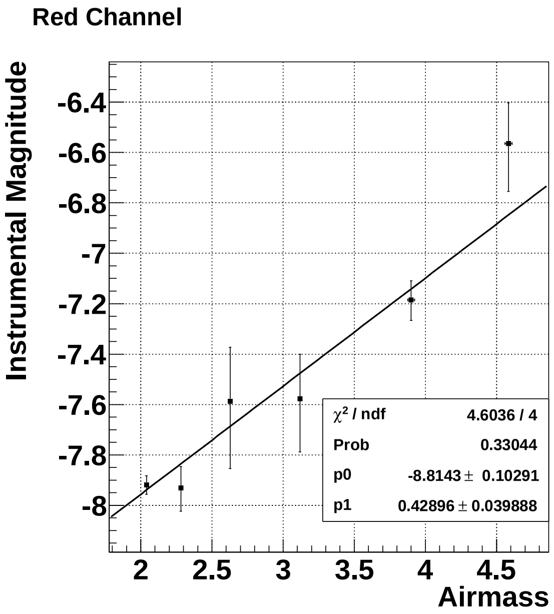

Figure B.51: Star extinction coefficient plots for λ - Tauri. Images used in plots were taken on the 13-12-2010 with camera settings of 1600 ISO, f-stop of 8.0 and exposure length of 20 seconds. The variable p1 is the value for the star extinction coefficient, where p0 is the instrumental magnitude that the Pentax camera would observe if no atmosphere was present.

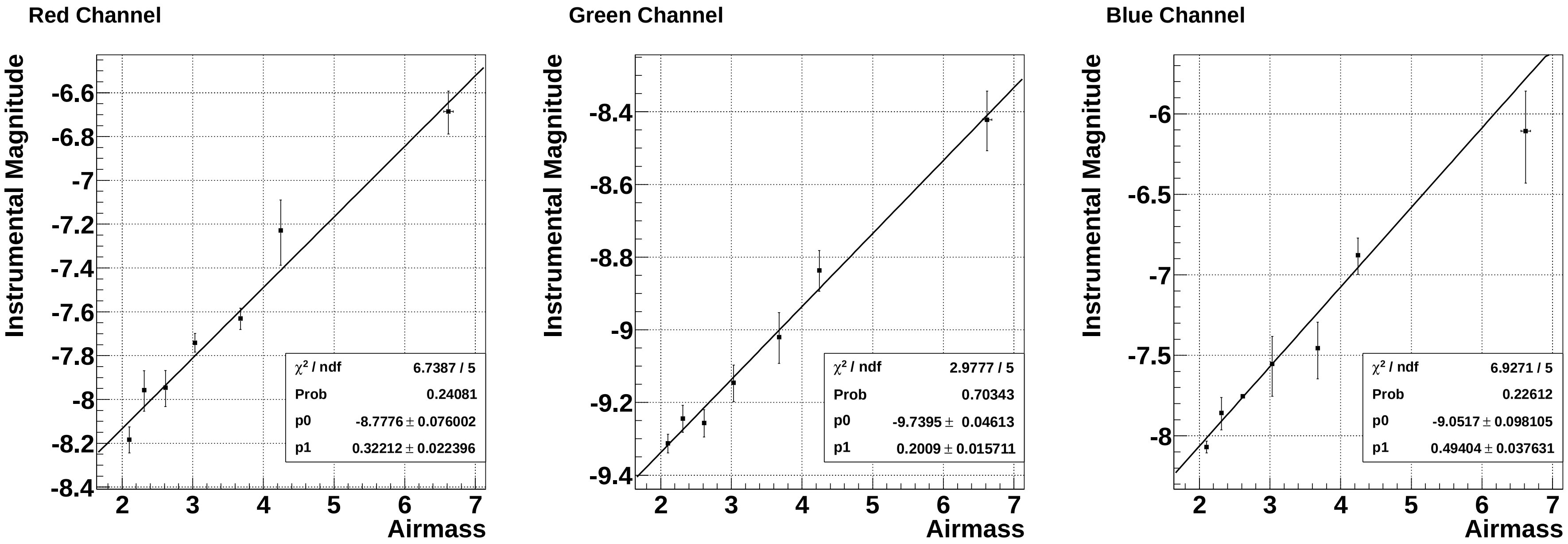

Figure B.52: Star extinction coefficient plots for ε - Tauri. Images used in plots were taken on the 13-12-2010 with camera settings of 1600 ISO, f-stop of 8.0 and exposure length of 20 seconds. The variable p1 is the value for the star extinction coefficient, where p0 is the instrumental magnitude that the Pentax camera would observe if no atmosphere was present.

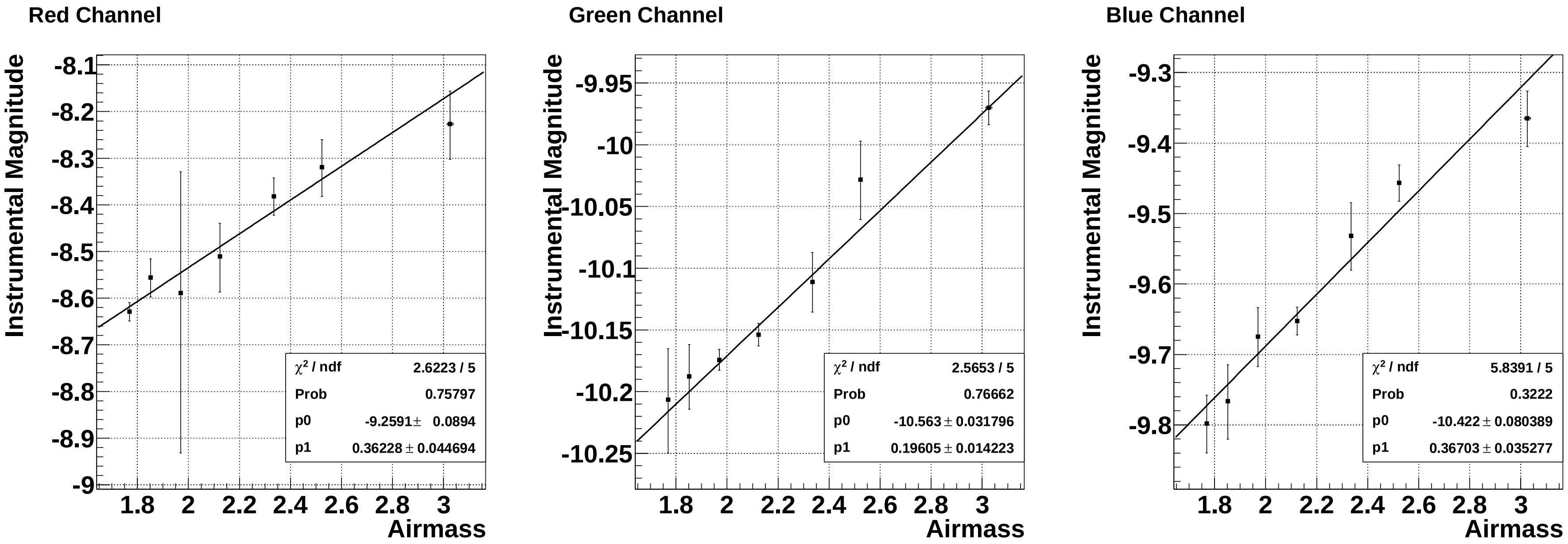

Figure B.53: Star extinction coefficient plots for ζ - Tauri. Images used in plots were taken on the 13-12-2010 with camera settings of 1600 ISO, f-stop of 8.0 and exposure length of 20 seconds. The variable p1 is the value for the star extinction coefficient, where p0 is the instrumental magnitude that the Pentax camera would observe if no atmosphere was present.

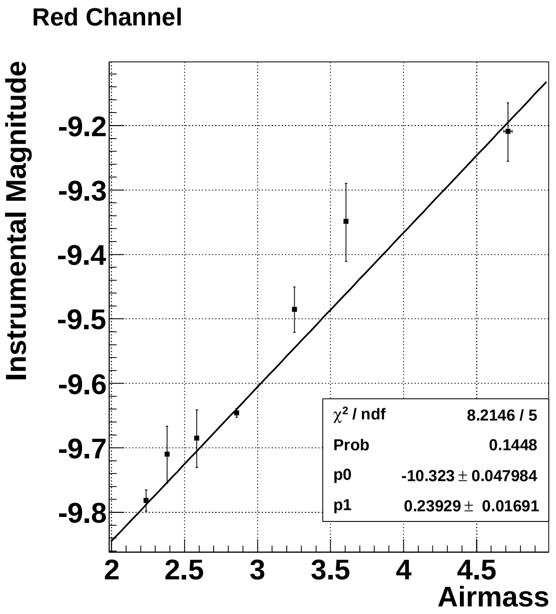

Figure B.54: Star extinction coefficient plots for β - Tauri. Images used in plots were taken on the 13-12-2010 with camera settings of 1600 ISO, f-stop of 8.0 and exposure length of 20 seconds. The variable p1 is the value for the star extinction coefficient, where p0 is the instrumental magnitude that the Pentax camera would observe if no atmosphere was present.

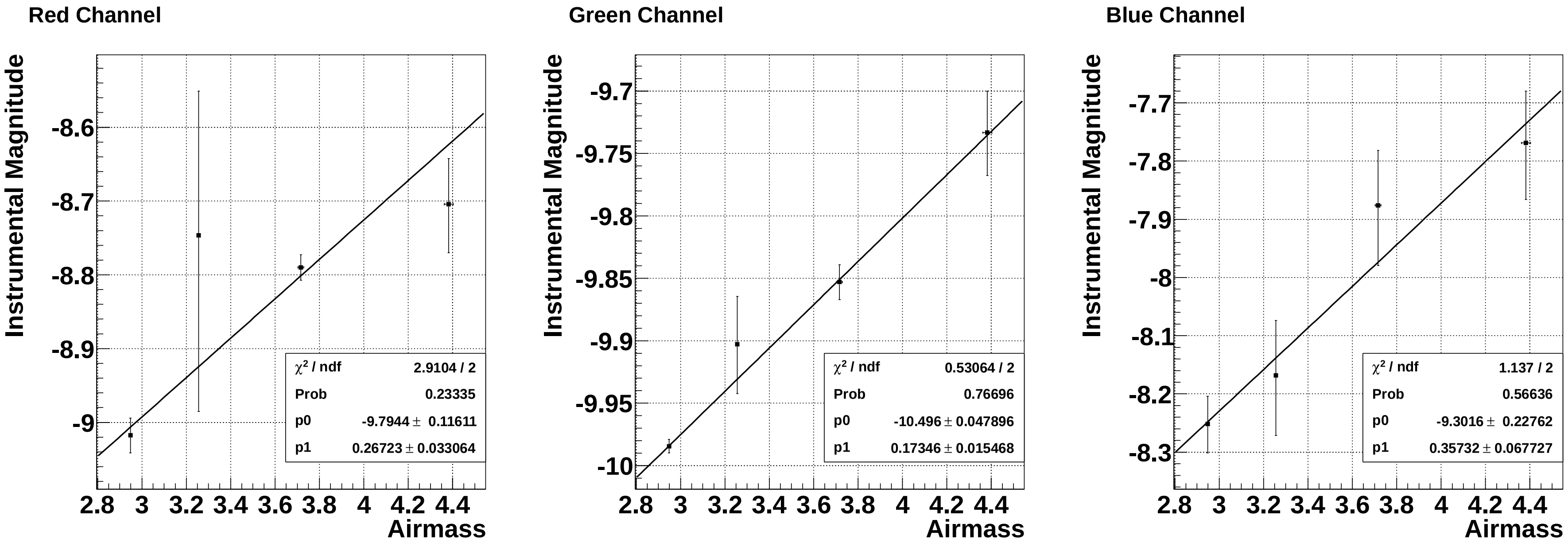

Figure B.55: Star extinction coefficient plots for ι - Aurigae. Images used in plots were taken on the 13-12-2010 with camera settings of 1600 ISO, f-stop of 8.0 and exposure length of 20 seconds. The variable p1 is the value for the star extinction coefficient, where p0 is the instrumental magnitude that the Pentax camera would observe if no atmosphere was present.

Appendix C

Coordinate Conversion and Plate Constant

I show the coordinate system conversions to go from an image plane to an equatorial system using the plate constant method. From the equatorial coordinate system, I show the conversion that was used to get to either the horizontal or galactic coordinate system.

The star-field image used to calculate the night sky background (NSB) had a series of coordinate systems applied for both analytical and aesthetic reasons. The analytical parts was to convert all of the NSB to one airmass. This was necessary as the image covered a range of airmass, which influences the measured NSB. First off, a plate constant [67] is applied to the image. The plate constant allows an right accession (RA) and declination (Dec) to be assigned to individual pixels. As the image was taken with the camera set on the largest FoV, a plate constant with "first-order" terms was used.

$$\mathrm{X = Ax + By + C + Gx^2 + Hy^2 + Ixy} \tag{C.1}$$

$$\mathrm{Y = Dx + Ey + F + Jx^2 + Ky^2 + Lxy} \tag{C.2}$$

where (x,y) are coordinates of the image pixels, X is the RA, Y is the Dec, and A to L are the plate constant. I found the plate constant by fitting the equations to known pixel, RA and Dec of stars within the image. Once the RA and Dec is assigned to each pixel, either a horizontal or galactic coordinate system can be applied. To calculate the airmass, the altitude of each pixel must be calculated. This can be done by converting from equatorial (RA and Dec) to horizontal (altitude and azimuth):

$$\mathrm{H = t} - \alpha \tag{C.3}$$

$$\sin(a) = \sin(\delta)\sin(\varphi) + \cos(\delta)\cos(\varphi)\cos(H) \tag{C.4}$$

$$\sin(A) = -\sin(H)\cos(\delta)/\cos(a) \tag{C.5}$$

where H is the local hour angle, α is the RA, δ is the Dec, φ is the observer latitude, a is the azimuth and A is the altitude.

The galactic coordinates were calculated to highlight the galactic plane within the star images used for the NSB measurements. The formulae that I used was taken from [68]. First off I define some of the parameters:

Galactic North Pole		**Epoch 2000.0**
Right Ascension	α_g	192.85°
Declination	δ_g	27.128°
Galactic Centre		
Right Ascension	α_C	266.4°
Declination	δ_C	-28.930°
Celestial Coordinates		
Right Ascension	α_X	
Declination	δ_X	

To convert from equatorial to galactic coordinates, start with calculating the galactic latitude (B):

$$\mathrm{B} = \arcsin\left[\sin(\delta_X)\cos(\delta_g) + \cos(\delta_X)\cos(\delta_g)\cos(\alpha_X - \alpha_g)\right] \tag{C.6}$$

To calculate the galactic longitude, three intermediate calculations must be made. The three intermediate calculations are:

$$\mathrm{J} = \frac{\sin(\delta_X)\cos(\delta_g) - \cos(\delta_X)\sin(\delta_g)\cos(\alpha_X - \alpha_g)}{\cos(\mathrm{B})} \tag{C.7}$$

$$\mathrm{K} = \arcsin\left[\frac{\cos(\delta_X)\sin(\alpha_X - \alpha_g)}{\cos(B)}\right] \tag{C.8}$$

$$\mathrm{Q} = \arccos\left[\frac{\sin(\delta_C)}{\cos(\delta_g)}\right] \tag{C.9}$$

From the intermediate calculations, the galactic longitude (L) is found via:

$$\text{if J} < 0\text{, then L} = \text{Q} + \text{K - } 180^\circ \tag{C.10}$$

$$\text{otherwise, L} = \text{Q - K} \tag{C.11}$$

$$\text{if L} < 0\text{, then L} = \text{L} + 360^\circ \tag{C.12}$$

Appendix D

NSB Uncertainty Plots

Uncertainty profiles from the process of measuring the night sky background (NSB) at Fowlers Gap. The process to measure the NSB is explained in Chapter 5. The uncertainty was calculated by measuring the fluctuations of pixel values within each 52 by 52 pixel grid. The fluctuations between pixel values are caused by differences in the incoming photon numbers seen by each pixels, and varying dark and thermal noise between pixels. The list of uncertainty profiles are:

- Uncertainty profile for Green channel for image taken on the 11-8-2010
- Uncertainty profile for Blue channel for image taken on the 11-8-2010
- Uncertainty profile for Green channel for image taken on the 13-12-2010
- Uncertainty profile for Blue channel for image taken on the 13-12-2010

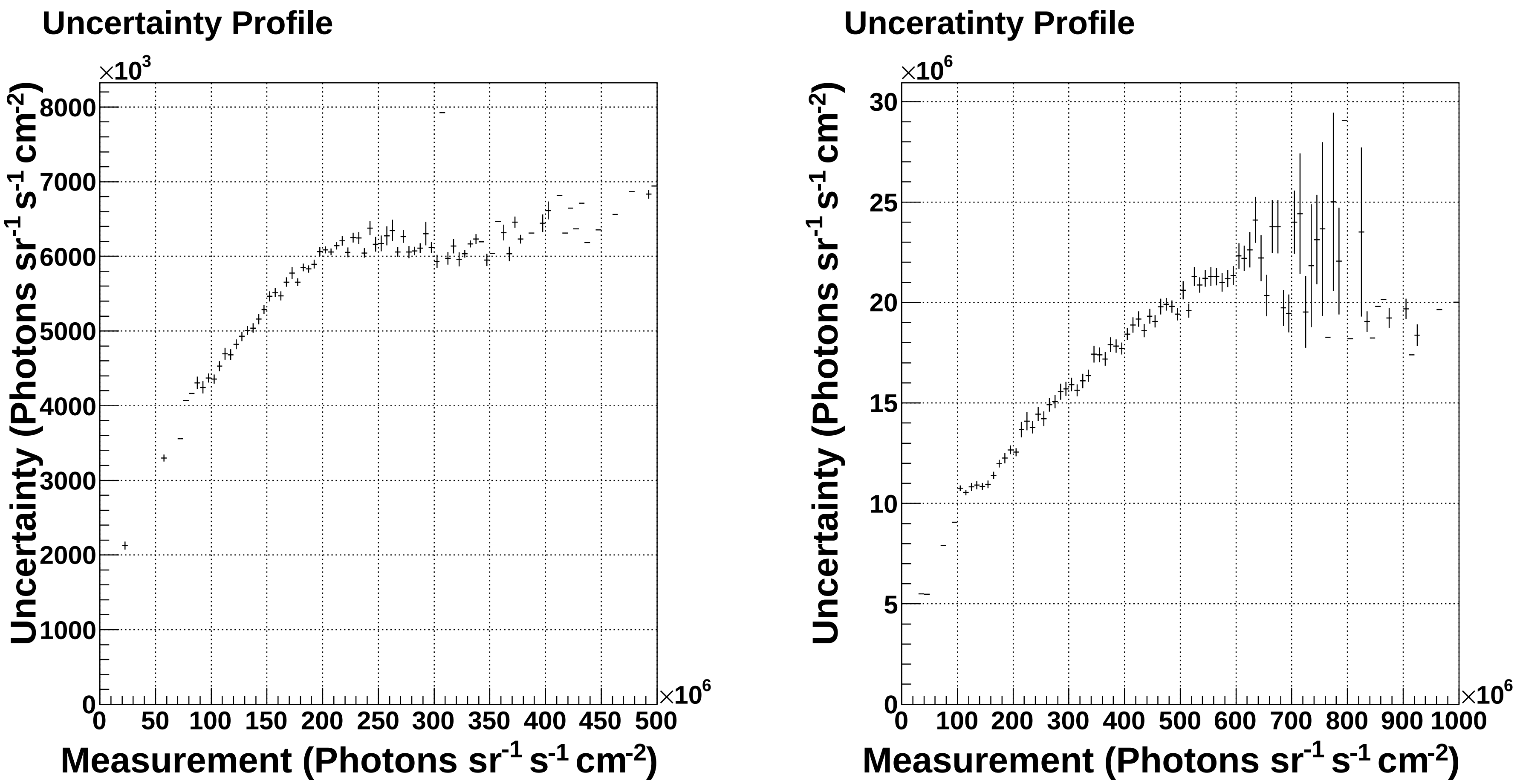

(a)

(b)

Figure D.1: Uncertainty profiles for the measured NSB values from the image taken on the 11-08-2010 at Fowlers Gap. (a) is the Green channel uncertainty profile and (b) is the blue channel uncertainty profile. Camera setting used was 400 ISO, exposure length of 20 seconds and f-stop of 3.5 .

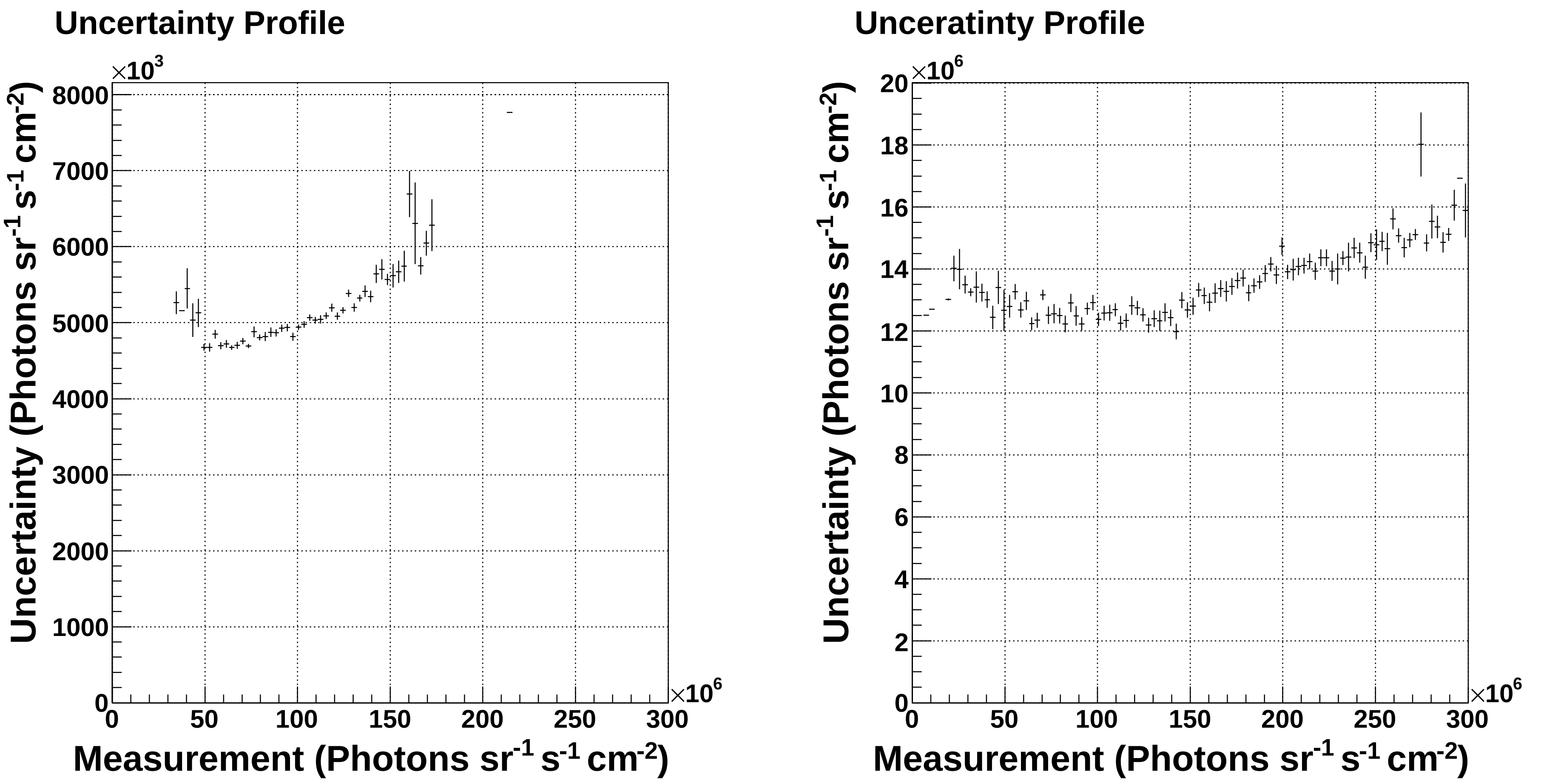

(a)

(b)

Figure D.2: Uncertainty profiles for the measured NSB values taken on the 13-12-2010 at Fowlers Gap. (a) is the Green channel uncertainty profile and (b) is the blue channel uncertainty profile. Camera setting used was 400 ISO, exposure length of 20 seconds and f-stop of 3.5 .

Bibliography

[1] Hess, V. F. (1912) Über Beoabachtungen der durchdringenden Strahlung bei sieben Freiballonfahrt. *Physikalische Zeitschrift*, **13**, 1084–1091.

[2] Cocconi, G. (1960) An air shower telescope and the detection of 10^{12} eV photon sources. V. I. Zatsepin & B. A. Khrenov (ed.), *Moscow Cosmic Ray Conference, Volume II: Extensive Air Showers and Cascades Process*, p. 309.

[3] Fazio, G. G., Helmken, H. F., O'Mongain, E., and Weekes, T. C. (1972) Detection of High-Energy Gamma Rays from the Crab Nebula. *Astrophysical Journal, Letters*, **175**, L117.

[4] Weekes, T. C., et al. (1989) Observation of TeV gamma rays from the Crab nebula using the atmospheric Cerenkov imaging technique. *Astrophysical Journal*, **342**, 379–395.

[5] Hillas, A. M. (1985) Cerenkov light images of EAS produced by primary gamma. vol. 3 of *International Cosmic Ray Conference, La Jolla*, pp. 445–448.

[6] HEGRA Project website ,
http://www.mpi-hd.mpg.de/hfm/CT/CT.html.

[7] H.E.S.S. Project website,
http://www.mpi-hd.mpg.de/hfm/HESS/HESS.html.

[8] CANGAROO Project website , *http://icrhp9.icrr.u-tokyo.ac.jp/*.

[9] MAGIC Project website , *http://wwwmagic.mppmu.mpg.de*.

[10] VERITAS Project website, *http://veritas.sao.arizona.edu/*.

[11] TeVCat, *http://tevcat.uchicago.edu/*. Last accessed Jul. 2012.

[12] Aharonian, F. A., et al. (2004) High-energy particle acceleration in the shell of a supernova remnant. *Nature*, **432**, 75–77.

[13] Aharonian, F., et al. (2007) Detection of extended very-high-energy γ-ray emission towards the young stellar cluster Westerlund 2. *Astronomy and Astrophysics*, **467**, 1075–1080.

[14] Aharonian, F., et al. (2005) Discovery of Very High Energy Gamma Rays Associated with an X-ray Binary. *Science*, **309**, 746–749.

[15] Quinn, J., et al. (1996) Detection of Gamma Rays with E > 300 GeV from Markarian 501. *Astrophysical Journal*, **456**, L83.

[16] Aharonian, F., et al. (2007) Primary particle acceleration above 100 TeV in the shell-type supernova remnant RX J1713.7-3946 with deep HESS observations. *A&A*, **464**, 235–243.

[17] Aharonian, F., et al. (2008) HESS very-high-energy gamma-ray sources without identified counterparts. *A&A*, **477**, 353–363.

[18] Aharonian, F., et al. (2006) Observations of the Crab nebula with HESS. *A&A*, **457**, 899–915.

[19] CTA Consortium, T. (2010) Design Concepts for the Cherenkov Telescope Array. *ArXiv e-prints*, (astro-ph.IM).

[20] Rowell, G. P., Stamatescu, V., Clay, R. W., Dawson, B. R., Protheroe, R. J., Smith, A. G. K., Thornton, G. J., and Wild, N. (2008) TenTen: A new IACT array for multi-TeV γ-ray astronomy. *Nuclear Instruments and Methods in Physics Research A*, **588**, 48–51.

[21] Schlenker, S. (2001), Simulation Study of the H.E.S.S. Single Telescope Trigger Rate, Diploma Thesis. Humboldt University of Berlin, Germany.

[22] Dunbar, R. (2007), Rejection of Night Sky Background in a new gamma-ray detection instrument: TenTen, Honours Thesis. University of Adelaide, Australia.

[23] Benn, C. R. and Ellison, S. L., La Palma Night-Sky Brightness. La Palma technical note 115, *http://www.ing.iac.es/Astronomy/observing/conditions/skybr/skybr.html*, last access Oct. 2011.

[24] May, B. (2008) *A Survey of Radial Velocities in the Zodiacal Dust Cloud*. Springer.

[25] Heitler, W. (1954) *The quantum theory of radiation*. (Clarendon Press, Ed. 3, Oxford).

[26] Gaisser, T. K. (1991) *Cosmic Rays and Particle Physics*. Cambridge University Press.

[27] Hillas, A. M. (1996) Differences between Gamma-Ray and Hadronic Showers. *Space Science Reviews*, **75**, 17–30.

[28] Jelley, J. V. (1958) *Cerenkov radiation and its applications*. (Pergamon, London).

[29] Bethe, H. A. (1953) Molière's theory of multiple scattering. *Phys. Rev.*, **89**, 1256–1266.

[30] Planetary Atmospheres: the Terrestrial Worlds, *http://burro.cwru.edu/Academics/Astr201/Atmosphere/atmosphere1.html*. Last Accessed May 2011.

[31] McCarthy, E. J. (1976) *Optics of the Atmosphere: Scattering by Molecules and Particles*. (John Wiley & Sons Inc, New York).

[32] Kyle, T. G. (1991) *Atmospheric Transmission: Emission & Scattering*. (Pergamon, London).

[33] Twomey, S. (1977) *Atmospheric Aerosols*. (Elsevier Scientific Pub. Co., New York).

[34] Berge, D. (2002), Development of an Algorithm for the Shower Reconstruction with the H.E.S.S. Telescope System, Mater Thesis. Humboldt University of Berlin, Germany.

[35] Konopelko, A., Lucarelli, F., Lampeitl, H., and Hofmann, W. (2002) Monte Carlo studies on the sensitivity of the HEGRA imaging atmospheric Cerenkov telescope system in observations of extended gamma-ray sources. *Journal of Physics G Nuclear Physics*, **28**, 2755–2770.

[36] Hofmann, W., Jung, I., Konopelko, A., Krawczynski, H., Lampeitl, H., and Pühlhofer, G. (1999) Comparison of techniques to reconstruct VHE gamma-ray showers from multiple stereoscopic Cherenkov images. *Astroparticle Physics*, **12**, 135–143.

[37] Heck, D. , et. al. Report FZKA 6019 (1998), Forschingzentrum Karlsruhe, *http://www-ik.fzk.de/corsika/physics_description/corsika_phs.html*.

[38] Fletcher, R. S., Gaisser, T. K., Lipari, P., and Stanev, T. (1994) Sibyll: An event generator for simulation of high energy cosmic ray cascades. *Physical Review C: Particles, Fields, Graviation & Cosmology*, **50**, 5710–5731.

[39] Bernlöhr, K. (2008) Simulation of imaging atmospheric Cherenkov telescopes with CORSIKA and sim_telarray. *Astroparticle Physics*, **30**, 149–158.

[40] Bernlöhr, K. (2005), sim_telarray v.24.

[41] Kneisys, F. X., et al. (1995), "The modtran 2/3 and lowtran 7 model". MODTRAN Report, 1-268.

[42] Schliesser, A. and Mirzoyan, R. (2005) Wide-field prime-focus imaging atmospheric Cherenkov telescopes: A systematic study. *Astroparticle Physics*, **24**, 382–390.

[43] Hofmann, W. and The H. E. S. S. Collaboration (2001) Status of the H.E.S.S. project. vol. 7 of *International Cosmic Ray Conference, Hamburg*, p. 2785.

[44] Cornils, R., Gillessen, S., Jung, I., Hofmann, W., and H. E. S. S. Collaboration (2005) Point spread function and long-term stability of the H.E.S.S. reflectors. F. A. Aharonian, H. J. Völk, & D. Horns (ed.), *High Energy Gamma-Ray Astronomy*, Feb., vol. 745 of *American Institute of Physics Conference Series*, pp. 736–741.

[45] The Pierre Auger Collaboration, et al. (2011) The Pierre Auger Observatory IV: Operation and Monitoring. *ArXiv e-prints*.

[46] High Resolution Fly'S Eye Collaboration, et al. (2006) A measurement of time-averaged aerosol optical depth using air-showers observed in stereo by HiRes. *Astroparticle Physics*, **25**, 93–97.

[47] Stamatescu, V., Rowell, G. P., Denman, J., Clay, R. W., Dawson, B. R., Smith, A. G. K., Sudholz, T., Thornton, G. J., and Wild, N. (2011) Timing analysis techniques at large core distances for multi-TeV gamma ray astronomy. *Astroparticle Physics*, **34**, 886–896.

[48] Bernloehr, K. (1999) Atmospheric effects on the Cherenkov technique. *International Cosmic Ray Conference*, vol. 5 of *International Cosmic Ray Conference*, p. 276.

[49] Veerabuthiran, S. (2004) High-altitude cirrus clouds and climate. *Resonance*, **9**, 23–32, 10.1007/BF02834985.

[50] Letessier-Selvon, A. and Stanev, T. (2011) Ultrahigh energy cosmic rays. *Reviews of Modern Physics*, **83**, 907–942, (astro-ph.HE).

[51] Janesick, J. R. (2001) *Scientific Charge-Coupled Devices (SPIE Press Monograph Vol. PM83)*. SPIE Publications.

[52] Pentax K10D DLSR camera manual,
http://www.pentax.jp/english/support/man-pdf/k10d.pdf.

[53] Adobe Digital Negative Specification,
http://www.adobe.com/products/photoshop/extend.displayTab2.html.

[54] Sterken, C. and Manfroid, J. (1992) *Astronomical Photometry, A Guide (Astrophysics and Space Science Library)*. Springer.

[55] Budding, E. and Demircan, O. (2007) *Introduction to Astronomical Photometry (Cambridge Observing Handbooks for Research Astronomers)*. Cambridge University Press.

[56] SIMBAD Astronomical Database, *http://simbad.u-strasbg.fr/simbad/*.

[57] Garstang, R. H. (1989) Night-sky brightness at observatories and sites. *Astronomical Society of the Pacific*, **101**, 306–329.

[58] Stallinga, S. and Rieger, B. (2010) Accuracy of the Gaussian Point Spread Function model in 2D localization microscopy. *Optics Express*, **18**, 24461.

[59] Fowlers Gap Research Station website,
http://www.fowlersgap.unsw.edu.au/.

[60] Thornton, G. J., Rowell, G. P., Denman, J., Clay, R. W., Dawson, B. R., Smith, A. G. K., Stamatescu, V., Sudholz, T., and Wild, N. Paper in preparation.

[61] Labate, L., Barbini, A., Gizzi, L. A., Gartside, L. M. R., and Neely, D. (2007/2008) Setup of a commercial digital slr, large area, triggerable ccd camera for optical laser-plasma diagnostics. *Central Laser Facility Annual Report*.

[62] Visual Spec Software, *http://astrosurf.com/vdesnox*. Last Accessed September 2011.

[63] Johnson Filter Responses, *http://spiff.rit.edu/classes/phys440/lectures/filters/filters.html*. Last Accessed May 2013.

[64] Hampf, D., Rowell, G., Wild, N., Sudholz, T., Horns, D., and Tluczykont, M. (2011) Measurement of night sky brightness in southern Australia. *Advances in Space Research*, **48**, 1017–1025.

[65] Preu, S., Hermann, G., Hofmann, W., and Kohnle, A. (2002) Study of the photon flux from the night sky at La Palma and Namibia, in the wavelength region relevant for imaging atmospheric Cherenkov telescopes. *Nuclear Instruments and Methods in Physics Research A*, **481**, 229–240.

[66] Benn, C. R. and Ellison, S. L. (1998) Brightness of the night sky over La Palma. *New Astronomy Reviews*, **42**, 503–507.

[67] Buchheim, R. (2007) *The Sky is Your Laboratory: Advanced Astronomy Projects for Amateurs (Springer Praxis Books / Popular Astronomy)*. Praxis.

[68] oocities.org, *http://www.oocities.org/alt_cosmos/files/galactic.pdf*. Last Accessed May 2011.